UNIVERSITAT AUTÒNOMA DE BARCELONA

DOCTORAL THESIS

Voxel Imaging PET Pathfinder: a Novel Approach to Positron Emission Tomography Based on Room Temperature Pixelated CdTe Detector

---

Author:
Ekaterina MIKHAYLOVA

Directors:
Prof. Mokhtar CHMEISSANI
Dr. Gianluca DE LORENZO

Tutor:
Prof. Enrique FERNANDEZ SANCHEZ

A thesis submitted in fulfilment of the requirements
for the degree of Doctor of Philosophy

in the

Physics Department

April 2014

"The human brain is a wonderful thing. It starts working the moment you are born, and never stops until you stand up to speak in public."

George Jessel

Acknowledgements

I would like to deeply thank people which during all these years have been leading me to the day of my Ph. D. defence:

- my director, Prof. Mokhtar Chmeissani, for giving me an opportunity to do a research on such an interesting and ambitious project as VIP, and for patiently teaching me the physics of PET.
- my supervisor, Dr. Gianluca De Lorenzo, for his work with me, for helping me with any questions and doubts, and for the leading my research.
- Dr. Machiel Kolstein for helping me in solving problems with the C++ coding.
- Jose Gabriel Macias Montero for explaining the principles of VIP electronics and the VIP smart-pixel functioning.

I am immensely grateful to the whole VIP team for sharing their experience with me, for their collaborative spirit, and their endless support on any issues: Yónatan Calderón, Dilber Uzun, Gerard Arino, Carles Puigdengoles, and Ricardo Martinez. A lot of thanks to the European Research Council (ERC) who funded this research through the Seventh Framework Programme (FP7).

Finally, I thank my parents, Aleksandr and Tatiana, for their continuous support and belief in me, my elder brother, Iliya, and his wife, Nadya, for their optimism and good sense of humor. I give a special gratitude to my dear fiance, Marc, and his family, for bringing love, confidence, and courage to my life.

Contents

List of Figures

List of Tables

Abbreviations

AD	**A**lzheimer s **D**isease
ADC	**A**nalog-to-**D**igital **C**onverter
APD	**A**valanche **P**hoto **D**iode
ASIC	**A**pplication **S**pecific **I**ntegrated **C**ircuit
BGO	$Bi_4Ge_3O_{12}$, bismuth germanate
CIE	**C**harge **I**nduction **E**fficiency
CNR	**C**ontrast-to-**N**oise **R**atio
CPU	**C**entral **P**rocessing **U**nit
CT	**C**omputed **T**omography
CZT	**C**admium **Z**inc **T**elluride
DAC	**D**igital-to-**A**nalog **C**onverter
DICOM	**D**igital **I**maging and **C**ommunications in **M**edicine
DOI	**D**epth **O**f **I**nteraction
ETM	**E**stimation of **T**rues **M**ethod
FBP	**F**iltered **B**ack**P**rojection
FDG	^{18}F-**F**luoro**D**eoxy**G**lucose
fMRI	**f**unctional **MRI**
FOV	**F**ield **O**f **V**iew
FT	**F**ourier **T**ransform
FWHM	**F**ull **W**idth **H**alf **M**aximum
FWTM	**F**ull **W**idth **T**enth **M**aximum
GAMOS	**G**EANT4-based **A**rchitecture for **M**edicine-**O**riented **S**imulations
GEANT	**GE**ometry **AN**d **T**racking
GSO	Gd_2SiO_5:Ce, gadolinium oxyorthosilicate
HV	**H**igh **V**oltage

LGSO	$\mathrm{Lu_{0.4}Gd_{1.6}SiO_5}$
LM	**L**ist **M**ode
LM-OSEM	**L**ist-**M**ode **O**rdered **S**ubset **E**xpectation **M**aximization
LOR	**L**ine **O**f **R**esponse
LSF	**L**ine **S**pread **F**unction
LSO	$\mathrm{Lu_2SiO_5}$:Ce, lutetium oxyorthosilicate
LV	**L**ow **V**oltage
LuYAP	**Lu**tetium-**Y**ttrium **A**luminum **P**erovskite
LYSO	**L**utetium-**Y**ttrium **O**xyortho**S**ilicate
MC	**M**onte **C**arlo
MC-PMT	**M**ulti-**C**hannel **PMT**
ML-EM	**M**aximum **L**ikelihood **E**xpectation **M**aximization
MLS	**M**ixed **L**utetium **S**ilicate
MRI	**M**agnetic **R**esonance **I**maging
MRS	**M**agnetic **R**esonance **S**pectroscopy
MSE	**M**ean **S**quare **E**rror
MTF	**M**odulation **T**ransfer **F**unction
NEC	**N**oise **E**quivalent **C**ount
NEMA	**N**ational **E**lectrical **M**anufacturers **A**ssociation
OE	**O**rigin **E**nsemble
OSEM	**O**rdered **S**ubset **E**xpectation **M**aximization
PCB	**P**rinted **C**ircuit **B**oard
PD	**P**arkinson s **D**isease
PEM	**P**ositron **E**mission **M**ammography
PET	**P**ositron **E**mission **T**omography
PMT	**P**hoto**M**ultiplier **T**ube
PSF	**P**oint **S**pread **F**unction
PS-PMT	**P**osition **S**ensitive **PMT**
QE	**Q**uantum **E**fficiency
RC	**R**ecovery **C**oefficient
RF	**R**adio **F**requency
ROC	**R**ead-**O**ut **C**hip
ROI	**R**egion **O**f **I**nterest

SF	**S**catter **F**raction
SiPM	**Si**licon **P**hoto**M**ultiplier
SNR	**S**ignal-to-**N**oise **R**atio
SOR	**S**pill-**O**ver **R**atio
SPECT	**S**ingle **P**hoton **E**mission **C**omputed **T**omography
SSRB	**S**ingle **S**lice **R**ebinning
STD	**ST**andard **D**eviations
STIR	**S**oftware for **T**omographic **I**mage **R**econstruction
TDC	**T**ime-to-**D**igital **C**onverter
TOF	**T**ime **O**f **F**light
VIP	**V**oxel **I**maging **P**ET
VOI	**V**olume **O**f **I**nterest
WB	**W**hole **B**ody
YSO	$\mathbf{Y}_2\mathbf{SiO}_5$:Ce, yttrium oxyorthosilicate

To my grandparents, survivors of the Second World War, Praskovia and Aleksandr, Nina and Nikolay, that dedicated their entire lives to build peace and happiness for their descendants.

Chapter 1

Introduction

During the past few years positron emission tomography (PET) has become a part of the mainstream clinical applications not only for Oncology, but also in Cardiology and Neuropsychiatry. PET is used in studies of brain metabolism, cardiac function, image sites of infection, and cancer detection world-wide every day. The increasing demand for precise metabolic images especially for the early diagnosis of tumors and other brain related diseases is motivating the research for high-resolution/high-sensitivity PET scanners.

The central aim of this research is the simulation and the evaluation of a novel conceptual PET scanner based on pixelated CdTe detector in the framework of the Voxel Imaging PET (VIP) Pathfinder project [1]. The novel design is simulated with the GEANT4-based Architecture for Medicine-Oriented Simulations (GAMOS) and including the expected CdTe and electronics specifics. The system is tested mostly following the prescriptions of the NEMA protocols for the evaluation of PET devices. Several tests are performed to assess the counting and the imaging performance of the VIP with the accurate modeling of the required experimental conditions. Furthermore, the VIP scanner is also evaluated in more challenging pseudo-clinical conditions with the simulation of the screening of a real human head.

The simulation results show that the excellent energy resolution of the CdTe detectors (down to 1.6% for 511 keV photons at room temperature), together with the small voxel size (1 mm $\times$ 1 mm $\times$ 2 mm), the high CdTe stopping power, and the crack-free ring geometry, give the new design the potential to overcome the intrinsic limitations of state-of-the-art crystal PETs characterized by relatively poor energy resolution ($\sim$ 10%) and large depth of interaction (DOI) uncertainty. The VIP scanner can achieve an image resolution as low as $\sim$ 1 mm full width at half maximum (FWHM) in all directions and collect virtually noise-free data producing excellent quality images in extremely challenging conditions such as the screening of a human head. High quality images can be obtained with significantly smaller number of collected events with respect to the currently available PETs. This characteristic can be used to either increase the throughput of a nuclear medicine hospital unit, or to decrease the injected dose per patient.

This thesis consists of 6 main chapters. The first three chapters include a review of the theoretical and historical background of PET, and its role in the nuclear medicine nowadays. The VIP scanner geometry and its distinctive features are described in the chapter number 5. Chapter 6 describes the simulation of the VIP scanner and study of the counting performance of the new design, while the chapter 7 is dedicated to optimization of the image reconstruction technique and the assessment of the quality of images obtained with the VIP scanner. Finally, the main results are summarized in the conclusive chapter.

Chapter 2

Physics Fundamentals

2.1 Positron physics

In 1928 Paul Dirac postulated that electrons can also have a positive charge [2]. His work did not predict a new particle, just allowed electrons to have either positive or negative charges. Dirac himself was very puzzled why the mathematical model he introduced to unify quantum mechanics and special relativity to explain concept of electron spin (the Dirac equation) allowed the equally valid negative-charge and positive-charge solutions. Later, in 1931, Dirac published a paper that predicted the existence of an unobserved particle that he called an "anti-electron" [3]. According to the paper, the "anti-electron" would have the same mass as an electron and would annihilate with an electron. Dirac's predictions turned true very soon, in 1932, when Carl Anderson experimentally observed these particles and renamed them to positrons [4]. Later it was shown that when positrons interact with electrons they annihilate giving rise to two photons which, in general, are emitted simultaneously in almost opposed directions. Both, Paul Dirac and Carl Anderson, received the Nobel Prize in physics for their contributions. At present, one of the most detailed characterization of the positron can be found in [5].

2.1.1 Positron production in isotope decays

The positrons observed by Carl Anderson were produced naturally in the upper atmosphere by the conversion of high-energy cosmic radiation into an electron-positron pair. Today we know that positrons can be produced in the so-called $\beta+$ decay where the nuclear transmutation of a proton into a neutron involves the emission of a positron (β^+) and an electron neutrino (ν_e) [6]:

$$p \rightarrow n + \beta^+ + \nu_e$$

In the Standard Model of particle physics the $\beta+$ decay is defined as a weak interaction that involves the transformation of an up quark (u) into a down quark (d) with the emission of a W^+ boson that immediately decays into a positron and an electron neutrino [7].

The spontaneous decay of free protons has never been observed because of their very long half-life (8.2×10^{33} years via positron decay [8]). Thus the $\beta+$ decay does not take place in free protons. However, it occurs in some unstable nuclides, that are generally of low atomic weight and with an excess of protons. Nowadays, positron-emitting radionuclides are produces under controlled laboratory conditions in particle accelerators. Due to the radioactive decay they get transformed into new nucleus that contain one proton less and therefore with the atomic number Z decreased by one unit. In standard notation, $\beta+$ decay is represented as:

$${}^{A}_{Z}X_N \ - \ {}^{A}_{Z-1}Y_{N+1} + e^+ + \nu_e \ (+\, e^-)$$

where X is a parent radionuclide and Y is a daughter nucleus. Since the daughter nucleus has an atomic number one unit less than the parent nucleus, an orbital electron must be ejected from the atom to balance the total charge.

2.1.2 Initial energy and positron range

Once emitted in a $\beta+$ decay, the positron has an *initial energy* that gets lost by interactions with the surrounding matter until, finally, the positron annihilates with an electron when both are essentially at rest. The distance that the positron travels in matter until it annihilates with an electron is known as the *positron range*. The positron range obviously depends on the energy with which the positron is emitted and the (electron) density of the surrounding matter. A list of common positron emitting radionuclides with their corresponding properties is presented in Table 2.1. According to

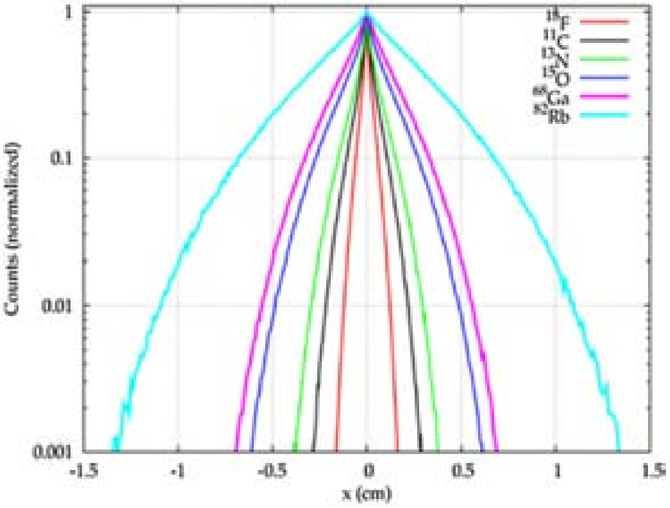

Figure 2.1: aPSF distributions for different positron emitters in water. The figure is taken from [9].

the table 2.1, the position range in water can be as big as several millimeters. Figure 2.1 shows one of the simulation result of the annihilation point spread function (aPSF) in water for different positron emitters [9]. The authors claim, that the expected error for the radial position is less than 0.1% for short-range isotopes (^{18}F, ^{11}C) and less than 1% for large-range isotopes (^{68}Ga, ^{82}Rb).

TABLE 2.1: Properties of common positron emitters. The table is taken from [10]

Radionuclide	Half-life (min)	$E_{\beta+,max}$ (MeV)	Max. β^+ range water (mm)	Average β^+ range in water (mm)
^{11}C	20.4	0.97	3.8	0.85
^{13}N	10	1.20	5.0	1.15
^{15}O	2	1.74	8.0	1.80
^{18}F	110	0.64	2.2	0.46
^{68}Ga	68	1.90	9.0	2.15
^{82}Rb	75 s	3.35	15.5	4.10

2.1.3 Annihilation photons, energy and non-collinearity

When positrons interact with matter they interact with electrons and eventually annihilate. The positron-electron annihilation generates two photons of 511 keV (the rest-mass equivalent of each particle) which, in general, are emitted simultaneously in almost exactly opposite directions [12] (Figure 2.2).

$$e^- + e^+ - \gamma + \gamma$$

When the positron reaches thermal velocities (a few eV), it can annihilate directly with an electron into two photons, or it first can form an atom called positronium (less probable process) [13]. Positronium is an unstable system that consists only of a single positron and a single electron rotating around the system s center of mass. Positronium can exist in two alternative states, parapositronium (spin = +1/2) with a lifetime of $1.26 \cdot 10^{-10}$ s [14], or orthopositronium (spin = +3/2) with a lifetime of $1.42 \cdot 10^{-7}$ s [15]. In case of the orthopositronium formation, the positron-electron annihilation results in the emission of odd number of photons, normally 3 photons are produced [16]. However, such 3-photon annihilation with respect to 2-photon annihilation occurs very rarely in liquids (less than 1% probability) [13].

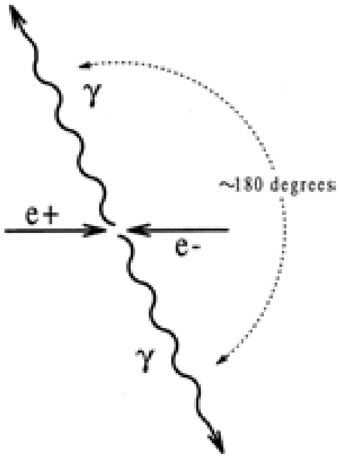

FIGURE 2.2: Schematic representation of electron-positron annihilation. The figure is taken from [11]

The back-to-back emission of annihilation photons is required for conservation of momentum for a stationary electron-positron pair. Nevertheless, because both particles are actually moving, the annihilation photons may be emitted in directions slightly off from the ideal by a few tenths of a degree. This effect is known as *non-collinearity* of the annihilation photons. This deviation from collinearity was measured and its value is $\approx 0.4°$ 0.5° full width at half maximum (FWHM) (Figure 2.3) [12].

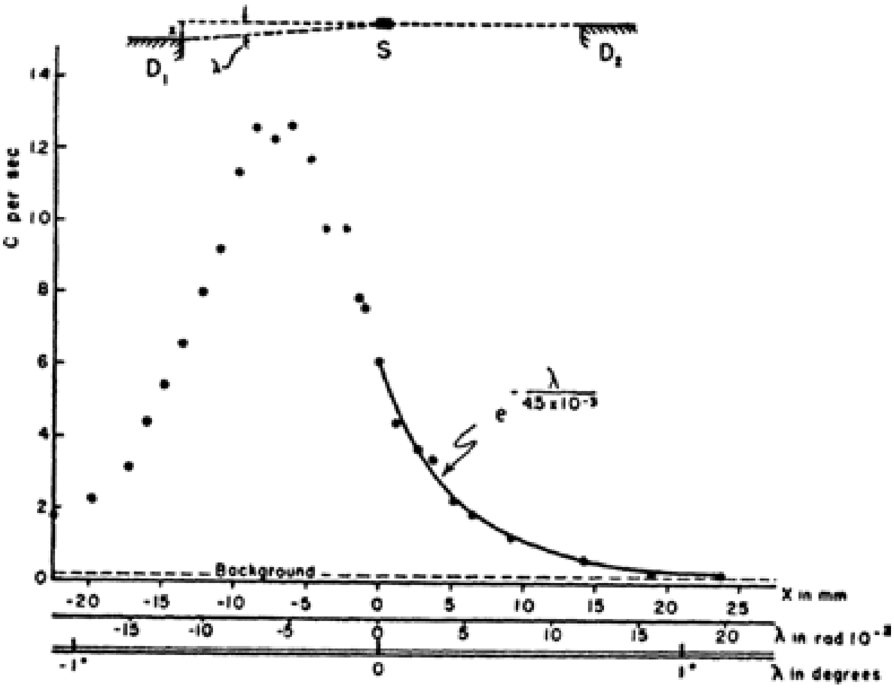

FIGURE 2.3: Photon-photon coincidences as a function of the position of one of the detecting counters [12].

2.2 Interaction of photons with matter

High-energy photons transfer their energy to matter in complex interactions with atoms, nuclei, and electrons. There are several possible interactions between photons and matter, of which only three are significant for 511 keV photons produced in e^-e^+ annihilations: the coherent (Rayleigh) scattering, the photoelectric effect, and the Compton (incoherent) scattering. Details about the three processes are provided in the following sections. For completeness, the pair production mechanism is also presented.

The likelihood of interaction of photons with matter is described in terms of *cross section* (σ) with units of cm^2/g. The total cross section (σ_{tot}) is defined as the sum of the cross sections of the individual interactions:

$$\sigma_{tot} = \sigma_{pe} + \sigma_{co} + \sigma_{pair} + \sigma_{ray} + ... \tag{2.1}$$

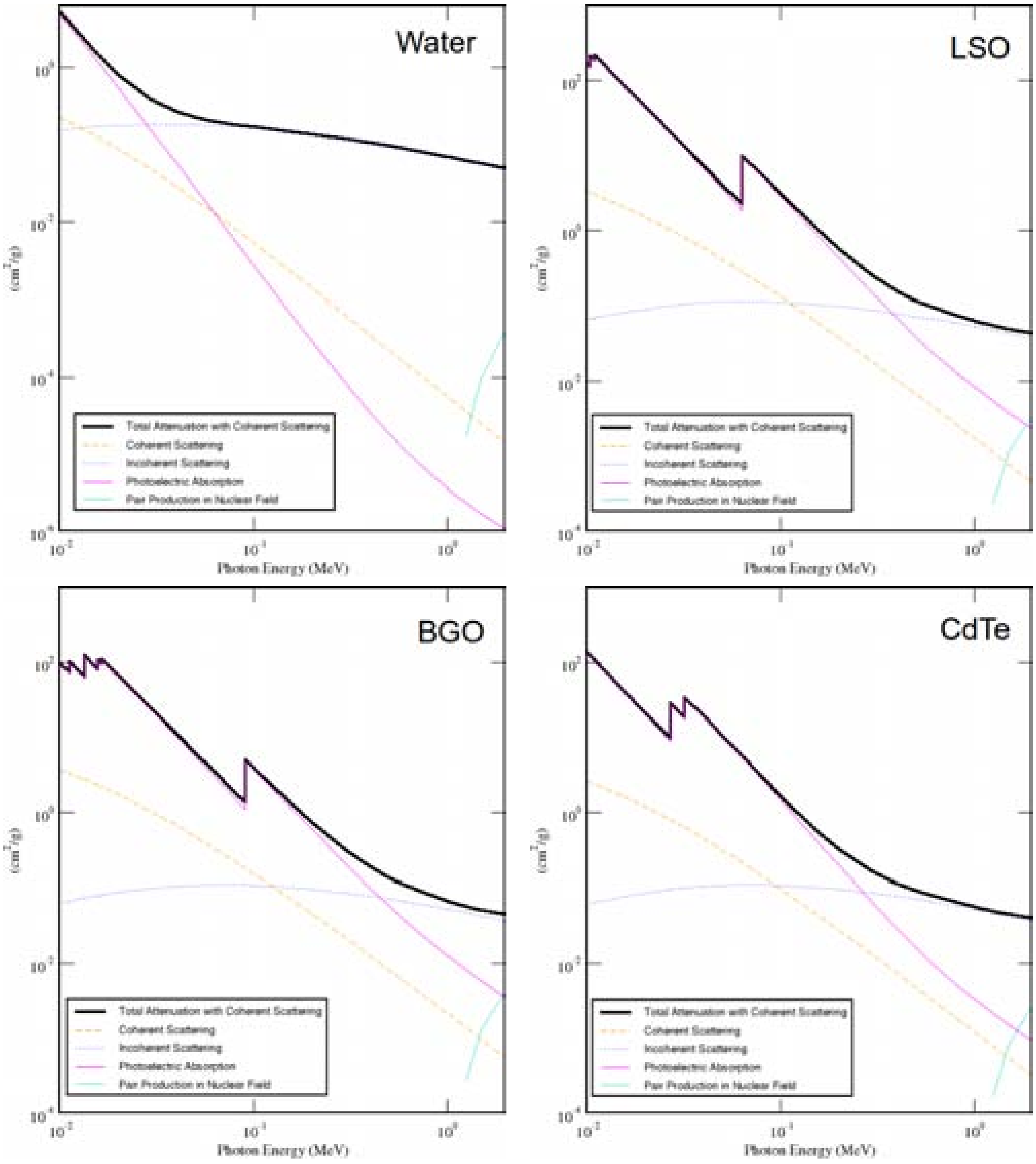

FIGURE 2.4: Total cross sections and its components for different materials. LSO is an inorganic scintillator (Lu_2SiO_5); BGO is an inorganic scintillator ($Bi_4Ge_3O_{12}$); and CdTe is a semiconductor detector. The plots are generated with [17].

where σ_{pe} is the cross section for the photoelectric effect, σ_{co} is the cross section for the Compton scattering, σ_{pair} is one for the pair production process, and σ_{ray} is one for the Rayleigh scattering. The total cross section of a given process depends on the energy of the initial photon, target density, the atomic mass of the target element, and a linear attenuation coefficient (μ) for the target material. Examples of total cross section and its components for water and some detector materials are shown in Figure 2.4.

As one can see in Figure 2.4, the Compton scattering (or incoherent) is the predominant process in water for photons with energy higher than ~100 keV and, usually, less than ~2 MeV. It means, that most of the annihilation photons (511 keV) in the water-like materials will be scattered. For the materials commonly employed for photon detection, the Compton scattering process is predominant for energies of photons greater than ~300 keV (for CdTe), ~400 keV (for LSO), and ~500 keV (for BGO). In case of lower energies (than the listed ones), the photoelectric effect is the dominant process. Thereby, a big part of the annihilation photons can undergo a single Compton scattering before producing a photoelectric effect in detector materials.

2.2.1 Coherent (Rayleigh) Scattering

Coherent or *Rayleigh scattering* is a type of scattering interaction that occurs between a photon and an atom as a whole. Because of the great mass of an atom, very little recoil energy is absorbed by the atom. The photon is therefore deflected with essentially no loss of energy. Rayleigh scattering is important only at relatively low energies ($\leq$ 50 keV).

2.2.2 The photoelectric effect

The *photoelectric effect* is an atomic absorption process in which an atom absorbs totally the energy of an incident photon. The photon disappears and the energy absorbed is used to eject an orbital electron from the atom (Figure 2.5). The ejected electron is called a *photoelectron*. It receives kinetic energy equal to the difference between the incident photon energy and the binding energy of the electron shell from which it was ejected. If sufficient photon energy is available the photoelectric effect is most likely to occur with an innermost possible shell electron. As the electron is ejected from the atom a more loosely bound outer orbital electron

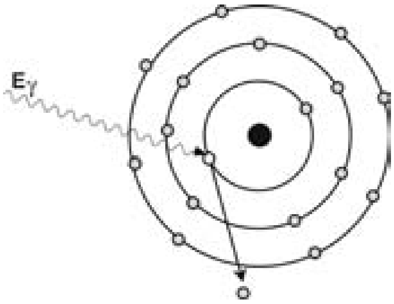

FIGURE 2.5: Schematic representation of the photoelectric effect. The incident photon transfers its energy to a photoelectron and disappears. The figure is taken from [18].

drops down to occupy the vacancy. In doing so, it will emit radiation itself (that is a characteristic X ray) due to the differences in the binding energy for the different electron levels. Alternately, instead of emitting an X ray, the atom may emit a second electron (Auger electron) to release the energy. The photoelectric effect dominates in water at energies less than approximately 100 keV.

2.2.3 Compton Scattering

Compton scattering is a collision between a photon and a loosely bound outer shell orbital electron of an atom (Figure 2.6). Because of the incident photon energy greatly exceeds the binding energy of the electron to the atom, the electron can be considered to be essentially free and at rest. The photon does not disappear in Compton scattering interaction. Instead, it is deflected through a scattering angle θ_c. Part of its energy is transferred to the *recoil electron* that gets ejected from the atom. The energy loss by the photon is divided between the small binding energy of the electron level and the kinetic energy imparted to the Compton recoil electron. The energy of the photon after the Compton scattering E'_γ can be calculated from the Compton equation:

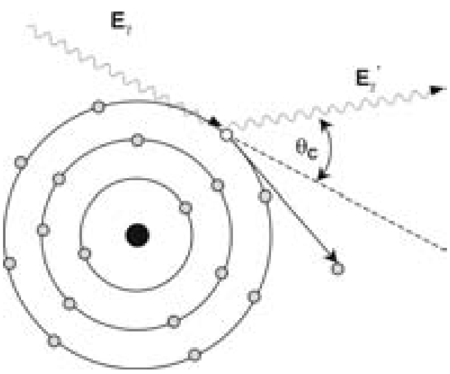

FIGURE 2.6: Schematic representation of Compton scattering. The incident photon transfers part of its energy to a Compton recoil electron and gets scattered in another direction of travel. The figure is taken from [18].

$$E'_\gamma = \frac{E_\gamma}{1 + \frac{E_\gamma}{m_0c^2}(1 - cos(\theta_c))} \tag{2.2}$$

where E_γ is initial photon energy, m_0c^2 is the photon rest energy and θ_c is a Compton angle.

The energy transferred does not depend on the density, atomic number, or any other property of the absorbing material. The amount of energy transferred to the recoil electron in Compton scattering ranges from nearly zero for $\theta_c \approx 0$ degrees up to some maximum value that occurs in 180-degree *backscattering events* depending on the initial energy of the photon. For instance, a 180° back-scattered annihilation photon will have an energy of 170 keV (it will transfer 341 keV). In spectroscopy, the highest energy that can be transferred, corresponding to full back-scattering, is called the *Compton edge*. Figure 2.7a represents an example of typical energy distribution for 511 keV photons. As one can see, the absorption (photoelectric) peak appears at 511 keV and the Compton edge is at ∼340 keV. The expression 2.2 is plotted in Figure 2.7b (solid line) for

511 keV annihilation photons. The plot illustrates that rather large angular deviations occur for a relatively small energy loss. In order to understand which scattering angles are dominated in water one can use Klein-Nishina equation [19] that calculates the probability of scattering:

$$\frac{d\sigma}{d\Omega} = Zr_0^2 \left(\frac{1}{1+\alpha(1-cos\theta_c)}\right)^2 \left(\frac{1+cos^2\theta_c}{2}\right)\left(1+\frac{\alpha^2(1-cos\theta_c)^2}{(1+cos^2\theta_c)(1+\alpha[1-cos\theta_c])}\right) \tag{2.3}$$

where $d\sigma/d\Omega$ is the differential scattering cross-section, Z is the atomic number of the scattering material, r_0 is the classical electron radius, and $\alpha = E_\gamma/m_0c^2$. For positron annihilation radiation ($\alpha = 1$) in water, the equation 2.3 can be reduced for first-order scattered events to give the relative probability of scatter as [18]:

$$\frac{d\sigma}{d\Omega} = \left(\frac{1}{2-cos\theta_c}\right)^2 \left(1+\frac{(1-cos\theta_c)^2}{(2-cos\theta_c)(1+cos^2\theta_c)}\right) \tag{2.4}$$

The function 2.4 for the range 0 180° is also plotted in Figure 2.7b [18]. The 511 keV photons scatter with small angles θ_c, and thus continue to move toward the forward direction to the direction of the incident photons.

2.2.4 Pair Production

Pair production occurs when a photon with energy greater than 1.022 MeV (twice the energy equivalent to the rest mass of an electron) interacts with the electric field of a charged particle. Usually the interaction is with an atomic nucleus, but occasionally it is with an electron. In pair production the photon disappears and its energy is used to create a positron-electron pair to conserve charge (Figure 2.8). This direct electron pair production in the electric field of a nucleus is the dominant interaction mechanism at high energies. Above the threshold of 1.022 MeV, the probability of pair production increases as energy increases. The energy sharing between the electron and the positron is more or less random from one interaction to another, usually within 20 80% sharing range. Normally the positron has slightly higher kinetic energy than the electron as the interaction of the particles with the nucleus causes an acceleration of the positron and a deceleration of the electron. The electron

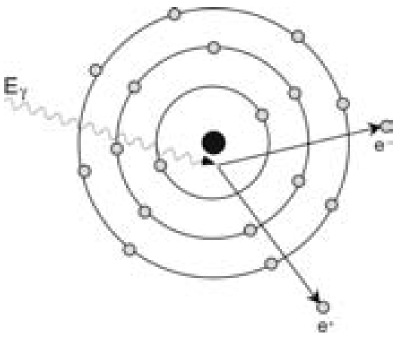

FIGURE 2.8: Schematic representation of the pair production. As a photon with energy higher than 1.022 MeV passes in the vicinity of a nucleus spontaneous formation of a positron and an electrons can occur. The figure is taken from [18].

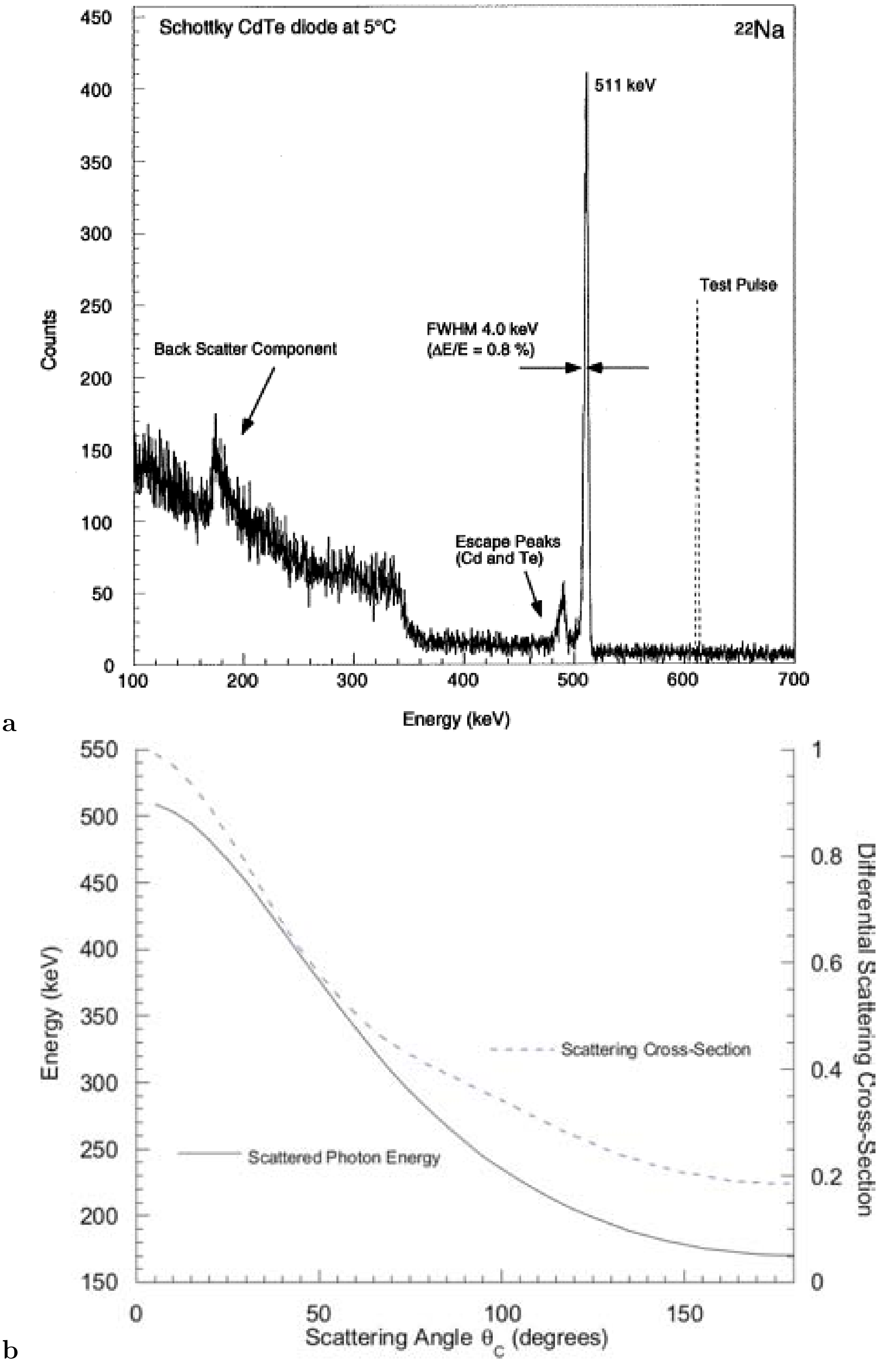

FIGURE 2.7: **a**: ^{22}Na spectroscopy. **b**: The angular probability distribution (scattering cross-section, broken line) and resultant energy (solid line) for Compton-scattered 511 keV photons. The figure is taken from [18].

and positron will dissipate their kinetic energies primarily in ionization and excitation interactions. Then the positron will undergo annihilation in the absorber as described earlier. Other particles can produce matter/antimatter pairs, such as protons, but, as the mass of the electron is much lower than the mass of the proton, a photon of lower energy is required for electron-positron pair production, thus making the process more probable.

2.3 Photo-detectors

The detection and measurement of gamma radiation is based on the interaction of photons with matter. There are three principal types of photon detectors: *gas-filled detectors*, *scintillators*, and *semiconductor detectors*. Depending on the final goal, the detectors can be used for incoming photons counting, measurements of the photon energy, position, arriving time, and particle identification. Below, each detector type is shortly reviewed.

2.3.1 Gas-filled detectors

The most commonly used gas-filled detectors for the photon counting are *ionization chambers*, *proportional counters*, and *Geiger-Mueller counters*.

The *ionization chamber* is the simplest and oldest gas-filled radiation detector. The principle of operation of the ionization chamber is based on effects of the ionization and excitation of gas molecules that are produced when a photon passes through the gas. All the charges created by the ionization are collected through the application of an electric field and derive an electric output signal. The simplest design of such a chamber is a parallel-plate capacitor (or, alternatively, cylinder arrangement) filled with an inert gas, such as argon (Figure 2.9). The electric field strength must be such that all positive and negative charges produced along the path of the photon are collected completely on the capacitor plates, but, at the same time, no secondary ionization from drifting electrons occurs.

The ionization chambers can be operated in a pulse mode or in a current mode. In the first case, an electric pulse induced by each individual incident photon is measured independently. The positive and negative charges that move in the electric field induce the charge in the capacitor plates. This change goes through a resistor of the electronic circuit and can be measured as a voltage pulse. In the case of the current mode, the used resistance is very large, and a measurement of individual particles entering the

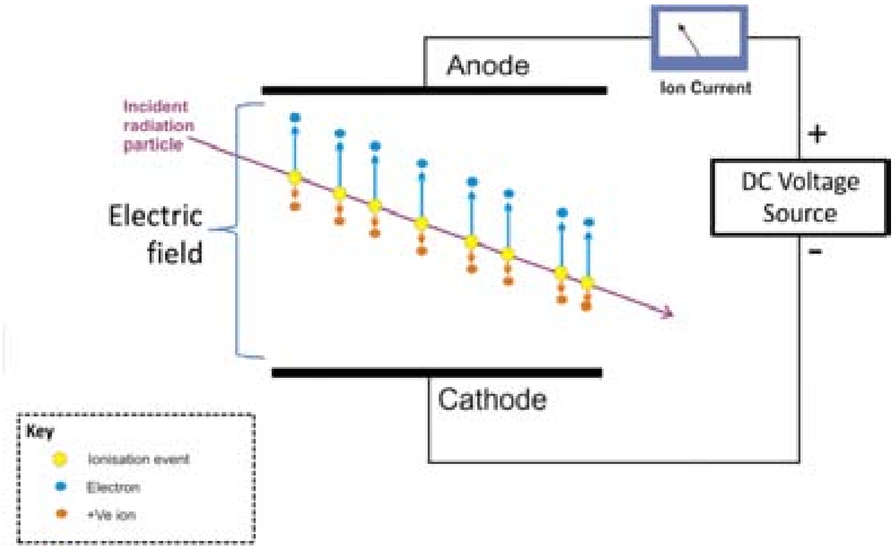

Figure 2.9: Schematic representation of ionization chamber operation principle. The figure is taken from [20].

chamber at a high rate is not possible. In this case, an average current is measured. In this mode the ionization chamber can be used, for example, to calibrate the intensity of radioactive sources. A main drawback of the ionization camera is that it cannot discriminate between radiation particles (photons or charged particles), neither produce an energy spectrum of incoming radiation. Like any other gas-filled detectors, it has a very low efficiency. Another disadvantage of the ionization camera is its time resolution. Depending on the camera design it can vary from few microseconds to a millisecond.

The *proportional counter* is an ionization chamber described above, but with the higher electric field applied. They usually have a cylindrical geometry with the cathode as a cylinder surface and the anode as a very thin wire going along the axis of the cylinder. The proportional counter geometry and applied electric field configuration are such that the positive and negative charges formed in the primary ionization process first drift a certain distance towards the electrodes (the cathode and anode respectively), just like in ionization chambers. Then, when the electrons get closer to the anode, the electric field strength becomes larger that the electrons gain enough kinetic energy to ionize other atoms or molecules of the gas. At this point a chain of ionization reactions is produced and it leads to an avalanche of electrons and ions (*Townsend avalanche*, Figure 2.10).

The proportional counters are usually operated in the pulse mode. The amount of change liberated by the primary ionization gets magnified by a so-called *gas amplification factor*. The voltage pulse detected at the electrodes also increases by the same factor. There is a configuration of electric field strength and gas pressure at which this amplification factor is independent on the amount of primary ionization. This means that the pulse measured

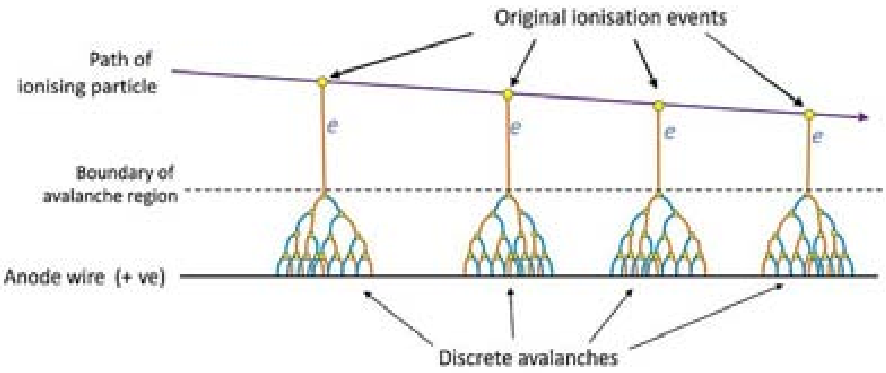

FIGURE 2.10: Schematic representation of avalanches in a proportional counter. The figure is taken from [21].

is proportional to the charge from the primary ionization process. This makes possible to measure the energy of incident radiation. This domain of electric strength field is called the *proportional region* (Figure 2.11). Proportional counters are usually used when the discrimination between detecting particles and/or levels of incident radiation must be known, for instance, for accurate measurement of radiation dose. The main drawback of such counters is a very low efficiency. The energy resolution of such proportional counters is usually ∼12%. The time resolution varies from hundreds of nanoseconds to a millisecond.

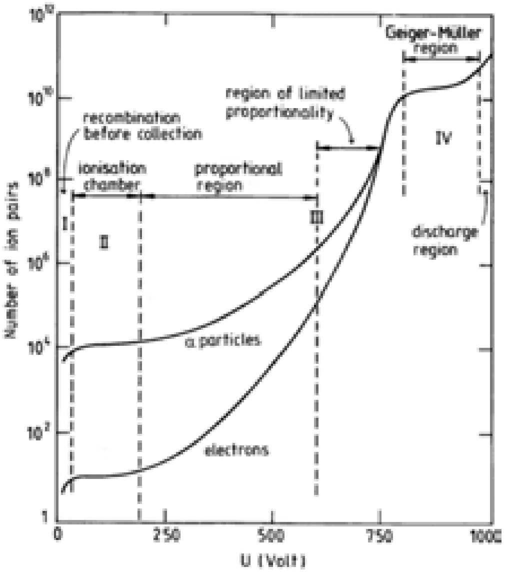

FIGURE 2.11: Gas amplification factor as a function voltage applied between anode and cathode for a wire cylinder ionization detection system. The figure is taken from [22].

Geiger-Mueller counters (or *Geiger tubes*) are also gas-filled cylindrical detectors based on ionization. Unlike the proportional counters, Geiger-Mueller counters utilize the electric field strength that is higher than one used for the proportional mode (Figure 2.11). Thus, the avalanche effect increases considerably. Here, one avalanche can itself create a second avalanche, and further, in a very short time, it can create an exponentially growing number of avalanches. Therefore, a Geiger-Mueller detector can function only as a simple counter of radiation and cannot be used for radiation spectroscopy because all information on the amount of energy deposited by the incident radiation is lost. A pulse from a Geiger tube represents a large amount of collected charge. Thus, the output pulse amplitude is also large, that allows considerably simplify the associated electronics. Additionally, the tubes themselves are relatively cheap. This simplicity, low cost, and ease of operation makes a Geiger-Mueller counter to be the best simple and economical radiation counting system. It led that Geiger-Mueller counters are still used in the present time. The main drawback of such counters is their large dead time, that greatly exceeds dead times of any other radiation detectors. Their time resolution varies from hundreds of microseconds to few milliseconds. Geiger-Mueller counters cannot differentiate which type of radiation is being detected nor the energy of the detected radiation. As other gas-filled detectors they have a very low efficiency.

2.3.2 Solid state scintillators

Nowadays one of the most popular type of particle detectors is the *solid state scintillation detector*. Basic operation principle of such a detector can be described following way. An incident particle or photon arrives to the scintillator and looses a part of its energy, exiting atoms of the scintillating material. Then, in some time, the atoms get unexcited and, at this point, they produce visible light. Typically, this light is propagated through light guides and directed onto the face of a photomultiplier tube (PMT) or another photo-sensor. The photo-sensor produce photoelectrons (or electron-hole pairs, depending on the sensor type), and amplify them in order to give a fast electronic pulse, that can be read by associated electronics.

The scintillators are characterized by following properties:

- scintillation efficiency;
- light output;
- stopping power;
- intrinsic energy resolution;
- linearity;
- scintillation decay time;
- transparency to its own scintillation light;
- index of reflection;
- hygroscopy;

The *scintillation efficiency* is the ability of the scintillator to convert kinetic energy of particles into detectable light. A good detector has high scintillation efficiency.

The *light output* is a number of photons emitted by the scintillator per unit of deposited energy. The higher the light output of the scintillator, the more defined pulse is produced and, thus, the better energy and spatial resolution the detector will have. The light output depends on the scintillation efficiency, the type of particle and its energy.

The *stopping power* determines the mean distance the incident particle travels until it stops after complete deposition of its energy. It depends on the density and effective atomic number of the detector material.

The *intrinsic energy resolution* is the ability of the detector to accurately measure the deposited energy. It is defined as the ratio of the FWHM of a given energy peak to the peak position, and usually expressed in %. Excellent energy resolution is needed when it is important to distinguish between photons that have undergone the Compton scattering in a sample and those that have remained unscattered. The intrinsic energy resolution depends on the inhomogeneity of the crystal structure and random variations in the production of light in it.

The *linearity* is the ability to create a light yield that is proportional to the deposited energy of the incident radiation. A good scintillation detector has a good linearity over a wide range of energy.

The *scintillation decay time* is the time period between the point when an atom of the detector material gets excited and the point when it decays to the ground state, emitting visible light. The decay time depends on the material of the scintillator. The shorter the decay time, the higher event rates the detector can handle. Short decay time is good for time-of-flight measurements. Additionally, faster light production within the scintillator (faster decay time) results in better timing resolution and it is important for coincidence detection of annihilation photons. The slow decay time leads to increased detector dead time and high random coincidences. Also, the decay time of the scintillator is a limiting factor in how many photon interactions a detector can process per unit of time and avoiding the pile-up effect.

The *transparency of scintillator to its own scintillation light* is important for good light collection.

The *index of reflection* should be low enough. Usually it should be as close as possible to $\approx$1.5, that is the same as the glass entrance window on a PMT, to provide minimal internal reflection at the scintillator crystal and PMT or other photo-sensor interface.

Other desirable properties of scintillating crystals are *non-hygroscopy* (so the detectors do not have to be protected from water vapor), fast *operation speed*, low *cost*, and *production capability and durability.*

Although there are many different scintillating materials, only a few are suitable for the detection of photon radiation from annihilation. All scintillating materials are divided into two groups: organic scintillators and inorganic ones. The organic scintillators usually are fast, but their light output is low. Alternatively, the inorganic materials typically have a high light output, high stopping power, and very good linearity, but they are relatively slow in the response time. Additionally the high light output of inorganic scintillators results in better energy resolution. All these makes inorganic scintillators extremely suitable for the detection of photon radiation from annihilation event. The most popular inorganic materials for this purpose are thallium-doped sodium iodide NaI(Tl), bismuth germanate $Bi_4Ge_3O_{12}$ (BGO), lutetium oxyorthosilicate doped with cerium Lu_2SiO_5:Ce (LSO), gadolinium oxyorthosilicate doped with cerium Gd_2SiO_5:Ce (GSO), and barium fluoride BaF_2. Some properties of these and other scintillators are shown in Table 2.2 [10]. Most of scintillating detectors are very fast (scintillation decay time is in the order of nanoseconds). Their time resolution varies from few hundred picoseconds to few hundred nanoseconds. This fact makes scintillators an excellent tool for the time measurements. One of the principle drawback is relatively low energy resolution.

Table 2.2: Physical properties of common inorganic scintillators for photon detection [10]

Property	NaI(Tl)	BGO	LSO	YSO	GSO	BaF_2
Effective Z	50	74	66	34	59	52
Density (g/cm^3)	3.7	7.1	7.4	4.5	6.7	4.9
Scintillation decay time (ns)	230	300	40	70	60	0.6
Photon yield (photons/keV)	38	6	29	46	10	2
Relative light output (%)	100	15	75	118	25	5
Linear attenuation coefficient, μ(cm^{-1})	0.35	0.96	0.87	0.39	0.70	0.44
Energy resolution (% at 511 keV)	6.6	20	10	12.5	8.5	11.4
Hygroscopy	yes	no	no	no	no	no

YSO: Yttrium oxyorthosilicate doped with Ce, Y_2SiO_5:Ce.

2.3.3 Semiconductor detectors

Semiconductor solid-state detectors work similar to gas-filled detectors: a crossing the detector incident particle creates electron-hole pairs that get separated by applied electric field. When an incident particle or a photon goes through the semiconductor material it excites electrons from the valence band. The excited electrons get transferred to the conduction band, leaving behind a hole in the valence band. Thus, the track of the passing particle gets surrounded by a tube of electrons and holes. The concentration of charges is quite high (10^{15} 10^{17} charges per cm^3) due to the fact that one electron-hole pair appears per 3 5 eV of absorbed incident radiation energy [23]. In order to separate these charges and collect electrons on the anode and holes on the cathode, before they recombine with each other, an electric field is applied. The electric field is generated by the cathode and the anode of the semiconductor detector. When charge is collected by the polarized electrodes, an electrical signal is generated and read by the associated electronics. The measured pulse is proportional to the collected charge from the primary ionization process. Thus, the energy of incident radiation can be measured. Additionally, since the concentration of charges is very high, the produced pulse is very large, so it allows to count individual incident particles.

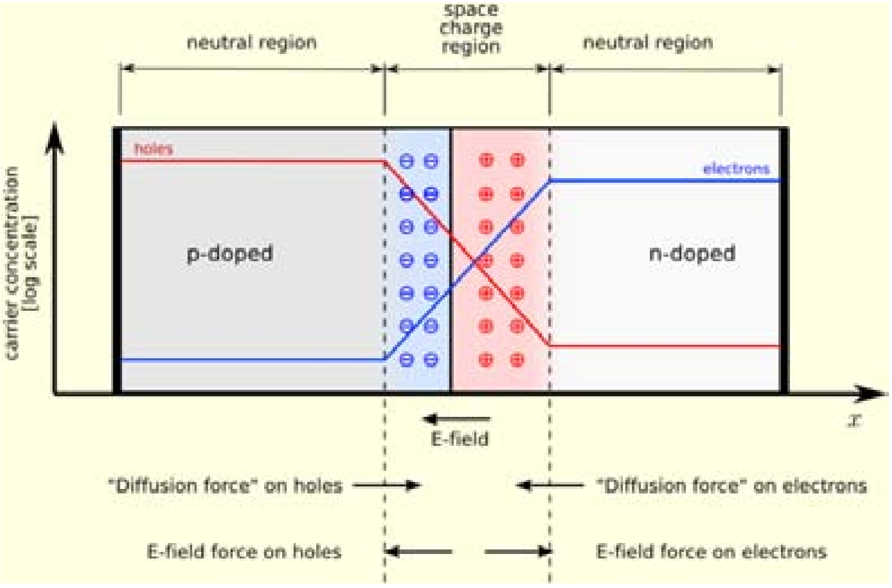

Figure 2.12: A p n junction in thermal equilibrium with zero-bias voltage applied. Electron and hole concentration are reported with blue and red lines, respectively. Gray regions are charge-neutral. Light-red zone is positively charged. Light-blue zone is negatively charged. The electric field is shown on the bottom, the electrostatic force on electrons and holes and the direction in which the diffusion tends to move electrons and holes. The figure is taken from [24].

The p n junction semiconductor crystals are usually used for the photon detection (Figure 2.12). In this semiconductor type, there is diffusion of electrons from the n to the p region and a diffusion of holes in the opposite direction. This process creates a voltage difference in the p n junction and the depletion region, i.e. a region where the charge carriers stay in the balance. When a photon goes through the detector, each electron that is created in the depletion region is accelerated into the n side and each created hole is accelerated into the p side. Thus, a spontaneous electric field gets generated. Normally, since the depletion region is usually small and the junction capacitance is high, this electric field has low intensity and does not allow the charge carriers to move quickly. In order to create higher electric field, the non-zero bias voltage has to be applied. However, the applied bias voltage creates some known problems in semiconductor crystals.

One of the problems is the *polarization* effect. The induced in the semiconductor electric field pairs the positive and negative charges in a certain way, thus, molecules gain electric dipole moment. The electric dipole moment get oriented along the electric field vector, and the semiconductor is said to be *polarized.* The polarization of semiconductor can be defined as the vector field that expresses the density of permanent or induced electric dipole moments in a semiconductor material. The polarization effect grows with time, because more and more molecules of semiconductor gain electric dipole moment. Typically, it leads to the reduction of speed of charge carries and, thus, increases the *charge trapping* effect. Thereby, it can lead to a time-dependent decrease in the counting rate, charge collection efficiency, depletion region thickness, and energy resolution of the detector. The polarization can be reduced by cycling the bias voltage (turning it off and on).

The second problem that arises in semiconductor detectors due to the high bias voltage is *leakage current.* In this condition, even in the absence of ionizing radiation, the detector will have a finite conductivity and therefore some electrons will go to the conduction band, creating holes in the valence band and move towards the electrodes. These unwanted spontaneous move of charge carriers is called the leakage current. This effect also occurs at the edges of the p n junction where relatively large voltage gradients over small distances take place. There is another additional reason of the leakage current. It is thermal generation of electron-hole pairs within the depletion region of the p n junction. In summary, the leakage current increases with the increase of the applied voltage, the crystal size (or its depletion region), and the crystal temperature. It also depends on humidity, and contamination of the detector surface. Random fluctuations of the leakage current produce steady electronic pulses and can represent a significant source of noise in detection of annihilation photons and, thus, worsen the energy resolution of the detector. Normally, in order to decrease the leakage current, one can cool down the detector and reduce the applied bias voltage.

Another problem of semiconductor detectors, usually related to the crystal impurities, is *charge trapping.* The charge trapping is a phenomenon of stopping the charge carries within the crystal for a relatively long time or forever, in case of their recombination. When electrons and holes move towards the electrodes they can be collected or get recombined. If semiconductor is perfectly pure, the average lifetime of the charge carries before recombination can reach ~ 1 second [25]. In reality, impurities always exist in the detector crystals. These impurities shorten the lifetimes by three or four orders of magnitude comparing to the ideal case. The impurities act as *traps* for charge carriers, i.e. electrons and holes get captured and immobilized for a relatively long period of time, preventing the contribution to the measured pulse. Sometimes, when the impurities catch both, electrons and holes, the recombination process takes place. The charge trapping can be also caused by defects and imperfections within the crystal lattice.

Semiconductor detectors have lower stopping efficiency for 511 keV photons than some scintillating crystals. Their time resolution is not as good as scintillator s one, and, usually, does not go lower than few nanoseconds. Moreover, they are more expensive than the scintillators and their manufacture is way harder. However, in spite of the all listed above problems, the solid-state detectors have excellent energy resolution (1% 4%) and, therefore, becoming a promising material for annihilation photon detection.

Usually, following semiconductor materials are used for the detection of incident radiation:

- silicon (Si);
- germanium (Ge);
- cadmium telluride (CdTe);
- cadmium zinc telluride (CZT).

The Ge semiconductor cannot operate at room temperature. The bandgap of this material is so narrow (Table 2.3), that the thermal energy of electrons is enough for crossing the bandgap and reaching the conduction band. Thus, Ge always have a background current at room temperature and needed to be cooled in order to have a clean signal induced by incident radiation. The Si has a wider bandgap (Table 2.3), thus, it is more preferable than Ge for the measurements at room temperature.

Since Si and Ge have a relatively low atomic number (Table 2.3), the impurities reduce their detection efficiency. The production of highly pure Si and Ge materials or introduction into the crystal matrix other impurities that donate electrons to compensate this effect is very expensive and time consuming, thus, not very practical.

In order to overcome the limitations of Si and Ge, the CdTe and CZT semiconductor materials are developed. Both have very similar properties (Table 2.3). CdTe and CZT can work at room temperature without producing background charge current, and they have high atomic numbers (Table 2.3) that lead to very good detection efficiency for relatively thin detectors. Their production is also expensive and complicated. Recently,

TABLE 2.3: Physical properties of common semiconductors for photon detection

Property	Si	Ge	CdTe	CZT
Z	14	32	48/52	48/30/52
Density (g/cm^3)	2.33	5.33	5.85	5.81
Bandgap at 300 K (eV)	1.12	0.663	$\sim$1.44	$\sim$1.6
Energy resolution (% at 511 keV)	$\sim$0.1 0.3	$\sim$0.1 0.3	$\sim$1	$\sim$2 3
Electron mobility (cm^2/Vs)	$\sim$1400	$\sim$3900	$\sim$1100	$\sim$1000
Hole mobility (cm^2/Vs)	$\sim$450	$\sim$1900	$\sim$100	$\sim$50

a CdTe Schottky diode detector is developed [26]. Such detector uses Schottky barrier instead of p n junction. The use of such Schottky contacts in CdTe diodes significantly reduces the leakage current when comparing to standard ohmic CZT detectors [26]. This allows to apply a very high bias voltage and make the detectors thinner (down to $\sim$0.5 mm thick). With a thin detector that can handle a high bias voltage, it is much easier to reach full charge collection. The full charge collection improves the energy resolution of the detector by reducing the hole tail (Figure 2.13) and the electronic noise [26].

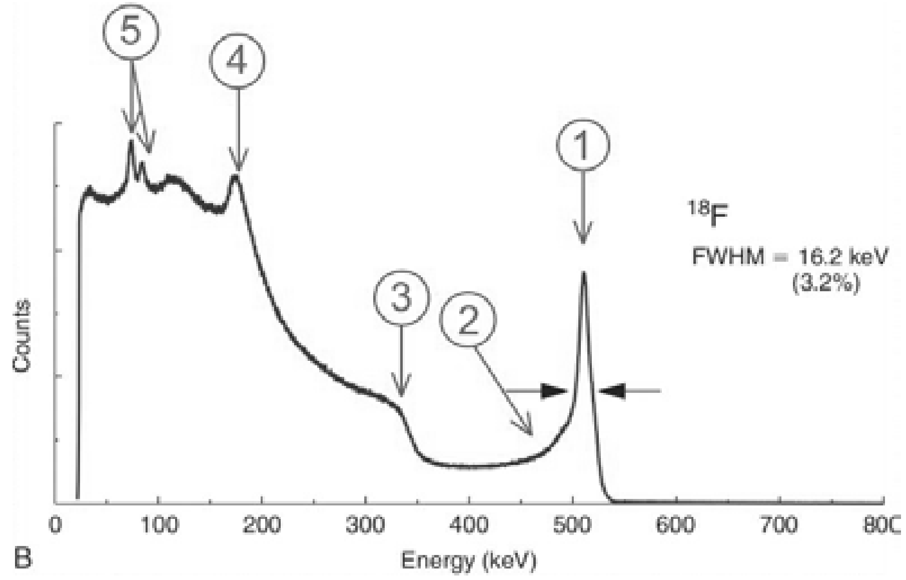

FIGURE 2.13: ^{18}F pulse-height spectra obtained with a CZT detector. ①: photoelectric peak ($E_{pe} = 511\ keV$); ②: hole tail caused by charge trapping and incomplete charge collection within the CZT crystal; ③: Compton edge ($E_{ce} = 341\ keV$); ④: backscatter peak ($E_b = 170\ keV$); ⑤: two peaks with energy of $E_1 = 73\ keV$ and $E_2 = 86\ keV$ that are caused by characteristic X-rays of lead from shielding material around the source in this experiment. The figure is taken from [23].

Chapter 3

Overview of the Positron Emission Tomography Imaging Technique

3.1 Basics of PET

The *Positron Emission Tomography* (PET) is a technique used in clinical medicine and biomedical (preclinical) research to create images that show how certain organs perform their physiological function. PET maps the concentration of position emitting radionuclides in the field of view (FOV) by detecting pairs of annihilation photons (Figure 3.1). The radionuclides are used to label different substances (pharmaceuticals), such as sugar, to create radiopharmaceuticals (Figure 3.1(1)). The radiopharmaceutical is injected into human (or animal) body and then transported by the blood circulation and incorporated into the organ of interest through the metabolism of the pharmaceutical (Figure 3.1(2)). For sugar, the relevant metabolic process is glucose utilization. After the radiopharmaceutical is injected into the patient, the patient is then positioned in the PET scanner (Figure 3.1(7)). In general, a PET scanner utilizes a ring of photo-detectors that surround the patient, and has special circuitry that is capable of identifying the photon pairs produced during annihilation (Figure 3.1(7)). When a photon pair from positron annihilation (Figure 3.1(6)) is detected in coincidence by two opposite detectors of the scanner, it is known that the annihilation (and thus decay event) took place somewhere along a straight line, called line of response (LOR), between those two detectors (Figure 3.1(7)). This information is stored in special matrices, called sinograms (Figure 3.1(8)), where each row in the matrix represents a parallel projection of the activity distribution in the patient at a specific angle and axial position. The sinograms are used to mathematically compute the three-dimensional distribution of the positron emitter, resulting in a series of tomographic emission images (Figure 3.1(9)). The images shown in Figure 3.1(9) are maps of radiopharmaceutical accumulation throughout the body reflecting glucose utilization by the different tissues.

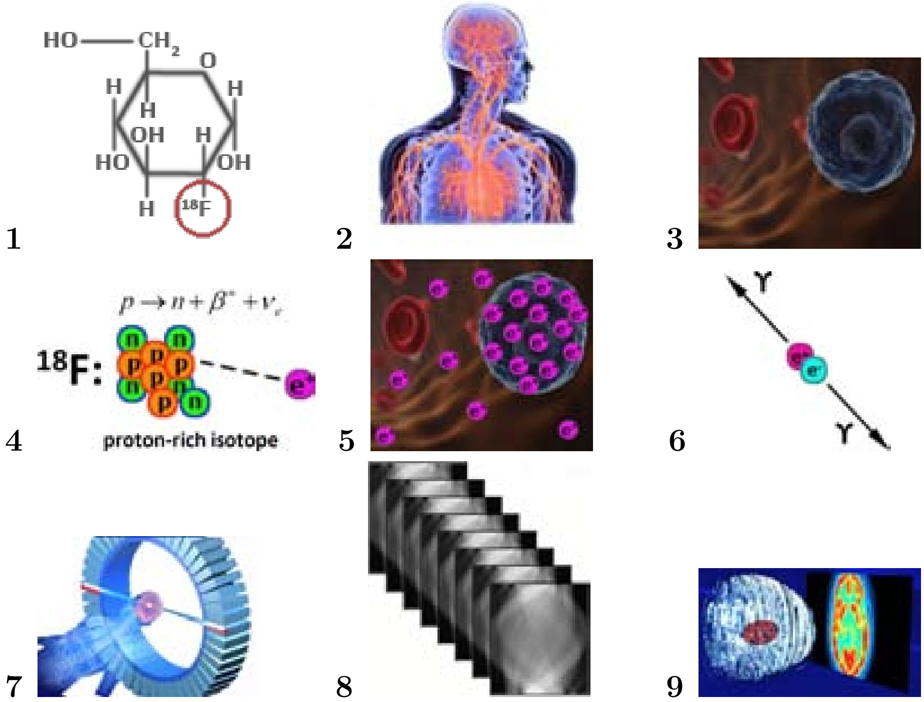

FIGURE 3.1: Physical principles of PET imaging. **1**: sugar labeled with a radionuclide is injected into a human body. Typical activity is 370 MBq; **2**: the radioactive agent is transported by the blood circulation and gets absorbed by the organs (glucose metabolism); **3**: tumor cells are characterized by higher glucose uptake; **4**: the agent that is used is a positron emitter; **5**: so, tumor cells release higher number of positrons with respect to neighbor tissues; **6**: each positron soon annihilates with an electron inside the body, producing a pair photons that go in opposite directions; **7**: a photon pair from positron annihilation is detected in coincidence by two opposite detectors of the scanner; **8**: the information from the detectors is stored in special matrices - sinograms; **9**: the sinograms are used to mathematically compute the three-dimensional distribution of the positron emitter, resulting in series of tomographic emission images.

3.2 Radiopharmaceuticals for use in PET

A *pharmaceutical* can be defined as any chemical substance intended for use in the medical diagnosis, cure, treatment, or prevention of diseases. The *radiopharmaceutical* is a pharmaceutical labeled with a radionuclide. Radiopharmaceuticals are normally used in nuclear medicine as tracers in the diagnosis and treatment of various diseases. Many tracers are being used to study more than a hundred different biophysical, biochemical, and pharmacological processes in the human body. They are used in many important clinical areas such as oncology, cardiology, and neuroscience. However, not all possible radiopharmaceuticals can be used for PET imaging. There are several requirements that PET tracers must complete. First of all its final *specific activity* should be high enough. The specific activity is defined by losses in radionuclide activity that occur during the chemical synthesis of the radiopharmaceutical. The *radiochemical purity* as well as the *chemical purity* should be higher than 95% and 99% correspondingly. The radiochemical purity is the fraction of the total activity in the sample that is present in the desired chemical or biologic form. Radiochemical impurities represent a problem because their distribution in the body is usually different. Thus, they can add a background to the reconstructed image. It is also very important that the labeling process produces a minimal interference in the physicochemical characteristics of the molecule. The chemical purity is the fraction of the sample that has the desired chemical form. Additionally, radiopharmaceuticals should be labeled with radionuclides of *half-lives* that are long enough to study the chosen biologic process, and be about the same duration as the *biologic half-life* of the radiopharmaceutical. The biologic half-life is the rate of clearance of the radiopharmaceutical from the body. It also defines the time that a radiopharmaceutical takes to circulate in blood before significant uptake in a target. Some radiopharmaceuticals have fast uptake and clearance, and others circulate in blood for a longer time and are uptaken very slowly by the tissues chosen for the study. Short-lived radionuclides with half-lives of minutes or less are not used to label radiopharmaceuticals with biologic half-lives of hours or days. The physical half-life of the radionuclide and the biologic half-life of the radiopharmaceutical determine the number of radioactive decays produced in a region of interest as a function of time. Therefore, both factors should be taken into account when setting the radiation dose to the patient. Finally, the radiopharmaceutical must not be *toxic* to not poison the patient.

All radioisotopes presented in Table 2.1 are used in PET. There are several important considerations that must be taken into account in the selection of positron emitters for PET studies. First of all, the mean energy of the positron should not be very high, because it is directly proportional to the positron range in tissue. If the positron range is big, the e^+e^- annihilation will happen far away from the decay event, that will worsen the spatial resolution of the PET system. The half-life of the radioisotope, as it was mentioned above, should be long enough to permit chemical synthesis and the PET study but, at the same time, not too long to avoid radiating the patient after the study is finished. Besides, the short half-life requires to have a dedicated cyclotron in the vicinity of the PET facility, and the radionuclides with too long half-life can cause problems in terms of storage and disposal. The radionuclides for use in PET must have specific chemical and physical properties that make them suitable for metabolic studies.

The positron emitters such as carbon (^{11}C), nitrogen (^{13}N), and oxygen (^{15}O) are very good for use in PET because they allow to label a lot of different organic molecules. However, their relatively short half-lives (see Table 2.1) limit the complexity of the molecules to be labeled and the range of processes that can be studied *in vivo*. Other positron emitters with relatively long half-lives such as ^{76}Br with $t_{1/2}$ of 16 hours, or ^{124}I with $t_{1/2}$ of 4.2 days are more suitable for complex labeling and long-term physiological changes studies. However, their presence is not very common in organic molecules, and their introduction can cause significant changes in the physicochemical properties of the molecule.

A notable exception is fluorine-18 (^{18}F, see Table 2.1), which has been used in PET with great success. On the one hand, its relatively short positron range (∼0.5 mm in water) permits to reach the sub-millimeter spatial resolution of the PET scanner. On the other hand, the relatively long half-life of ^{18}F allows its distribution within a radius of a few hundred kilometers from the site of production, thus avoiding the need of cyclotrons in the hospitals. The ^{18}F is a substitute for the hydrogen atom. Therefore, the substitution of hydrogen by ^{18}F is the most common form of labeling in PET, because the changes introduced in a molecule by this substitution are minimal [27]. Deoxyglucose labeled with ^{18}F form ^{18}F-fluorodeoxyglucose (FDG) [28]. The synthesis method provides a stable product with good labeling yield, high specific activity, high purity, and high tissue selectivity. FDG, as a glucose analog, is taken up by high-glucose-using cells such as brain, kidney, and cancer cells [29]. Nowadays it is the most effective and powerful radiopharmaceutical of all time. FDG is a single tracer that makes it possible to study brain metabolism, cardiac function, image sites of infection, and detect cancer in thousands of scans world-wide every day.

3.3 Acquisition modes

As already mentioned, PET is based on the detection in coincidence of the two 511 keV annihilation photons that originate from β^+ emitting sources. The data collected by a PET system can be acquired in three basic ways: frame mode, list mode, and gated imaging. In each scanner operation mode different coincidence logic is used.

In *frame-mode* acquisition individual events are sorted into their appropriate x-y locations within the digital image matrix immediately after their position signals are digitized. After a preset amount of time has elapsed or after a preset number of counts have been recorded, the acquisition of data for the image is stopped and the pixel values ($p(x, y)$ = number of counts per pixel) are stored in the computer memory. When a series of such images is obtained sequentially, individual images in the sequence are referred to as frames . The image matrix size (number of pixels that the image is consist of) must be specified before the acquisition begins. In this mode the coincidence is usually calculated on the fly with specific circuits.

In *list-mode* acquisition, the incoming information about detected events is digitized but it is not sorted immediately into an image grid. This information can contain the coordinates, energy, the arriving time of individual event, e.t.c. It is also possible to add additional information, for instance, position or movements of the patient. In this mode the coincidences are found after the data is acquired (off-line) and it permits retrospective framing. The list-mode acquisition provide greater flexibility for data analysis. However, it is not an efficient method for memory usage during the acquisition for conventional imaging, especially for high-count images, because every recorded event occupies a memory location.

In *gated imaging mode*, data are acquired in synchrony with the heart beat or with the breathing cycle, so that all images are acquired at the same time during the motion cycle. This helps reduce blurring and other possible image artifacts induced by body motion. In this mode, as well as in the frame-mode acquisition, the coincidence is calculated on-line.

3.4 Two-dimensional and 3-dimensional data acquisition

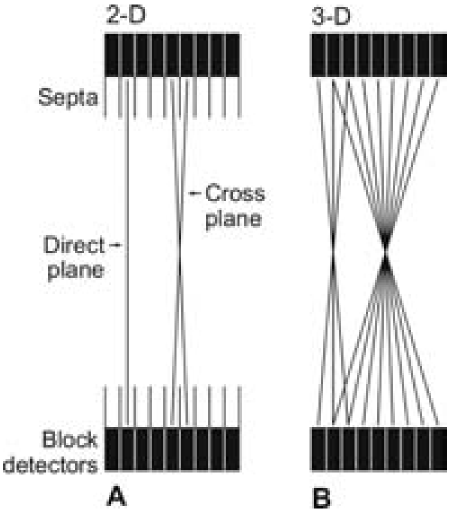

FIGURE 3.2: 2-D (**A**) and 3-D (**B**) data acquisition schemes in PET. The figure is taken from [10].

Originally, most PET scanners were designed with axial collimators or septa, made of tungsten or lead, between each ring of detectors. As shown in Figure 3.2A, the septa allows to be detected only those photons that are emitted parallel to the plane of the detector ring. This is known as *2-D data acquisition*. The septa provide efficient rejection of scattered events. It also reduces the single-channel counting rate, thereby lowering the random coincidence rate thus leaving only the true coincidences to be recorded. Detector pairs connected in coincidence in the same ring give the *direct plane* event. To improve sensitivity in 2-D acquisition, detector pairs in two adjacent rings are connected in a coincidence circuit (Figure 3.2A). It can be done, for instance, with slight modification of the lengths of the septa. Coincidence events from a detector pair in this arrangement are detected and averaged and positioned on the so-called *cross plane* that falls midway between two adjacent detector rings (Figure 3.2A). Because the cross planes receive data from two different LORs, they have roughly twice the sensitivity (and therefore twice the counting rates) as the direct planes. Instead of two adjacent rings, such cross planes can be obtained from other nearby rings that are connected in coincidence. For an n-ring system, there are n direct planes and n-1 cross planes obtained in 2-D acquisition. Thus, a total of 2n-1 sinograms are generated, each of which produces a transaxial image slice. As a larger number of the cross planes are accepted, the sensitivity increases. However there is a loss of spatial resolution in the axial direction.

To increase the sensitivity of a scanner, the *3-dimensional (3-D) acquisition* has been introduced in which the septa are removed from the PET scanner and data are obtained for all possible LORs (Figure 3.2B). This mode usually increases the sensitivity by a factor of almost 4 to 8 over 2-D acquisitions. If there are n rings in the PET scanner, all ring combinations are accepted and so n^2 sinograms are obtained. However, the number of scattered and random photons also are increased, thus degrading the spatial resolution as well as requiring more computer memory. As a trade-off, one can limit the angle of acceptance to cut off the random and scattered radiations at the cost of sensitivity. This can be achieved by connecting in coincidence each detector to a fewer number of opposite detectors than N/2. The sensitivity in 3-D mode is highest at the axial center of the field of view and gradually falls off toward the periphery.

Reconstruction of 3-D PET data also is more complex, because they cannot be sorted into a set of independent 2-D slices. Thus, fully 3-D reconstruction algorithms should be used. In case of the 3-D reconstruction computation times are roughly an order of magnitude longer than for 2-D reconstruction, because they involve computations in three dimensions rather than two. Nevertheless, because of the dramatic improvement in sensitivity and growing computer power, 3-D acquisition is widely used in modern PET scanners.

3.5 Classification of detected events

In PET an event is regarded as valid if:

- two photons are detected within a predefined time window known as the coincidence window,
- the resulting LOR formed between them is within a valid acceptance angle of the tomograph,

- the energy deposited in the crystal by both photons is within the selected *energy window*. The energy window is the selected upper and lower levels on the energy spectrum that define the detected photon energy range used to produce the image.

The events that satisfy these conditions are often called *prompt events* (or *"prompts"*). However, some of the prompt events can be undesired events because one or both of the photons can be scattered or the coincidence is the result of the accidental detection of two photons from unrelated positron annihilations (Figure 3.3) [18].

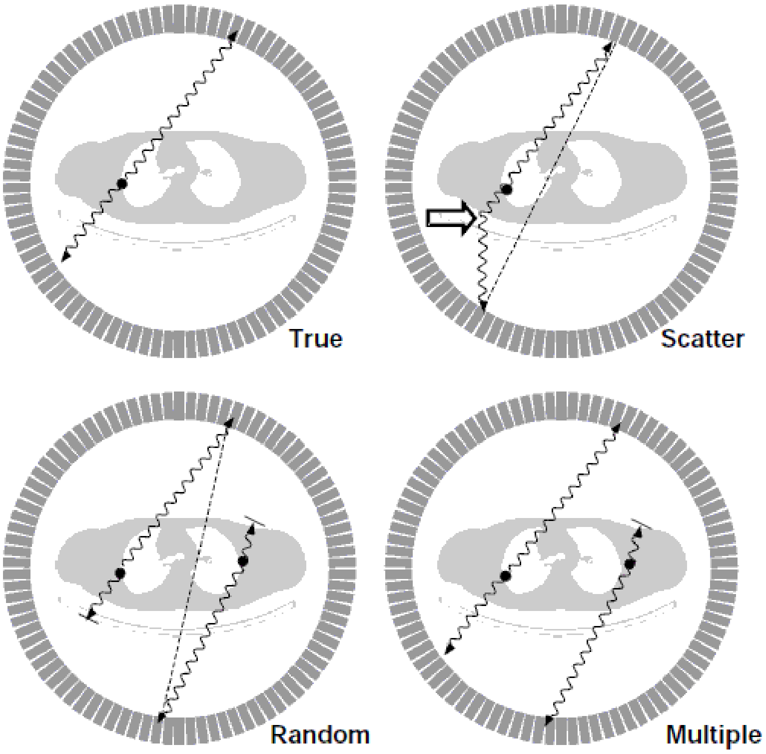

FIGURE 3.3: The various coincidence events that can be recorded in PET are shown. The black circle indicates the location of positron annihilation. From top left clockwise the events shown are: a true coincidence, a scattered event where one of the photons undergo a Compton interaction within the imaged body (indicated by the open arrow), a multiple coincidence arising from two positron annihilations in which three events are counted, and a random coincidence arising from two positrons in which one of the photons from each positron annihilation is counted. In the case of the scattered event and the random event, the mis-assigned LOR is indicated by the dashed line. The figure is taken from [18].

The terminology commonly used to describe the different kind of events in PET detection are:

- A *single* event is a single photon counted by a detector;

- A *true* coincidence is an event that derives from a single e^+e^- annihilation. Both the annihilation photons reach detectors on opposite sides of the tomograph without interacting significantly with the surrounding atoms and are recorded within the coincidence time window;
- A *random* coincidence occurs when two nuclei decay at approximately the same time. After annihilation of both positrons, four photons are emitted. Two of these photons from different annihilations are counted within the time window and are considered to have come from the same positron, while the other two are lost. These events are initially regarded as valid prompt events, but are spatially uncorrelated with the distribution of tracer. Random events add to the background causing artifacts and loss of image contrast;
- *Multiple* (or triple) events are similar to random events, except that three events from two annihilations are detected within the coincidence time window. Due to the ambiguity in deciding which pair of events arises from the same annihilation, the event is disregarded.
- *Scattered* events arise when one or both of the photons from a single positron annihilation detected within the coincidence time window have undergone a Compton interaction. As it was explained above, Compton scattering causes a loss of the energy of the photon and a change in direction. Due to the relatively poor energy resolution of most PET detectors ($\sim$10% at 511 keV), many photons scattered within the emitting volume cannot be discriminated against on the basis of their loss in energy and scattered events can account for up to 50% of the prompts. The consequence of counting a scattered event is that the LOR assigned to the event is uncorrelated with the origin of the annihilation event. This causes inconsistencies in the projection data, and leads to contrast deterioration and inaccurate quantification in the final image. Scattering arises from the object containing the radiotracer, the gantry of the tomograph, the floor and walls in the room, and also within the detector itself.

The prompt count rate is given by the sum of the true plus random plus scattered event rates. The ratio between the number of prompt events and the total number of annihilation events produced in the FOV is called *sensitivity* of the PET scanner. The ratio between true coincidences and prompt coincidences is called *signal-to-noise ratio* (SNR or S/N).

3.6 Tomographic image reconstruction

3.6.1 Definitions: LORs, projections, and sinograms

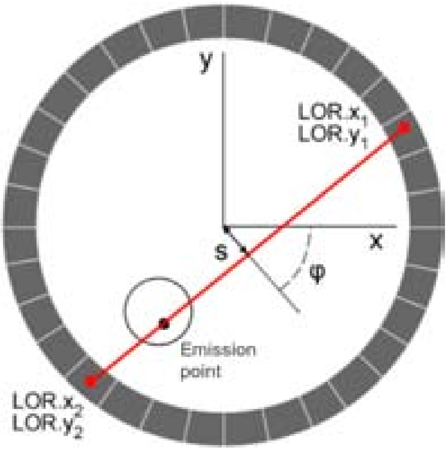

FIGURE 3.4: A LOR, defined as detection coordinates (x1, y1, x2, y2). The figure is taken from [30].

The two photons are detected within a time window characteristic of the system in use, with the source laying along the straight line connecting the centers of the two detectors, called the *line of response* (LOR). It is not known where along the LOR the event occurred, since photons are accepted within the set time window and their exact times of arrival are not compared. The only information we have is the positions of the two detectors that registered the event, i.e., the location of the LOR is established by the (X, Y, Z) coordinates of the two detectors. The position of the LOR is usually determined in terms of polar coordinates (Figure 3.4). In a full ring system, the data are collected simultaneously by all detector pairs, whereas in partial ring systems, the detector assembly is rotated around the patient in angular increments to collect the data. In acquiring the coincidence events, three steps are followed:

- the location of the detector pair in the detector ring is determined for each coincident event;
- the pulse height of the photon detected is checked if it is within the pulse energy window set for 511 keV;
- the position of the LOR is defined and the event is stored in the computer memory.

A full set of parallel LORs at a specific angle ϕ recorded across the detector is called a *projection*, or a *projection profile*:

$$p(s, \phi) = \int_{-\infty}^{\infty} f(x, y) dy_r \tag{3.1}$$

where $f(x, y)$ is a two-dimensional representation of the activity distribution, s is the radial coordinate, and y_r is the transversal direction coordinate.

The projections from all angles can be arranged in a matrix called *sinogram*. The name sinogram arises from the fact that the path of a point object located at a specific (x, y)

position traces out a sine curve in the matrix (Figure 3.5). The coincidence events in PET systems are stored in the form of a sinogram. Sinograms are the basis of most of the image reconstruction schemes. An example of a sinogram of a simple object is shown in Figure 3.6.

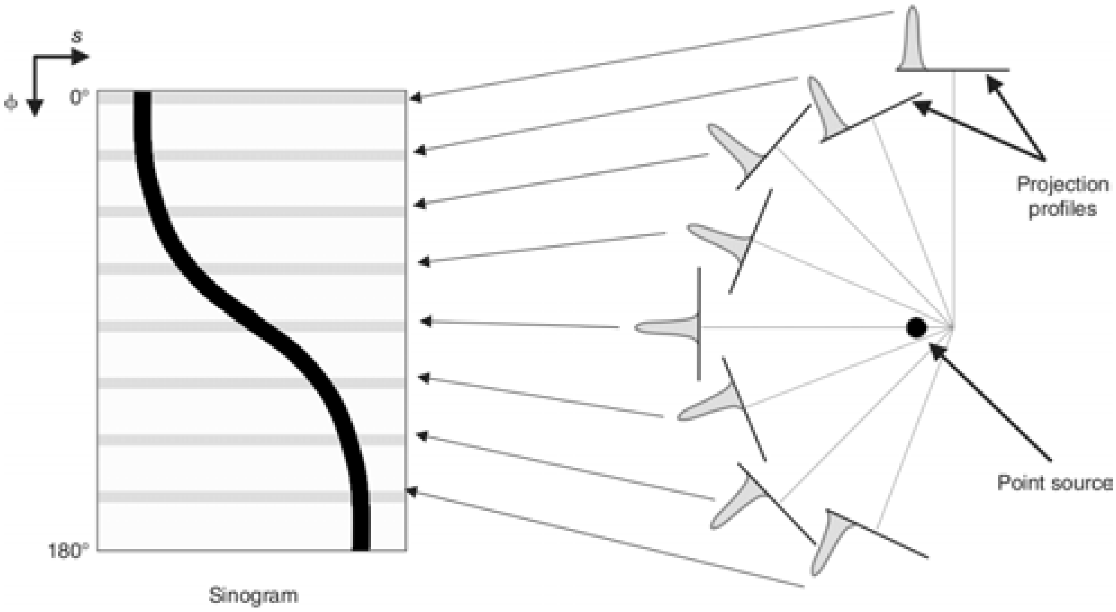

FIGURE 3.5: Two-dimensional intensity display of a set of projection profiles, known as a sinogram. Each row in the display corresponds to an individual projection profile, sequentially displayed from top to bottom. A point source of radioactivity traces out a sinusoidal path in the sinogram. The figure is taken from [23].

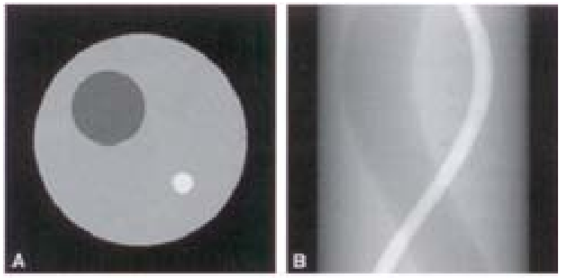

FIGURE 3.6: **A**: a PET phantom. The brighter the color the higher the dose uptake. **B**: sinogram of this phantom. The figure is taken from [23].

The PET technology together with image reconstruction techniques provide us with 3-D maps of radiopharmaceutical distribution inside the patient. Nowadays the majority of scans are acquired in 3-D mode. However, the 3-D data are more complex, harder to handle and process than the 2-D data. Thus, the 3-D data are often rebinned into 2-D format for further reconstruction. In this case, the final reconstructed 3-D image represents a stack of 2-D reconstructed layers of structures lying within a selected plane of the 3-D object. This approach of getting images is called the *tomographic imaging*.

Final tomographic images obtained with a PET scanner are the result of the application of an image reconstruction algorithm. There are many different reconstruction methods that can be generally classified into either analytic or iterative methods. The most commonly used methods, representatives of the two families, are the *filtered backprojection* (FBP) algorithm, the *maximum-likelihood expectation-maximization* (ML-EM) algorithm, and its speeded up version called *ordered subset expectation maximization* (OSEM) method. Relatively recent iterative reconstruction techniques that are getting popular are the *list-mode OSEM* (LM-OSEM) and the *origin ensemble* (OE) algorithms. The basic features of the listed methods are described below.

3.6.2 Filtered backprojection (FBP)

The 2-D FBP reconstruction algorithm is probably the most commonly used algorithm in tomographic images. It is an analytic method and therefore it is very fast. The reconstruction speed, however, is not the only reason why FBP is important: analytic algorithms are linear and thereby allow an easier control of the spatial resolution and noise correlations in the reconstruction. Figure 3.7 demonstrates the basic FBP steps. The projection profiles acquired at N projection angles in the spatial domain are expressed in terms of a Fourier series in the frequency domain as the sum of a series of sinusoidal waves of different amplitudes, spatial frequencies and phase shifts running across the image. The 1-D Fourier transform (FT) of the image profile is necessary to apply a filter to each FT profile. After the filtering, the inverse FT of each FT profile is computed. This way one gets filtered projection profiles. Finally, the conventional *backprojection* [31] [32] is performed using the filtered profiles.

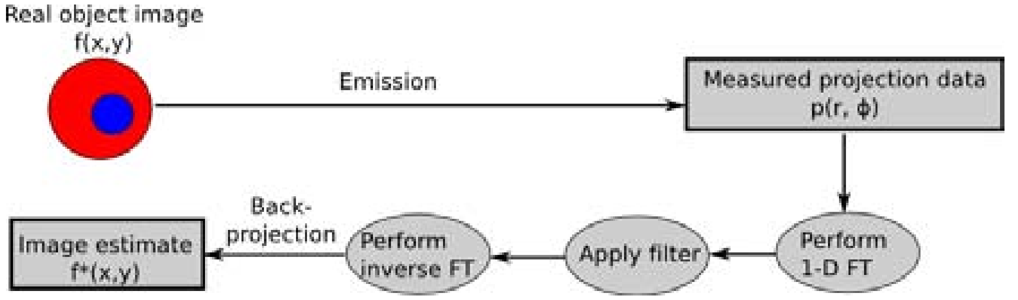

FIGURE 3.7: The concept of the filtered backprojection image reconstruction algorithm.

The backprojection is an operation of the image reconstruction from the LORs acquired by the detector. The principles of the backprojection for a point-like source are shown in Figure 3.8 [23]. First of all, projection profiles $p(s, \phi)$ are acquired at different angles around the source (Figure 3.8A). Then, each value of $p(s, \phi)$ is placed back into the

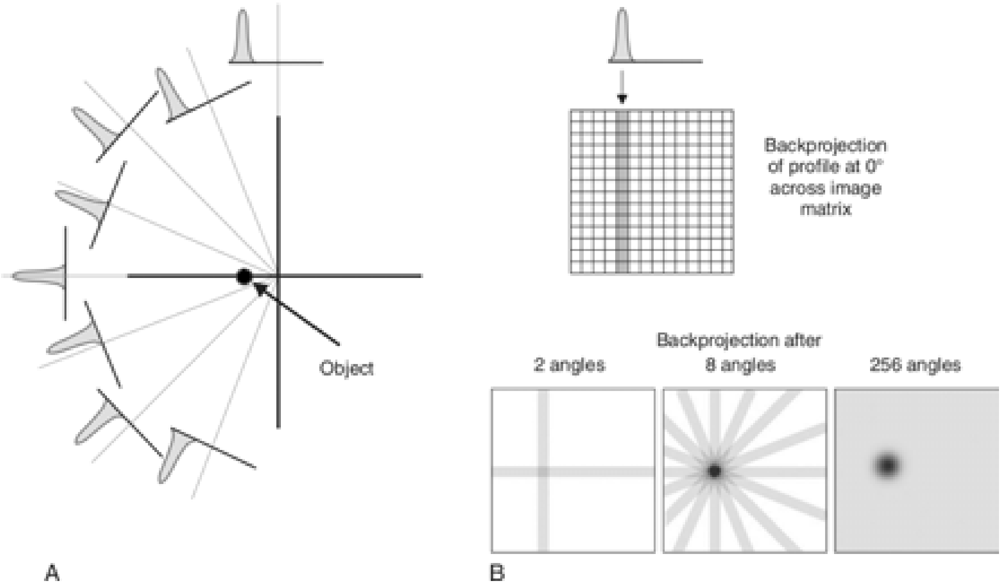

FIGURE 3.8: Illustration of the steps in backprojection. **A**: projection profiles for a point source for different projection angles. **B**: backprojection of one profile across the image at the angle corresponding to the profile. This is repeated for all projection profiles to obtain the backprojected image. The figure is taken from [23].

image grid along the appropriate LOR with an equal weight for all of the pixels (see Figure 3.8B). The equal weight (a constant value) is placed into all pixels along the LOR, because the knowledge of where the values came from is lost in the projection step. In principle, a simple backprojection of all the collected projections is enough to reconstruct the true source distribution. However, the finite sampling of projection angles and the uniform distribution of the photon count values along the LORs generates artifacts. In the reconstructed image there are regions to which some counts are attributed but that in reality have no activity, like a gray background that appears around the point-like source as shown in Figure 3.8B. As a result, the image gets blurred when compared to the original source distribution [31]. The magnitude of the blurring decreases in proportion to $1/r$, where r is the distance from the source. Thus, a simple backprojection is unsatisfactory to reconstruct good images.

In order to avoid the blurring an analytic method can be used, called *direct FT reconstruction*. If a noise-free data and ideal LORs (thus, ideal projection profiles) are used, this method can produce an exact representation of the object. The direct FT reconstruction represents image profiles as a sum of sine and cosine functions of different spatial frequencies, k, and based on the *central slice theorem*. Basically, this theorem says that the FT of the projection of a 2-D object along the projection angle ϕ (i.e. the FT of a profile $p(s, \phi)$), is equal to the value of the FT of the object measured through the origin and along the same angle ϕ, in the spatial-frequency domain [23].

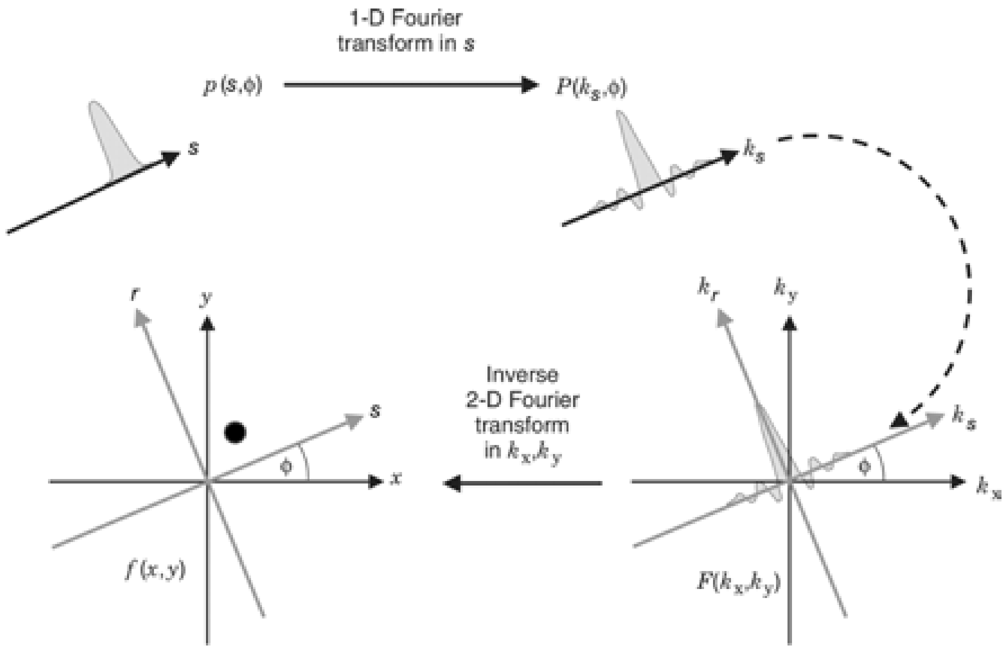

FIGURE 3.9: Concepts of the central slice theorem. *Left*: $p(s, \phi)$ is a 1-D profile of the 2-D object $f(x, y)$ at projection angle ϕ. The theorem states that the 1-D FT of this projection profile (*right*) is equal to the values of the 2-D FT of the object, $F(k_x, k_y)$, along a line through the origin of k-space at the same angle ϕ. The figure is taken from [23].

Figure 3.9 illustrates this concept. The direct FT reconstruction calculates the real source distribution (or the 2-D object) $f(x, y)$ following the steps:

1. Calculate the 1-D FT of each profile.
2. Put all the values of these FTs on a polar grid to obtain the 2-D function $P(k_s, \phi)$. Then these values are need to be interpolated to a Cartesian grid in the spatial-frequency domain in order to obtain $F(k_x, k_y)$.
3. Calculate 2-D inverse FT that gives the image of the object.

The interpolation from polar to Cartesian coordinates in step 2 is computationally intensive and can cause artifacts in the image. This makes the direct FT reconstruction an unpopular method. However, the FT of the projection profiles and the representation of the data in spatial-frequency domain plays an important role in the data filtering in the FBP methods.

3.6.2.1 Filtering

Once the FT of each profile is computed, the filtering can be applied to each profile in the spatial-frequency domain to avoid the blurring of the image from the backprojection. Filtering is a mathematical technique applied during reconstruction to improve the appearance of the image. First of all, a *ramp filter* is applied to each Fourier transformed profile in the spatial-frequency domain. In frequency domain, it is defined as [34]:

$$H_R(k_x, k_y) = \ k \ = (k_x^2 + k_y^2)^{1/2} \qquad (3.2)$$

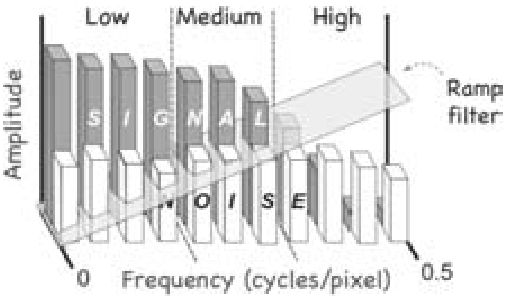

FIGURE 3.10: Effect of the ramp filter in the spatial-frequency domain. The image is taken from [33].

where k_x and k_y are spatial frequency. The ramp filter is a *high-pass filter* named for its shape in the spatial-frequency domain. High-pass filters retain high-frequency data and discard low-frequency data. So, the ramp filter selectively amplifies high-frequency components relative to low-frequency components. It is designed to reduce the $1/r$ blurring resulting from backprojection and to sharpen image details. Figure 3.10 shows how the ramp filter removes the blurring artifact while keeping both signal and noise data.

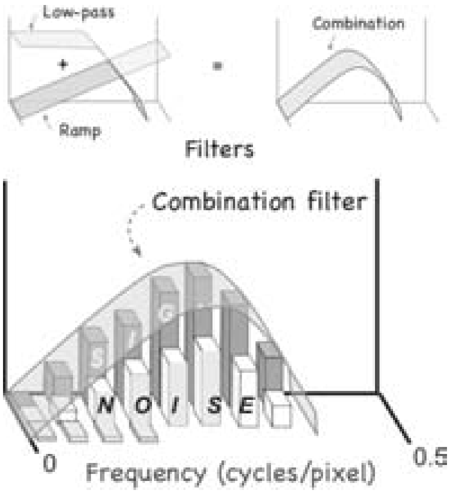

FIGURE 3.11: Effect of a combination of low-pass and ramp filters on signal data, and statistical noise. The figure is taken from [33].

The high-pass ramp filter is usually applied together with a *low-pass* filter in order to reduce the amplified high-frequency noise. Low-pass filters retain low-frequency data and reject high-frequency data. Low-pass filters help to reduce high-frequency noise while retaining signal, which is predominantly composed of low- and middle-frequency data (Figure 3.11). There are many low-pass filters available to process PET data. The most popular filters are following: Hann, Hamming, Butterworth, Wiener, and Parzen. Each filter has a different shape (Figure 3.12), and thus, they modify the image differently. For instance, the Parzen filter greatly smooths data. The Hann and Hamming filters are filters with some smoothing but a relatively greater acceptance of mid- and high-frequency data than the Parzen filter. The

Butterworth filter allows the user to adjust the relative degree of high-frequency wave acceptance. The Butterworth and Hann filters are also flexible filters in that their shape can be altered by specifying certain parameters. The broad, light gray band in Figure 3.12 roughly delineates the possible range of shapes of the Hann filter; the darker gray band delineates the possible shapes of the Butterworth filter.

The filters are usually characterized by the *cutoff frequency.* The cutoff frequency is the maximum frequency the filter passes. If the cutoff frequency is greater than the *Nyquist frequency* (half of the sampling frequency or 0.5 cycles/pixel), the filter is sharp terminated at the Nyquist frequency of 0.5 cycles/pixel, i.e. eliminates the all frequencies that are higher than the 0.5 cycles/pixel. Nyquist frequency is the minimum fundamental frequency useful for showing that two adjacent points are separate objects, and it is always equal to 0.5 cycles/pixel (see an example in Figure 3.14). Although the Nyquist frequency is always 0.5 cycles/pixel, the numeric value when expressed in cycles/cm is a function of the pixel size. For instance, for a pixel size of 0.5 cm, the Nyquist frequency is 1.0 cycle/cm; for a pixel size of 0.25 cm, it is 2 cycles/cm.

The filters such as Hann 3.3, Hamming 3.4, and Parzen 3.5 are characterized only by the cutoff frequency [34]:

$$H(f) = \begin{cases} 0.50 + 0.50\cos\left(\frac{\pi f}{f_m}\right), & 0 \leq f \leq f_m \\ 0, & \text{otherwise} \end{cases} \tag{3.3}$$

$$H(f) = \begin{cases} 0.54 + 0.46\cos\left(\frac{\pi f}{f_m}\right), & 0 \leq f \leq f_m \\ 0, & \text{otherwise} \end{cases} \tag{3.4}$$

$$P(f) = \begin{cases} f - 6\,f\left(\frac{|f|}{f_m}\right)^2 \times \left(1 - \frac{|f|}{f_m}\right), & f < \frac{f_m}{2} \\ 2\,f\left(1 - \frac{|f|}{f_m}\right)^3, & \frac{f_m}{2} < f < f_m \\ 0, & f \geq f_m \end{cases} \tag{3.5}$$

where f are the spatial frequencies of the image, and f_m is the cutoff frequency.

The Butterworth filter is also characterized by the *order*:

$$B(f) = \frac{1}{(1 + (f/f_m))^{2n}} \tag{3.6}$$

where n is the order of the filter. The order controls the slope of the curve (see Figure 3.13).

Hann and Butterworth filters with different cutoff frequencies are shown in Figure 3.13.

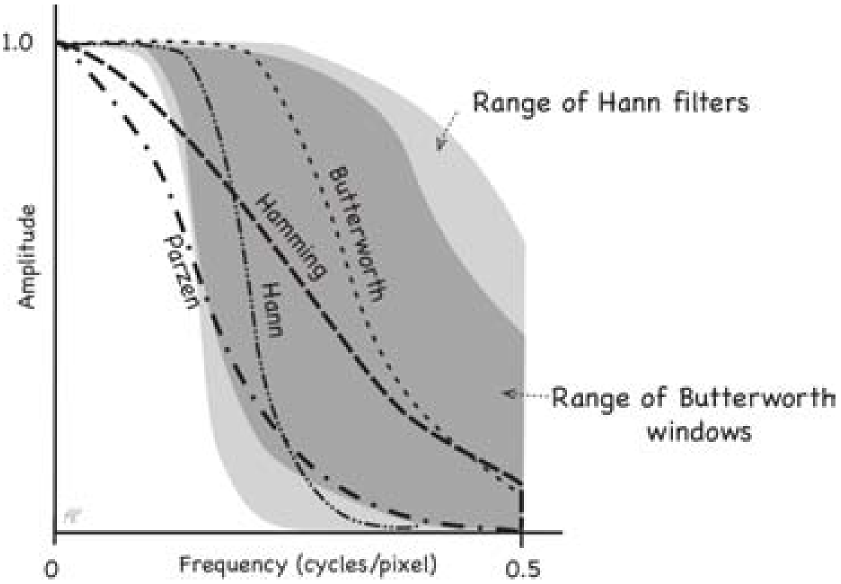

FIGURE 3.12: Commonly used low-pass filters. The figure is taken from [33].

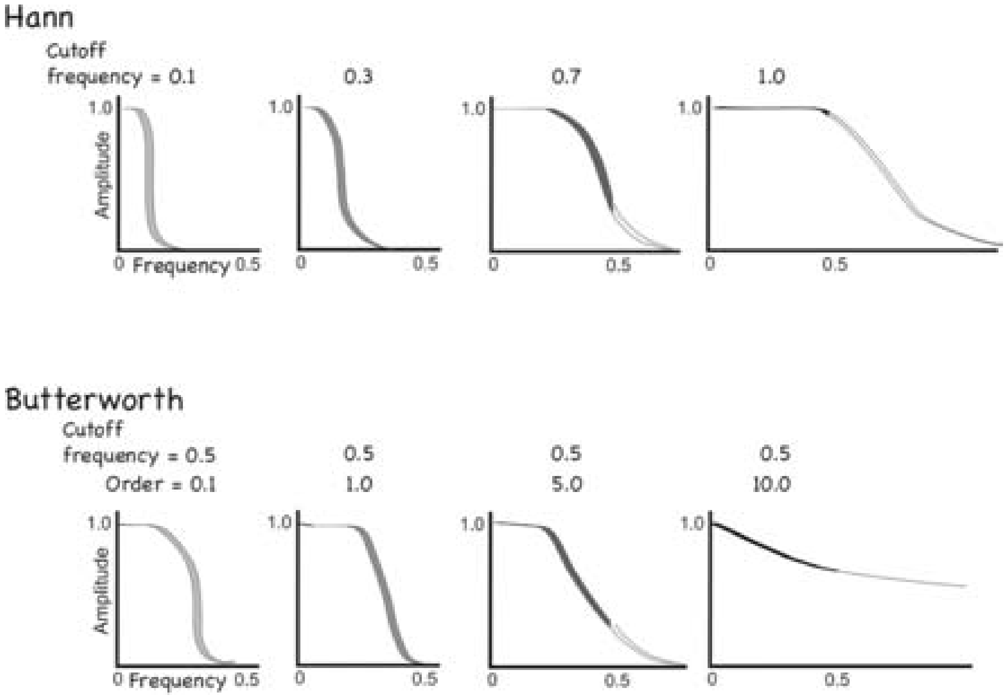

FIGURE 3.13: The Butterworth and Hann windows (filters) can be modified to match the characteristics of the data set. The figure is taken from [33].

FIGURE 3.14: The demonstration of the Nyquist frequency. The extremum (the minimum or the maximum) of the sine wave turns on a pixel. A frequency of 0.25 cycles/pixel causes only every second pixel to turn on. For a frequency of 0.5 cycles/pixel (Nyquist frequency), each pixel is on. At higher frequencies each pixel is also on. The figure is taken from [33].

3.6.3 Ordered subset expectation maximization and maximum likelihood expectation maximization algorithms

ML-EM [35] and OSEM [36] are iterative image reconstruction algorithms. The iterative methods are computationally more intensive than FBP, but since the computer processing speed continues to improve they are finding their way into general use. One of the advantages of iterative reconstruction techniques is that they are less sensitive to the imperfections of the detector and the dataset. In iterative methods, an initial estimate of an image is made. Often the initial estimate is very simple, such as a blank or uniform image. Then the projections are computed from the estimated image, using a process called *forward projection.* This process is exactly the inverse of backprojection. It is performed by summing up the intensities along the potential photon paths for all projections through the estimated image. Afterwards, this set of computed projections (or sinogram) is compared with the actually measured projections (or sinogram). If there is a difference between the estimated and measured projections, corrections are made to improve the estimated image, and a new iteration is performed to assess the convergence between the estimated and measured projections. Iterations are continued until a reasonable agreement between the two sets of projections is achieved.

ML-EM and OSEM are similar and the most widely used iterative algorithms in PET. Figure 3.15 demonstrates the schematic concept of ML-EM. ML-EM method incorporates statistical considerations to compute the most-likely source distribution that would have created the observed projection data, including the effects of counting statistics. Specifically, it assigns greater weight to high-count elements of a profile and less weight to low-count regions.

The maximum-likelihood algorithms are based on the definition of a response system matrix mapping the probabilities of all the possible combination of data for a given FOV. The iterative ML-EM formula has the following form:

$$f_j^{k+1} = \frac{f_j^k}{\sum_{i=1}^{N} t_{ij}} \sum_{i=1}^{N} \frac{y_i t_{ij}}{\sum_{b=1}^{M} t_{ib} f_b^k} \tag{3.7}$$

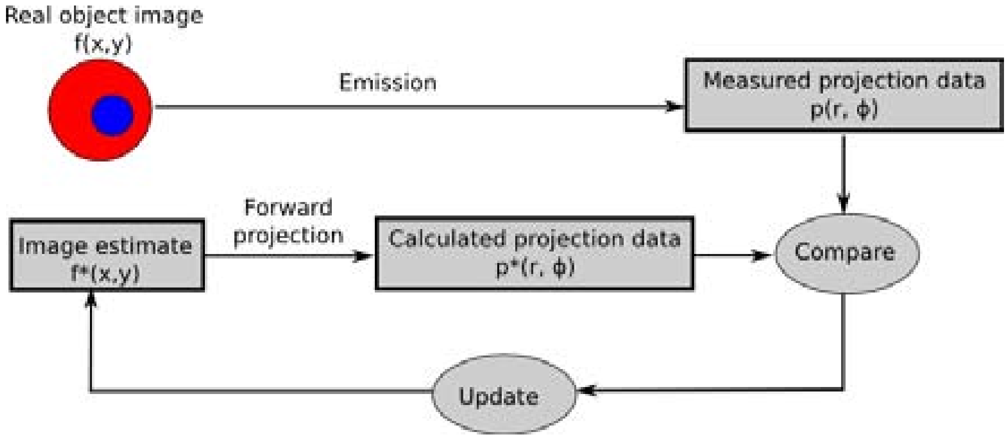

FIGURE 3.15: The concept of the ML-EM image reconstruction algorithm.

where N is the total number of bins of the defined response system matrix and M is the total number of reconstructing image pixels. The sum $\sum_{i=1}^{N} t_{ij} = s_j$ is the sensitivity, or the probability that a photon emitted from image pixel j is detected anywhere. The t_{ij} is the probability that a photon emitted from image pixel j is collected in bin i of the response matrix. The y_i is the measured data (number of counts) in bin i. Finally, f_j^k is the estimation of the intensity of pixel j (i.e., the image estimate) at the iteration number k.

In the ML-EM algorithm, all collected projection profiles are considered at each iteration. One way to speed up the convergence rate of an iterative algorithm is to make more frequent image updates. In the OSEM algorithm, the projection views are grouped in different sets (called subsets), the algorithm goes through the subsets in a specified order, and the image is updated after each subset is considered. The update equation has the following form:

$$f_j^{(k,l+1)} = \frac{f_j^{(k,l)}}{\sum_{i \in S_l} t_{ij}} \sum_{i \in S_l} \frac{y_i t_{ij}}{\sum_{b=1}^{M} t_{ib} f_b^{(k,l)}} \tag{3.8}$$

where $f_j^{(k,l)}$ is the image estimate at the iteration number k and the subset number l. The S_l means the l-th subset. Increasing the number of subsets accelerates the convergence rate but may increase the noise as well. Roughly speaking, if there are N subsets, the ML-EM algorithm may accelerate about N times. The acceleration of approximately 10 times is possible with very little increase in noise.

3.6.4 List-mode ordered subset expectation maximization

LM-OSEM [37] [38] is also an iterative algorithm but, unlike maximum-likelihood algorithms, that uses the binned data and sums over the system matrix bins (see Eq. 3.7 3.8), LM-OSEM only considers and sums over the detected events that are presented in list-mode. The LM-OSEM image reconstruction method is getting popular because the use of list-mode data has certain advantages. One of them is that the complexity of the algorithm is independent of the number of LORs, that makes it suitable for high resolution scanners. This system response matrix of maximum-likelihood algorithms can be huge because its size is proportional to the number of all possible LORs. Since the number of detectors of modern high-resolution PET scanners increases continuously and the system matrix produces by maximum-likelihood methods is needed to be loaded in the computer memory, often this memory is not big enough. The list-mode can be streamed from disk storage and processed event-by-event. The a-posteriori approach reduces considerably the amount of memory needed by ML-EM and OSEM to map the system matrix. The maximum-likelihood algorithms usually pre-process the data by binning it into evenly-spaced angular sinograms. This process changes the Poisson nature of the data. LM-OSEM instead act on the raw data as it was recorded by the scanner, preserving the statistics of the data.

The iterative LM-OSEM formula has the same form as one for the conventional OSEM (Eq. 3.8) with two exceptions. First of all, in LM-OSEM, each measurement in the list-mode is considered as a unique , so that $y_i = 1$ for each detected photon, and $y_i = 0$ for the infinite number of possible events not detected in the current measurement. The value N is the total number of detected measurements instead of the number of detector bins. The second exception is that the sensitivity is no longer the sum over the detected events $s_j = \sum_{i=1}^{N} t_{ij}$, but rather, it is the integral over all possible events i originating from source element j, including those for which $y_j = 0$. The LM-OSEM iteration consists of two steps:

- forward projection of the image estimate f onto the detector: $\sum_{b=1}^{M} t_{ib} f_b^{(k,l)}$, where t_{ib} is the transition probability for event i to have originated from FOV bin b and M is the number of bins in the FOV that are intersected by the LOR of event i.
- backprojection of the measured data, weighted with the forward projected data, providing an update correction for the image estimate.

Thus, the LM-OSEM update equation is:

$$f_j^{(k,l+1)} = \frac{f_j^{(k,l)}}{s_j} \sum_{i \in S_l} \frac{t_{ij}}{\sum_{b=1}^{M} t_{ib} f_b^{(k,l)}} \tag{3.9}$$

The quality of the final image depends on how the values t_{ij} and s_j are defined. The simplest and the best for CPU time consuming and computation memory way is to set these values to one. Another simple method assumes uniform sensitivity and perfect energy and spatial resolution of the detectors, and ignores physical effects such as the Compton scattering of photons. The probabilities t_{ij} are approximated as some constant times the line integral of the LOR through pixel j. This technique has two advantages. The uniform sensitivity approximation makes the method to be independent of the imaging system, and the coefficients t_{ij} can be generated trivially during a fast initial back-projection operation that is usually done to obtain an initial estimation of image. Finally, t_{ij} and s_j can be computed based on the calculation of probability of each event to occur, starting from a particular FOV bin, taking into account its particular cross-section.

Another benefit of using list-mode data is that the energy and detection time are known for each event. This allows to apply corrections for photon scattering, perform dynamic reconstruction or use time-of-flight information in the reconstruction (for scanners with very good time resolution). Nevertheless, due to the large number of pixels in the FOV along LORs, it can still be very time consuming.

3.6.5 Origin ensemble

OE [39] is a stochastic and relatively fast converging technique. The main features of OE are following:

- its convergence speed does not depend on the number of detector voxels;
- it does not require forward- and backprojection operations nor voxelization of the image space;
- it is suitable for any scanner geometry;
- it accepts the raw list-mode data from scanners.

The reconstruction process can be described following way. First of all, each entry of the list-mode data provides the LOR coordinates. Then, for each entry a random position is assigned along the LOR and the event density matrix D stores the number of entries for each FOV voxel location L. At this point, it is necessary to ensure that the chosen random positions (origins) along LORs are all inside the FOV. Image is defined as a set of origins of events. Current set of origins of events in the ensemble is described by the vector Y that contains $3N$ parameters corresponding to the three-dimensional coordinates of the events, where N is the number of events. Then, the algorithm randomly moves the available event origins along the corresponding LORs, generating system state transitions governed by the acceptance probabilities. During one iteration, the following steps are done for each event:

- A new random location L_{i+1} is selected on the corresponding LOR inside the FOV.
- This new location at this iteration L_{i+1} is accepted with certain probability P, comparing the event density $D_{L_{i+1}}$ at the new location with the density D_{L_i} at the old location for this event:

  $$P(Y_i \quad Y_{i+1}) = min[1, \frac{D_{L_{i+1}} + 1}{D_{L_i}}], \tag{3.10}$$

  where the current set of origins of events is described by the vector Y_i.
- When the new location for the event is accepted, the density matrix D is immediately updated accordingly before moving onwards to the next event.

Additionally, the OE algorithm can be modified to model the physics of photon detection, thus allowing to vary the selected position according to the resolution recovery mechanism. However, due to the stochastic nature of the algorithm, in order to get a good quality image, various trial runs should be executed and the final result should be an average of these trial runs.

3.7 Factors that limit the image quality

One can define the *image quality* as the faithfulness of the reconstructed image with respect to the imaged object. The essential characteristics of image quality in nuclear medicine are:

- spatial resolution;
- contrast;
- noise.

Spatial resolution is the minimal distance at which two points (or lines) can be still distinguished. In PET it refers to the ability of the scanner to provide sharp and detailed images. A number of factors contribute to the lack of sharpness in the images. All of them are reviewed in the next section.

The *image contrast* is the measure of differences in intensity in parts of the image corresponding to different levels of radioactive uptake. The contrast can be also defined as the ratio of number of detected radioactive decays in a region of interest relative to the number of detected decays in the surrounding region. Good image contrast is crucial for quantitative image analysis. If the size of an object of interest is larger than the spatial resolution of the scanner, but its contrast is low, the object might be indistinguishable.

The *image noise* can be statistical (or random) and structured. The *statistical noise (or random noise)* causes the mottled appearance of reconstructed images. It is caused by random statistical variations in counting rate. The *structured noise* refers to all non-random variations of the counting rate. For instance, it can arise from the radionuclide distribution or/and from imaging system artifacts (see section 3.8).

Additional distortions of PET images are caused by image *artifacts*. The artifacts are artificial image features such as dust or scratches in photographs, that can arise from physics processes (i.e. attenuation of photons), scanner geometry, imperfections of the detectors (i.e. variation in detection efficiency), dead detector voxels, and image reconstruction processes. Since artifacts can cause incorrect measurements, it is important to recognize and avoid them, and understand their origins and reasons.

All the factors that influence the final image quality can be divided into three main groups: intrinsic limitations set by physics, detector related limitations, and other sources of limitations. All of them are reviewed and described below.

3.7.1 Intrinsic limitations set by physics

3.7.1.1 Spatial resolution

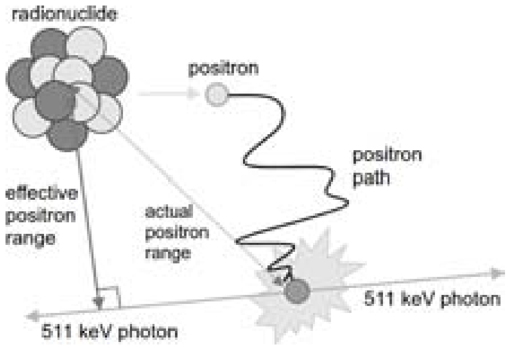

Figure 3.16: Effective positron range. The figure is taken from [23].

One of the main limiting factors to the image quality is the *finite positron range*. The positron range depends on the energy with which it is emitted and the (electron) density of the surrounding matter. According to the Table 2.1, the maximum energies of the positrons emitted from radionuclides used in PET are in the range of 0.5 to 4 MeV. Thus, the positron range can reach several millimeters (up to 2 cm) in water (Figure 2.1). The positron range introduces an uncertainty in the location of the nuclear decay event, and, thus, degrades the spatial resolution of the scanner [40]. Among all radioisotopes used in PET, the ^{18}F emits positron with the smallest energy producing the shortest average (or *effective*) positron range of 0.46 mm (Table 2.1). The effective positron range (R_p) is the average distance from the emitting nucleus to the end of the actual positron range, measured perpendicular to a line defined by the direction of the annihilation photons (Figure 3.16).

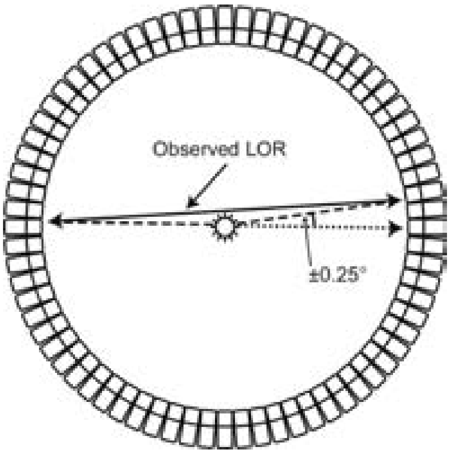

FIGURE 3.17: Non-collinearity of annihilation photons. The figure is taken from [10].

The second limitation is the *non-collinearity* of annihilation photons due to residual momentum of the positron at the moment of the annihilation (Figure 2.3). The non-collinearity contributes to the uncertainty in the localization of the annihilation point and, thereby, degrades the spatial resolution of the scanner (Figure 3.17). Obviously, the larger diameter of the scanner, the bigger the contribution from non-collinearity. The displacement from the real LOR due to the non-collinearity (R_{180}) is linearly dependent on the detector ring diameter (D) and can be calculated as:

$$R_{180} = 0.0022D \tag{3.11}$$

According to the Eq. 3.11 this displacement reaches 1.8 to 2 mm for 80-cm to 90-cm PET scanners, and up to 0.93 mm for head PET scanners of 42-cm diameter. This effect together with the positron range set a fundamental lower limit of the spatial resolution that can be achieved in PET technology.

3.7.2 Detector related limitations

3.7.2.1 Spatial resolution

The spatial resolution of a PET scanner that consists of discrete detector elements is determined by the *width of the detector element* (d). When a photon hits an individual detector (voxel), the exact position of the hit is not known. The error R_{det} of the hit position is normally equal to $d/2$ at mid-position between the two opposite detectors, and to d at the face of either detector. Thus, full-ring PET scanners have a spatial resolution that is radially dependent. It is best at the center of the FOV and becomes worse at the periphery of the FOV. For instance, for a 6 mm detector width, the R_{det} is

∼3 mm at the center of the FOV and ∼6 mm at the edge of the FOV. Thus, in order to achieve a spatial resolution better than 1 mm, a very fine detector pixelation is needed.

Another error is due to the *parallax error* or *depth-of-interaction effect*. The parallax error appears after a photon, that enters a detector, travels a certain distance before depositing all its energy. Sometimes, PET systems are not capable to measure the exact point of the energy deposition, known as the *depth of interaction* (DOI), and the corresponding end of the reconstructed LOR is assigned to the center of the entrance surface of the detector element. The Figure 3.18 shows two different possible LORs for a single annihilation event occurring near the edge of the ring of detectors. The parallax error can produce significant deviations from the real position, leading to a deterioration of the spatial resolution. The larger the depth of individual detectors, the bigger the error from the parallax error. The depth-of-interaction effect can be reduced using thin crystal with high stopping power or using a system (or an algorithm) that is able to measure the photon DOI within the crystal [41] [42]. The use of a PET scanner with larger diameter relative to the size of the object being imaged, produces less parallax error, since the annihilation events will be more centrally located and the photons will cross the detector at a less oblique angle.

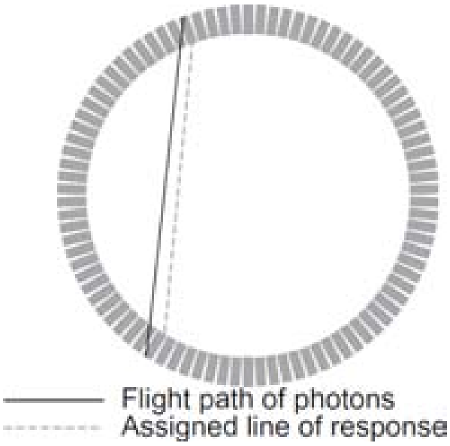

Figure 3.18: Schematic representation of the parallax error. The figure is taken from [18].

3.7.3 Other sources of limitations

3.7.3.1 Spatial resolution

The additional factors that worsen the spatial resolution of the PET system are: reconstruction method used, patient motion, and pixelization effect in the image. Normally *image reconstruction methods* use spatial filters. They are applied to suppress noise in the reconstructed image. Application of filters with a selected cutoff frequency results in the additional degradation of the spatial resolution of the scanner. Usually, the fewer the number of counts collected in an image, the lower the filter cutoff frequency is used and the greater the loss of spatial resolution.

The next effect that degrades spatial resolution is the sampling error (K). Figure 3.19 shows a collection of possible LORs in a PET scanner, As one can see, the sampling in the FOV is not uniform. There are image pixels that include a very big number of LORs, when others include just few LORs. An error due to the sampling is usually a factor of 1.25 [43].

Patient motion also affects final image sharpness. The most problematic motions are cardiac- or breathing-related patient motion, because the duration of the screening time is usually much bigger than these motions period, and the image blurring is the biggest. In order to reduce the influence from this motions gated-imaging techniques are used, especially in cardiac studies. Breath-holding and special breathing technique also are used to minimize blurring caused by respiratory motion. Additionally, some systems have special setups that can measure the external motion and use that information to correct the image. Small amounts of patient motion can be corrected by special correction algorithms that automatically shift the projection views to align the organ of interest.

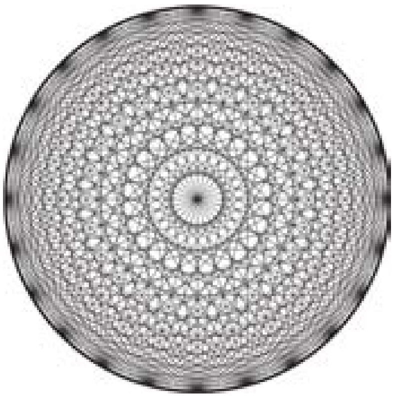

FIGURE 3.19: Schematic representation of the sampling error. Some of image pixels are well sampled (have many LORs crossing them), while other image pixels are very bad sampled (include only a few LORs). The figure is taken from [43].

Reconstructed images are digital, i.e. they consist of discrete pixels. The size of the image pixels sets a limit on the spatial resolution of the image. In order to avoid the pixelation effects and significant loss of image detail, the image pixel size (Δr) should not be larger than about one third of the expected spatial resolution, that is expressed in FWHM of the point spread function (PSF) or line spread function (LSF) [23]:

$$\Delta r \leq \frac{FWHM}{3} \tag{3.12}$$

When choosing the image pixel size, one should take into account that the smaller the pixel the more statistic is needed to keep desirable SNR of individual pixel. According to [23], the SNR of individual pixel (SNR_{pixel}) degrades with the decrease of the pixel size in the following proportion:

$$SNR_{pixel} \approx \sqrt{\frac{12N_{image}}{\pi^2(D/\Delta r)^3}} \tag{3.13}$$

where, N_{image} is a total number of coincidences recorded during the imaging, D is a image matrix size with pixel size Δr. Thus, for very small pixels and limited statistic one will suffer from statistical noise.

Combining all the factors that affect the spatial resolution, the overall spatial resolution R_{sys} of a PET scanner can be estimated by [44]:

$$R_{sys} \approx K \times \sqrt{R_{det}^2 + R_p^2 + R_{180}^2} \tag{3.14}$$

3.7.3.2 Contrast

There are a lot of factors that affect the image contrast in a varying degree. First of all, the image contrast is determined by the *properties of the radiopharmaceuticals*, discussed in the section 3.2. The choice of a radiopharmaceutical that has high lesion-to-background uptake is crucial for getting high contrast. Another common factor that can suppress the contrast significantly is *background counting rates* that are distributed more or less uniformly over the FOV. The background counting rates can arise from several sources, such as scatter, random and multiple coincidences. The number of collected coincidences or the *count density* also affects the image contrast. The smaller the count density, the bigger the statistical noise. So, it is important to collect a certain minimum number of counts to reach good image contrast. The necessary count density usually depends on the dosage of the radiopharmaceutical, the tracer uptake by the organ of interest, screening time, and the detection efficiency of the scanner. Image contrast also depends on the *size of a lesion of interest* relative to system spatial resolution and its *surrounding background.* Precisely, it depends on the background activity and on whether it is a cold (no activity in the lesion) or hot (there is activity in the lesion) lesion. Normally, hot lesions have high contrast when compared to lower background, and cold lesions can be missed in the surrounding higher activity background tissues, especially if they have relatively small size. Finally, patient s motion also reduces the image contrast.

3.7.3.3 Image noise

Usually, factors that affect image contrast also affect the statistical noise levels in the image. For example, the *background counting rates* increase the statistical noise levels in the image. The structured noise also can arise from imaging system artifacts, such as non-uniformities in PET images. An estimation of the noise level can be obtained by making an image without an object between the source and the detector. Additionally, the noise level can be estimated by calculating the SNR, or, in the terminology of images, the *contrast-to-noise ratio* (CNR).

3.8 Correction techniques and image artifacts

When photons pass through the absorber medium, they undergo one or a combination of four processes (photoelectric interaction, Compton scattering, pair production, and Rayleigh scattering) depending on their energy, or they are transmitted out of the absorber without any interaction. The combined effect of the 4 processes is called the *attenuation of the photons*. In order to reconstruct an image of high quality, an exact correction for attenuation is necessary. However, accurate attenuation correction is not so easy to achieve in practice. Besides, there are many other factors that potentially impact on the accuracy and precision of PET measurements. Among them:

- count-rate losses due to dead time limitations;
- variations in detector efficiency;
- acceptance of unwanted scattered and random coincidences;
- dilution of the signal from small structures (*partial volume effect*).

Each of these factors contributes to the sinogram in a different way depending on the 2-D or 3-D acquisition and therefore must be well corrected when producing images.

3.8.1 Data normalization

Modern PET scanners can have more than 20 000 detectors arranged in blocks and coupled to several hundred PMTs. Each detector may have small physical variations, variations in the gain of PM tubes, and geometrical ones [45]. Since the photons travel with different angles of incidence, there also may be differences in the effective thickness of detectors. Because of these variations the detection sensitivity of a detector pair varies from pair to pair, resulting in the non-uniformity of the raw data. The correction for this effect caused by different detector efficiency and geometric factors is known as *normalization* [46] [47].

The most straightforward approach to the normalization is to record the number of counts detected by each coincidence detector pair by exposing uniformly all pairs to the same homogeneous radiation source. The source usually extends through the axial FOV, occupies almost all transaxial FOV of a scanner, and does not have any other subject inside of it. A scan with this kind of source is called a *blank scan*. The source can be made of, for instance, of radioactive water. Then data are collected for all detector pairs in 2-D or 3-D mode. In an ideal scanner, each detector pair (i, j) would record the same number of counts N (within statistical limits). In reality, some detector pairs record more counts and some record less counts because of efficiency and geometry variations. The normalization factor $Norm_{i,j}$ is calculated for a specific pair by dividing the average of counts of all coincidence detector pairs (LORs) N by the individual coincidence detector pair count $N_{i,j}$:

$$Norm_{i,j} = \frac{N}{N_{i,j}} \tag{3.15}$$

The normalization factor is then applied to each detector pair data in a scan of a patient $C_{i,j}$ as follows:

$$C_{Norm_{i,j}} = C_{i,j} \cdot Norm_{i,j} \tag{3.16}$$

where $C_{i,j}$ are the measured counts and $C_{Norm_{i,j}}$ are the corrected counts. This correction is applied to the projection (sinogram) data prior to image reconstruction.

Statistical errors due to the finite number of counts in the normalization scan will increase the noise levels in the corrected data, that is undesirable. In order to achieve a small statistical uncertainty in the normalization factor a very long normalization scan is needed to accumulate a very large number of counts. It is the main problem of the straightforward approach. Therefore, often this approach gets modified to reduce the number of required counts without increasing statistical noise. Most of the modified methods are based on computing the efficiencies of the individual detector elements, rather than all possible detector pairs, and then combining them to estimate the efficiency of the full detector [48].

3.8.2 Attenuation correction

The most important factor that degrades the image quality and the quantitative accuracy in PET is the attenuation of photons in tissues [49]. Therefore, the attenuation correction is by far the largest single correction in PET [23].

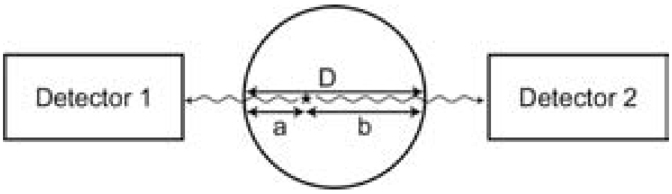

FIGURE 3.20: Two 511 keV photons detected by two detectors after traversing different tissue thicknesses a and b. D is equal to the sum of a and b. Attenuation is independent of location of annihilation, and depends on the total dimension of the body. The figure is taken from [10].

Since annihilation photons from radiotracers located in the center of the patient have to pass through a larger amount of tissue to reach the detector than those present in the peripheral organs, the photons emitted in the former case get more attenuated. The probability P that both annihilation photons will reach the detector is given by the product of their individual probabilities [10]:

$$P = e^{-\mu a} \cdot e^{-\mu b} = e^{-\mu(a+b)} = e^{-\mu D} \tag{3.17}$$

where μ is the linear attenuation coefficient of 511 keV photons in the tissue, a and b are the tissue thicknesses traversed by the two 511 keV photons along the line of response Figure 3.20, and D is the total thickness of the body. As one can see from the equation 3.17, the probability P is independent of the source location along the LOR.

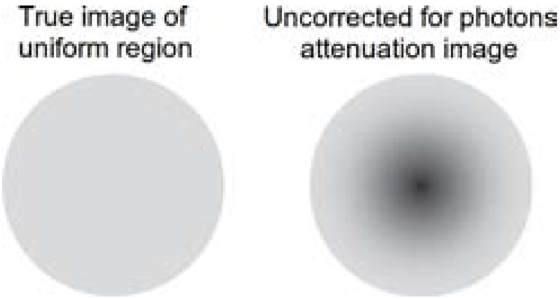

Figure 3.21: True image and reconstructed image without attenuation correction.

Photon attenuation causes non-uniformities in the images, because of the loss of relatively more coincidence events from the central tissues than the peripheral tissues of an organ (Figure 3.21). Therefore, corrections must be made for this attenuation of photons in the body tissue. There are several ways to perform the attenuation correction. The easiest way is known as *Chang's multiplicative method* [50] [51]. This methods is a simple theoretical calculation based on Eq. 3.17. It can be applied for attenuation correction based on the knowledge of μ and the contour of an organ, such as the head, where uniform attenuation can be assumed [52]. An initial image is formed by FBP without any corrections, and this image is used to estimate the outline of the body part being imaged and therefore the distance (D) that the photons have to travel through tissue to the detector. Each projection can then be scaled up by an appropriate factor given by $e^{+\mu D}$. However, in organs in the thorax (for instance, heart), attenuation is not uniform due to the prevalence of various tissue structures, and the Chang s method cannot be applied. In this case the transmission method can be employed.

The *transmission method* includes two steps: the *blank scan* and the *transmission scan.* In this method one uses a thin rod source that contains a positron emitter with a long half-life, for instance ^{68}Ge ($t_{1/2} \sim 271$ days). The source is placed into the PET FOV along the axis of the scanner and rotates around the central axis, so that all detector pairs expose to radiation uniformly (Figure 3.22) [53] [54] [55]. The first step is the coincidence measurement made without a patient (or subject) in the scanner (blank scan). In the second step, the patient (or subject) is placed in the scanner and the measurement is repeated (transmission scan). The attenuation correction factor A for a detector pair (i.e, each LOR) (i, j) is given by:

$$A_{i,j} = \frac{Blank_{i,j}}{Trans_{i,j}} \tag{3.18}$$

where $Blank_{i,j}$ and $Trans_{i,j}$ are the counts in the blank and transmission scans for the detector pair. These factors are then applied to all individual LOR counts in the sinogram obtained in the subsequent patient s emission study. The blank scan is performed only once a day. The transmission scan is performed prior to injecting the patient with the radiotracer. Between the transmission and emission scan the patient should not move to avoid serious artifacts (e.g. areas of too high or too low radiotracer uptake) in the final images. In order to reduce the total screening time, the *post-injection transmission scanning* [56] [57] [58] and *simultaneous emission/transmission scanning* [59] [60] [61] [62] [63] techniques are developed.

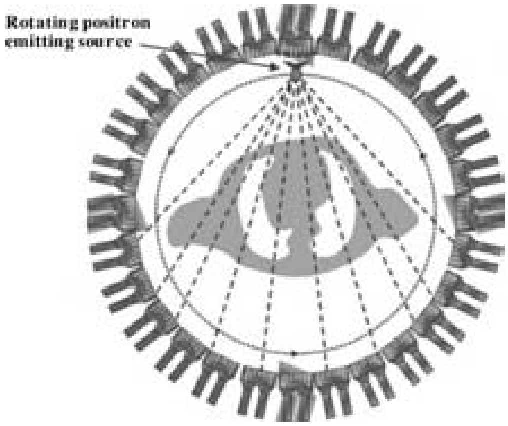

FIGURE 3.22: Coincidence measurements using a rotating positron-emitting rod source. The figure is taken from [18].

Still another approach to the measurement of transmission data is to combine a Computed tomography (CT) scanner with a PET system [64]. The resulting data are taken at energy that is very different from 511 keV, so the data must be scaled to use for attenuation correction of the emission data [65].

3.8.3 Correction for random coincidences

Random or *"accidental" coincidences* happen when two unrelated 511 keV photons from two different positron annihilations are detected within the coincidence time window (see Figure 3.3). Random coincidences add a relatively uniform background across the imaging FOV suppressing contact and causing artifacts. They can cause significant errors in areas which have very low activity. Random coincidences rise with the increase of the energy window width, the coincidence time window, and with increasing activity (varies as the square of activity according to the Eq. 3.19).

If two detectors i and j are considered, then the rate of random events (R^r_{ij}) is given by [10]

$$R^r_{ij} = 2\tau C_i C_j \tag{3.19}$$

where 2τ is the coincidence resolving time of the system in nanoseconds, and C_i and C_j are the single count rates in counts/sec in the individual detectors i and j. However, the relationship of the rates also depends on the implementation of the counting electronics.

The number of random coincidences detected may be reduced by shortening the coincidence time window. However, the window should be big enough not to loose true coincidences due to the difference in arrival times or statistical variations in the triggering of the event timing circuitry. Thus, the selection of the coincidence window is a trade-off between minimizing the acceptance of randoms and minimizing the loss of sensitivity to true coincidences. Usually, the coincidence time window is set to 2-3 times the FWHM timing resolution of the PET scanner. Another way to reduce the detection of random event is to use the shielding of the detectors from activity that lies outside the tomograph FOV [66].

There are few methods for the correction of the random coincidences. The most common method is the *delayed window* method. This approach employs two coincidence circuits - one with the standard time window (usually 6 12 ns) and another with a delayed time window (typically about 60 ns after an event is recorded) using the same energy window. The standard circuit is used to measure the total number of coincidences. No true nor scattered coincidences will be detected in the delayed window, because photons from the same decay will always arrive at the detectors within a few ns of each other. Thus, the additional measurement being delayed well beyond the standard coincidence resolving time means that only accidental coincidences are recorded. For a given source, the rate of random coincidences in the delayed and standard windows will be the same within statistical variations, because the rate at which uncorrelated photons hit the detector is the same for both windows. The correction for random coincidences is made by subtracting the delayed window counts from the total number of coincidence events provided by the standard window for the detector pair.

An alternative correction method is to measure the single count rates C_i and C_j on each detector i and j for a given time window. These measured values can be used to estimate the corresponding values of R^r_{ij} using Eq. 3.19, which are then subtracted from the acquired prompts between the detector pair.

3.8.4 Correction for scattered coincidences

The 511 keV annihilation photons that undergo Compton scattering while passing through a body move in the forward direction without much loss of energy [67]. A lot of scattered photons can fall within the energy window of the scanner set for 511 keV photons and can be detected within the coincidence time window (Figure 3.3). Additionally, the Compton scattering also happens in the detector itself. The scattered radiation leads to a fog background in the reconstructed images, generally more concentrated towards the center of the image. This decreases the image contrast, leads to errors in the reconstructed activity concentration and can cause artifacts. The scatter contribution increases with the density and depth of the body tissue, the density of the detector material, the activity in the patient, and the energy window width of the PET system. The fraction of scattered events in PET can be very high. Typically, it ranges from 10 15% in 2-D mode to more than 40% in 3-D mode (due to the absence of the lead septa) in modern PET scanners based on scintillators. The large value of scattered fraction arises due to three main reasons:

- the predominant interaction in body tissues and detectors for 511 keV is Compton scattering;
- relatively wide energy acceptance window used in crystal PET;
- only one of the two annihilation photons needs to be scattered.

The simplest method for scatter correction is based on taking the counts just outside the FOV, where no true coincidence counts are expected. The outside counts contain both random and scattered events. Thus, after correcting for random coincidences, the only events left in these counts are those that are mispositioned due to the scattering. Then, the signal intensity is measured and normally fit to a 1-D Gaussian [68]. This approach is based on the fact that the scatter distribution contains mainly low spatial frequencies and form tails in the projection profiles. The measured and fitted scatter tails function is then can be subtracted from the projection profiles recorded inside the patient to give the corrected image. This method assumes that scattering is uniform throughout the FOV. Therefore, it works reasonably well for relatively homogeneous organs such as the brain, but, it cannot be used for the abdomen.

Another method for the scatter correction is to use multiple energy window techniques [18].

An alternative method is called the estimation of trues method (ETM) which also uses two windows. In this case the lower window is 450 650 keV, and the upper window is between 550 and 650 keV. One can make the assumption that all of the events in the upper window arise from photons that have not been scattered. These data are then scaled appropriately to equal the number of events recorded in the lower window, and these scaled data are then subtracted from the photopeak energy window.

Finally, a very efficient but also very computationally intensive and time-consuming method is a simulation-based scatter correction [18]. This technique uses information from the original scatter-contaminated image and the CT-obtained attenuation maps to derive the correction. Since the physics of photon interactions in matter is well understood, it is possible to simulate these processes and, using the two images, estimate a distribution of scattered events and their contribution to individual profiles. The estimated contribution of scattered radiation then is subtracted from the projection profiles and the reconstruction is repeated with the scatter-corrected data.

3.8.5 Pile-up and correction for dead time losses

Since radioactive decay is a random process, there is always some probability that a prompt event will be lost because it occurs in the detector too quickly after arriving of a previous event. At high count-rates, the fraction of events falling in this category can become very significant. In PET technique there is always a certain maximum count rate that a system can record. This limitation takes place due to *pile-up* and *dead time* effects at high counting rates.

The *pulse pile-up* events are usually two (or more) photons that arrive simultaneously to the individual detector element and (their energies) get summed up. If these events are two (or more) Compton scattered photons, the resultant peak may fall within the energy acceptance window. This leads the event to be counted but be mispositioned because of the two unrelated events. The pile-up events can cause image distortion at high count rates.

The *dead time* is defined as the time of processing an event during which the detector (more precisely, the whole PET system in the case of the frame-mode acquisition, and an individual detector element in the case of the list-mode acquisition) is not able to record and process a second event, which will be lost [69]. This loss is called the *dead-time loss.*

The main effect of the pile-up and dead time effects is a loss of the linear relationship between the number of coincidence events registered by the PET scanner and the total activity inside the FOV. Thus, without a dead time correction the concentration of radioactivity will be underestimated at high counting rates.

The degree to which a system suffers from dead time is highly dependent on its design and electronics being used. One source of dead time is the integration time, that is, the time spent integrating the charge from the photo-detector. Moreover, the detector electronics usually has a reset time, during which it is unable to accept further events. Another sources are the time needed for analog to digital conversion and the data transmission speed [18].

Dead time correction is made by empirical measurement of observed count rates as a function of increasing concentrations of activity. The measurement is usually performed for a range of object sizes and at different energy thresholds. From these data, the dead time is calculated and a correction is applied to compensate for the dead-time loss. Some systems apply a global dead time correction factor for the system, whereas others apply corrections to individual pairs of detector modules.

3.8.6 Image artifacts: partial-volume effect

Because of the limit of the spatial resolution of PET scanners, hot structures relative to a cold background, that are smaller than twice the resolution of the scanner, show partial loss of intensity, and the activity around the structure appears to be smeared over a larger area than it occupies in the reconstructed image. While the total counts are preserved, the object appears to be larger and to have a lower activity concentration than it actually has. Similarly, a cold spot relative to a hot background would appear smaller with high activity concentration. Such underestimation and overestimation of activities around smaller structures in the reconstructed images is called *partial-volume effect* [70], and this reduces the contrast between high and low uptake regions. While the count loss, the efficiency disuniformity, and the random/scattered event contamination influence the image as a whole, the partial volume effect has a crucial impact on recognizing the small-size lesions surrounded by the medium background activity.

A correction factor, called the *recovery coefficient* (RC) can be applied. The RC is the ratio of the reconstructed count density to the true count density of the object of interest. It is determined by measuring the count density of different objects containing the same activity but with sizes larger as well as smaller than the spatial resolution of the system. Normally, the RCs would be 1 for larger objects. In principle, an RC correction factor can be applied to correct for the partial-volume underestimation of concentrations for small objects. This approach works well in phantom studies in which object sizes are well characterized. However, the sizes of the in-vivo structures are not precisely known, and so the phantom RC data may not be accurate for these structures, unless high-resolution anatomic information is available from another modality such as CT or magnetic resonance imaging (MRI).

Sometimes, the object of interest has low radiotracer accumulation relative to surrounding structures and activity from these surrounding areas spills over into the structure of interest. The effect due to contamination of activity from the neighboring tissues to cold areas is called *spillover* effect. The spillover effect occurs as a result of the same resolution effects described previously. In all cases, partial-volume effects cause the reduction of the contrast between areas of high radiotracer uptake and those of low uptake and to lead to underestimation or overestimation of radiotracer concentrations. This can be the dominant source of error in quantitative PET studies of small structures and must be carefully considered when comparing images of different-sized objects.

3.8.7 Image artifacts due to reconstruction process

As it was mentioned, the most popular reconstruction method is FBP. This method involves the use of the FT of the data for filtering. This process can create certain image artifacts. Projection data are not continuous functions but discrete point-by-point samples of projection profiles. The distance between the sample points (or image pixel size) is the *linear sampling distance*. Projection profiles are acquired only at a finite number of *angular sampling intervals* around the object. The wrong choice of linear and angular sampling intervals and the cutoff frequency of the low-pass filter cause the appearance of the artifacts on the final image.

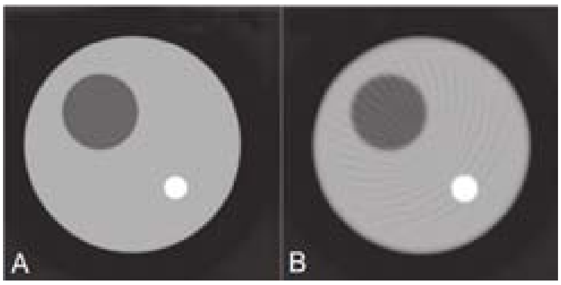

FIGURE 3.23: **A:** simulated phantom. **B:** aliasing artifact due to the coarse sampling. The image is taken from [23].

If the chosen linear sampling distance is too large (the image pixel size is too big), an image artifact known as *aliasing* occurs [23]. When it happens, a sharp edge in a projection is badly approximated, resulting in a high-frequency damped oscillation around the edge. During reconstruction, this error is backprojected along the line tangent to the edge in the image. The example of the aliasing artifact is shown in Figure 3.23. In order to avoid this artifact it is enough to fulfill the sampling requirement of Eq. 3.12.

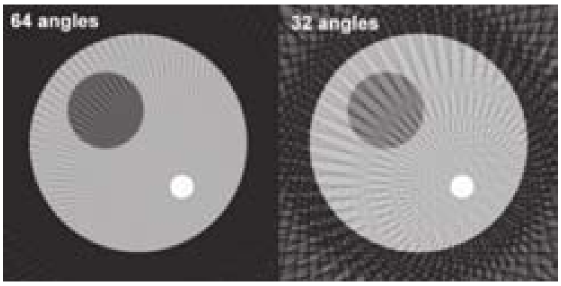

FIGURE 3.24: Artifact due to the choice of too small number of angular samples. The image is taken from [23].

If the number of chosen angular views is too small (or, the same, angular sampling interval is too big), alternating dark and bright streaks occur in the peripheral image region where the sampling density is smallest. An example of this so-called streak artifact is shown in Figure 3.24. In order to avoid the *angular undersampling artifact*, the minimum number of angular views (N_{views}) should be approximately the length of the 180° arc over which projections are acquired divided by the linear sampling distance (Δr):

$$N_{views} \geq \frac{\pi D}{2\Delta r} \tag{3.20}$$

where D is diameter of the FOV.

Another artifact that can appear during the reconstruction is the *ringing artifact.* Fourier transformed data includes high-frequency components. These components are necessary for good representation of the sharp edges of an object. However, the application of a low-pass filter to the Fourier transformed data can create the ringing artifacts in object space [71]. Normally, the use of different filter parameters helps to avoid this artifact.

3.8.8 Other image artifacts

Additional artifacts appear when a PET scanner does not cover 180-degree arc and does not collect data at certain angles. In this case geometric distortions are produced on the reconstructed image. Figure 3.25 demonstrates such distortions. Normally, they are perpendicular to the direction of the absent projections. It can happen that the FOV of the detector does not provide full coverage from all directions. This is also a common reason of artifacts appearance.

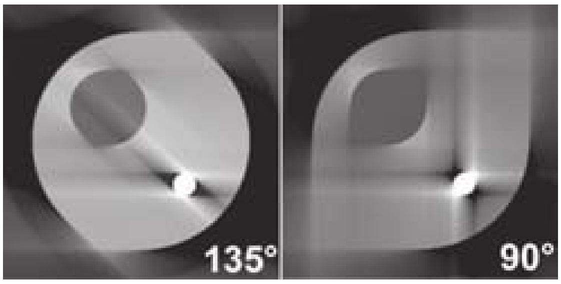

FIGURE 3.25: Artifacts due to that fact that the ring geometry of the scanner is not full. The image is taken from [23].

Two other possible sources of artifacts are patient movement and missing or distorted values in individual profiles caused by instrumentation failures, such as an unstable element in a detector array.

Chapter 4

PET in Nuclear Medicine

4.1 Brief history of PET

Functional imaging with positron-emitting isotopes was first proposed in the early 1950s as an imaging technique that could offer greater sensitivity (detection efficiency) than conventional nuclear medicine techniques with single photon-emitting isotopes such as Single photon emission computed tomography (SPECT).

A very first and simple prototype of positron scanner that used two opposed NaI detectors connected to PMTs and coincidence detection was designed and built in 1950 under the direction of Gordon L. Brownell in the Physics Research Laboratory (PRL) at Massachusetts General Hospital (MGH) within only six months [73]. The screenings of patients with suspected brain tumors started almost immediately. The results were encouraging and were published in 1951 [74]. In the same year independent studies on annihilation radiation detection were performed and published by Wrenn, Good, and Handler [75]. The first attempt to record three-dimensional data in positron detection was done just a bit later, in 1953 [72].

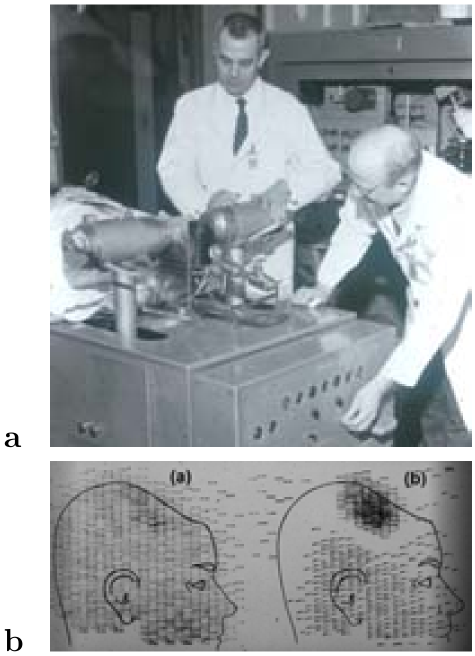

FIGURE 4.1: **a**: First clinical positron imaging device. Drs. Brownell (left) and Aronow are shown with the scanner (1953). **b**: Examples of scans of patient with recurring brain tumor obtained by this device. (Reproduced from [72]). The figures are taken from [73].

Figure 4.2: PC-I, the first tomographic PET imaging device. The figure is taken from [73].

The next clinical positron imaging device built in 1952 (Figure 4.1a) followed the same general concepts of the instrument constructed in 1950 but included many refinements. It produced a low resolution image but was remarkable sensitive in determining whether a tumor existed [73]. An example of two scans of a patient is shown in Figure 4.1b.

One of the early PET prototypes including also a commercial version was developed in the middle 1960s and results were published in 1968 [76]. It was made of two rows of nine detectors each in coincidence with three detectors in the opposite row. The scanner was designed specifically for brain imaging and served for that purpose in a clinical setting for about 10 years.

The first computed tomographic imaging device named PC-I (Figure 4.2) was designed in 1968, completed in 1969, first tested in 1971 and reported in 1972 [77] [78]. It used 2-dimensional arrays of detectors.

At about the same time, in 1970, David Chesler created and tested by computer simulation the FBP algorithm [79] [80] [81], an image reconstruction method that is still the most commonly used in clinical practice. The FBP algorithm was soon applied to data from the PC-I scanner. Brain images obtained with PC-I and reconstructed with FBP are presented in Figure 4.3. PC-I was the first device to obtain PET images and, together with its improved rotate-translate version, PC-II, that was constructed during 1971-1976, remained the only PET devices in use for animal and human imaging for almost a decade [73].

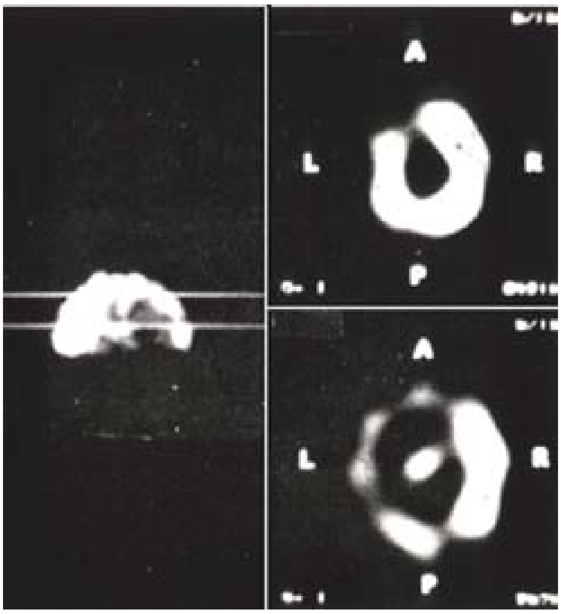

Figure 4.3: Example of a brain study using PC-I and ^{68}Ga. The image is reconstructed with FBP.The figure is taken from [73].

Later, the first proposals of ring systems were published in [82] and [83], in 1973 and 1975 respectively. Then, it was proposed to use a much larger number of detectors individually connected to small phototubes in order to increase sampling to reconstruct images of better quality. This concept was realized in the Donner ring developed in Berkeley [84]. However, in order to get better spatial resolution of a ring system it was necessary to reduce the size of individual detectors, what was impossible due to the relatively big size of PMTs. A few years later a design that permitted to use multiple small detectors identified by a smaller number of phototubes was introduced [85] [86]. This idea was used in two PET systems developed at MGH, PCR-I [87] (Figure 4.4) and PCR-II [88] [89]. PCR-I used a ring design while PCR-II used a cylindrical design. PCR-I was used for 16 years for different studies especially for brain, heart and cancers studies in small animals, dogs and primates [73]. The results obtained with PCR-I gave rise to development of special PET scanners for small animals in the whole world.

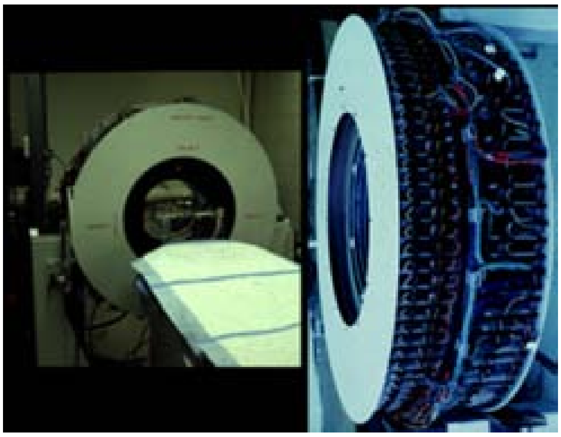

FIGURE 4.4: PCR-I, a single ring positron emission tomograph. Left: tomograph with cot and computer. Right: the electronic assembly. The figure is taken from [73].

However, PET, probably because of relatively low spatial resolution, could not compete with the explosive growth of the CT technique during the 1970s, nor, during the 1980s, with the comparable growth of MRI. Only in 1990s PET was recognized as an important technique for imaging cancer by mapping glucose uptake of body with FDG. The high utilization of glucose by malignant cells allows cancerous tissues to be identified anywhere in the body, even though it may have no anatomic correlate that would allow identification on a CT scan (Figure 4.5) [90].

As we can see from Figure 4.5 (left), the composite of PET and CT systems yields a combination of anatomic, functional and molecular information. Thus the PET/CT hybrid imaging systems are powerful and efficient instrument for tumor diagnostic. The same will be true for PET/MRI hybrid device, and huge effort is being dedicated to the development of commercially available clinical systems for simultaneous PET/MRI images [91].

Today, researches are focused on improving PET scanners to reach two principal goals: high spatial resolution and high sensitivity. Scientists are considering new scanner geometries, new detector materials, new techniques for the image reconstruction, and new radiopharmaceuticals.

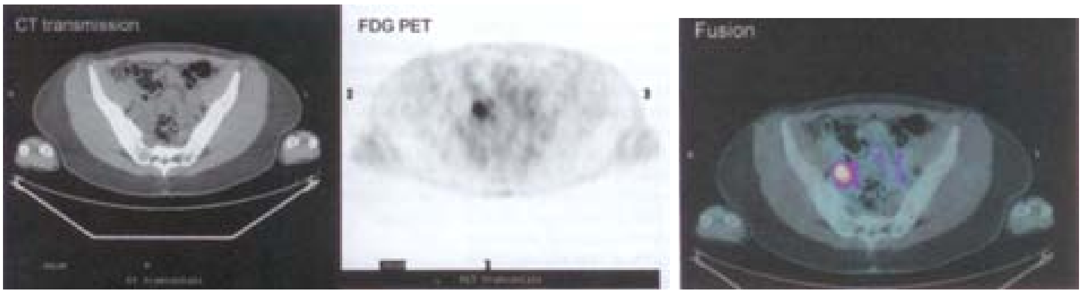

FIGURE 4.5: The transaxial image through the pelvis of a 31-year-old woman. Left: pelvic CT scan does not demonstrate any pathology. Center: PET scan clearly shows the place of FDG uptake. Right: the fusion image. The figures are taken from [90].

4.2 State-of-the-art PET scanners

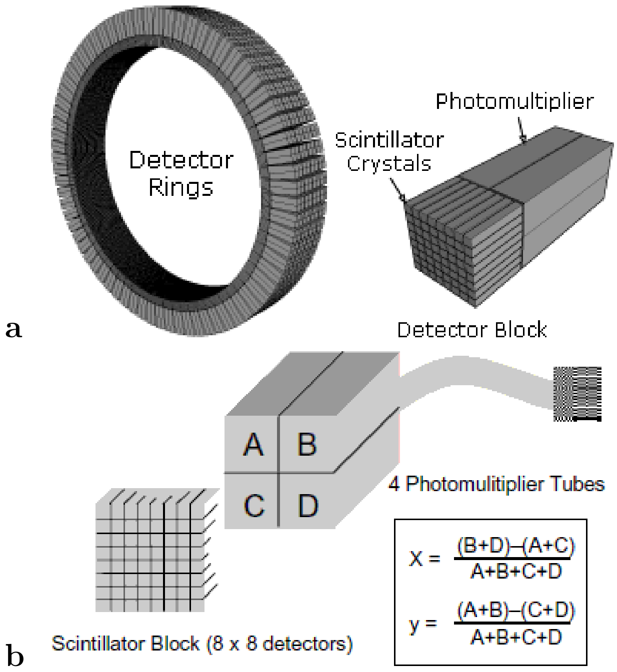

FIGURE 4.6: **a**: Typical geometry of modern PET systems. The figure is taken from [90]. **b**: A schematic diagram of the block detector system, shown here as an 8×8 array of detectors, and the four PMTs. The light shared between the PMTs is used to calculate the x and y position signals, with the equations shown. The figure is taken from [18].

Nowadays, the most frequently used detectors in PET are inorganic solid scintillation detectors because of their good stopping power, good energy resolution, relatively low cost, and relatively simple mounting. In modern PET systems the crystals are organized to a so-called block detector. The block detector is a rectangular parallelepiped made of a scintillator, sectioned by partial saw cuts into discrete detector elements to which a number (usually four) of PMTs are attached. Such a PET scanner, and a schematic diagram of the block detector system are shown in Figure 4.6. Typically, each block detector is about 3 cm deep and grooved into an array of 6 × 8, 7 × 8, or 8 × 8 elements by making partial cuts through the crystal with a saw. The cuts are made at varying depths, with the deepest cut at the edge of the block. The grooves between the elements are filled with an opaque reflective material that prevents optical spillover between elements but facilitates sharing of light among the PMTs.

The width of the detector elements determines the spatial resolution of the imaging device and is normally 3 to 5 mm in modern PET scanners. A PET scanner can contain many block detectors, the number of which varies with the manufacturer. These detectors are arranged in arrays in full rings or partial rings in different configurations. The number of rings usually varies from 18 to 32 depending on the manufacturer. The use of PMTs results a very good SNR for low light levels and is the primary reason for their success and applicability for scintillation detectors. The main drawback of a PMT is the low efficiency in the emission and escape of a photo-electron from the cathode after the deposition of energy by a single scintillation photon. This property is called the *Quantum Efficiency* (QE) of the PMT and it is typically 25% for most of the PMTs.

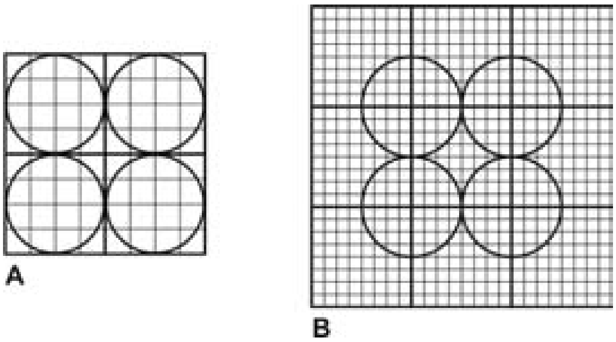

FIGURE 4.7: **A**: PMTs assigned in 4 quadrants separately. **B**: Each PMT shares 4 quadrants of 4 block detectors and improves the spatial resolution. The figure is taken from [10].

A modification of the basic block detector has been made such that each PMT covers four quadrants of four different blocks (Figure 4.7). The technique of quadrant sharing [92] permits the use of larger (in size) PMTs and reduces the total number of PM tubes used in the PET scanner. This design improves the spatial resolution relative to the basic design, because it allows to use smaller crystals (normally, half the size in each (x and y) direction). However, it has the disadvantage of increased dead time due to the need to analyze signals from bigger numbers of PMTs (usually nine instead of four) for a signal event.

In order to have a dead time as short as possible together with a good spatial resolution a so-called one-to-one coupling can be used, when a single crystal is glued to an individual photo-detector. In this case, to achieve spatial resolution better than 3 mm, very small photo-detectors are needed.

Another option can be the coupling of individual channels of a Position Sensitive PMT (PS-PMT) or a Multi-Channel PMT (MC-PMT) to the small crystals [93]. The PS-PMT has a fine grid dynode structure that restricts the spread of photoelectrons thereby providing a position-sensitive energy measurement within a single PMT enclosure [94]. The MC-PMT has several very small channels instead of a single PMT enclosure. It uses a 2-D array of glass capillary dynodes each of which is a few microns wide.

One can use Avalanche Photo Diodes (APDs) [95] instead of PMTs. The APD provides an internal amplification of the signal, thereby improving the SNR comparing to other types of photodiodes. The APDs are normally developed either as individual components or in an array, so they are ideal for use in such a detector design [96] [97]. Additionally, they are not affected by a strong magnetic field, so they can be used in hybrid PET/MRI systems [98]. However, the SNR of the APDs is several orders of magnitude lower than the PMTs give. More importantly, APD gains are sensitive to small temperature variations as well as changes in the applied bias voltage that can lead to practical problems of stability in their implementation for a complete PET scanner.

Other devices as PIN diodes or more recently and very popular silicon photomultipliers (SiPMs) are also being used [99] [100]. SiPMs are built from an APD array set on common Si substrate. Normally, each APD element has a very small pixel pitch that varies from 20×20 to 100×100 μm^2. Their density can be as high as 1000 per mm^2. Each APD is connected to the others and operates in Geiger-mode. In PET imaging, SiPMs represent a very good replacement for the conventional PMTs because of their high *gain* (the ability of a photosensor to amplify the input signal expressed in volts per photon), low bias voltage and fast response. Additionally, they are compact and compatible with magnetic fields. Table 4.1 summaries some basic characteristics of SiPMs and conventional PMTs for their comparison. As one can see, SiPMs combine the fast response of PMTs with the magnetic field insensitivity and easy segmentation of APDs, that makes them very popular photo-sensors for the PET technique nowadays.

TABLE 4.1: Characteristics of SiPM and PMT

Parameter	**SiPM**	**PMT**
Quantum efficiency	<40%	20-30%
Gain	10^5-10^6	10^5-10^7
Bias Voltage, V	~50	1000-2000
Timing jitter at FWHM, ns	0.1	0.3
Magnetic field Compatibility	Yes	No

4.3 Current trend in PET clinical applications

PET scanners are currently used in a large variety of clinical applications, such as tumor diagnostics and treatment, clinical cardiology, and clinical neurology. In the following sections, each of these aspects is reviewed.

4.3.1 Tumor diagnosis

A tumor is an abnormal mass of tissue that is created due to abnormal growth of cells. It can be *benign* or *malignant*. Benign tumors are not cancers. Tumor can usually be removed and, normally, they do not spread to other parts of the body and do not come back. Additionally, benign tumors rarely cause death. Instead, malignant tumors are made of cancerous cells. They grow chaotically, without any control or order. They can invade and destroy the surrounding tissues. The most dangerous thing is that cancerous cells can escape from their original place, invade the bloodstream and lymph system and travel around the whole body attaching to any organ and, finally, continue to grow there. This process is called the *metastasis* and it results in new tumors within the body.

Nowadays, the PET systems together with the FDG tracers are most commonly used for cancer diagnosis [101]. PET measures the metabolic rate of the glucose utilization. Since, cancer cells absorb higher levels of glucose (that is preliminarily labeled with ^{18}F isotope), they have a much higher metabolic rate than other cells. If some region of the body is cancerous, it will accumulate more labeled glucose (i.e. FDG) and the number of β^+ decays will be higher there than in the surrounding tissue. Thus, the cancer location can be spot by PET by looking at the distribution of the FDG in the patient s body.

PET screenings play an important role for the cancer staging, patient treatment schedule, assessment and monitoring of treatment response [102]. A PET scan can identify many forms of cancer, such as lung, breast, brain, neck, colorectal, lymphoma (a type of blood cancer) and melanoma [90]. Moreover, it can distinguish between benign and malignant tumors [103]. One of the most significant features of the PET technology is that it can detect anomalies in cellular activity, normally before any anatomical change takes place. Often, such anomalies can be detected by PET before structural changes can be measured by the ultrasound, X-rays, CT, or MRI techniques. Additionally, a high-resolution PET scanner can spot metastasis localization and estimate intratumoral inhomogeneity [104], that is crucially important for the efficiency of any radiation therapy.

Unlike whole-body (WB) PET, some PET systems are developed to observe only specific organs as, for example, positron emission mammography (PEM) [105] [106]. The organ dedicated PET systems are optimized for their purpose. They are usually smaller than the WB PET and can be placed much closer to the organ of interest of a patient in order to increase the solid angle coverage and gain good sensitivity. Normally, smaller individual crystals are used in these systems, so they have better spatial resolution and, sometimes, are able to measure the DOI. Additionally, due to the small size, the organ dedicated PET is cheaper than any WB PET. Thus, better performance in sensitivity and spatial resolution for a lower cost, makes these systems very popular and useful. For instance, a PEM system can be adapted to guide the biopsy [107], to serve the diagnosis with image fusion, to help when there are the geometric constraints of data acquisition, e.t.c.

Finally, PET is widely used in radiation therapy planning of various malignant tumors. The PET guided tumor treatment is very important for successful radiotherapy [108] [109]. It helps to generate dose distributions such that a tumor gets the highest portion of the dose while minimizing the dose delivery to the surrounding normal tissues [110] [111]. Very often a PET/CT scan is used for the radiation therapy planning. PET can detect areas of disease that are not visible for CT, and CT provides better spatial resolution and anatomical information. Additionally, CT data can be used for the attenuation correction of the PET data [112] [113]. Thereby, the use of the PET/CT hybrid system allows to improve the image quality as quantitatively as visually. PET/CT is a very promising technique for the efficient and accurate radiation therapy planning, however, there are some certain technical challenges and problems to work on to make use of its full potential [114].

4.3.2 Brain diseases

The most challenging screenings are related to brain pathologies, like brain tumors, the Alzheimer s disease (AD), Parkinson s disease (PD) and epilepsy. Among all the tumor kinds, the *brain tumor* is one of the most dangerous and intractable disease. The American Brain Tumor Association [115] asserts that brain tumors are:

- the second leading cause of cancer-related deaths in children (males and females) under age 20 (leukemia is the first);
- the second leading cause of cancer-related deaths in males ages 20-39;
- the fifth leading cause of cancer-related deaths in females ages 20-39 [116].

The National Cancer Institute (NCI) at the National Institutes of Health (USA) defines brain tumor as the growth of abnormal cells in the tissues of the brain. Brain tumor can be benign and malignant.

Alzheimer's disease currently affects an estimated 30 million people worldwide [117]. It is a disease that destroys certain parts of brain and causes the loss of memory, problems with thinking, and at least one area of behavior seriously enough to interfere with daily life. There is no cure for the disease, only some medications exist to help to ease symptoms and improve quality of life for people with AD and their caregivers. AD is a progressive disease, and eventually leads to death. Usually, AD is diagnosed in people of age over 65 years [118] although it can also occur much earlier. Today, there is a worldwide effort under way to find better ways to treat the disease, delay its onset, and prevent it from developing.

Parkinson's and Alzheimer s diseases are different form of the dementia. PD is a progressive disorder of the nervous system that affects movements. Just as AD, it cannot be cured, but special medications can help to improve the symptoms. It usually starts with trembling of the hands and head and, as it progresses, it can become difficult to walk, complete simple tasks, and talk.

Epilepsy is a brain disorder that causes seizures. The seizures happen because neurons in the brain transmit the wrong signals. There is no cure for epilepsy, but certain medications usually control well seizures for most people.

Metabolic activity reflected by FDG-PET can provide important diagnostic related to brain tumors, AD, PD, and epilepsy. However, pathologic variations in the brain FDG uptake can be very challenging to spot due to the high background that results from the glucose metabolism of the normal brain. FDG-PET studies show that in case of AD, as well as in case of PD, the glucose uptake in the affected area of the brain (normally, temporoparietal areas) is lower than in the rest of the health brain [119] [120]. The use of special radiopharmaceuticals (such as ^{11}C-methylpiperidin-4-yl propionate (^{11}C-PMP)) help distinguish patients with AD from PD dementia [90]. The main clinical use of PET in epilepsy is to localize epileptogenic focus in patients with focal epilepsy in order to perform a further surgery. In case of the focal epilepsy, the glucose metabolism in the region of the epileptogenic focus are increased during the seizure period [121] and after it for 24 to 48 hours [122].

4.3.3 Cardiovascular pathologies

In cardiology studies PET is used to determine how much heart muscle is damaged by a heart disease or a heart attack by injecting the FDG tracer. Normally, heart cells that are damaged or destroyed by a heart disease or a heart attack use a very little amount of glucose or they do not uptake glucose at all. Healthy cells and cells that are recovering from injury use bigger amount of glucose. The FDG-PET technique in this field is used for several purposes, such as to confirm heart damage indicated by other tests, to measure how badly heart tissue is damaged after a heart attack or by a heart disease, and to decide if a patient needs a surgery, a heart transplant, or other procedures [123] [124].

Another tracer, labeled with Rubidium-82 (^{82}Rb), allows to measure blood circulation in the heart arteries. PET screenings with ^{82}Rb are used to find the *coronary artery disease* [125]. The coronary arteries of a patient with this disease get completely or partially blocked. It reduces blood flow to the heart muscle and leads to the deprivation of oxygen in it. The coronary artery disease often causes an increased possibility of having a myocardial infarction, or a heart attack. Patients with this disease normally suffer chest pain and shortness of breath. PET studies in this case are very important for the decision of the best treatment, and the schedule of following tests.

In order to reduce image blurring and avoid other artifacts due to the heart beat and breathing motion the gated imaging mode of data acquisition is used (see section 3.3). In this case, PET screenings should be gated to the electrocardiogram signal from the heart, such that data from certain portions of the cardiac cycle gets isolated. This procedure improves image sharpness and contrast.

4.4 PET in research

Many PET systems are not designed for clinical application, but for research studies. This type of scanners are called *pre-clinical* or *small-animal* PET and they are usually characterized by a small FOV (just enough to fit a small animal), high sensitivity, better image quality, and lower cost. Normally, small-size animals such as mice, rats, and, sometimes, nonhuman primates are used for the research purposes. The advantage of pre-clinical PET technique is that the same animal can be studied during a long time, permitting a continuous study of disease model and various interventions over periods of days, weeks, and months. Additionally, a lot of radiotracers are evaluated in animal models using pre-clinical PET scanners. Finally, an important advantage of using small animal PET systems is that imaging provides a bridge between the animal model and human studies. A valid concern in the use of animal models relates to how well that model predicts what will happen in the human. This technique provides the opportunity to perform exactly the same experiments in mouse and human, facilitating direct comparison and appropriate interpretation of the animal model data.

PET studies of the nonhuman primates are used in the investigation of new pharmaceuticals and in the development of new PET tracers; The mouse is a suitable animal for creating human disease models and for trying to understand mammalian biology. Mice are physiologically and genetically similar to humans. Most human genes have a related mouse gene, allowing mice to be used to mimic many human diseases. Additionally, the mouse studies are economically beneficial, because of their rapid rate of reproduction (up to 250 descendants from a pair of mice per year), and it is relatively cheap to maintain mouse colonies. Rat models are important in several fields of biology and are favored as experimental animals, particularly in neuroscience. There are several reasons of it. One one them is historical (many useful experimental models were established in rats before starting to use of mice). Another reason is related to the ease of surgical manipulations, anatomical and developmental studies because of the larger rat brain (roughly 3.3 grams compared to the 0.45 gram mouse brain). Thus, the rat brain will probably remain an important experimental system in the close future and is another appropriate target for small animal PET systems.

The image quality of small-animal scanners is required to be much better than one of usual PET systems. Better image quality is reached due to several factors. First of all, since small-size animals are used as mice and rats, the number of produced scattered events is considerably lower when compared to the whole human body study. Pre-clinical PET systems normally have a narrow timing window to minimize random coincidences. These two factors lower the image noise and, thus, improve image contrast. Additionally, small FOV allows to reduce the error from the non-collinearity, thereby improving the spatial resolution, that also influences on the final image quality. The absolute sensitivity of the pre-clinical scanner should be better than the sensitivity of the typical PET for clinical purposes. Since the number of detected counts per image pixel directly affects the SNR of the reconstructed images, it directly affects the final image quality. If the sensitivity criterion is not satisfied, statistical noise in the reconstructed images will require spatial smoothing which will degrade the spatial resolution. In principle, in case of animal studies, the necessary sensitivity can be reached by injecting larger amounts of radioactivity. However, there are some fundamental issues that limit how far the injected dose can be raised. One of them is that the dose levels should be low enough to not perturb the biological system under study. Also, the random coincidences are proportional to the square of the injected activity and increase rapidly as the injected dose is increased. This is problematic in small animal PET studies because in many circumstances the entire animal (and therefore the entire injected dose) is within the FOV and cannot be shielded if the whole body is being imaged.

4.5 Future PET generation

Nowadays, there are three major trends of PET development: time-of-flight (TOF) PETs, simultaneous PET/MRI hybrid systems, and PETs based on semiconductor diode detectors. Each technique has advantages and drawbacks, and each one is shortly reviewed below.

4.5.1 Time-of-flight (TOF) PET

When a coincidence event is detected, usually, one only knows that an annihilation took place somewhere along the LOR between the two detectors. If it was possible to measure the exact arrival time of two photons, assuming perfect collinearity, one could know precise location of the annihilation. The time of flight taken by annihilation photons to reach a detector is of the order of hundreds of picoseconds. It is less than the time resolution of most of the PET scanners. However, nowadays, the modern scanners with fast scintillating crystals and fast electronics can measure the arrival time with a time resolution better than 1 ns. Thus, the annihilation event can be localized along a line segment instead of the complete line. The faster the detectors the shorter the segment. The segment s length (Δx) can be calculated as follow [126]:

$$\Delta x = \frac{1}{2} c \Delta t \tag{4.1}$$

where c is the speed of light and Δt is the time difference in measuring the coincidence (TOF PET time resolution). For instance, for 500 ps time resolution, the annihilation is located along a ~7.5-cm line segment. PET scanners that use this technique are called *time-of-flight* PETs. Normally, a TOF PET obtains images of significantly better quality comparing to conventional PET scanners [127]. For TOF PET, extremely fast scintillators, such as BaF_2 (barium fluoride) or CsF (cesium fluoride) are used [128] [129]. The advantage of estimating the location of the annihilation point is the improved SNR obtained in the acquired image, arising due to a reduction in noise propagation during the image reconstruction process [130]. However, since BaF_2 and CsF also have a very low stopping power, TOF scanners have a reduced sensitivity that has the opposite effect of lowering the SNR. Hence, the overall design of such scanners requires a careful trade-off between the scanner sensitivity and the TOF measurement so that the overall SNR for the scanner remains high. Nevertheless, recently it was proposed a TOF technique that utilizes LSO crystals [131] [132], already implemented in a commercially available clinical device [133]. Even bigger improvements of the time resolution is expected with the design and development of new photo-detectors [134]. It was already shown that a time resolution better than 200 ps can be achieved by using digital SiPMs [135].

4.5.2 Hybrid imaging

The PET technique provides *functional imaging*, that represents physiological processes of the organism, such as blood flow and glucose metabolism. The current resolution of a PET scanner is of the order of a few mm. MRI and CT provide *anatomical imaging*, that accurately visualize the structure of the organism with great details. MRI and CT can reach a spatial resolution in the μm domain. When combined, the two imaging modalities provide extremely valuable information to doctor about both the exact location and the nature of the anomalies. The combination can be done visually, using special software, or with simultaneous screening using PET/CT and PET/MRI hybrid systems. The last method has become very popular, because it provides significant clinical advantages [136] [137].

Nowadays, the most popular and common combination is a PET/CT hybrid system. As it was mentioned in the subsection 3.8.2, the CT data can be used in PET/CT to correct for photon attenuation. The acquisition of the CT data is usually done immediately before or after acquisition of the PET data, so a very good temporal and spatial correlation between the images is achieved. Thus, PET/CT provides images with better quality (through attenuation maps with less noise), and adds the anatomical information. The first hybrid PET/CT scanner appeared quite recently, in 2000 [138]. First commercial PET/CT systems appeared soon after. They were the Discovery LS (GE Healthcare), the Biograph (CTI PET Systems, later part of Siemens Medical Solutions) [139], and the Gemini (Philips Medical Systems). Hybrid systems have revolutionized the PET technique. In the 1990s PET scanners were normally used only in research and very rarely used in clinical applications. But, with the advent of hybrid PET/CT systems, PET has become a mainstream diagnostic imaging tool.

Recently, the interest of the use of the PET/MRI hybrid system has also increased. Just like CT, MRI provides an anatomical reference for localization of lesions discovered by PET. Nowadays, state-of-the-art high-field (7 11 T) MRI systems are able to visualize super-fine structures (e.g. neuronal bundles in the pons, fine blood vessels) with great image contrast. At the same time, modern high-resolution PET systems are capable of imaging metabolic processes with high spatial resolution and sensitivity. Thus, the combination of two powerful techniques can significantly increase the level of the current knowledge about the human brain, the most complex biological organ. In clinical practice, PET/MRI hybrids, as well as PET systems, can be used in neurology [140], oncology [141], and cardiology [142]. Comparing to PET/CT systems, PET/MR has several advantages:

- Improved soft tissue contrast. MRI provides much greater soft tissue contrast than CT, making it especially useful in neurological, musculoskeletal, cardiovascular, and oncological imaging. Some tumors can be distinguished in MRI and not in CT.

- Reduced exposure to ionizing radiation. Unlike CT, MRI does not use any ionizing radiation. Instead, it uses a powerful magnetic field to align the magnetization of hydrogen atoms in the body.

- True simultaneous acquisition. As opposed to sequential acquisition in combined PET/CT, integrated PET/MR allows true simultaneous acquisition.

- MR-based motion correction. Due to the simultaneous acquisition and the lack of ionizing radiation, real-time MRI data can be used to account for the patient motion during the PET acquisition.

- A wide range of MRI measurements. MRI provides functional MRI (fMRI), diffusion imaging, perfusion imaging, and Magnetic Resonance Spectroscopy (MRS). All of these can add useful information to the functional measurements by PET.

- Decrease in positron range [143]. The positron range is reduced in the plane perpendicular to the main magnetic field (but not in the direction parallel to it). The resulting gain in in-plane spatial resolution is clinically insignificant for low-energy isotopes (e. g. ^{18}F) but might be relevant for high-energy isotopes (e. g. ^{82}Rb), especially when higher magnetic fields ($\geq$7 T) are used.

Since the PMTs cannot work in a strong magnetic field, the APDs or SiPMs are normally used in PET/MRI systems. The simultaneous APD-based PET/MRI hybrid system has been already developed for animal use and showed a success in a tumor finding [144]. An APD-based PET/MRI hybrid system for humans has been also developed [145]. APDs and SiPMs are not affected by strong magnetic field, so their use allows true simultaneous acquisition and requires a smaller scanner room [98]. However, APDs have a limited timing resolution [146], that increases the rate of random coincidences and, additionally, makes impossible to use APDs for TOF PET measurements. SiPMs allow a time resolution sufficient for TOF capabilities.

Another important challenge in PET/MR scanners is the attenuation correction. As opposed to CT, MR does not provide direct information about the density of tissue.

At present, PET/MRI hybrids are very promising diagnostic systems. However, there is still a lot of work to be done for their improvement and optimization.

4.5.3 Beyond the scintillating crystals

Every year the semiconductor diode detectors (Si, CZT, and CdTe) become more and more popular for use in PET. Due to their excellent energy resolution, which is very important for the reducing of scattered events, high Z semiconductor detectors are becoming a promising material for the new generation of PET scanners. Moreover, it is also possible to distinguish multiple interactions inside the detectors due to the possibility of the electronic pixelization. Semiconductor detectors are generally thin and can be operated in stacks, providing DOI information.

Thereby, a PET scanner based on room temperature semiconductor detectors, such as CdTe and CZT, has several advantages when comparing to a PET system based on scintillating crystals:

- it has excellent energy resolution at room temperature.
- it has very good spatial resolution due to the fact that the location of the photon interaction can be defined within a $0.5 \times 0.5 \times 0.5$ mm^3 cubic volume, because of the small size of cloud of electron-hole pairs.
- unlike the scintillating crystals, where the generated signal is indirect (firstly, the X-ray converts to visible photons and then the visible photons convert to electrons), in semiconductor PETs the pixel readout is direct, that improves the energy resolution.
- the number of signal carriers produced in semiconductors is more than an order of magnitude higher than in crystals. It improves the energy resolution of the scanner;
- DOI is known, based on the voxel position;
- finally, semiconductor detector assembly are more compact and maneuverable than crystals coupled to PMTs;

The possible drawbacks, that a Cd(Zn)Te PET scanner may suffer of, are following :

- to reach a very good spatial resolution, it is necessary to use thousands, or even tens of thousands, of individual channels of electronics;
- the PET scanner is considerably more expensive;

One of the advantages of CdTe and CZT with respect to the scintillating crystals is their high electron-hole yield that is approx. 200 e-h/keV comparing to 38 photons/keV yield of Na(I) [18]. For the scintillation detectors, the amount of photons that will reach the photo-detector depends on the length of the crystal, and the way the crystal is wrapped and coupled to the photo-detector. The effective numbers electrons/keV depends very much on the QE of the photo-detector. One can sense that full yield of the crystal is easily 10 times (not mentioning the non-uniformity of the light response) less than that of CdTe/CZT.

There are several drawbacks of CdTe/CZT. First of all, they are expensive. One reason for the high cost is that there is not much suppliers and at the same time the material is being used on very small scale. However, the trend in the use of Cd(Zn)Te in future CT machines is increasing every year [147]. Thus, one can expect, in the foreseen future, to see significant drop in the price of such detector and at the same time significant improvements in the quality and quantity that can be delivered. Additionally, the slow mobility of the holes, which is 10 times slower than the one of the electrons, makes these detectors have relatively poor timing resolution (10 ns) compared to scintillators. For this reason, it will not be possible to construct TOF PET using CdTe or CZT. Even though one can use the different mobilities between holes and electron as an advantage to measure the DOI along the drift field [148], it is still desirable to reduce the impact of slow charge carriers on the time resolution. A possible solution is to use thin detectors, say 1 or 2 mm that are biased at 1000 V/mm. At such high bias value the detector at room temperature will suffer high leakage current and this will deteriorate the energy resolution. To solve this problem one can use Schottky contacts and operate the detector at low temperature, say at around -5°C. This will make it possible to reduce the leakage current by a factor of 100. The cooling can be considered as drawback but it is achievable and it does not need cryogenic expertise. The Schottky contact will help to reduce the leakage current but it makes the detector polarized quite fast. This requires recycling the high voltage (that is ramp down and then up) to maintain the detector operating in excellent spectroscopy conditions. Finally, CdTe/CZT does not have high stopping power like current crystals used in PET.

Although the all difficulties and expense of growing large pieces of CdTe and CZT with required purity, they are now being used in some PET devices and show good results [149] [150] [151] [152] [153].

Chapter 5

The Voxel Imaging PET Pathfinder Project

5.1 A novel design

The Voxel Imaging PET (VIP) pathfinder is an ambitious project aimed to overcome the intrinsic limitations of modern scintillators based PET scanners. The scanner is currently under development in the framework of the VIP pathfinder project [154]. The VIP PET uses electronically pixelated room temperature solid-state CdTe detectors and has a new unique design that allows to:

- achieve a competitive detection efficiency for 511 keV photons with a seamless ring geometry and a stopping power of 4 cm CdTe;
- improve the spatial resolution using pixelated structure of the individual detectors;
- eliminate the parallax error by yielding very precisely reconstructed LOR with a true 3-D detector and a density of 450 channels per cm^3;
- achieve very high SNR by rejecting most of the scattered events due to the excellent energy resolution of CdTe detectors

In addition, the response of the detector is not affected by the strength of the magnetic field and the VIP design can be in principle a potential candidate for developing simultaneous PET/MRI hybrid imaging systems. Moreover, the VIP modular design allows to package the detector in different shapes and for different functionalities: e.g. a WB PET, a small-animal PET, a PEM scanner [105], a Compton camera [155]. Since the clinical applications related to brain pathologies are among the challenging screenings, the VIP is presented as a human brain dedicated PET. Its particular design features suppress the huge amount of scattered events that are due to high density passive material such as human skull in the FOV and that would lead to lower contrast and higher noise images.

5.1.1 The VIP module

The VIP scanner has a modular design based on the conceptually new detector module shown in Figure 5.1. The module hosts 4 pixelated CdTe detectors with 10 mm × 20 mm size and 2 mm thickness. The 2000 V high voltage (HV) is applied such that the electric field is perpendicular to the surface with resulting 1000 V/mm bias and an expected energy resolution of 1.6% for 511 keV photons at room temperature [156]. Each of the CdTe detectors is electronically pixelated into 200 voxels of 1 × 1 × 2 mm^3 pitch, for an accurate photon impact point measurement, and bonded to a thinned read-out chip (ROC) and then mounted on a kapton printed circuit board (PCB). One of the essential ideas is reducing the passive material by thinning the ROC and the kapton PCB down to 50 μm each. The conductive glue between the ROC, the CdTe detectors, and the kapton PCB will occupy an additional thickness of 15 μm. The combined attenuation coefficient of the passive material accounts for less than 2% compared to 2 mm CdTe. A distinctive characteristic of the VIP is that the module can be given a trapezoidal shape to form a scanner ring without cracks to boost the system sensitivity. This idea has been already implemented earlier by using continuous NaI scintillating crystals [157]. The VIP module, by design, is made to point to the center of the PET cylinder with the 511 keV photons entering from the edge of the CdTe detector. Therefore, even though CdTe has lower density and thus significantly lower stopping power than scintillating crystals such as LSO, the depth of the VIP module

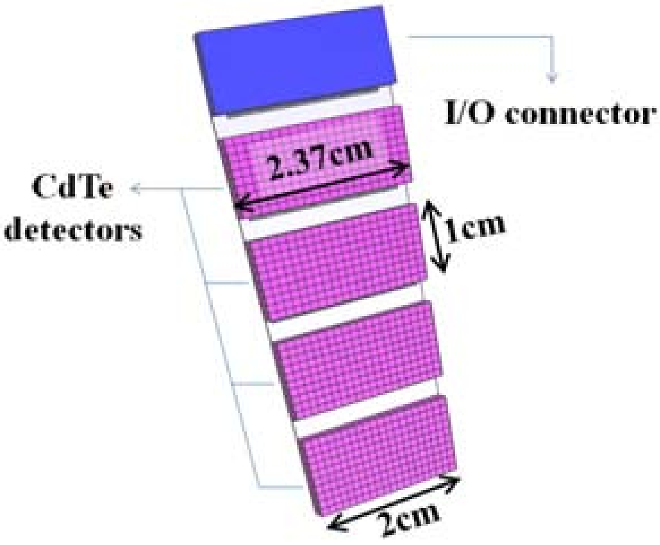

Figure 5.1: Conceptually new design of an individual VIP detector module. It is made of 4 CdTe pixelated detectors. Each pixelated detector contains 200 voxels (3-D pixels) with dimensions 1 mm × 1 mm × 2 mm. The blue piece at one end of the kapton PCB is a connector to couple the detector module to a bus of signals.

can be extended in radial direction by adding CdTe detectors as much as needed to reach the necessary detection efficiency. In the proposed design, incident radiation traverses a minimum of 4 cm CdTe with 70% of singles 511 keV photons being completely absorbed. The pixelated structure of the PET scanner will significantly improve the spatial resolution and exclude the DOI effect.

5.1.2 The full ring

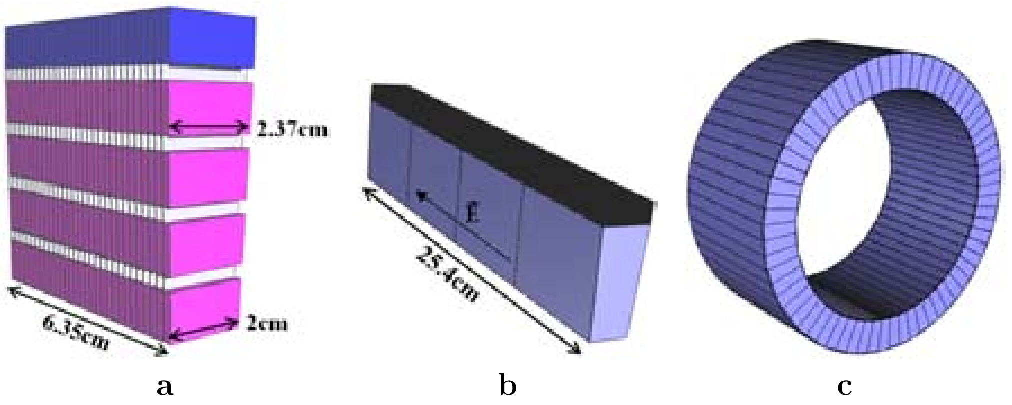

Figure 5.2: **a**: A VIP module block that is made of 30 detector modules and contains 24000 voxels. Its top part will have PCB with connectors (not shown) so that it can be connected to the outer bus for the I/O signals as well as for the LV and HV supplier. **b**: A VIP ring section formed from 4 module blocks connected to the same bus (black region). The full VIP scanner consists of 66 such sections. **c**: General view of the VIP scanner. Due to the trapezoidal shape of the CdTe detectors the system does not have cracks in between ring sections.

The next unit of the VIP scanner is a module block that consists of 30 detector modules stacked together (Figure 5.2a). Thereafter, 4 such module blocks connected to the same electronic bus form a VIP section (Figure 5.2b). The electric field $\vec{E}$ inside the detector is directed as shown in Figure 5.2b and therefore it is parallel to the magnetic field $\vec{B}$ of a possible MRI scanner. It is shown in [156] that in such a configuration, with $\vec{E} \times \vec{B} = 0$, the response of the detector is not affected by the strength of the magnetic field and the VIP design can be in principle a potential candidate for developing simultaneous PET/MRI imaging systems. However, the impact of radio frequency (RF) on the VIP system, as well as the influence of the VIP scanner itself with the accompanying electronics to the SNR of an MR image, has not been assessed. Finally, when 66 sections are put together, they form a cylindrical seamless PET scanner (Figure 5.2c) with a total of 6,336,000 detector voxels. The complete scanner has an inner diameter of 42 cm, an outer diameter of 54 cm, and an axial length of 25.4 cm to match the typical size of a brain PET. With a such big number of channels the signal processing, described in the following section, represents a big challenge.

5.1.3 The VIP ASIC

Due to the large number of individual channels, the design of the electronics for the signal processing and readout is a crucial and unique feature of the VIP project. For each channel independently, the VIP readout will provide a digitized value of the energy, the time stamp of every photon detection, and the position of the channel where the detection happened. The signal processing takes place in-situ with the electric layers located in between adjacent detector modules. To obtain the energy and time information, each channel is bonded to a pixel hosting a fully integrated front-end electronics for a total surface of 1 × 1 mm^2 per channel. Figure 5.3 shows the architecture of the proposed application specific integrated circuit (ASIC) for the pixelated CdTe detectors of the VIP project. The ASIC consists of two main areas. The first one is a 2-D array of independent pixel electronics of 10 × 10 pixels that will be connected to the pixelated CdTe detector via bump-bonding. The second are is the location of the back-end of the ASIC. The whole chip has dimensions of 10 mm × 13 mm where the back-end circuitry occupies the area of 3 mm × 10 mm. The ASIC back-end contains an analog section and a digital section. The analog section includes a band-gap and current reference circuit, a temperature sensor, and a 6-bit global threshold digital-to-analog converter (DAC). The digital part contains the time to digital converter (TDC), the digital controller, a configuration register, and the identification register.

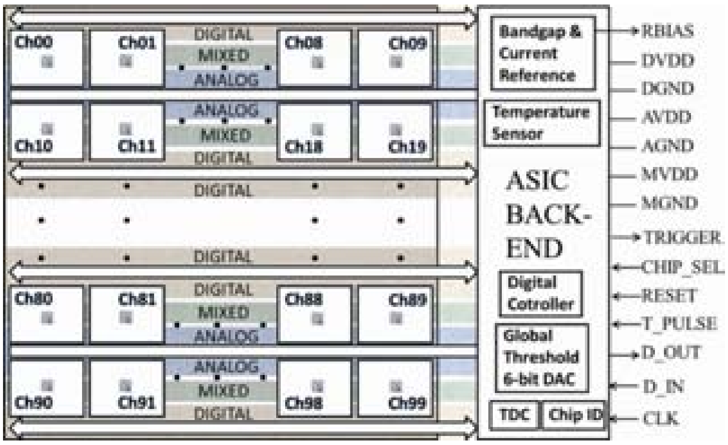

FIGURE 5.3: Architecture of the proposed readout integrated circuit for the pixelated CdTe detectors of the VIP project [158].

Figure 5.4 shows the architecture of an individual channels (pixel electronics). It consists of three main sections: the analog front-end electronics (Figure 5.4 top part), the mixed-signal circuits such as the analog-to-digital converters (ADCs) and the DACs (Figure 5.4 central part), and the digital circuits such as digital controller and configuration registers (Figure 5.4 bottom part). Each of 100 channels has the same architecture, but the

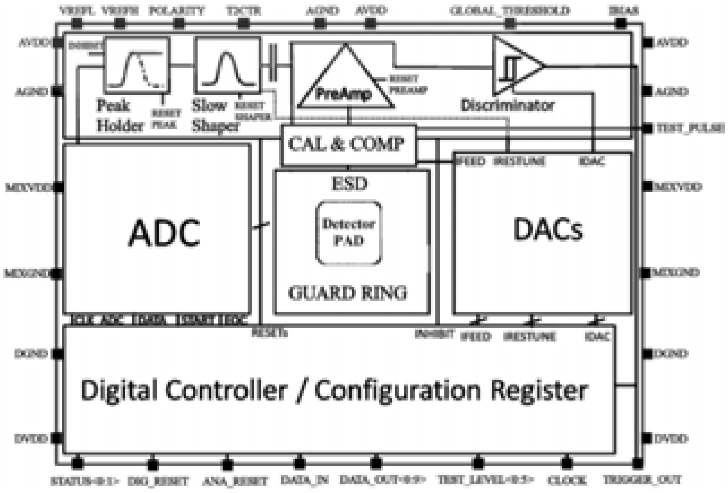

FIGURE 5.4: Architecture of the proposed pixel readout electronics [158].

three sections can be flipped horizontally according to the position of the supply lines shown in Figure 5.3. Each channel has its own preamplifier, a detector leakage compensator, a pulse shaper and a peak & hold circuit, DACs, and one ADC, a discriminator, a tunable threshold level with a digital controller, and a pulse feeding. This solution is called smart-pixel . Its design, the development status, and the results of the successful characterization of the preliminary prototypes are described in detail in [158]. The proposed design of the ASIC allows to optimize the front-end electronics in terms of noise and time response for high-density voxel imaging systems based on pixelated CdTe detectors. The smart-pixel has the advantage of compactness and of the robustness of having the analog front-end and the analog to digital conversion optimized for minimum parasitic loading and/or coupling. To knowledge of the author, to this day, no other design with the specifications and functionality of the VIP smart-pixel has been developed. In this approach, the ASIC design transforms each channel into a completely independent self-triggered detector operating standalone.

5.2 System specifications

Detectors that are currently used in the nuclear medicine can be characterized by following specifications:

- energy resolution;
- coincidence time resolution;
- timing resolution;

- dead time;
- measuring time;
- magnetic field compatibility.

In [156] the characterization of CdTe detector in terms of energy resolution and time of response was done. A resolution of 0.98% at 511 keV has been achieved with a 4 mm × 4 mm × 2 mm detector at 900 V/mm and -7 ℃. The energy resolution acquired with the same setup at room-temperature and 500 V/mm for ^{22}Na isotope is 1.57% [156]. The *time coincidence resolution* in the scanner is defined by two parameters: the resolution time of the detection system and the time coincidence window. The arrival time of a photon to a detector is randomly blurred following a Gaussian distribution according to the time resolution of the system. The *timing resolution* of a PET detector describes the uncertainty in the time determination of the arrival of a single photon as measured by the detection chain, on an event-by-event basis. The timing resolution of a PET detector is important for the detection of two photons originating from a single coincident event. Obtaining good timing resolution of a PET detector is a challenging goal since correlated photons arrive to detectors with time differences of a few hundreds of picoseconds. In case of 2 mm thick CdTe, the time resolution depends on the location of the impact point along the 2 mm distance between anode and cathode. This is due to the significant difference between hole and electron drift speed (approx. 1:10) [69]. Since timing resolution represents the variability in the arrival times for different events, it needs to be properly accounted for when detecting coincident events. When a photon reaches a detector producing a single event trigger, all detectors allowed in coincidence are looked for another single event trigger within the time coincidence window. The size of the coincidence time window should be chosen taking into account the timing resolution of the system. Since the amount of random coincidences is proportional to the coincidence timing window, a narrow window helps reducing their occurrence. At the same bias and temperature conditions (900 V/mm and -7 ℃), two identical CdTe detectors show a coincidence time FWHM of 25 ns [156].

PET scanners may be regarded as a series of subsystems (individual channels), each of which requires a minimum amount of time to elapse between successive events, for them to be registered as separated. Since radioactive decay is a random process, there is always a finite probability that successive events will occur within any minimum time interval. The total time required to complete the signal processing is the sum of the measuring time plus the dead time. During the measuring time interval, a single channel is not able to distinguish hits that come to the same detector from different events. These hits become a single merged hit for the detector. The expected measuring time of a single

VIP voxel is 20 μs. Once the energy merging is complete, a single channel becomes unable to process a second event for a minimum time interval represented by the dead time. The resulting event loss (the dead-time loss) is a serious problem at high count rates and varies with different PET systems. One source of dead time is the time needed for analog to digital conversion and the data transmission speed. Thus the dead-time loss can be reduced by using detectors with faster electronics components. Based on the technology being used for the VIP scanner the expected dead time is 130 μs (per voxel). Given the huge number of channels, the VIP scanner is expected to be immune to dead-time loss up to very high activity.

5.2.1 Advantages and drawbacks

The VIP system has certain advantages as well as drawbacks when compared to a similar PET scanner based on the scintillation detectors. Some features of CdTe are described in the sections 2.3.3 and 4.5.3. In this section one discusses the merits and the issues of the whole VIP system.

To obtain an ideal LOR one needs to have a well segmented detector and at the same time a good energy resolution to make sure that there is no scattered process involved. Both features are realized in VIP, but difficult to achieve by crystal scintillating detector. First is not easy to segment the crystal to millimeter size voxel (i.e., 3-D pixel) and this creates a limitation on the spatial resolution that can be achieved with crystal. In addition, the signal is generated in the crystal is indirect and this creates a limitation on the energy resolution when it is compared to Si or Cd(Zn)Te.

Using trapezoidal parallelepiped shape scintillating crystal will help to make the PET crack free but such crystal will suffer from non-uniformity of light response. One approach, that is used in high energy physics, to make the light yield uniform, for such of crystal, is to wrap it with a paper that has been blackened in gradual way, to absorb part of the light, instead of reflecting it back to the crystal. This trick reduces the non-uniformity of light emission within the crystal but does not solve it 100%. With CdTe such problem does not exist.

Based on the current price of CdTe detector, the cost of VIP scanner is rather expensive when compared with typical PET based on scintillating crystals. However the price of VIP is comparable to the fully operational CdTe PET described in [153], with the exception that the pixel resolution of VIP is better, it has less dead material, and it is more compact in size.

Additional possible issue of VIP is the complexity. In spite of the integration of the device is complex, it is much simpler than what has been described in [153]. Instead of handling tiny coplanar detectors presented in [153], VIP uses flip chip process which allows us to speed up the production while reducing the voxel size to 1 mm × 1 mm × 2 mm compared to 4 mm × 7.5 mm × 1 mm from [153]. Moreover, the technology that can handle the usage of a huge amount of channels is also already available. An example of such technology was previously proposed in [159] in the frame of Dear-Mama project.

Finally, CdTe does not have high stopping power like current crystals used in PET. However using VIP module design one can use as much CdTe detectors along the radial direction of the PET scanner as needed to achieve an adequate sensitivity at no cost on the time stamp, spatial, and energy resolution.

In summary the VIP-CdTe PET design can:

- Achieve better energy resolution than what the PET based on scintillators can provide.
- Use as much as needed of CdTe to achieve high detection efficiency without compromising on the spatial, timing, and energy resolution.
- Obtain excellent LOR and even recovery of Compton scattered events due to high voxel density ($450/\text{cm}^3$).
- The large number of channels, each with the corresponding smart pixel (preamp, shaper, peak-hold, and ADC) allows the detector to handle high rate without pile-up.
- Have trapezoidal shape of the module that makes the VIP PET crack free, without affecting the spatial, the time, and the energy resolution.

5.3 Other applications

The VIP PEM scanner and the VIP Compton Camera are currently being developed in the framework of the VIP pathfinder project. Their design and features are shortly reviewed in the following sections.

5.3.1 PEM

A PEM system is an organ-dedicated PET scanner for breast cancer detection with a restricted FOV to achieve higher cancer detection performance in terms of both sensitivity and specificity with respect to the conventional WB PET scanners. Additional advantages are a lower cost and lower necessary dose. The VIP PEM is based on the same VIP module shown in Figure 5.1 but shaped to a parallelepiped form instead of trapezoidal one (Figure 5.5A). Each CdTe detector has following dimensions: 2 cm × 1 cm surface and 2 mm thickness. The CdTe detectors are segmented into 1 mm × 1 mm pixels for a total of 4 × 200 channels per module.

The VIP modular design allows to build virtually any detector geometry by stacking the needed number of modules in arbitrary patterns. Following the typical coplanar design, the VIP mammograph consists of two parallel paddles, each one hosting one sliding detector head (Figure 5.5B). The two heads are made of 80 modules each, arranged along two parallel lines of 40 modules for a total of 64000 channels per head. The head section is 170 mm wide along the x-axis and 40 mm wide along the z-axis, and the two detector heads must slide axially for a complete scan of the 170 mm × 60 mm × 240 mm FOV.

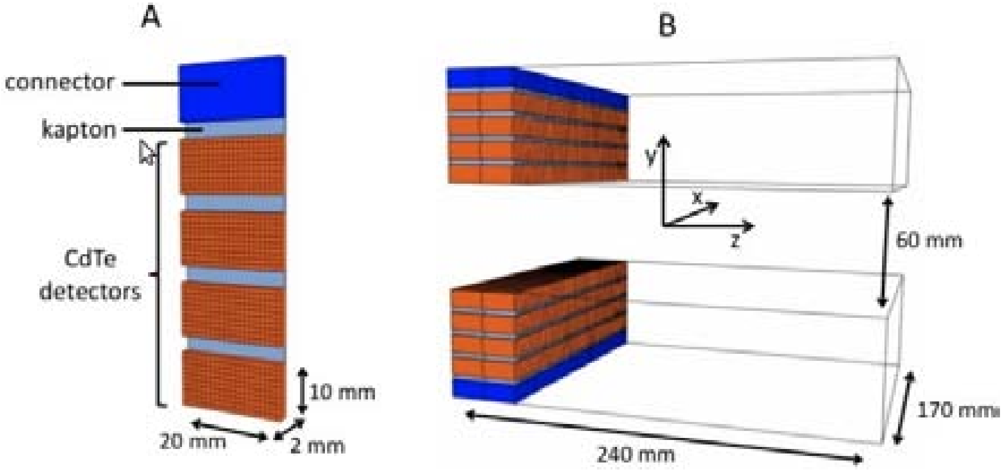

FIGURE 5.5: **A**: basic detector module. **B**: full VIP PEM detector [105].

5.3.2 Compton camera

Compton gamma cameras for nuclear medicine was proposed as an alternative to the SPECT technique. SPECT, just like PET, produces tomographic images of the activity of radioactive tracers. However, whereas PET obtains images from annihilation photon pairs, SPECT uses single photons to produce images. An advantage of SPECT is that different isotopes can be used simultaneously, with a large choice of radio tracers available that emit single or double gammas with different energies. Also, because SPECT detectors do not need to have full angular coverage, they are cheaper. A disadvantage of SPECT is the use of mechanical collimation to reject photons that do not travel along a path within a certain angle, which makes that SPECT has a significant lower efficiency than PET. A low efficiency means that a higher radiotracer dose or a longer exposure time is necessary to obtain an image with sufficient quality, which is not in the advantage of the patient. Additionally, unless one uses a multi-headed gamma camera, in SPECT, in order to acquire complete tomographic images, it is necessary to rotate the gamma camera and obtain projections at different angles during the rotation. Finally, the use of the mechanical collimator restrict the spatial resolution of the scanner, that cannot be better than the size of the collimator.

Compton gamma cameras overcome the SPECT limitations by using the kinematics of Compton scattering (instead of mechanical collimation) to localize the radioactive source. Photons emitted by a radioactive source scatter (via the Compton scattering process), depositing some of their energy in the scatterer detector and, subsequently, are absorbed in the absorber detector (via the photoelectric effect) where all of its remaining energy is completely deposited (Figure 5.6). Hence, the choice of the material for the scatterer detector depends on the attenuation strength of Compton scattering in the detector material, whereas for the absorber, it depends on the attenuation strength of the photoelectric attenuation in the used material. The original gamma ray source is located on the surface of the Compton cone (see Figure 5.6) identified by the cone axis and apex, determined from the hit locations, and the scattering angle θ_c that can be calculated from the equation 2.2. However, because the momentum of the electron the gamma scatters from is unknown, Eq. 2.2 is only approximately valid. This deviation of the relation between scattering angle and energy deposited in the scatterer detector is known as the *Doppler broadening* effect [160] [161]. Without knowledge of the momentum of the recoil electron, the Doppler broadening effect, in addition to the energy resolution, contributes to the smearing of the Compton scattering angle. The advantages of a Compton camera over a SPECT camera are: higher sensitivity, larger FOV, larger energy range of gamma sources, and it is not necessary to be rotated to obtain 3-D images.

A schematic view of the VIP Compton camera design is shown in Figure 5.6. The scatterer and the absorber are made of electronically pixelated Si and CdTe detectors, respectively. The distance between scatterer and absorber and the thickness of both detectors are optimized for the best compromise between spatial resolution and detection efficiency [155]. The absorber detector of the Compton camera has a parallelepiped shape of size 540 mm × 380 mm × 62 mm and a nominal thickness of 4 cm. Each absorber module (Figure 5.6) is the VIP module shown in Figure 5.1 that has a parallelepiped shape. The scatterer detector has a parallelepiped shape with a 540 mm × 380 mm × 26 mm size and a nominal thickness of 2 cm. The scatterer module (Figure 5.6) is made of 19 Si pixelated detectors of 10 × 10 voxels each. Voxels of 1 mm × 1 mm × 2 mm size are chosen for consistency with CdTe sensors, although Si can be made much thinner at acceptable cost. The choice of Si for the scatterer detector is justified by its optimal Compton cross section and a relatively small Doppler broadening effect compared to other semiconductor materials [160]. The advantages of the proposed design are: easy portability, functioning at room temperatures, excellent energy resolution of about 1.6% at 511 keV, and excellent spatial resolution with millimeter-size voxels and operational in strong magnetic fields.

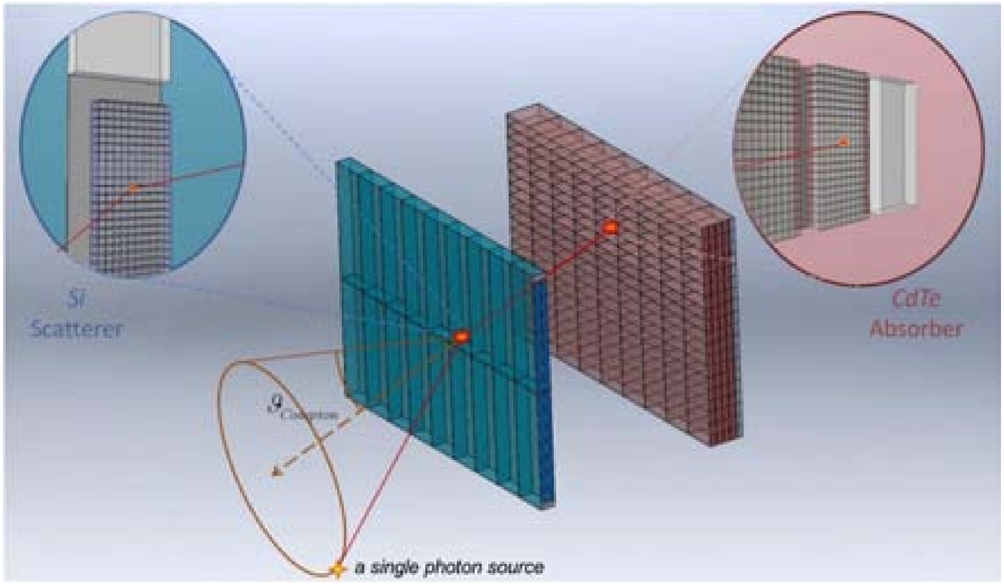

Figure 5.6: The VIP Compton camera [155].

5.4 Data selection and processing

Due to the large number of channels in the full PET scanner, each channel is treated as an independent detector with data collected in list mode (LM) and processed off-line. Hit entries of the data list are characterized by the (x,y,z) position of the center of the correspondent voxel, the collected energy, and the time stamp. The coincidence searching algorithm processes the LM data to group consecutive hits lying inside a coincidence time window of 20 ns. Within a group of coincident hits, energies of hits whose reciprocal distance is below 1.45 mm are added together and the new position assigned to the E-weighted centroid. The merging radius is chosen in order to recover up to 99% of the deposited energy that secondary particles can deposit away from the original impact point (Figure 5.7). After merging, only coincidences with two hits are considered, with both the corresponding energies equal to 511 keV ± 8 keV.

Approximately two thirds of 511 keV photons in CdTe undergo one or more Compton scatterings before the final photoelectric interaction and the total photon energy must

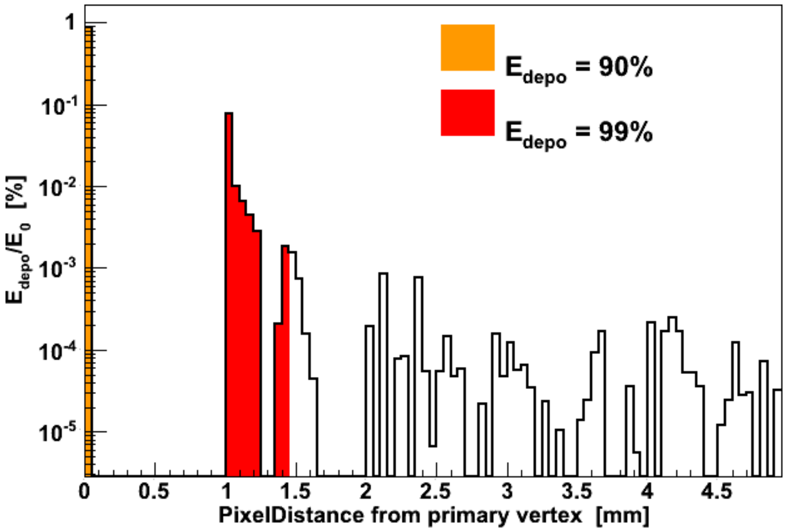

Figure 5.7: Deposited energy profile after photoelectric interaction of 500 keV photons in CdTe material. The gaps in the distribution are due to the pixelization of the CdTe detector where the energy collected in one pixel is always assigned to the center of the pixel.

be reconstructed out of a multiple hit signature with fraction of the energy deposited in distant voxels. The high granularity of the VIP detector offers the possibility of defining elaborated algorithms to reconstruct the Compton sequence and recover the otherwise ambiguous events. The complexity of such algorithms is independent of the flexibility of the ASIC since they are applied off-line to the LM data set. Currently, five different algorithms have been studied to identify the first impact point of a multi-hit sequence:

1. Choose the pixel with the highest energy deposition.
2. Choose the pixel with the second highest energy deposition.
3. Choose the pixel with minimum energy deposition.
4. Choose the pixel with the smallest radius (pixel closer to the source).
5. Base the choice on the reconstruction of the Compton angle.

When applied to the VIP detector, the first algorithm gives 58.37% of true LORs while the second reaches 66.6%. With the third method we get 60.4% of correct LORs. The algorithm number 4 is based on the fact that with 511 keV photons the probability of a forward Compton is bigger than the probability of a back scattering. This algorithm finds 70% of right first interaction points. Finally, algorithm number 5, in its current version, is applied only to events with three total hits from two annihilation photons, where one of the two photons is assumed to undergo directly a photoelectric interaction (Figure 5.8, hit a), while the other one suffers a single Compton scattering before being completely absorbed (Figure 5.8 hits b and c). In order to define which hit comes first between b and c, two possible Compton angles dbc and ecb are calculated from the Compton equation 2.2. The same Compton angles can be calculated from the geometrical factors (spatial coordinates of the hits b and c). The configuration that best agrees with the Compton equation is chosen. This method yields 81.5% of correct LORs and it is very effective mostly because of the excellent energy and spatial resolution of the pixelated CdTe detectors.

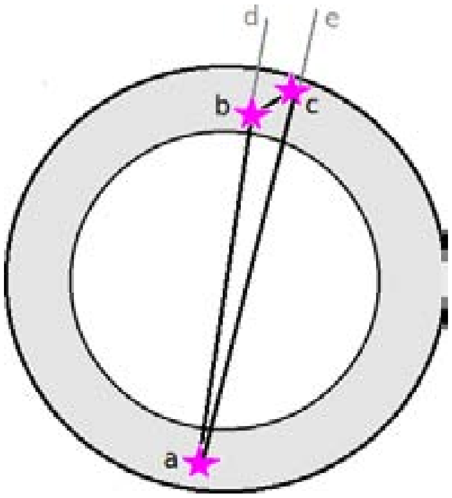

FIGURE 5.8: Example of a coincidence event where one of the two photons is directly absorbed with a photoelectric interaction without scattering inside the detector (hit *a*) and the other photon suffers only a single Compton scattering (hits *b* and *c*). As one can see, in this case there are two possible LORs: *ab* and *ac*.

The choice of the right algorithm to use in the present analysis aims to maximize both the purity of the Compton reconstructed sample, and the selection efficiency. The best trade-off is obtained with algorithm number 4 because the fifth algorithm, though providing the best signal purity, is penalized in terms of efficiency, because in its current version it works only with three-hit events.

The study of different Compton merging algorithm was performed using the simulated data. The computer modeling of the VIP scanner is described in detail in the next chapter.

Chapter 6

Simulation Technique and Evaluation of the VIP Counting Performance

In order to evaluate the VIP system performance and assess its image quality, the whole VIP geometry was simulated using GEANT4-based Architecture for Medicine-Oriented Simulations (GAMOS) [162]. This chapter consists of two parts. The first part includes the description of the VIP PET simulation with GAMOS, including the assumptions, the limitations, and the validation of the used simulation technique.

The second part presents the evaluation of the counting performance of the simulated VIP system. The evaluation is performed following the prescriptions of two common PET protocols: the National Electrical Manufacturers Association (NEMA) NU 2-2001 protocol [163], and the NEMA NU 4-2008 protocol [164]. Since the geometry of the VIP is optimized for brain scan, the system is evaluated following the prescriptions of the NEMA NU 2-2001 protocol, that is used for WB and head PET scanners. Nevertheless, despite the relatively big FOV, the VIP performance is closer to a high-resolution high-sensitivity small-FOV PET than to a WB PET. For this reason, the system is put through further testing following the NEMA NU 4-2008 protocol for small animal PET. The aim of the both standards is to propose a standardized method for evaluating and comparison of PET systems. The documents describe procedures for acquiring and analyzing data using standard phantoms and sources. According to the document, measurements of the scatter fraction (SF), sensitivity, count losses, and random coincidence rate should be performed.

6.1 The GAMOS toolkit

The goal of GAMOS is to provide a reliable software framework that serves a user to accurately simulate an experimental setup without having to code in C++ and with minimum knowledge of Geant4 [165].

Geant4 is a Monte Carlo (MC) code written in C++ object oriented programming language for simulation of the passage of particles through matter. The user of Geant4 has to describe the geometry of the particle detection system, its structure and spatial position, define initial particles, and choose an appropriate physics list for this application. Geant4 simulation has the following structure:

- An *event* is any creation of a new particle. It consists of a set of initial particles created by the user, all secondary particles produced in interactions, and a set of detector responses to these particles as they are transported through the geometry. The event can contain particle tracks, hits and digitizations.
- A *track* is evolution of a particle track s state. The track starts when a particle is born and ends when the particle dies. It contains only information about the initial state and the current state. Tracks consist of steps.
- A *step* is a part of a track between two any interactions of a particle. It contains the initial and final points plus the differential information (energy loss on the step, time of flight spent by the step, etc.).
- A *hit* is a snapshot of a physical interaction or an accumulation of interactions of a track or tracks in a sensitive detector component.
- A *digit* represents a detector output, such as and ADC/TDC count or a trigger signal. A digit is created from one or more hits and/or other digits.

GAMOS uses the Geant4 libraries and offers a variety of predefined detector applications for PET, SPECT and Compton camera. The program simulates the detector signals and write them into a file in a format compatible with the popular and commonly used Software for tomographic image reconstruction (STIR) [166]. The user can choose which signals to simulate by using special commands, and, also, include different detector effects such as energy resolution, measuring time, dead time, etc. Another very useful feature of GAMOS is a detailed simulation of the hits created in a detector and the classification of PET, SPECT and Compton camera detected events. It also gives the detailed information about each step of every produced particle, if needed. Additionally, after the simulation is finished, the user is provided with a huge amount of histograms for better understanding and control of the setup behavior. Moreover, the user can create and add new C++ classes and user commands, without the need to modify the GAMOS code. This possibility is based on the plug-in technology. This flexibility allows GAMOS produce any kind of simulation achievable with the Geant4 software.

6.2 The simulation of the VIP scanner

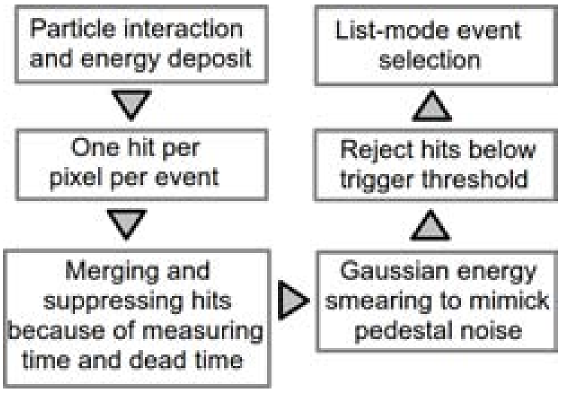

Figure 6.1: Current simulation logic sequence.

The specifics used for the simulation of the VIP scanner are summarized in Table 6.1. For the simulation, the logic scheme presented in Figure 6.1 is used to mimic the real scanner signal processing logic. In the VIP simulation, for each event (e.g. a positron emission from a ^{18}F source), the energies that primary (e.g. 511 keV photons) and secondary particles deposit in the detector s pixels get summed to get one resulting hit per pixel per event. The smart-pixel slow shaper integrates the deposited energy with 20 μs peak time. After digitizing the peak value, the time needed to reset the pixel electronic before the next event is 130 μs. The 150 μs total signal processing time allows each channel to handle easily 6 kHz with negligible pile-up [158]. To simulate the effect of the electronic measuring time and dead time, all energy depositions within the same voxel and within the first 20 μs window time contribute to the total energy of a single hit; energies deposited right after and within the 130 μs dead time, are lost. A Gaussian smearing is applied to the total hit energy to mimic the pedestal noise and the energy resolution of the CdTe. A channel triggers if the total collected energy exceeds the 20 keV trigger threshold defined as the 10 σ noise level above the base line of the amplifier. The trigger defines the time stamp of the hit as measured by the TDC with 0.1 ns resolution. Additional smearing is considered due to the asymmetry between electron and hole mobilities [167] and to the jitter of the electronic discriminator as measured in [158]. A direct measurement of the coincidence time resolution [168] shows that for energy close to the 20 keV trigger threshold, a time coincidence window as wide as 20 ns is needed to detect at least 70% of the photon pairs. The counting performance evaluation reported in the following section indicates that with such a coincidence time window no significant pile-up effect (here pile-up means a loss of the coincidences mostly due to the appearance of multiple events) is expected up to 10^7 Bq activity in the FOV and the system can handle up to 10^8 Bq without saturation [1].

Table 6.1: VIP scanner simulation parameters

Material	CdTe
Axial length	25.4 cm
Inner radius	21 cm
Outer radius	27 cm
Radial width	40 mm
Energy resolution FWHM	1.57% [156]
Dead time per voxel	130μs
Measuring time per voxel	20μs
Coincidence time	20 ns
CdTe Voxel size (mm^3)	1x1x2
ROC thickness	50 μm
PCB thickness	50 μm
Glue thickness	15 μm

6.3 Assumptions and limitations

The simulation of the VIP scanner is performed with certain assumptions. The first group of these assumptions is related to some limitations in physics processes simulation. Geant4 simulates the production of positrons and interactions of particles with matter in a good accordance with the physics laws. The distribution of the initial energies of positions produced from a decay of a certain isotope is read from a file, provided by the GAMOS software. The data for the file is taken from the `http://ie.lbl.gov/toi.html`. The simulation of the non-collinearity of annihilation photons is performed, however the model is based on the typical distribution of the annihilation angles in water. Taking into account that the human body mainly consists of water, the model is expected to provide faithful results. The attenuation of photons is well simulated in Geant4.

The second group of the assumptions is related to the simulation of the VIP geometry. Actually, the entire simulated geometry of the system is quite approximate: the thickness of the electronics layers and the geometry structure might change when the real scanner will be mounted. In the simulation the glue layer is uniformly distributed on the surface of each VIP detector module. In the reality, the glue will be dispensed under each VIP chip. The glue might be thicker. In the simulation all 6,336,000 detector voxels are absolutely the same and each one works perfectly. In the real life, a some voxels can be damaged and/or function wrong or not function at all.

The third group of limitations is related to the simulation of the electronics and detector responses to the incident radiation. First of all, it is impossible to simulate the response of a single detector coupled to the chip. Instead, a simple model of the detector behavior is created and tested. The model shows good agreement with the experimental results [169]. Additionally, the simulation of the CdTe detector itself is very approximate. After the photon ionizes the detector material, it is assumed that the drift of holes and electrons always starts from the center of the voxel. The charge trapping is not simulated at all. However, an accurate model study performed with the COMSOL Multiphysics software [170] shows that at 2000 V bias voltage the impact of the charge trapping is expected to be negligible (Figure 6.2). In the real life, the detectors get polarized and the voltage cycling is needed. This fact is neither taken into account in the simulation. It means, that in the reality the screenings will take more time, that the duration presented in the simulation results. The most important phenomenon that is missed in the simulation is the charge sharing.

Finally, the last limitations are related to the use of DICOM files, that are necessary to simulate complicated phantoms, such as a human brain. When working with DICOM files in GAMOS, one should take into account that the true radioisotope distribution information gets lost after following procedures:

1. transformation real data from a human s head to a CT image (DICOM file);
2. transformation of the obtained CT image to a Geant4 compatible format.

The factors listed above distort the simulation results. However, as the following section proofs, the simulation results are faithful enough to predict the expected performance of the future VIP PET system.

6.4 Validation of the simulation

The VIP project is under development and the results presented in this work are based on simulation using GAMOS software package. However, we are aware that it is not completely fair to compare the VIP simulation results with the current state of the art PET systems. In order to prove that our simulation gives realistic results the ECAT HRRT scanner is also simulated with GAMOS (see section 6.5) and the obtained results are compared with the results published in [171]. The results of this exercise are summarized in Table 6.2. Over all one can see that GAMOS prediction is very realistic. For example, the spatial resolution of HRRT in the center of the FOV is predicted within an error of 7%, and about 20% at 10 cm from the center of the FOV. The error in predicting the SF is about 15%, while the error in predicting total sensitivity is on average around 25%. Therefore, we can say with more confidence that what we have claimed is not far from the reality given that we have used as an input to GAMOS the pixel

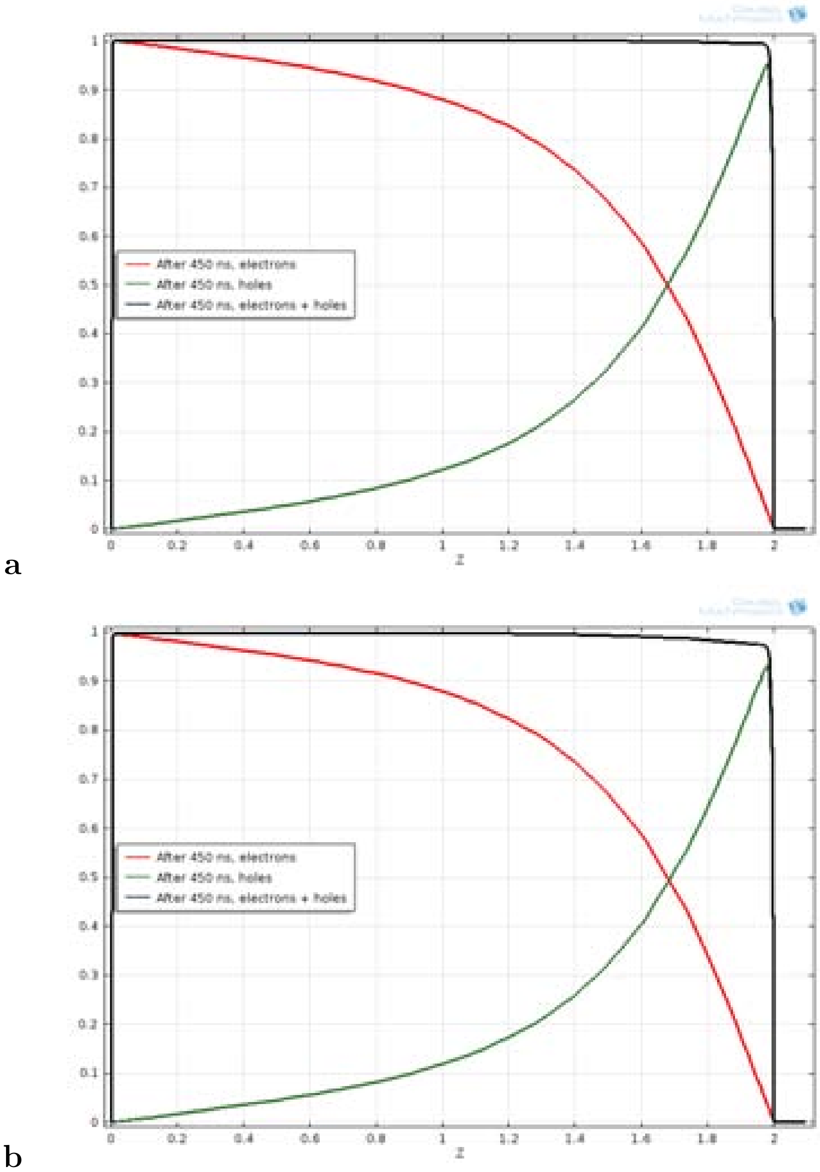

FIGURE 6.2: The charge induction efficiency (CIE) versus depth of interaction (arc length). **a**: charge trapping is not included to the simulation. **b**: charge trapping is included. As one can see, only for holes generated really close to the anodes (plot **b**), there is some trapping (the total CIE is slightly smaller than in plot **a**).

detector response that has been measured in the lab for both energy resolution and time coincidence.

To make the simulation results more robust, in addition to the ECAT HRRT exercise, the VIP simulation was repeated assuming considerably worse values for some critical parameters. The following defects to mimic more realistic situation were added:

- Smearing the energy resolution from 1.57% to 5%.
- Increasing the dead material by 100% (that is doubling it).

Table 6.2: Comparison of the characteristics of the simulated ECAT HRRT scanner with GAMOS and the data published in [171]

		Our HRRT simulated data	HRRT published data
Spatial resolution (mm) near the center of the FOV	Transverse radial	2.16	2.3
	Transverse tangential	2.16	2.3
	Axial	2.78	2.5
Spatial resolution (mm) at 10 cm radius from the center of the FOV	Transverse radial	2.24	3.2
	Transverse tangential	2.23	3.2
	Axial	3.6	3.4
SF		52%	45%
Total sensitivity		3.9%	2.5% - 3.3%

- Assuming 1% dead channels (∼60 k voxels).

The results of such simulation with the defects and comparison with the data obtained without defects is demonstrated in Table 6.3. As one can see the biggest impact is on the SF, that has increased by a factor of 3, and on the total sensitivity, that has dropped by 25%, but overall the VIP scanner in such a worst case scenario is still performing considerably well.

Table 6.3: Comparison of the simulated VIP scanner performance with standard and smeared parameters

		Standard	Smeared
Spatial resolution (mm) near the center of the FOV	Transverse radial	0.694	0.799
	Transverse tangential	0.694	0.799
	Axial	1.3	1.5
Spatial resolution (mm) at 10 cm radius from the center of the FOV	Transverse radial	0.696	0.739
	Transverse tangential	0.902	1.024
	Axial	1.904	2.688
SF		3.95%	11.26%
Total sensitivity (cps/kBq)		14.37	11.41
NEC peak (kcps)		122	88
NEC peak activity (MBq)		56.2	31.6

6.5 Evaluation of counting performance using NEMA documentation

The counting performance evaluation of any PET scanner includes measurements of the sensitivity of a PET system, its SF, and counting rates. The method, phantoms, radionuclides being used, radioactive source distribution and dose, data collection, processing, analysis, and the results of each measurement are described in detail in the next sections 6.6, 6.7, and 6.8. The simulation results of the VIP system are compared with real measurements of several commercial PET scanners. Results from the NEMA NU 2-2001 tests are compared to the measurements of the HRRT Siemens ECAT PET scanner [171] and the G-PET [172] from Philips Medical Systems.

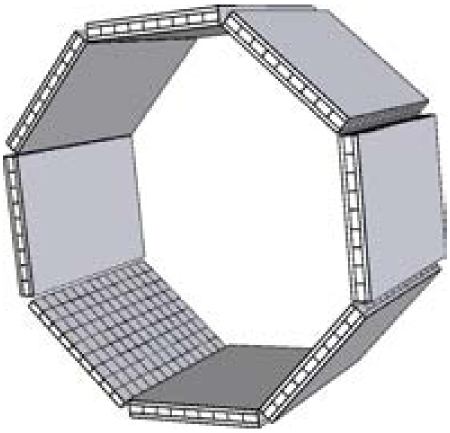

FIGURE 6.3: The HRRT Siemens ECAT PET geometry simulated with GAMOS. Each sector of the octagon consists of 9 crystals in the transverse direction and 13 crystals in the axial direction (117 crystals in total).

The ECAT HRRT is a 3-D (no septa) brain scanner based on double layered scintillating crystals of 16.8 mm wide and 10 mm deep. The double layered crystals are needed to achieve photon detection with DOI information. The first layer is made of LSO and the second layer is made of cerium doped lutetium-yttrium oxyorthosilicate (LYSO). Each layer of all scintillating crystals is cut into a 8 × 8 matrix to give 2.1 mm × 2.1 mm wide detector elements. The total 117 (9 × 13) such double layered crystals are viewed by 140 (10 × 14) PMTs and form a sector. The detector heads have a quadrant sharing detector block design [173] [174]. Eight sectors are arranged in an octagon as shown in Figure 6.3. The FOV of the ECAT HRRT scanner is 312 mm in diameter and 250 mm in axial direction. Its energy acceptance window is 350 650 keV, the energy resolution is 15% in FWHM, the dead time is 320 ns, and the coincidence is 6 ns. The dead time affects the whole crystal block. The data can be stored in list mode.

G-PET is a fully 3-D scanner (no interplane septa) with ring design. Its inner ring diameter is 30 cm (a patient aperture) and the axial FOV is 25.6 cm. G-PET is made of 4 × 4 × 10 mm^3 GSO crystals with energy resolution 10% in FWHM. The total number of crystals is 18,560 that are arranged in 58 rings of 320 crystals each. The crystals are coupled to 288 PMTs (8 rows × 36 columns) that are arranged in a hexagonal lattice. The energy acceptance window is 410 665 keV.

The obtained simulation results from the NEMA NU 4-2008 tests are compared with the real measurements of four commercial small-animal PET scanners: the rPET-1 (SEDECAL, S.A., Madrid, Spain) [175], the ClearPET (Raytest Isotopenmessgeraete GmbH, Mannheim, Germany) [175], the Inveon DPET (Siemens) [176], and the LabPET-8^{TM} (GE healthcare Technologies, Waukesha , WI) [177]. ClearPET is a 3-D scanner that has a full ring geometry with an axial FOV of 11 cm. Its transaxial FOV can be changed from 9.4 cm for mouse imaging to 14.4 cm for rat or primate imaging. The ClearPET scanner consists of double layer pixelated scintillators coupled to PMTs: the first (front) layer is a LYSO crystal and the second (back) layer is a lutetium-yttrium aluminum perovskite (LuYAP) crystal. Each crystal (LYSO and LuYAP) has surface of 2 × 2 mm^2 and deep of 10 mm. The energy acceptance window can be set to 100 750 keV, 250 750 keV, and 400 750 keV. The coincidence time window is 12 ns. The data is collected in list mode.

The rPET-1 scanner consists of a single layer of mixed lutetium silicate (MLS) crystals. Each crystal is pixelated and has dimensions of 1.4 × 1.4 × 12 mm^3. The crystals are coupled to PMTs and form two planar block detectors that rotate around an object being imaged. The rPET-1 has equal transaxial and axial FOV of 45.6 mm. Its energy acceptance window can be set to 100 700 keV, 250 650 keV, and 400 700 keV. The coincidence time window is 3.8 ns. The rPET-1 uses 3-D list-mode data acquisition

The Inveon DPET consists of 64 block detectors that are arranged in 4 contiguous rings. Each detector block is made of 20 × 20 matrix of LSO crystals coupled to a PMT. Each crystal is 10 mm deep and has surface area of 1.51 × 1.51 mm^2. It is a 3-D the scanner that has axial FOV of 127 mm and the ring diameter of 161 mm. The average energy resolution for the system is 14.6%. The energy acceptance window can be set to 250 625 keV and 350 625 keV. The timing window is 3.432 ns. The 3-D data is acquired in list mode.

Finally, the LabPET-8^{TM} system has ring geometry and consists of 32 detector rings. Each ring includes 192 double layer LYSO and Lu$_{0.4}$Gd$_{1.6}$SiO$_5$ LGSO crystals coupled to APD detectors. Each crystal has dimensions of 2 × 2 × 14 mm^3 which are optically coupled one after the other. The transaxial FOV of LabPET-8^{TM} is 100 mm and the axial one is 75 mm. The scanner uses a 250 650 keV energy window and 22 ns coincidence time window. The 3-D data is acquired in list mode.

6.6 Sensitivity test

The sensitivity of PET scanners represents the ability of detecting coincident photons from inside the FOV of the scanner. It is defined as the number of prompt counts per time unit detected by the device for each unit of activity present in a source. The sensitivity is normally expressed in counts per second per Becquerel (cps/Bq) and depends on the geometry and stopping power of the detectors for 511 keV photons. Small-diameter and large axial FOV geometries typically lead to high-sensitivity scanners. High stopping power material also increases the overall sensitivity of the system. The purpose of a sensitivity measurement on a positron tomograph is primarily to facilitate comparisons between different systems, as, in general, the higher the sensitivity the better the SNR in the reconstructed image (neglecting dead time effects).

6.6.1 According to NEMA NU 2-2001

6.6.1.1 Method

In this test the sensitivity is measured for a phantom that represents a thin 700 ± 5 mm long plastic tube filled with radioactive water. The outer diameter of the tube should be less than 3.9 mm. It should be placed in the center of the transaxial FOV and aligned with the axial direction of the tomograph (Figure 6.4(a)). The total 5 measurements (or tests) must be performed for the sensitivity calculation. In each test the plastic tube should be inserted into increasing number of metal sleeves (from 1 to 5) such that in each next measurement the annihilation photons need to traverse bigger thickness of metal (Figure 6.4(b)). The sleeves have the same length as the tube (700 mm), the constant thickness of 2.5 mm, and different inner and outer diameters indicated by the NEMA NU 2-2001 standard (Table 6.4).

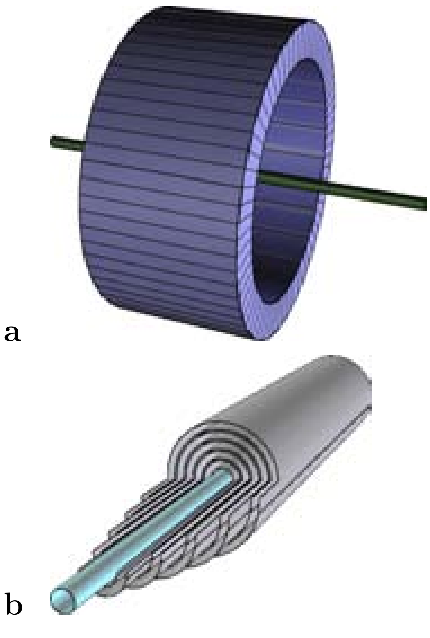

Figure 6.4: **a**: the position of the radioactive source in the NEMA NU 2-2001 sensitivity test. **b**: a section of the NEMA NU 2-2001 sensitivity source (blue) inserted into 5 concentric metal sleeves.

The radionuclide employed for the sensitivity measurement should be ^{18}F. The activity used should be low enough so that the counting losses are less than 1%, and the random event rate is less than 5% of the true rate. The minimum number of collected true coincidences is required to be 10,000 per image slice. In order to define number of coincidences in a slice, a single slice rebinning (SSRB) [178] should be used while reconstructing the image.

After total 5 tests are done, the total system sensitivity (S_{tot}) can be calculated by the following formula:

$$S_{tot} = \frac{R_{corr,0}}{A} \tag{6.1}$$

where A is the total activity of the source in Bq, and $R_{corr,0}$ is the count rate with no photon attenuation (no metal sleeves) that is unknown. In order to calculate $R_{corr,0}$, the following procedure has to be performed. For each measurement j and each slice i, the count rate $R_{j,i}$ (in counts per second) should be calculated by dividing the counts collected in the slice by the acquisition time T_{acq}. Then, this rate should be corrected for isotope decay using the following formula:

$$R_{corr,j,i} = R_{j,i} \cdot 2^{\frac{T_j - T}{T_{1/2}}} \tag{6.2}$$

where $R_{corr,j,i}$ is the new corrected count rate, T_j is the acquisition time for measurement j, T is the moment of time when the source radioactivity A was measured, and $T_{1/2}$ is the half-life of the radioisotope. After, the value $R_{corr,j}$ should be calculated by summing the $R_{corr,j,i}$ from each slice. Finally, the data should be fit to the following equation:

$$R_{corr,j} = R_{corr,0} \cdot e^{-2\mu X_j} \tag{6.3}$$

where X_j is the total metal sleeves thickness for the j^{th} measurement, and μ is the photon attenuation coefficient in metal in mm^{-1}, which is allowed to vary to compensate for the small amount of scattered radiation. The value $R_{corr,0}$ should be found from this fit.

In order to evaluate the sensitivity at different radial position, the whole test can be repeated with the source placed at 10 cm radial offset from the center of the transaxial FOV. Additionally, the axial sensitivity profile can be gotten by computing the sensitivity for each slice S_i:

$$S_i = \frac{R_{corr,0,i}}{R_{corr,0}} \cdot S_{tot} \tag{6.4}$$

6.6.1.2 Simulation approach, results, and comparison

Since the simulation is used, the attenuation free measurement is directly performed by simulating a 70-cm-long ideal 511 keV back-to-back gamma line source with no surrounding material. Thus, the value $R_{corr,0}$ can be calculated directly from the simulation. The source is placed in the center of the transaxial FOV along the axial direction and has

Table 6.4: Dimensions of the metal sleeves for the NEMA NU 2-2001 sensitivity test

Tube number	Inner diameter (mm)	Outer diameter (mm)	Length (mm)
1	3.9	6.4	700
2	7.0	9.5	700
3	10.2	12.7	700
4	13.4	15.9	700
5	16.6	19.1	700

an activity of 5 MBq. As required by NEMA, the activity is low enough for counting losses to be less than 1%, and the random event rate is less than 5% of the rate of true coincidences (see the results from the section 6.8.1). The resulting total system sensitivity of the simulated VIP scanner $S_{VIP_{tot}}$ is **14.37 cps/kBq**.

For comparison, the total system sensitivity of the G-PET is ∼3 times smaller than the VIP one (4.79 cps/kBq) [172]. The published absolute (percentage) line-source sensitivity (S_{abs}) of HRRT ECAT PET ranges from 2.5% to 3.3% [171]. One can find the total sensitivity expressed in cps/Bq using the following formula:

$$S_{tot} = \frac{BR \cdot S_{abs}}{100} \tag{6.5}$$

where BR is the branching ratio of the isotope. Taking into account that the branching ratio of ^{18}F is 0.9686 [179], the total sensitivity of the HRRT ECAT scanner ranges from 24.215 to 31.964 cps/kBq, that is ∼2 times higher than the sensitivity of VIP PET, but almost a half of the counts are scattered events (see section 6.7.1).

Solid angle coverage normalization. The values presented above are strongly dependent on the geometrical acceptance of the different scanners and a fair comparison requires their normalization to the solid angle. In the assumption of a line source along the axial center of the scanner, the solid angle coverage (Ω) is calculated using the formula:

$$\Omega = \frac{4 \cdot \int_0^{2\pi} \int_0^{L/2} \int_0^{atan(\frac{L_{det}/2-x}{R_{det}})} sin\Theta d\Theta dx d\varphi}{4\pi \cdot L} \tag{6.6}$$

where L_{det} and R_{det} are the axial length and the radius of the scanner, L is the minimum between the axial length of the scanner and the source length, and Θ and φ are the polar and azimuthal angle, respectively.

After normalization, the specific sensitivities of the three scanners are 27.3%, 5.138%, and 28.65% 37.8% for the VIP, G-PET, and HRRT ECAT systems respectively.

The total system sensitivities of the three scanners are summarized in Table 6.5.

TABLE 6.5: Sensitivity values calculated in accordance with the NEMA NU 2-2001

Parameter	**VIP**	**G-PET**	**HRRT**
Energy window(keV)	503 519	410 665	350 650
S_{tot}(cps/kBq)	14.37	4.79	~24.175 31.911
Ω normalized S_{tot}	27.3%	5.138%	28.65% 37.8%

HRRT achieves the highest effective sensitivity thanks to the use of 10 mm thick high-density (7.4 g/cm^3) LSO/LYSO crystals, while the G-PET scanner employs 10 mm thick GSO crystals that have smaller density of 6.71 g/cm^3. The density of CdTe is even smaller than the density of GSO material; it is equal to 6.2 g/cm^3. However, due to the implementation of 4 cm CdTe and the crack-free geometry, the VIP scanner provides a competitive sensitivity. It also should be considered that while having comparable sensitivity, the SF of the VIP PET is by an order of magnitude smaller than the other presented scanners have (section 6.7.1).

6.6.2 According to NEMA NU 4-2008

6.6.2.1 Method

In this procedure, a small ^{22}Na point-like source (no bigger than 0.3 mm in diameter) with small concentration of activity is placed into the center of a 10 × 10 × 10 mm^3 acrylic cube. The NEMA NU 4-2008 standard requires the activity concentration to be less than that at which either the dead-time losses exceed 5% or the random coincidence rate exceeds 5% of the total event rate. The first measurement should be done with the acrylic cube positioned in the center of FOV of the scanner, both axially and transaxially. The required minimum of 10,000 true coincidences must be acquired at this location and at positions stepped axially at 4 mm increments, covering the axial FOV of the whole scanner. The measurements at each position must be analyzed. At each axial position i, the sensitivity (S_i) can be calculated as:

$$S_i = \frac{R_i - R_{B,i}}{A} \tag{6.7}$$

where A is the activity of the source measured in Bq, R_i is the rate of total counts collected in slice (source position) i, expressed in cps, and $R_{B,i}$ is the background event rate acquired without sources in the FOV.

The relative sensitivity for acquisition i is given by:

$$S_{A,i} = \frac{S_i}{0.9060} \times 100 \tag{6.8}$$

where 0.9060 is the branching ratio of ^{22}Na. The total system sensitivity can be computed as follows:

$$S_{tot} = \frac{1}{N} \cdot \sum_{all,i} S_i; \tag{6.9}$$

$$S_{A,tot} = \frac{1}{N} \cdot \sum_{all,i} S_{A,i} \tag{6.10}$$

where N is a total number of image slices (or, the same, source positions). It is also required to calculate the system sensitivity for the mouse phantom (SM_{tot}) by the following formula:

$$SM_{tot} = \frac{1}{N_{central7cm}} \cdot \sum_{central7cm} S_i; \tag{6.11}$$

$$SM_{A,tot} = \frac{1}{N_{central7cm}} \cdot \sum_{central7cm} S_{A,i} \tag{6.12}$$

Finally, the system sensitivity for the rat phantom (SR_{tot}) should be also computed using the following formula:

$$SR_{tot} = \frac{1}{N_{central15cm}} \cdot \sum_{central15cm} S_i; \tag{6.13}$$

$$SR_{A,tot} = \frac{1}{N_{central15cm}} \cdot \sum_{central15cm} S_{A,i} \tag{6.14}$$

In addition, the NEMA NU 4-2008 standard requires to obtain the axial sensitivity profile by plotting the sensitivity $S_{A,i}$ for each slice.

6.6.2.2 Simulation approach, results, and comparison

In this test, the ^{22}Na point-like source of 0.1 mm in diameter with activity of 1 MBq placed inside the acrylic cube is simulated. The activity concentration of 1 MBq satisfies to the NEMA requirements (see the results in the section 6.8.2). A total of 65 measurements are simulated and analyzed. The total system sensitivity is calculated as the average of the all sensitivities computed for each slice using the formula 6.7. In the case of simulation $R_{B,i} = 0$.

Table 6.6 summarizes the results of the test. Sensitivity values for other commercial scanners are also indicated for comparison. The axial sensitivity profile of the VIP scanner obtained by plotting the absolute sensitivity S_A for each slice number is shown in Figure 6.5.

Table 6.6: Sensitivity values calculated in accordance with the NEMA NU 4-2008

Parameter	**VIP**	**ClearPET**	**rPET-1**
Energy window(keV)	503–519	250–750	250–650
S_{tot}(cps/Bq)	0.021	0.01698	0.00418
$S_{A\ tot}$(%)	2.31	1.87	0.46
SM_{tot}(cps/Bq)	0.038	0.02108	0.00418
$SM_{A\ tot}$(%)	4.24	2.32	0.46
SR_{tot}(cps/Bq)	0.038	-	-
$SR_{A\ tot}$(%)	4.2	-	-

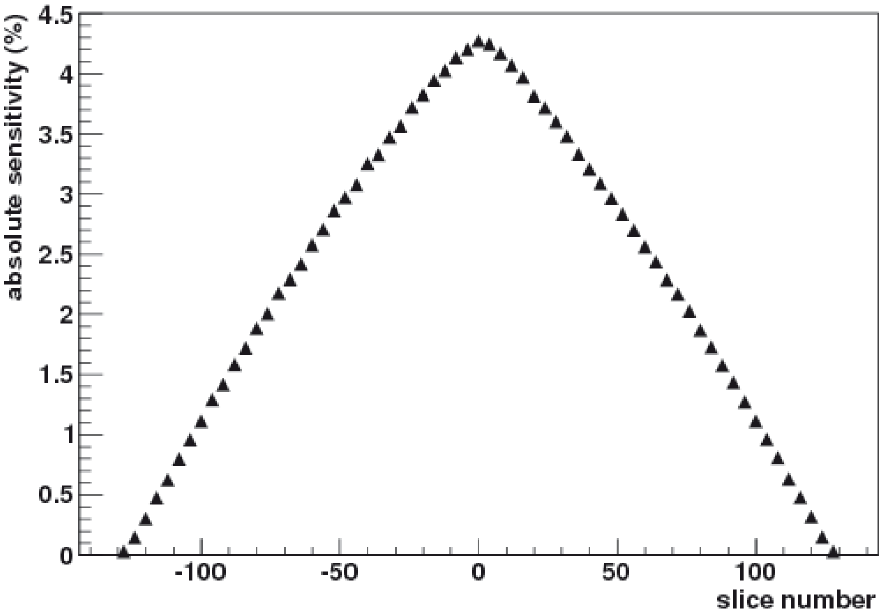

Figure 6.5: Axial absolute sensitivity profile along the axial FOV of the VIP scanner for the energy window of 503-519 keV measured following the NEMA NU 4-2008.

Solid angle coverage normalization. After normalization to the solid angle coverage, the specific sensitivities of the scanners are 39.9%, 11.5%, and 3.5% for the VIP, ClearPET, and rPET-1 systems respectively.

The sensitivity of the VIP scanner is comparable to the values published for the rPET-1 and the ClearPET though the energy windows of the two commercial scanners are considerably wider than the one employed in the VIP PET. The total system sensitivities of the Inveon DPET and the LabPET-8^{TM} are not compared, because they are computed different way. Additionally, the values of the sensitivity for the VIP system can be increased by relaxing the requirements on the accepted coincidences.

6.7 Measurements of the scatter fraction

The purpose of the SF test is to measure the relative system sensitivity to the scattered radiation. The NEMA document defines the SF as the ratio of scattered events to total events, which are measured at a sufficiently low counting rate such that random coincidences, dead-time effects, and pileup are negligible:

$$SF = \frac{C_s}{C_{TOT}} \tag{6.15}$$

where C_s is the number of scattered counts and C_{TOT} is the sum of true and scattered counts. As it was mentioned, the scattering of annihilation photons leads to mistaken positioned coincidence events and thus adds noise to the reconstructed image. Various designs and implemented energy resolution cause PET scanners to have different sensitivities to scattered radiation. A lower scatter fraction is more desirable, in spite of the accuracy of the scatter correction method, because correction techniques cannot completely compensate for the noise introduced by the unwanted events and can add bias to the image.

6.7.1 According to NEMA NU 2-2001

6.7.1.1 Method

For brain scanners, the NEMA NU 2-2001 protocol recommends to use a phantom described in the NEMA NU 2-1994 standard, since it is smaller than one from the NEMA NU 2-2001 and, thus, more suitable for brain studies. The phantom is a polymethyl methacrylate cylinder with an outside diameter of 203 ± 3 mm and a wall thickness of 3 ± 1 mm. Its inner length is 190 ± 1 mm. It should be placed in the axial and transaxial center of the tomograph s FOV and aligned with the axial direction of the scanner. The phantom is filled with non-radioactive water (a scatterer medium) and includes a line source insert that should be placed parallel to the long axis of the cylinder at three different radial positions: at 0, 45, and 90 mm off the center with an accuracy of ± 3 mm. The line source insert must be a cylinder, filled with radioactivity, that has the length of at least 185 mm and no larger than 2 mm in its other dimensions. The radionuclide for the SF measurements is ^{18}F with the activity low enough to have negligible random event rate (less than 5% of the total event rate) or the dead-time losses (less than 5%).

The total three measurements (one for each radial position of the line insert) should be performed for the SF calculation. At least 200,000 coincidences per each image slice should be collected. The acquisition time must be equal for each measurement. The acquired data should be corrected for dead-time losses and random coincidences, but not for scattered coincidences or photon attenuation.

After three measurements are done, the protocol describes the procedure of analysis of the collected sinograms, and prescribes to estimate the SF (SF_i) for each slice i as:

$$SF_i = \frac{\frac{C_{s,i,1}}{A_{ave,1}} + 8(\frac{C_{s,i,2}}{A_{ave,2}}) + 10.75(\frac{C_{s,i,3}}{A_{ave,3}})}{\frac{C_{TOT,i,1}}{A_{ave,1}} + 8(\frac{C_{TOT,i,2}}{A_{ave,2}}) + 10.75(\frac{C_{TOT,i,3}}{A_{ave,3}})} \tag{6.16}$$

where $C_{s,i}$ is the number of scattered counts for the slice i, $C_{TOT,i}$ is the sum of true plus scattered counts, and A_{ave} is the average radioactivity during data acquisition over the time interval for the line source at each position. The subscripts 1, 2, and 3 correspond to three radial positions of the line source: 0, 45 mm, and 90 mm respectively. The average SF of the SF_i should be computed as the system SF for uniform sources.

6.7.1.2 Simulation approach, results, and comparison

As mentioned, with real detectors the number of scattered events should be estimated from a sinogram profile. However, since the VIP test is based on simulated data, the exact number of true, scattered, and random events are known, as well as the average radioactivity of the source (1 MBq). The calculated average SF of the VIP is **3.95%**.

For comparison, the average SF of the G-PET scanner, for the same test, is 39% for an energy window 410 665 keV [172], and for HRRT ECAT PET is 45% [171]. Both SF values are nominal of PET based on scintillating crystal detectors.

6.7.2 According to NEMA NU 4-2008

6.7.2.1 Method

According to the NEMA NU 4-2008, the SF test should be a part of the counting performance test described in the section 6.8.2. The last measurements taking with low activity of a source in the counting performance test are used to calculate the SF of a scanner. According to the protocol, the SF can be computed as the ratio of scattered to total counts (the number of scattered counts can be found from sinograms), or from the counting rates, calculated in the section 6.8.2. Here, the SF test is described and the system SF is computed as the ratio of the scattered counts to the collected total counts. In the section 6.8.2, the system SF is calculated again using the counting rates of the scanner.

The NEMA NU 4-2008 specifies three different test phantom designs for measurement of the SF: mouse-size, rat-size and primate-size phantoms. This is due to the different sizes of small animal PET systems. The measurements should be done using one or more phantoms depending on the application the scanner is used for.

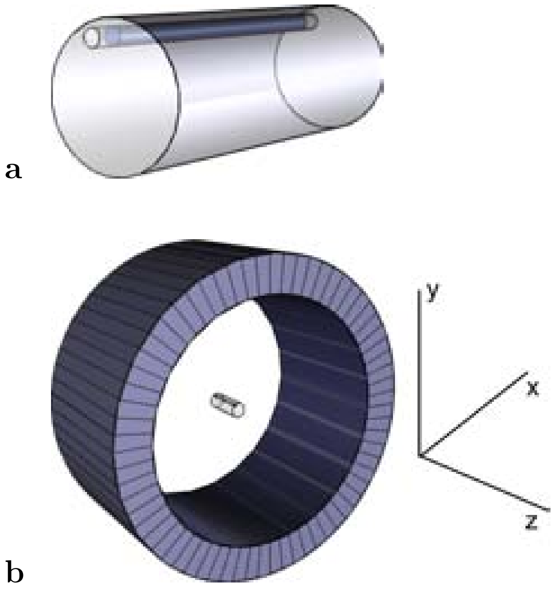

FIGURE 6.6: **a**: the simulated mouse-size phantom. **b**: the phantom placed in the center of FOV of the VIP scanner.

The mouse-like phantom is a solid cylinder made of high density polyethylene (density 0.96 ± 0.1 g/cm^3). It has a length of 70 ± 0.5 mm and it is 25 ± 0.5 mm in diameter. There is a cylindrical hole (3.2 mm in diameter) drilled parallel to the central axis at a radial distance of 10 mm. The rat-like phantom as well as the monkey-like phantom are made of the same material as the mouse-like phantom and have similar geometry. The rat-size phantom is a solid 150 ± 0.5 mm-long cylinder with the diameter of 50 ± 0.5 mm. The cylindrical hole is drilled at a radial distance of 17.5 mm and has 3.2 mm in diameter. The monkey-size cylindrical phantom has the length of 400 mm and the diameter of 100 mm. The hole is drilled at a distance of 30 mm from the center. The line source is a flexible tube with a fillable section 10 mm shorter than the length of the corresponding phantom. It is get filled with a known activity concentration and inserted into the drilled hole of each phantom.

The VIP test is focused on the mouse-size phantom studies for fair comparison with the other PET systems since the mouse-size phantom appears in the most published results. In this case the line source is 60 mm long. The line source insert can be filled with ^{18}F or ^{11}C water solution. The activity concentration is required to be low enough so that the random event rate is less than 1% of the true event rate. The phantom should be placed in the center of the FOV parallel to the z-axis (axial direction) of the scanner (Figure 6.6).

At least a minimum of 500,000 total coincidences must be collected. Any data correction, such as attenuation, scattered, random etc, including real-time subtraction of random events, should not be applied to the acquired data. Oblique sinograms should be unified into a single sinogram for each slice by the SSRB technique, conserving the number of counts. The SF for each slice i (SF_i) is required to be calculated as:

$$SF_i = \frac{\sum_j C_{r+s,i,j}}{\sum_j C_{TOT,i,j}} \tag{6.17}$$

where j is the acquisition number (in case of several data taking), $C_{r+s,i,j}$ is random plus scattered events counts in the slice i, and $C_{TOT,i,j}$ is the total event counts in the slice i. Assuming the negligible number of random events, $C_{r+s,i,j}$ consists only of scattered event counts, and $C_{TOT,i,j}$ consists of true and scattered event counts. The values of $C_{r+s,i,j}$ and $C_{TOT,i,j}$ can be estimated from a sinogram profile by a procedure described in the NEMA NU 4-2008 standard. The system SF of a PET scanner is computed as:

$$SF = \frac{\sum_i \sum_j C_{r+s,i,j}}{\sum_i \sum_j C_{TOT,i,j}} \tag{6.18}$$

6.7.2.2 Simulation approach, results, and comparison

The ^{18}F radionuclide with activity concentration of 10 MBq is chosen to calculate VIP SF. It is the same activity concentration as one from the last measurement of the counting rates test described in 6.8.2. This concentration is low enough so that the random event rate is less than 1% of the true event rate (see the results in the section 6.8.2), as the NEMA NU 4-2008 standard requires. The number of the scattered and total counts are known from the simulation. The formula 6.18 gives **0.71%** SF of the VIP system, while current state-of-the-art brain PET scanners and small animal PET systems normally have SF $\geq$ 10% for the same phantom. The published SF of the ClearPET and the rPET-1 are 31.1% and 24.2%, respectively [175]. The LabPET-8^{TM} SF is 19% [177] and the Inveon DPET pre-clinical tomograph has SF equal to 7.8% [176].

The unprecedented signal purity of VIP is due to the excellent energy resolution of the CdTe detectors and the resulting narrow energy acceptance window, something not easy to achieve with scintillating crystals.

6.8 Counting rate performance

The purpose of the test is to measure the effect of the system dead time and the generation of random coincidence events at several levels of source activity. At higher activity levels, coincidence events are lost because of system dead time, whereas the rate of random coincidences rises. It is necessary to measure the counting rate performance (both dead time losses and randoms) as a function of activity to understand the scanner s behavior for a wide range of scanning conditions. It is also required to measure noise equivalent count (NEC) rate. The NEC rate is defined as the count rate which would have resulted in the same SNR in the absence of scattered and random events. It is always less than the observed count rate.

For the counting rate performance evaluation, a source of relatively high activity is placed in the FOV of a PET scanner, and the data acquisition starts. The measurements should be taken while the activity of the source decays over several half-lives. As the source activity decays, random event rate decline more rapidly than does true event rate: the random rate is proportional to $2\tau A^2$, when the true rate is proportional to A. Here 2τ is the coincidence time window, and A is the source activity. Thus, eventually, the random rate becomes negligible. As the activity decays, the efficiency of the PET scanner in processing coincidence events improves, resulting in negligible count losses. Measurement of the true coincidence count rate with negligible random rate and count losses calibrate the response of the system for estimating count losses at higher activity levels.

6.8.1 According to NEMA NU 2-2001

6.8.1.1 Method

For brain scanners, the NEMA NU 2-2001 protocol recommends to use the phantom of the NEMA NU 2-1994, because it is smaller and, thus, more suitable for brain studies. The phantom is a polymethyl methacrylate cylinder with an outside diameter of 203 ± 3 mm and a wall thickness of 3 ± 1 mm. Its inner length is 190 ± 1 mm. It should be placed in the axial and transaxial center of the tomograph s FOV and aligned with the axial direction of the scanner. The phantom is entirely filled with radioactive water of relatively high and known activity concentration. The radionuclide used for this counting performance measurement should be ^{18}F.

The NEMA protocol requires to collect data at intervals more frequent than half of the radionuclide half-life ($T_{1/2}$), until count loss rates of true events are less than 1% of the total, and the random rate is less than 1% of the true rate. The individual acquisition times ($T_{acq,j}$) is required to be less than one-fourth of $T_{1/2}$. Sinograms should be generated for slices within the central 17 cm of the axial FOV of a tomograph, even if the axial FOV is longer than 17 cm. If the axial FOV is less than 17 cm, then the sinograms should be produced for the entire FOV. No data corrections should be applied.

After the event acquisition is done, the NEMA NU 2-1994 requires to sum the counts in each sinogram over a rectangular region of interest (ROI_i) created in each slice i. Each

ROI_i should have 240 mm in width and placed in the transaxial center of the FOV. This procedure gives a value of total number of collected coincidences $C_{ROI,t+s+r,i,j}$ (i.e., true plus scattered plus random counts) for each slice i and each acquisition j. The random counts $C_{ROI,r,i,j}$ should be subtracted from $C_{ROI,t+s+r,i,j}$ to obtain value of $C_{ROI,t+s,i,j}$ (i.e., true plus scattered counts). The value of $C_{ROI,r,i,j}$ can be obtained using any standard method, as, for instance, one of procedures described in section 3.8.3. After, the true and random event rates can be calculated. The true event rate ($R_{ROI,t,i,j}$) can be calculated as:

$$R_{ROI,t,i,j} = \frac{C_{ROI,t+s,i,j}}{T_{acq,j}}(1 - SF_i) \tag{6.19}$$

where $T_{acq,j}$ is the acquisition time of each measurement j, and SF_i is the SF obtained in the section 6.7.1. The random event rate ($R_{ROI,r,i,j}$) can be calculated as:

$$R_{ROI,r,i,j} = \frac{C_{ROI,r,i,j}}{T_{acq,j}} \tag{6.20}$$

The system true and random rates ($R_{ROI,t,sys,j}$ and $R_{ROI,r,sys,j}$ respectively) can be calculated using the following formulas:

$$R_{ROI,t,sys,j} = \sum_{number\ of\ slices} R_{ROI,t,i,j} \tag{6.21}$$

$$R_{ROI,r,sys,j} = \sum_{number\ of\ slices} R_{ROI,r,i,j} \tag{6.22}$$

6.8.1.2 Simulation approach, results, and comparison

The initial activity of the phantom is chosen to be 562 MBq and gets reduced down to 10 MBq. The number of total, true, scattered, and random counts are known from the simulation, so there is no need to estimate these values from the sinograms. The acquisition time $T_{acq,j}$ is calculated as ratio of the total number of simulated events (positron emissions) to the total activity concentration of measurement j. The counting rates are shown in Figure 6.7 as a function of both total and specific activity. The specific activity is the total activity of the phantom divided by the phantom volume (5966 mL). Additionally, the total count rate ($R_{ROI,TOT,j}$) and the NEC rate ($R_{ROI,NEC,j}$) are calculated and plotted, although it is not required by the NEMA NU 2-1994 document. The total count rate ($R_{ROI,TOT,i,j}$) is computed as:

$$R_{ROI,TOT,i,j} = \frac{C_{ROI,TOT,i,j}}{T_{acq,j}} \tag{6.23}$$

where $C_{ROI,TOT,i,j}$ is the total number of counts in the ROI drawn in the slice i of the measurement j. The system total rate ($R_{ROI,TOT,sys,j}$) is the sum of $R_{ROI,TOT,i,j}$ over

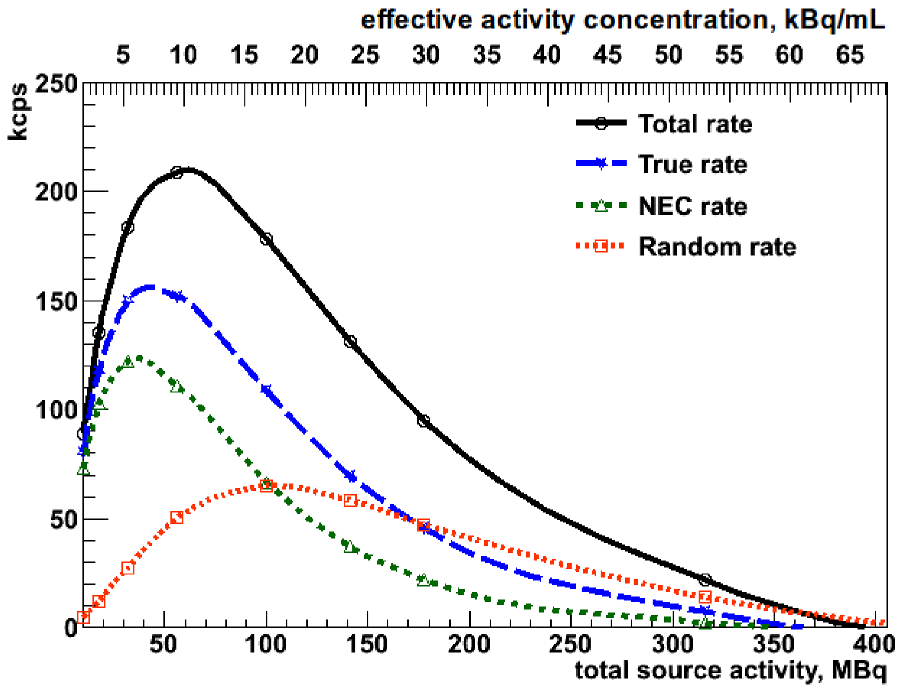

FIGURE 6.7: NEMA NU 2-1994 VIP scanner counting rates as a function of effective activity concentration and total source activity.

all slices. The NEC rate ($R_{ROI,NEC,i,j}$) can be calculated using the formula from the NEMA NU 2-2001 protocol:

$$R_{ROI,NEC,i,j} = \frac{R^2_{ROI,t,i,j}}{R_{ROI,TOT,i,j}} \tag{6.24}$$

As always, the system NEC rate ($R_{ROI,NEC,sys,j}$) is the sum of $R_{ROI,NEC,i,j}$ over all slices. The peak values of $R_{ROI,t,sys,j}$ and $R_{ROI,NEC,sys,j}$ ($R_{t,peak}$ and $R_{NEC,peak}$ respectively) with the corresponding specific activity values ($a_{t,peak}$ and $a_{NEC,peak}$) are reported and compared to the results of the G-PET and the ECAT HRRT systems in Table 6.7. The plot of the count rates measured with the G-PET scanner is shown in Figure 6.8.

TABLE 6.7: NEMA NU 2-1994 counting rates measurements of the VIP

Parameter	VIP	G-PET	HRRT
Energy window (keV)	503 519	410 665	350 650
$R_{NEC,peak}$(kcps)	122	60	148
$a_{NEC,peak}$(kBq/mL)	5.3	7.40	-
$R_{t,peak}$(kcps)	152	132	-
$a_{t,peak}$(kBq/mL)	9.43	13.69	-

Solid angle coverage normalization.

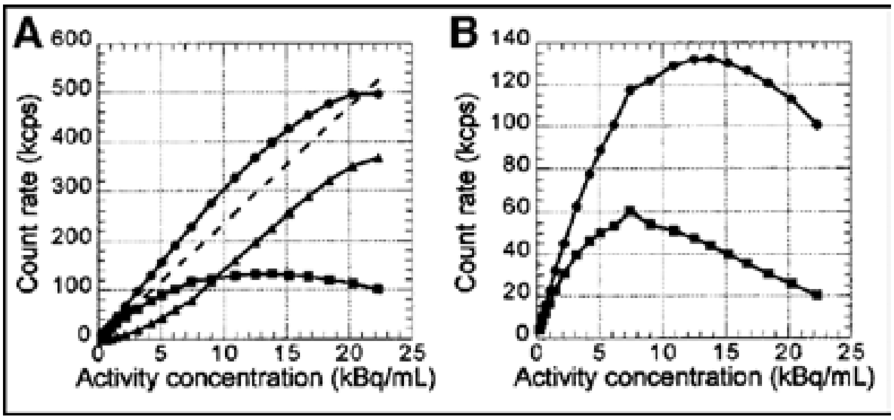

FIGURE 6.8: NEMA NU 2-1994 G-PET counting rates published in [172]. **A**: total (●), true (■), and random (▲) coincidence rates. The dashed line is the true rate, extrapolated to case of no dead-time losses. **B**: True (●) and NEC (■) rates.

For a fair comparison of the counting performance one can normalize the rate values to the portion of the solid angle covered by the different scanners around the emitting source. The solid angle coverage is calculated by formula 6.6. After normalization, VIP achieves the NEC peak of 1765 kcps, G-PET reaches the value of 488.3 kcps, and ECAT HRRT reaches 1356 kcps.

6.8.2 According to NEMA NU 4-2008

6.8.2.1 Method

For this test, the NEMA NU 4-2008 standard requires to use the same mouse-size, rat-size, or monkey-size phantoms as described in section 6.7.2. The mouse-like phantom is used for the VIP counting rates calculation. The line source insert should be filled with ^{18}F or ^{11}C radionuclide of high initial activity concentration. The procedure of data taking is the same as described in the section 6.8.1. Several data acquisition should be done while the activity decays. In each acquisition at least 500,000 prompt events should be collected. No data corrections should be applied. Oblique sinograms must be rebinned the using SSRB procedure conserving the number of counts in the sinograms.

From the sinograms, the total event rate($R_{TOT,i,j}$) for each slice i and each acquisition j can be calculated as:

$$R_{TOT,i,j} = \frac{C_{TOT,i,j}}{T_{acq,j}} \tag{6.25}$$

where $C_{TOT,i,j}$ is the total number of counts (true plus random plus scattered events), and $T_{acq,j}$ is the acquisition time of each measurement. After, the system total event rate ($R_{TOT,j}$) can be calculated as the sum of $R_{TOT,i,j}$ over all slices.

The true event rate ($R_{t,i,j}$) can be computed using the following formula:

$$R_{t,i,j} = \frac{C_{TOT,i,j} - C_{r+s,i,j}}{T_{acq,j}} \tag{6.26}$$

where $C_{r+s,i,j}$ is the number of random plus scattered events in the sinogram i. The value of $C_{r+s,i,j}$ can be estimated from sinograms by procedure described in the NEMA NU 4-2008 document. Again, the system true event rate $R_{t,j}$ is calculated as the sum of $R_{t,i,j}$ over all slices i.

The random event rate is calculated differently depending on the PET scanner being tested. For system that can estimate random coincidences ($C_{r,i,j}$), the random event rate $R_{r,i,j}$ is calculated as:

$$R_{r,i,j} = \frac{C_{r,i,j}}{T_{acq,j}} \tag{6.27}$$

For the systems that do not estimate random coincidences, the random rate can be computed as:

$$R_{r,i,j} = R_{TOT,i,j} - \frac{R_{t,i,j}}{1 - SF_i} \tag{6.28}$$

The system random event rate ($R_{r,j}$) should be calculated as the sum of $R_{r,i,j}$ over all slices i.

The NEMA NU 4-2008 requires to calculate the scattered event rate $R_{s,i,j}$ as:

$$R_{s,i,j} = R_{TOT,i,j} - R_{t,i,j} - R_{r,i,j} - R_{int,i} \tag{6.29}$$

where $R_{int,i}$ is the intrinsic true count rate. It is equal to zero for PET systems made of detector material without intrinsic radioactivity. If there is intrinsic radioactivity, $R_{int,i}$ can be computed using the same phantom as for the counting rate measurements centered in the center of the FOV, but without any activity in the line source insert. At least 10,000 coincidences should be collected for each slice during the data taking. The sinograms should be formed using the SSRB technique. Then the value of $R_{int,i}$ can be calculated as:

$$R_{int,i} = \frac{R_{t,i}}{T_{acq}} \tag{6.30}$$

The system scattered event rate $R_{s,j}$ is the sum of $R_{s,i,j}$ over all slices i.

Finally, the NEC rate ($R_{NEC,i,j}$) for each slice should be calculated. For the PET systems that do not perform direct random event subtraction, $R_{NEC,i,j}$ is computed as:

$$R_{NEC,i,j} = \frac{R^2_{t,i,j}}{R_{TOT,i,j}} \tag{6.31}$$

For systems that use direct random event subtraction the NEC rate should be found using the following formula:

$$R_{NEC,i,j} = \frac{R^2_{t,i,j}}{R_{TOT,i,j} + R_{r,i,j}} \tag{6.32}$$

The system NEC count rate $R_{NEC,j}$ is the sum of $R_{NEC,i,j}$ over all slices i.

The plot of the calculated total, true, NEC, scattered, and random event rates as functions of the activity concentration should be obtained. The peak true counting rate ($R_{t,peak}$) and peak NEC rate ($R_{NEC,peak}$) should be also determined, along with the activity concentrations at which these peak rates occur ($a_{t,peak}$ and $a_{NEC,peak}$).

Additionally, in this test, the system SF for each measurement j should be calculated from the counting rates by applying this formula:

$$SF_j = \frac{R_{s,j}}{R_{t,j} + R_{s,j}} \tag{6.33}$$

6.8.2.2 Simulation approach, results, and comparison

In this test the initial activity is 562 MBq and gets reduced down to 10 MBq. The count rates are plotted in Figure 6.9 as a function of both total and specific activity. The specific activity is computed as the total activity divided by the mouse-size phantom volume (34.34 mL).

For comparison, the counting rate performance of the ClearPET and rPET-1 systems for the same phantom are shown in Figure 6.10. Figure 6.11 shows the same result for the LabPET-8^{TM} (a) and the published NEC rate of the Inveon DPET scanner (b). Values of $R_{t,peak}$, $R_{NEC,peak}$, $a_{t,peak}$, and $a_{NEC,peak}$ for all scanners are summarized and compared in Table 6.8.

TABLE 6.8: Parameters of the counting rates measurements for different scanners

Parameter	**VIP**	**ClearPET**	**rPET-1**	**LabPET-8^{TM}**	**Inveon DPET**
Transverse FOV (mm)	420	94 144	45.6	100	161
Energy window (keV)	503 519	250-750	250 650	250 650	350 625
$R_{t,peak}$(kcps)	989.3	126.0	78.9	320	1670
$R_{NEC,peak}$(kcps)	908	73.4	29.2	183	1670
SF	0.78%	31.0%	24.2%	19%	7.8%
$a_{t,peak}$(MBq/mL)	1.6	0.75	1.35	2.5	3.8
$a_{NEC,peak}$(MBq/mL)	1.6	0.51	1.35	2.07	3.8

As one can see from the NEC curve comparison in Figure 6.12, the VIP scanner has the potential to outperform the other commercial PETs.

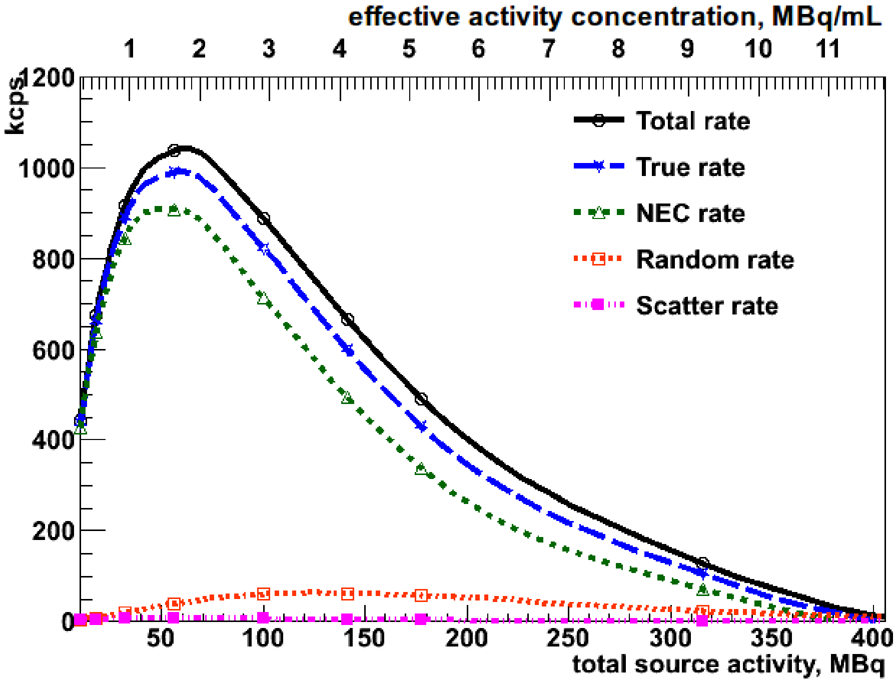

FIGURE 6.9: NEMA NU 4-2008 VIP scanner counting rates as a function of effective activity concentration and total source activity of a line source for the mouse-size phantom.

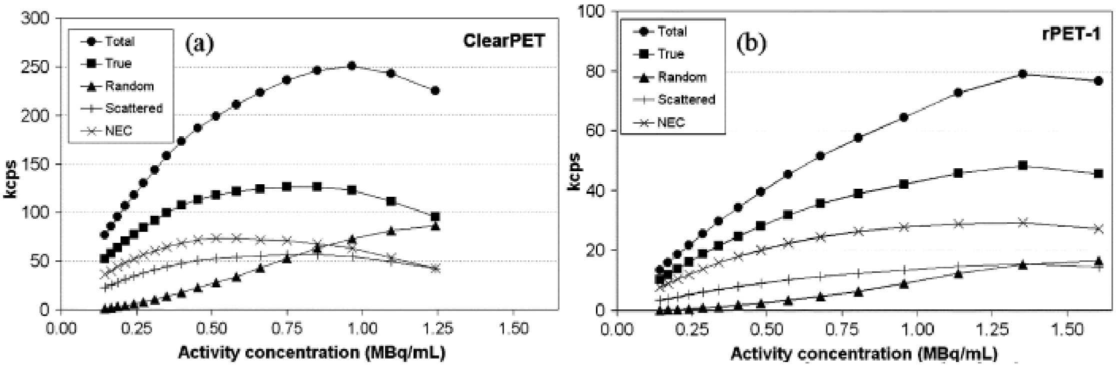

FIGURE 6.10: ClearPET (**a**) and rPET (**b**) counting rate performance plots as a function of effective activity concentration of the line source for the mouse-size phantom. The figures are taken from [175].

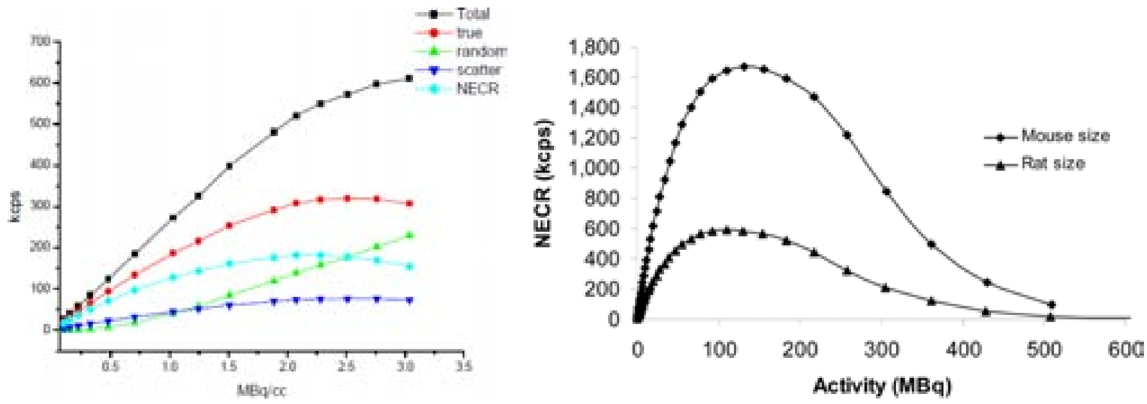

a **b**

FIGURE 6.11: **a**: LabPET-8^{TM} counting rate performance plots as a function of effective activity concentration for the mouse-size phantom published in [177]. **b**: Inveon DPET NEC rate as a function of total activity for mouse-size (diamond) and rat-size (triangle) phantoms published in [176].

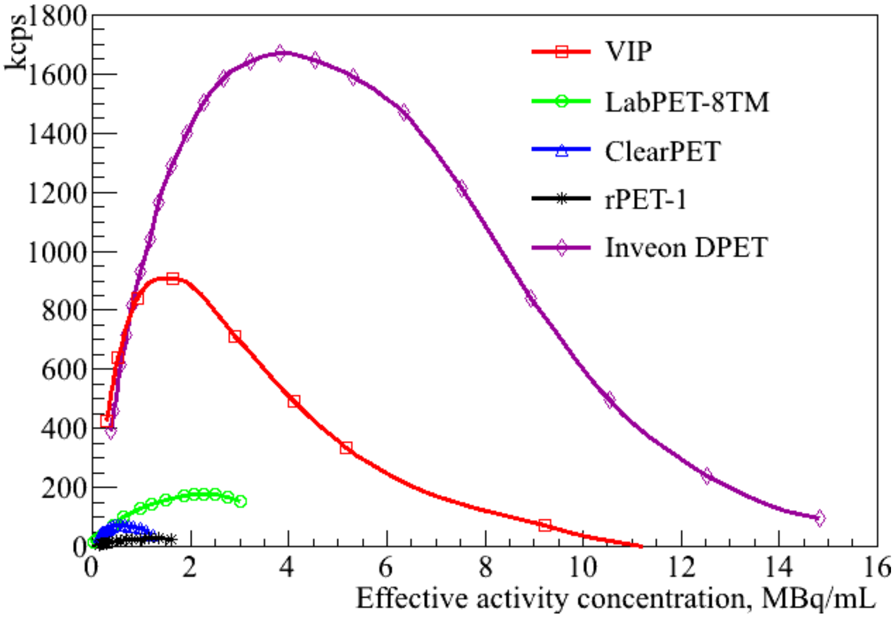

FIGURE 6.12: The NEC rates comparison between the VIP, ClearPET, rPET-1, LabPET-8^{TM}, and the Inveon DPET scanners.

Solid angle coverage normalization. The solid angle coverage normalization is also performed for a fair comparison of the counting performance of different small animal PET scanners. The solid angle coverage is calculated by formula 6.6. After normalization, VIP achieves the NEC peak value 30 times higher NEC peak than the rPET-1 ($7.7 \cdot 10^6$ cps vs $2.5 \cdot 10^5$ cps), and 25 times the NEC peak of the ClearPET ($7.7 \cdot 10^6$ cps vs $3.1 \cdot 10^5$ cps). The the NEC peak of the VIP scanner is $\sim$4 times as high as the NEC peak of the LabPET-8^{TM}($1.95 \cdot 10^6$ cps), and $\sim$1.5 as low as the one of the Inveon DPET system($11.58 \cdot 10^6$ cps).

The high counting rates that the VIP achieves in both NEMA tests are due to the combination of two factors. On the one hand, the significantly better energy resolution of CdTe with respect to scintillating crystals provides a cleaner signal with very low scattered event counting. On the other hand, the extremely high number of channels of the VIP makes the random rate affected only by the coincidence time window with no effect from to the dead time of the individual channels.

Chapter 7

VIP Image Reconstruction

The simulation result of the counting performance indicates that the VIP design has the potential to provide high detection sensitivity together with high signal purity, that are currently achievable only by small animal PET employed in research. The crack-free geometry of the VIP scanner with 4-cm-thick CdTe detectors provides a sensitivity of 14.37 cps/kBq according to the NEMA NU 2-2001 standard [163], and 21 cps/kBq according to NEMA NU 4-2008. A very low SF of 3.95% and 0.73%, according to NEMA NU 2-2001 and to NEMA NU 4-2008, respectively, is achieved due to the good energy resolution provided by the CdTe detectors. The high number of channels in the VIP scanner makes the full system less affected by the dead time of the individual detector voxels. The calculated NEC curve has a peak value of 122 kcps at 5.3 kBq/mL for NEMA NU 2-2001 and 908 kcps at 1.6 MBq/mL for NEMA NU 4-2008. Additionally, the reference [1] shows that the VIP allows to dramatically shorten the scan time and thereby lower the image blurring due to the motion of patients. On the other hand, the patient dose can be significantly reduced while keeping the typical time window for screening of 20 minutes.

However, even if the VIP scanner is capable to obtain a high-purity sample, the final image quality depends on the image reconstruction method and the reconstruction parameters being used. The use of an inappropriate reconstruction algorithm can distort the final image, lowering its quality and adding artifacts. The choice of reconstruction technique is one of the crucial factors in getting a good final image. For this reason the designers of PET systems often develop their own algorithm (or modify existing algorithms) to adapt it to the specifics of the scanner. In case of the VIP PET scanner, we test and evaluate a few standard methods to pick the optimal one in terms of image quality and reconstruction time.

This chapter describes the optimization of the image reconstruction for the VIP PET scanner, the standardized image quality tests from NEMA NU 2-2001 and NEMA NU 4-2001, and includes the results and comparison with other PET systems. Three different image reconstruction methods are considered. The first is the 2-D FBP reconstruction algorithm with the SSRB technique (described in section 3.6.2), the second one is OSEM (described in section 3.6.3), and, finally, the last method considered in the following analysis is the LM-OSEM (described in section 3.6.4). The OE algorithm (described in section 3.6.5) has been also analyzed. However, since it shows poor results, thus it is not used for the VIP reconstruction. In order to evaluate the performance of each reconstruction method three different modalities are used: the bias, the variance and the mean square error (MSE) measurements [180]; calculation of the modulation transfer function (MTF) curve [181]; and the region of interest (ROI) analysis [164].

7.1 Optimization of the reconstruction parameters

7.1.1 Method

One can find the best reconstruction parameters and compare performance of various reconstruction techniques using image quality metrics such as the bias, the variance, and the average MSE [180]. The *bias* indicates how much difference is generated between the reconstructed group average image and the true image. The true image is a emitting points map (i.e. true distribution of annihilation events) of the phantom being used for the bias, variance, and average MSE calculation. For the calculation, the true image and each image from the considering group must have the same image matrix. For a group of images, the bias can be calculated as following:

$$Bias = \frac{1}{N} \cdot \sum_{i=1}^{N} (\bar{X}_i - X_i^{True})^2 \tag{7.1}$$

Where N is the total number of pixels in the whole image (or in the ROI), X_i^{True} is the number of counts in the i^{th} pixel of the true image, and $\bar{X}_i$ is the number of counts in the i^{th} pixel of the average image. The $\bar{X}_i$ can be calculated as:

$$\bar{X}_i = \frac{1}{M} \cdot \sum_{j=1}^{M} X_i^j \tag{7.2}$$

Where M is the total number of images in the considering group, and X_i^j is the number of counts in the i^{th} pixel of the j^{th} image.

The *variance* is a measure of how consistent the several reconstructed images are. It is computed as following:

$$Variance = \frac{1}{NM} \cdot \sum_{i=1}^{N} \sum_{j=1}^{M} (X_i^j - \bar{X}_i)^2 \tag{7.3}$$

The *MSE* measures the difference between a reconstructed image and the true image. It is a trade-off between the bias and the variance.

$$MSE^j = \frac{1}{N} \cdot \sum_{i=1}^{N} (X_i^j - X_i^{True})^2 \tag{7.4}$$

Where MSE^j is the mean square error between the j^{th} image and the true image. The MSE is calculated for each image in the group. Then, the average MSE is computed as the arithmetic mean of all the MSE for a given image set.

Varying the parameters of the different algorithms (such as cutoff frequency, number of iterations) and comparing these image quality metrics, one finds the optimum reconstruction parameters for each of the algorithms. The best image is the one that gives the lowest value of the average MSE.

For the quality metrics calculation we chose a small-animal PET phantom described in NEMA NU 4-2008 protocol. The phantom is simulated with GAMOS and shown in Figure 7.1(a). The phantom is made of polymethylmethacrylate and has internal dimensions of 50 mm in length and 30 mm in diameter. It consists of three parts: two lids and the main body. The main body has 5 drilled through rods of 1, 2, 3, 4, and 5 mm in diameter, respectively. Their length is 20 mm. The top lid has two cylindric chambers of 14 mm in length and 8 mm in diameter. The main body s chamber, as well as the rods, are filled with ^{18}F radioactive water of 3.7 MBq total activity. One of the top lid s chambers is filled with air and the other one is filled with non-radioactive water in order to create two cold (non-radioactive) regions. The phantom is placed into the center of VIP such that the axis of its main body is aligned with the axial axis of the scanner FOV (Figure 7.1(b)).

7.1.2 Results

A total of 10 million coincidences are collected to reconstruct the image. All images are reconstructed using the 2-D FBP, 2-D OSEM, and, LM-OSEM algorithms. No attenuation, scatter, random correction, or normalization is applied for any reconstruction algorithm. The image pixel size is set to 0.25 mm and the slice thickness is set to 2 mm.

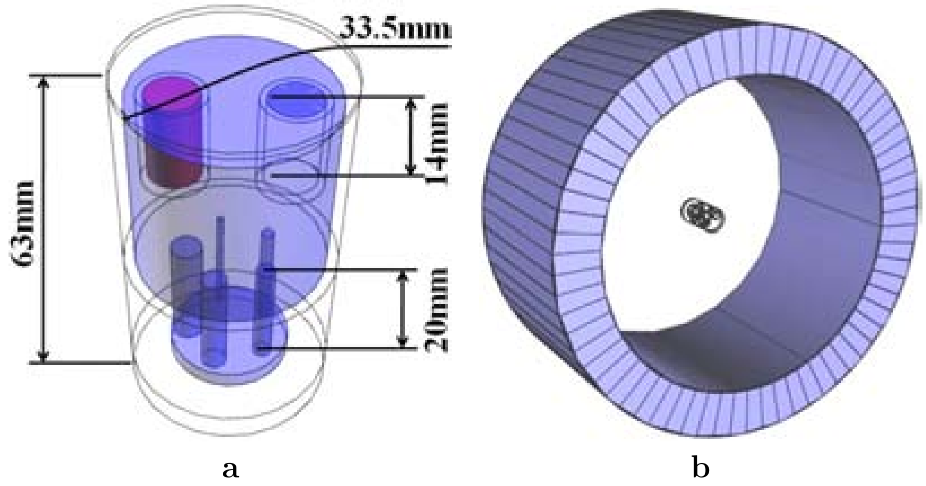

FIGURE 7.1: **a**: NEMA NU 4-2008 image quality phantom simulated with GAMOS. **b**: The position of the phantom in the FOV of VIP.

The bias, variance and average MSE are measured for sets of 10 images. The images are reconstructed from 10 data sets (10 collections of LORs) with a single varying reconstruction parameter for each method. The cutoff frequency relative to Nyquist frequency for the Hamming filter was varied for every run of the 2-D FBP algorithm. The result is shown in figure 7.2a. As one can see the optimal value for the cutoff frequency is 0.15, where the average MSE has the lowest value (33.5352). The OSEM reconstruction method is tested by varying the number of iterations. Each time 2 subsets are used. The resulting bias, variance and average MSE are shown in figure 7.2c. The average MSE shows a minimum value (76.84) for 2 iterations. Finally, the LM-OSEM algorithm is tested also varying number of iterations and using 2 subsets for each run. The result is shown in figure 7.2d. The minimum average MSE has a value 29.7853 for 4 iterations. The images of three phantom regions (the cold inserts, the uniform region, and the 5 hot rods) obtained with optimal parameters for each of the algorithms are shown in figure 7.3.

7.2 Reconstruction of the Derenzo phantom

7.2.1 Method

The performance of the three image reconstruction algorithms for the VIP PET is additionally evaluated with the Derenzo phantom [182]. This phantom is widely used for the assessment of the spatial resolution of PET scanners. The Derenzo phantom is made of a circular piece of plastic with drilled through rods. It consists of 5 segments, each

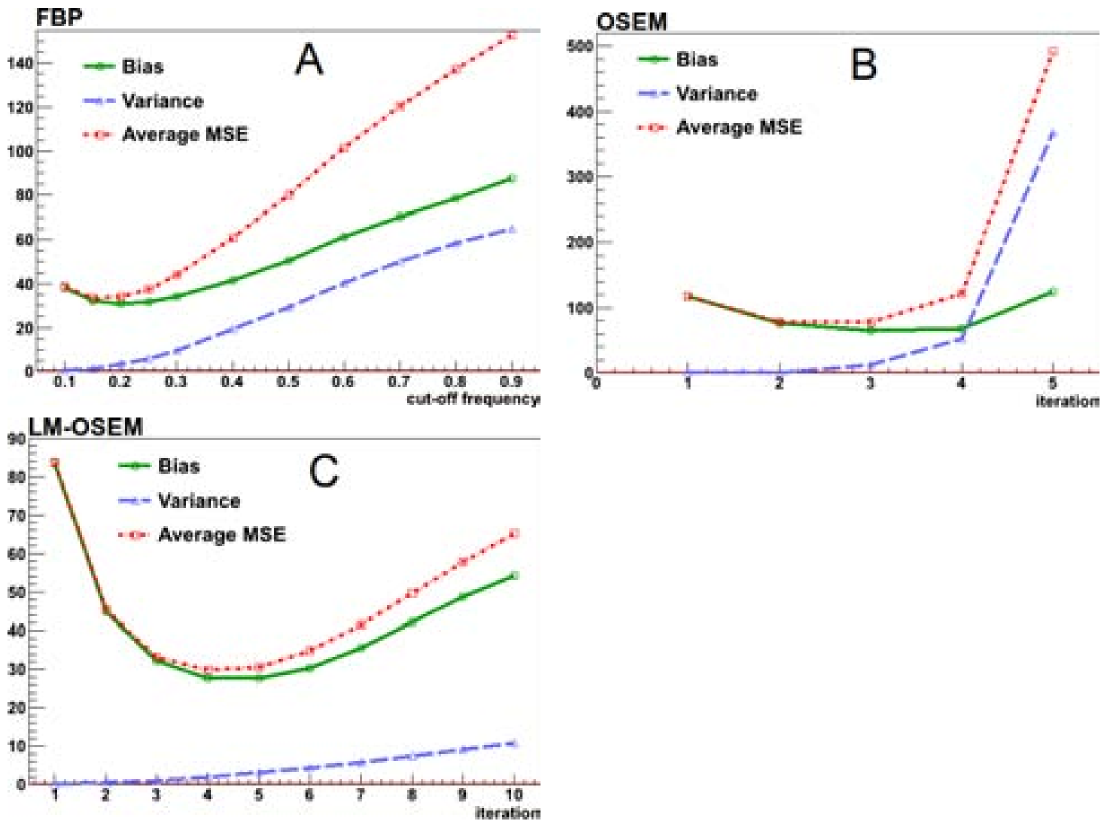

FIGURE 7.2: Image quality metrics versus: **A:** cutoff frequency for FBP with a Hamming filter, **B:** number of iterations for OSEM, **C:** number of iterations for LM-OSEM

containing rods of length 12 mm and with varying diameters (Figure 7.4). The distances between the rods of different segments are also different.

The rods of the phantom are filled with the ^{18}F radioactive isotope of 1 MBq total activity.

7.2.2 Results

The image of the Derenzo phantom is reconstructed with FBP, OSEM, and LM-OSEM methods using the optimized parameters for each algorithm found in the section 7.1. The total of 1 million coincidences are acquired for the reconstruction. The results are shown in Figure 7.5.

Each reconstruction method produces good images with well-defined smallest rods. However, the images reconstructed with OSEM are noisier comparing to FBP and LM-OSEM.

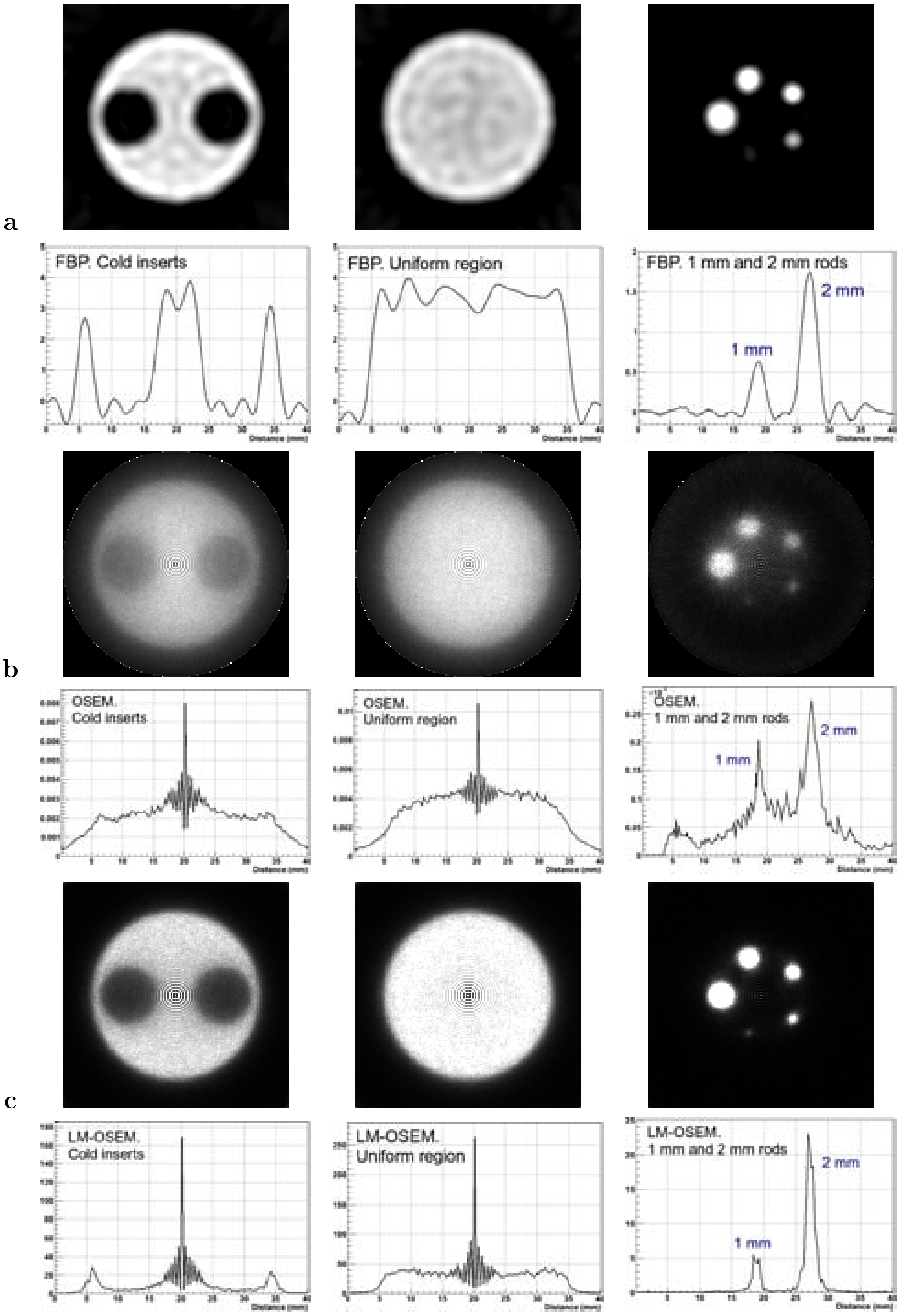

FIGURE 7.3: **a:** FBP reconstructed image with a Hamming filter (cutoff frequency = 0.15) and the corresponding line profiles. **b:** OSEM reconstructed image after 2 iterations and 2 subsets (no filters) and the corresponding line profiles. **c:** LM-OSEM reconstructed image after 4 iteration and 2 subsets (no filters) and the corresponding line profiles.

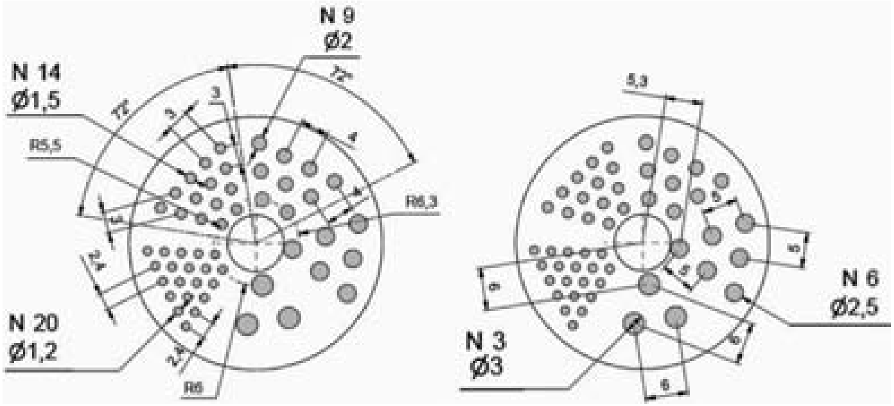

FIGURE 7.4: Schematic drawing of the Derenzo phantom used in the simulation.

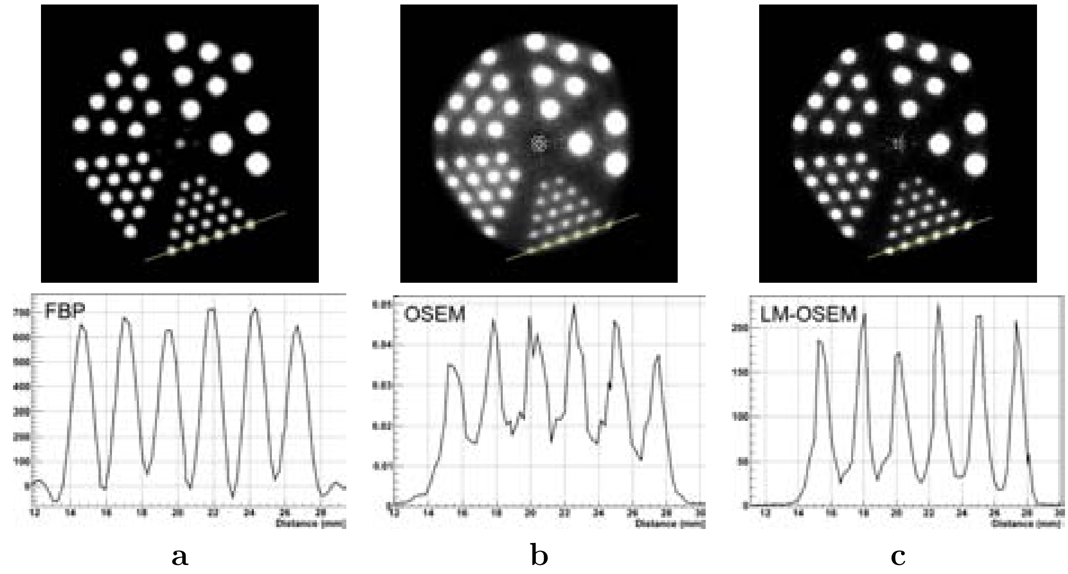

FIGURE 7.5: Derenzo phantom reconstructed with different methods and with the optimized parameters found for each method and corresponding line profiles for 6 smallest rods. **a**: 2-D FBP, Hamming filter with cutoff frequency = 0.15; **b**: OSEM after 2 iterations with 2 subsets (no filters); **c**: LM-OSEM after 4 iterations with 2 subsets (no filters).

7.3 MTF test

7.3.1 Method

The performance of the reconstruction algorithms can be evaluated by comparison of the MTF curves obtained for each method. Computation of the MTF is one of the most complete methods to characterize completely in a quantitative way the spatial resolution of a scanner in tomography. Modulation is synonym of contrast in optics. The modulation (or contrast) corresponds to resolving power of an imager. The MTF shows how this contrast changes while reducing the size of a test phantom. The test phantom for the MTF measurements can be a bar-pattern phantom where hot (radioactive) and cold (non-radioactive) bars are getting reduced from pair to pair (Figure 7.6(A)). If one measures the modulation (contrast) of the hot (or cold) bars of the true image, it will stay the same (say 100%) for the all hot (cold) bars independently of their width and the distance between them (Figure 7.6(C)). However, normally, the reconstructed images are blurred, and, the smaller the size of an object the worse its contrast, as it is presented in Figure 7.6(B). If to plot the dependence of the amplitudes of the sinusoidal curve shown in Figure 7.6(D) on the number of line pairs (one line pair is one hot and one cold bars) per a length unit (i.e. cm), one gets the MTF curve (Figure 7.7). Thus, the MTF shows how the modulation (contrast) changes while reducing the size of the line pairs of the bar phantom. Figure 7.7 shows examples of 2 different MTFs. The spatial resolution of the scanner is one where the MTF equals to 0.5. Normally, two adjacent bars patterns cannot be distinguished when the MTF drops below a value of ∼0.1. Thus, the minimum resolvable bar pattern for a scanner can be estimated using the MTF curve. Good low-frequency response better represents large low-contrast lesions, while good high-frequency response is better for fine details and sharp edges [23].

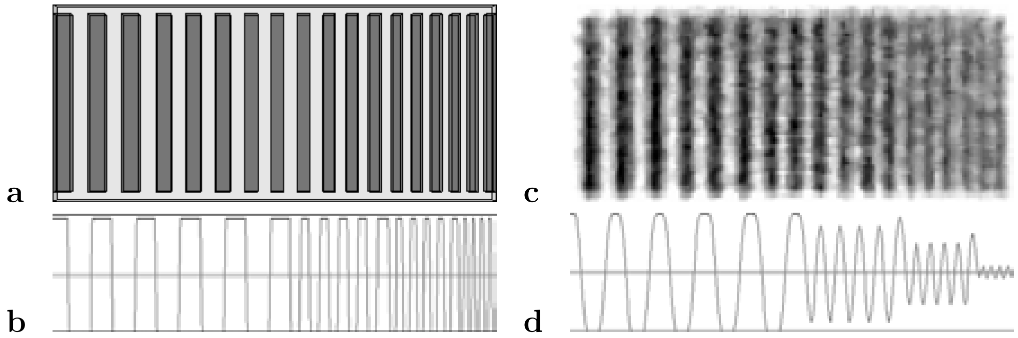

FIGURE 7.6: **a**: example of a bar-pattern phantom for the MTF measurements. **b**: contrast of the hot and cold bars. **c**: reconstructed bar phantom. **d**: contrast of the hot and cold bars of the reconstructed phantom.

The MTF can be also calculated from the PSF or LSF as a magnitude of its 2-D (or 1-D) Fourier transform (FT):

$$MTF(u,v) = FT(PSF(x,y)) \tag{7.5}$$

The 1-D FT of a profile recorded through the center of the PSF gives the MTF of the system in the direction of the profile. It is a good approach (respect to 2-D MTF from 2-D FT of the 2-D PSF) when a reconstructed point-like source has a symmetrical shape

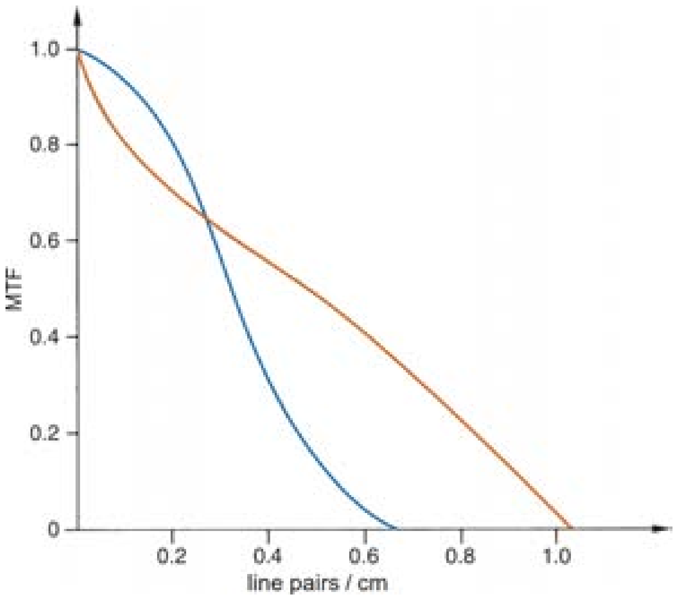

FIGURE 7.7: MTF curves for two different collimators. One has better low-frequency resolution for coarse details (blue line), whereas the other is better for fine details (orange line). The figure is taken from [23].

in all directions. In case of the VIP scanner such good symmetry is reached if the point-like radiation source is placed near the center of the axial and transaxial FOV of the system (see section 7.4).

To obtain the PSF an ideal 511 keV back-to-back gamma point-like source of low activity is simulated. It is placed in the center of the axial FOV and at 5 mm off the center of the transaxial FOV in order to avoid a central artifact. The images of the point-like source are reconstructed using the optimal number of iterations (found in the section 7.1) for each iterative reconstruction method. In case of the 2-D FBP algorithm no smoothing is used in order to not blur the image and, thus, to not lose the spatial resolution. After the reconstruction the MTFs are computed. As a general rule the smaller image pixel size the better spatial resolution can be reached by a scanner and, thus, the more detailed image can be obtained. However, increasing the voxel density in the FOV corresponds to reducing the statistics per voxel with the effect of increasing the image noise. The PSF of the scanner is ~1 mm in the center of the FOV according to the results in the section 7.4. Thus, a pixel size of 0.25 mm is chosen to fulfill the sampling requirement (Eq. 3.12) [23]:

7.3.2 Results

The results on the measured MTFs is presented in Figure 7.8. One can see the LM-OSEM method with 4 iterations and 2 subsets and 2-D FBP (no smoothing) have similar MTF curves. OSEM (after 2 iterations and 2 subsets) shows worse result than LM-OSEM and FBP. The reason of it is the lack of computer memory to handle the probability distribution for 6,336,000 detector voxels, so that the voxels had to be merged to reduce the multiplicity. The spatial resolution of the VIP scanner at the MTF values of 0.5 and 0.1 for each reconstruction algorithm are presented in Table 7.1.

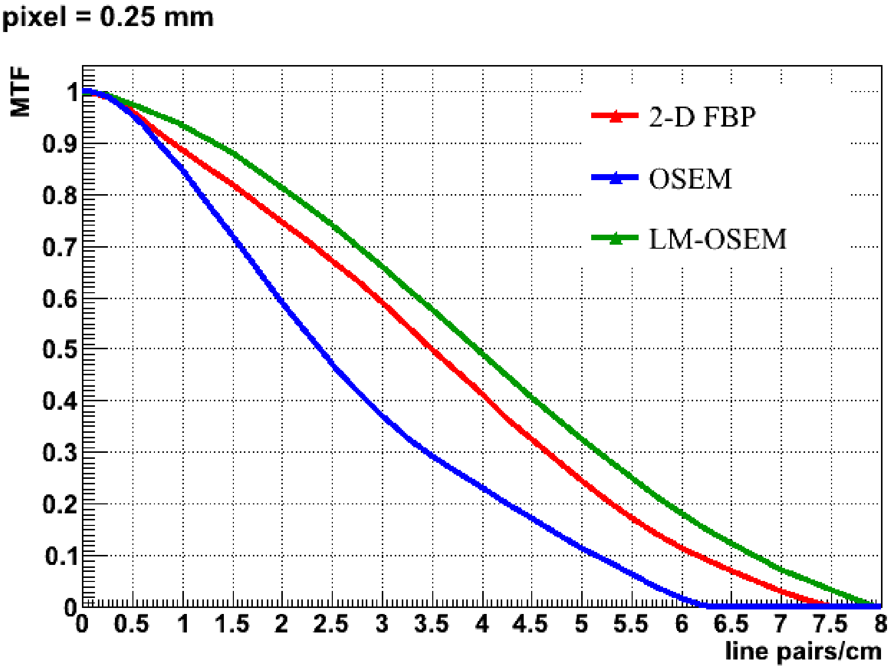

FIGURE 7.8: The MTFs obtained from the reconstructed PSF.

TABLE 7.1: MTF test results for the VIP PET scanner

	2-D FBP cutoff = 1	OSEM 2 iterations	LM-OSEM 4 iterations
at MTF = 0.5 corresponding line width	3.5 lp/cm 1.43 mm	2.38 lp/cm 2.1 mm	3.95 lp/cm 1.27 mm
at MTF = 0.1 corresponding line width	6.15 lp/cm 0.81 mm	5.15 lp/cm 0.97 mm	6.725 lp/cm 0.74 mm

7.4 Spatial resolution test

Spatial resolution is the minimum distance between two point-like sources at which the scanner is still able to distinguish them. The spatial resolution is usually characterized by the FWHM and the full width at tenth maximum (FWTM) of the reconstructed PSF obtained from the measurement of the activity distribution of a compact radioactive point source. Resolution in PET is normally specified separately in transaxial (radial and tangential resolutions) and axial (axial resolution) directions.

7.4.1 According to NEMA NU 2-2001

7.4.1.1 Method

In this study, spatial resolution should be measured using the ^{18}F point-like source, with activity low enough so that either the percent dead-time losses are less than 5% or the random rate does not exceed 5% of the total event rate. The radioactive source should be placed inside a glass capillary with an inside diameter of 1 mm or less and an outside diameter of less than 2 mm. The length of the source inside the capillary should be less than 1 mm.

NEMA NU 2-2001 requires to take data at six different positions (inside the FOV of the scanner) of the capillary with the source:

1. at $z = 0$, $x = 0$, and $y = 1\ cm$;
2. at $z = 0$, $x = 0$, and $y = 10\ cm$;
3. at $z = 0$, $x = 10\ cm$, and $y = 0$;
4. at $z = 1/4$ of the axial FOV, $x = 0$, and $y = 1\ cm$;
5. at $z = 1/4$ of the axial FOV, $x = 0$, and $y = 10\ cm$;
6. at $z = 1/4$ of the axial FOV, $x = 10\ cm$, and $y = 0$;

where z is the axial, x is the horizontal, and y is the vertical axis. At each position, at least 10^5 counts should be collected. The images should be reconstructed by FBP without applying any smoothing.

Both FWHM and FWTM of the point source response function in all 3 direction (radial, tangential, and axial) should be determined by forming the line profiles at each direction. The all line profiles should go through the voxel with the highest number of counts. The spatial resolution (FWHM and FWTM) should be determined by linear interpolation between adjacent pixels at half (one-tenth) the maximum value of the line profile function. The maximum value should be determined by a parabolic fit using the peak point and its two nearest neighboring points. Values should be converted to distance in mm by multiplication by the pixel size. Averaged radial (R), tangential (T), and axial (A) spatial resolution values (FWHM and FWTM) should be calculated using the following formulas for different source positions.

At 1 cm radius ($x = 0$, $y = 1\ cm$):

$$R_1 = T_1 = \frac{1}{4} \cdot \Big(xFWHM_{z=0} + yFWHM_{z=0} + xFWHM_{z=1/4FOV} + yFWHM_{z=1/4FOV} \Big) \quad (7.6)$$

$$A_1 = \frac{1}{2} \cdot \Big(zFWHM_{z=0} + zFWHM_{z=1/4FOV} \Big) \quad (7.7)$$

At 10 cm radius:

$$R_{10} = \frac{1}{4} \cdot \Big(xFWHM_{z=0,x=10,y=0} + yFWHM_{z=0,x=0,y=10} + + xFWHM_{z=1/4FOV,x=10,y=0} + yFWHM_{z=1/4FOV,x=0,y=10} \Big) \quad (7.8)$$

$$T_{10} = \frac{1}{4} \cdot \Big(yFWHM_{z=0,x=10,y=0} + xFWHM_{z=0,x=0,y=10} + + yFWHM_{z=1/4FOV,x=10,y=0} + xFWHM_{z=1/4FOV,x=0,y=10} \Big) \quad (7.9)$$

$$A_{10} = \frac{1}{4} \cdot \Big(zFWHM_{z=0,x=10,y=0} + zFWHM_{z=0,x=0,y=10} + + zFWHM_{z=1/4FOV,x=10,y=0} + zFWHM_{z=1/4FOV,x=0,y=10} \Big) \quad (7.10)$$

The same formulas should be used to calculated the spatial resolutions at FWTM.

7.4.1.2 Simulation approach, results, and comparison

A ^{18}F point-like source of 1 MBq activity inside the glass capillary is used for the spatial resolution test. This activity is low enough that the random rate does not exceed 5% of the total event rate (see results of the section 6.8.1). The point source is a 0.1-mm-diameter water sphere. All dimensions of the capillary are smaller then 1 mm. At least 10^5 coincidences are collected per measurement. Images are reconstructed with the SSRB FBP algorithm without applying smoothing. The values of the FWHM of the three spatial components of the measured PSF are calculated in the accordance with NEMA NU 2-2001 and summarized in Table 7.2.

The reported transverse and axial resolutions of the HRRT scanner varies across the FOV from ∼2.3 to ∼3.2 mm and from ∼2.5 to ∼3.4 mm respectively. The spatial

Table 7.2: Spatial resolution of VIP according to NEMA NU 2-2001

Radial position (mm)	10	100
Radial res. (mm)	0.98	1.31
Tangential res. (mm)	0.98	1.35
Axial res. (mm)	1.26	2.03

resolution of the G-PET scanner near the center of the FOV is 4.1 mm in the transverse direction and 5.2 mm in the axial direction. While state-of-the-art head PET scanners struggle to deliver resolutions below 5 mm FWHM, the VIP PET reaches ∼1 mm PSF.

7.4.2 According to NEMA NU 4-2008

7.4.2.1 Method

In order to compare VIP with small animal PET scanners, the spatial resolution is also measured using the NEMA NU 4-2008 standard. For the test the same ^{22}Na point source inside the $10 \times 10 \times 10$ mm^3 acrylic cube, described in the section 6.6.2 is used. The activity of the radionuclide should be less than that at which either the dead-time losses exceed 5% or the random coincidence rate exceeds 5% of the total event rate. The NEMA NU 4-2008 protocol requires to do measurements with the source located at the axial center of the FOV and at one fourth of the axial FOV from the center (at distance of 63.5 mm from the center in case of the VIP scanner) and at the following radial distances from the center: 5 mm, 10 mm, 15 mm, 25 mm and further at increments of 25 mm to the edge of the scanner s FOV. For each source position at least 10^5 coincidences should be collected. After the data acquisition is done, the images should be reconstructed with 2-D or 3-D FBP, without smoothing the data.

The FWHM and FWTM of the point source response function in radial, tangential, and axial directions should be determined by forming the line profiles at each direction. The all line profiles should go through the voxel with the highest number of counts. The FWHM and FWTM values should be determined by linear interpolation between adjacent pixels at half (one-tenth) the maximum value of the line profile function. The maximum value should be determined by a parabolic fit using the peak point and its two nearest neighboring points. Values should be converted to distance in mm by multiplication by the pixel size.

7.4.2.2 Simulation approach, results, and comparison

A ^{22}Na source with activity of 1 MBq generates random coincidence rate less than 5% of the total event rate (see results in the section 6.8.2). At least 10^5 coincidences are collected per measurement. Images are reconstructed using the SSRB and 2-D FBP reconstruction with no smoothing. The FWHM of the response PSF in all 3 directions is measured. The results of the radial, tangential, and axial spatial resolution in terms of FWHM are graphically presented in Figure 7.9 as a function of radial and axial offsets. The slice thickness of the reconstructed image is 0.5 mm and the pixel size is 0.25 mm.

In the reference [183] it is shown that in the case of an ideal detector with zero energy resolution, full angular coverage, infinite sensitivity, and capable of reconstructing the photon hit position within a 1 mm^3 voxel, the best achievable resolution is 0.8 mm. Figure 7.9 shows that the VIP perform very closely to such an ideal detector.

Figures 7.10A, 7.10B, and 7.10C show the results of spatial resolution test for Inveon, LabPET-8^{TM}, ClearPET and rPET-1 small-animal scanners respectively for comparison. In such ideal conditions of negligible contamination from scattered and random events, the transaxial spatial resolution of VIP scanner is ~2 times better than the spatial resolution of any other PET presented in Figure 7.10. The gap between the performance of the VIP and the other scanners is expected to become even more significant in the case of more challenging conditions including high activity in a dense medium.

7.5 The image quality evaluation

For a proper evaluation and comparison of the imaging performance of different PET scanners, it is necessary to simulate a typical imaging condition with a standardized phantom. The phantom study can give indications of image quality for this particular imaging situation. The purpose of the image quality test is to learn the PET scanner s response in different activity distribution conditions, such as cold regions in a hot uniform background, hot areas in a less hot uniform background, hot uniform background, the hot lesions in a dense scattering volume without activity. The RCs measured in the hot rods included in a dense volume without any background activity, indicate the spatial resolution of the scanner. The noise in the uniform region indicates the SNR performance, while the uniformity in this region is a measure of attenuation and scatter correction performance. The activity measured in the cold regions (in a hot background activity) is indicative of the scatter correction performance. The imaging of the hot lesions in a less hot background indicates how good the scanner can distinguish different activity concentration.

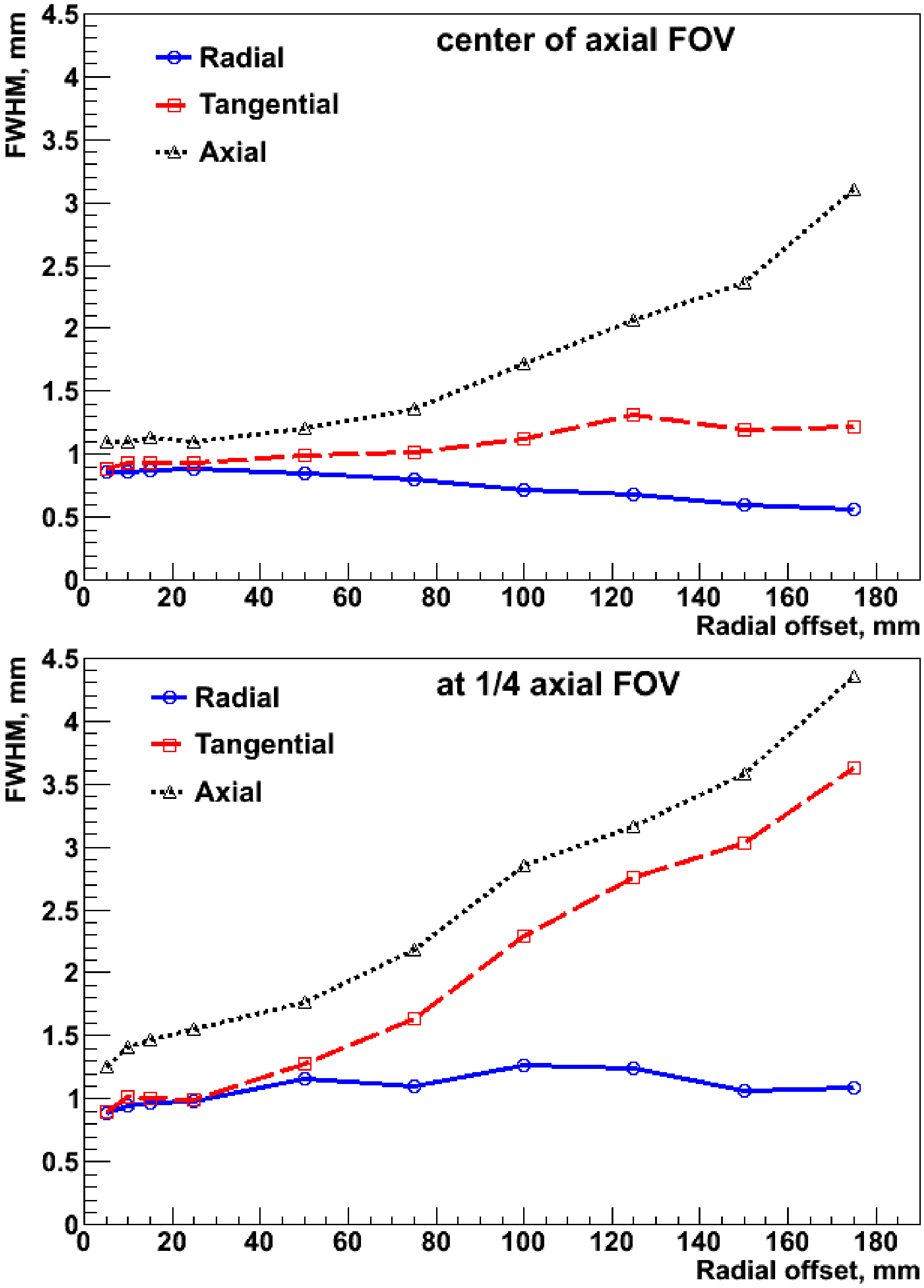

Figure 7.9: VIP radial, tangential, and axial spatial resolution as a function of radial offset reported as FWHM according to NEMA NU 4-2008.

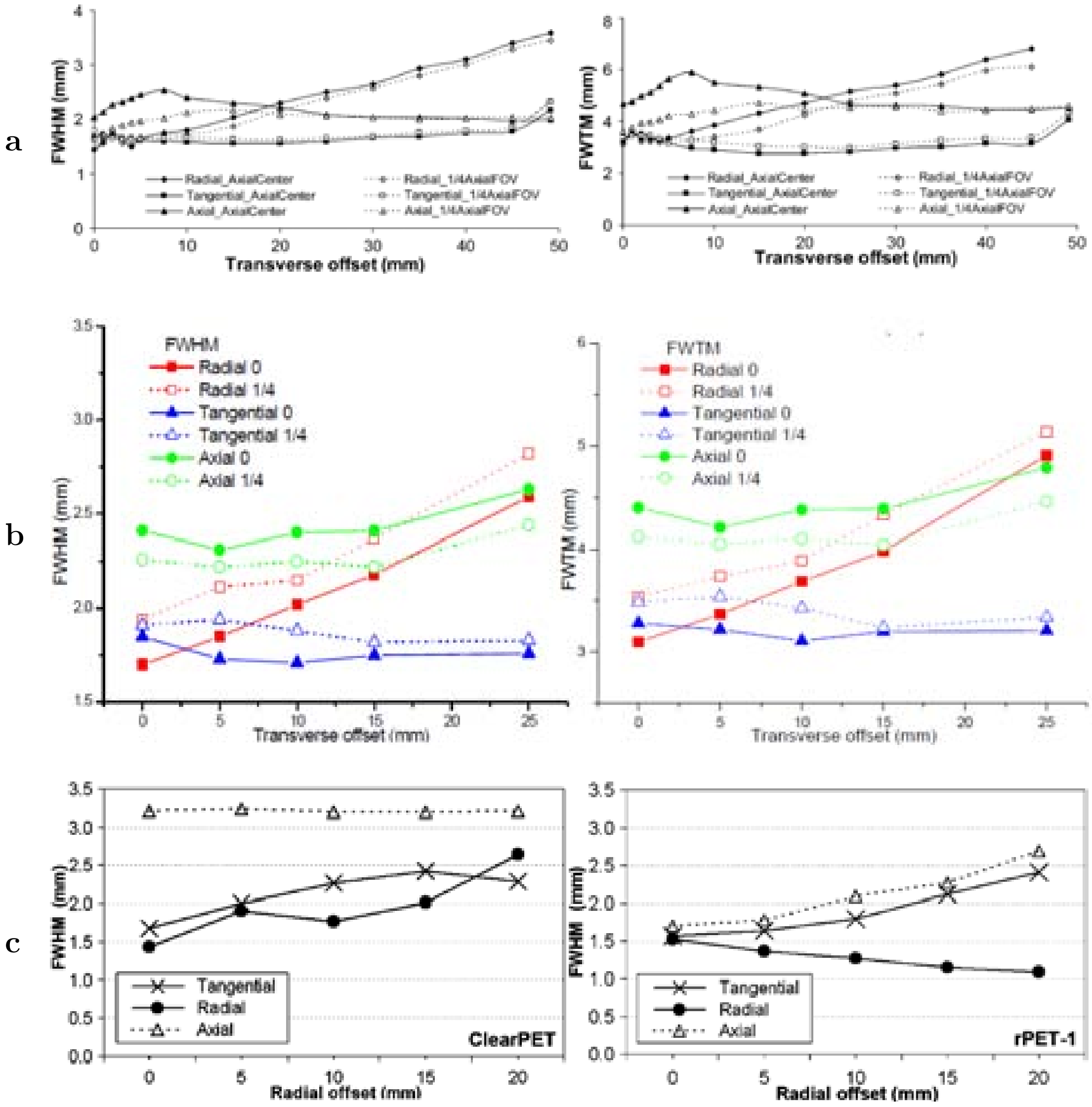

FIGURE 7.10: Spatial resolution test results of Inveon DPET published in [176] (**a**), LabPET-8^{T}M published in [177] (**b**), ClearPET (**c**, left), and rPET-1 (**c**, right) published in [175]. For ClearPET and rPET-1 the result is shown only in case of measurements in the axial center of FOV.

The image quality evaluation is done using two standardized phantoms described in the NEMA NU 2-2001 and NEMA NU 4-2008 protocols and, additionally, two modified versions of these phantoms. The modified phantoms are needed to find out how the scanner performs in more challenging conditions.

7.5.1 Small animal phantom analysis

7.5.1.1 Method

According to the NEMA NU 4-2008 protocol prescription, the small animal phantom should be simulated for the image quality evaluation. The phantom, its position in the scanner, and the activity concentration are the same as presented in the section 7.1 (Figure 7.1). It is necessary to collect data during 20 minutes, excluding the time required for the attenuation measurements.

The images should be reconstructed applying all available corrections to the data. The chosen reconstruction algorithm (including number of iterations, filters or other smoothing), image matrix size, image pixel size, slice thickness, and other reconstruction parameters should give the best image quality.

In order to evaluate image quality, the NEMA NU 4-2008 standard requires to calculate three different merits:

- uniformity;
- RCs;
- Spill-over ratios (SORs).

Additionally, percentage standard deviations (%STD) should be calculated for each merit.

The *uniformity* should be measured in the uniform region (central part) of the phantom. It is a measure of attenuation and scatter correction performance. The noise (%STD) in the uniform region indicates the SNR performance. In order to measure the uniformity, the NEMA NU 4-2008 standard requires to draw a 22.5 mm diameter and 10 mm long cylindrical volume of interest (VOI) over the center of the uniform region of the small animal phantom. The average activity concentration, the maximum and minimum values, and the %STD inside the VOI should be measured. The %STD is calculated as the standard deviation divided by the mean value of the VOI multiplied by 100%.

The *recovery coefficient* (RC) can be defined as a contrast, i.e. the measured activity concentration divided by the actual activity concentration. The RCs measured in the hot rods included in a dense volume without any background activity indicate the spatial resolution of the scanner. The RCs should be calculated for each of 5 hot rods. The image slices that cover the central 10 mm length of the rods should be averaged to get a single slice of lower noise. Then, circular ROIs should be drawn around each averaged rod with diameters twice the physical diameter of the rods. The maximum values in each of the ROIs should be measured. Then, five line profiles along the rods in the axial direction should be created. The line profiles must go through the voxels with the maximum values. The voxel values measured along each line profile, divided by the mean activity concentration found in the uniformity test should be used to calculate the mean and the %STD of the RC for each hot rod. The %STD of the RCs ($\%STD_{RC}$) should be calculated using the following formula:

$$\%STD_{RC} = 100 \cdot \sqrt{\left(\frac{STD_{line\ profile}}{Mean_{line\ profile}}\right)^2 + \left(\frac{STD_{Uniformity}}{Mean_{Uniformity}}\right)^2} \tag{7.11}$$

The *spill-over ratio* (SOR) is the activity concentration in cold regions relative to the mean activity concentration in the hot background. The SOR values measured in the cold regions that are inside hot background activity indicate the scatter correction performance. In order to calculate SOR values, VOIs of 4 mm in diameters and 7.5 mm in length should be drawn in the water- and air-filled cylindrical inserts. The ratio of the mean in each cold insert to the mean found in the uniformity test gives SOR values. The %STD of the SORs ($\%STD_{SOR}$) should be calculated as follows:

$$\%STD_{SOR} = 100 \cdot \sqrt{\left(\frac{STD_{SOR}}{Mean_{SOR}}\right)^2 + \left(\frac{STD_{Uniformity}}{Mean_{Uniformity}}\right)^2} \tag{7.12}$$

7.5.1.2 Simulation approach, results, and comparison

The image quality of VIP is evaluated for different reconstruction algorithms in order to compare their performance. The used algorithms are 2-D FBP, OSEM, and LM-OSEM. For the image quality evaluation the best images (that have the minimum value of the average MSE) of the NEMA NU 4-2008 small animal phantom obtained in the section 7.1 are used (Figure 7.3). The collected 10 million coincidences correspond to ∼2 minutes acquisition time, that is 10 times shorter than the acquisition time required by the protocol. For each reconstruction algorithm the pixel size is 0.25 mm and the slice thickness is 2 mm. No attenuation, scatter or random corrections are applied to any image. Since the data come from the simulation, no normalization is necessary. For the NEMA NU 4-2008 image quality merits calculation, a C++ code program is developed. It reads the images in the interfile format [184] and computes the all parameters according to the NEMA NU 4-2008 standard procedure. The merits values for each reconstruction algorithm are summarized in Table 7.3. Table 7.3 shows that the images reconstructed with the 2-D FBP and the LM-OSEM methods have the highest contrast. The 2-D FBP algorithm gives the lowest level of noise. Thus, the 2-D FBP algorithm

Table 7.3: Image quality parameters of the phantom data obtained with VIP-PET and reconstructed by different algorithms

Parameter	FBP cut-off = 0.15	OSEM 2 iterations	LM-OSEM 4 iterations
RC(%STD) 1 mm	0.3(12.7%)	0.053(19.7%)	0.28(22.1%)
RC(%STD) 2 mm	0.796(11.1%)	0.088(22.8%)	0.8(23.4%)
RC(%STD) 3 mm	1.2(10.1%)	0.14(19.4%)	1.0(26.8%)
RC(%STD) 4 mm	1.2(10.2%)	0.2(20.5%)	1.0(26.7%)
RC(%STD) 5 mm	1.19(10.8%)	0.17(20.8%)	0.85(29.8%)
Uniformity max.	4.66	0.0117	284
Uniformity min.	2.08	0.002	6.34
Uniformity mean	3.44	0.004	34.6
Uniformity %STD	9.74%	10.5%	16.99%
SOR(%STD) water	0.025(18.9%)	0.51(12.6%)	0.22(21.4%)
SOR(%STD) air	0.035(19.7%)	0.5(14.9%)	0.22(18.2%)

with the Hamming filter and the cut-off frequency of 0.15 gives the best image quality in term of higher contrast, lower noise, and better uniformity. The OSEM algorithm produce images of inferior quality when compared to FBP and LM-OSEM. In this case additional optimization and the data correction are necessary to obtain better quality images.

The comparison of the reconstructed images of the VIP, Inveon, LabPET-8^{TM} scanners are presented in Figures 7.11. A comparison of the RC values obtained for the three scanners is shown in Figure 7.12. Overall, the images obtained with the VIP scanner show better contrast and comparable noise with respect to the other scanners. As expected, the three scanners have similar imaging performance in the absence of dense scattering volume around the image target.

7.5.1.3 Small animal phantom in water sphere

The VIP scanner is designed to achieve images of very high quality in challenging conditions as, for instance, the imaging of a human head. Therefore, the system is expected to be relatively immune from scattered events contamination with no deterioration of the imaging performance in the presence of a dense scattering volume between the emitting source and the scanner ring. For this reason, an additional test with the NEMA NU 4-2008 small animal phantom is performed. In this test, the phantom is placed into a water sphere with a radius of 150 mm. A total of 10 million coincidence sinograms are collected to reconstruct the image for a total 3.7 MBq activity in the FOV.

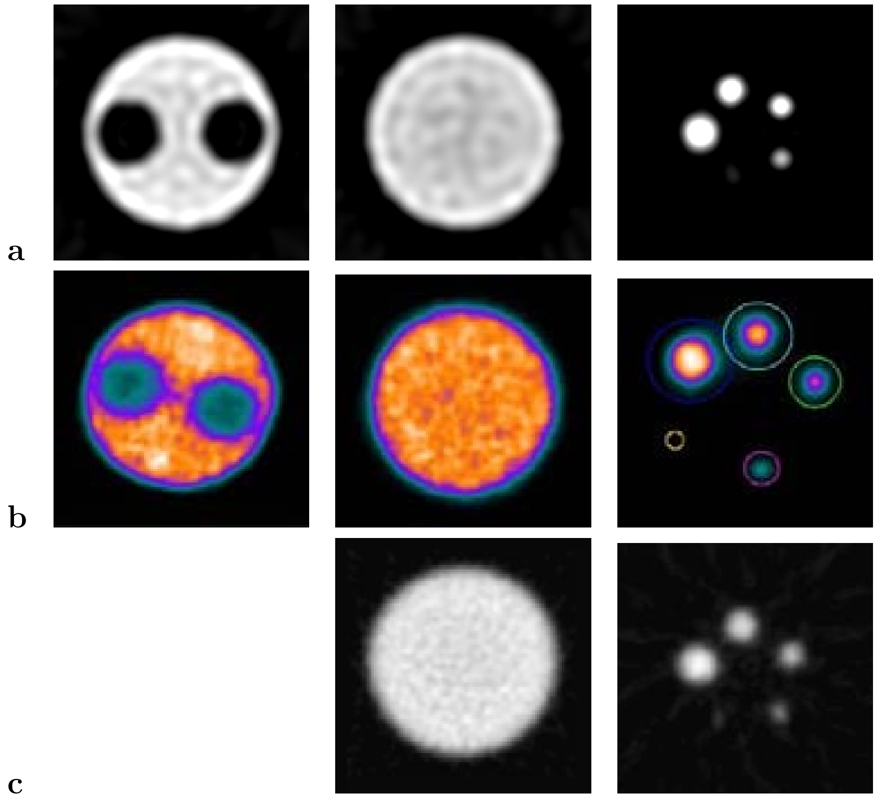

FIGURE 7.11: **a:** VIP. Small animal phantom reconstructed with 2-D FBP. **b:** LabPET-8^{TM}. Small animal phantom reconstructed with 2-D MLEM. The figure is taken from [177]. **c:** Inveon DPET. Small animal phantom reconstructed with 2-D FBP. The figure is taken from [176].

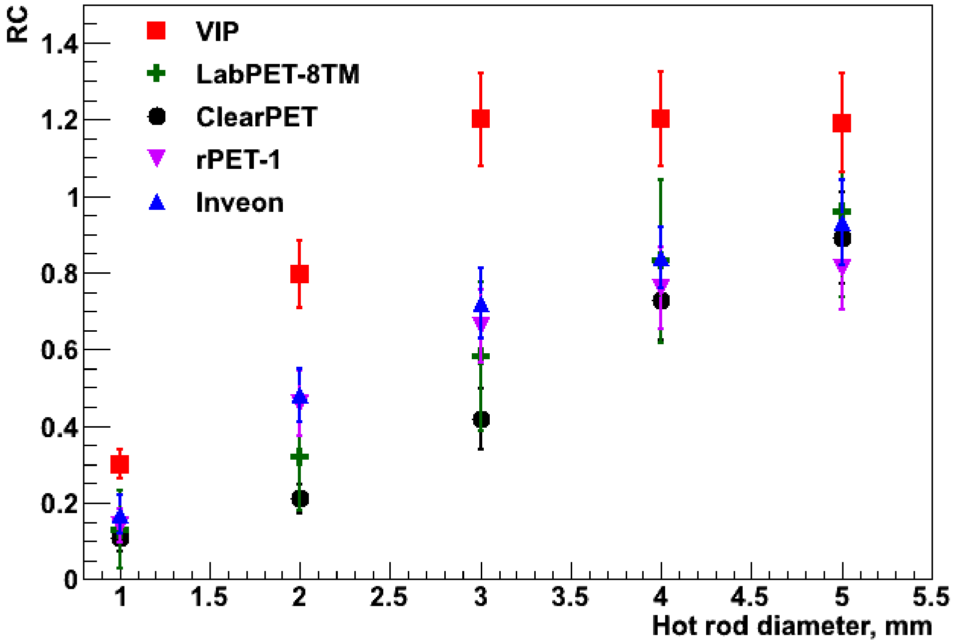

FIGURE 7.12: Comparison of RC of five rods of different size ranging between 1 and 5 mm for 5 different scanners.

The image is reconstructed with the 2-D FBP algorithm. Neither attenuation, scatter, random corrections, nor normalization is applied. The pixel size is 0.25 mm and the slice thickness is 2 mm. A generalized Hamming window with 0.15 cutoff frequency relative to Nyquist frequency is used for filtering in order to limit the amplification of statistical noise. Figure 7.14 presents the reconstructed images of the hot rods, uniform region, and cold inserts with corresponding activity line profiles. The RCs for each rod, the minimum, the maximum and the mean uniformity values of the center part of the phantom, and the SOR of the two cold regions are summarized and compared in Table 7.4. The image quality parameters obtained for the standard test are the one with the phantom in air are very similar. Nevertheless, one should keep in mind that the VIP ring is at least three times larger in diameter than a typical small animal PET.

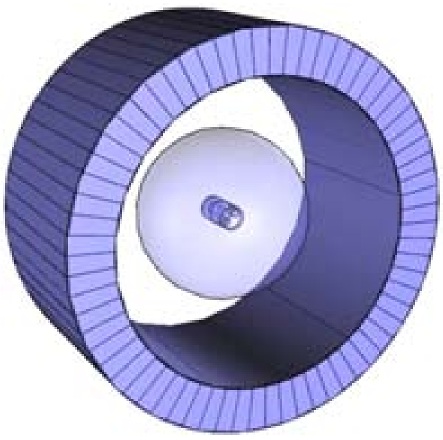

Figure 7.13: NEMA NU 4-2008 phantom placed in water sphere with radius of 150 mm. The contamination from the scattered events is significantly increased.

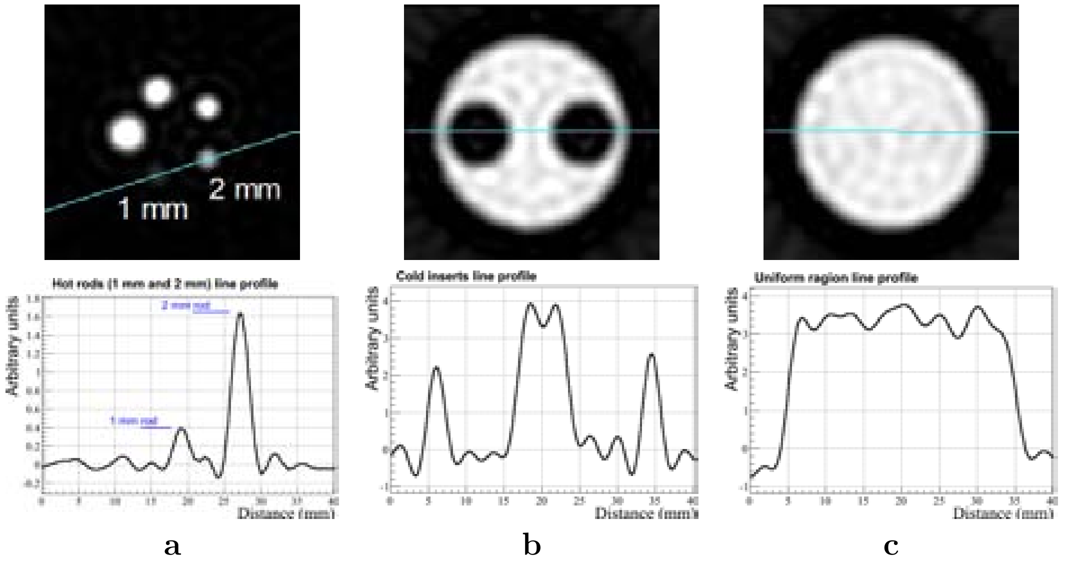

Figure 7.14: Reconstructed images of the NEMA NU 4-2008 phantom placed inside a non-radioactive water sphere. Corresponding activity line profiles along the 1 mm and 2 mm hot rods region (**a**), the cold inserts region (**b**), the uniform region (**c**).

The comparison of the two images in Figures 7.14 and 7.3(a) as well as the parameters from Table 7.4, **show no significant deterioration of the VIP image quality in the presence of a dense scattering volume**. This is an important feature of the VIP scanner, not achievable by standard devices based on scintillating crystals. This is due to the excellent energy resolution of CdTe and the resulting very narrow energy acceptance window.

Table 7.4: VIP image quality parameters comparison for NEMA NU 4-2008 phantom placed in air and in water

Parameter	In air	In water
RC(%STD) 1 mm	0.3(12.7%)	0.31(19.1%)
RC(%STD) 2 mm	0.796(11.1%)	0.77(10.3%)
RC(%STD) 3 mm	1.2(10.1%)	1.2(10.5%)
RC(%STD) 4 mm	1.2(10.2%)	1.2(10.2%)
RC(%STD) 5 mm	1.19(10.8%)	1.17(10.1%)
Uniformity max.	4.66	4.49
Uniformity min.	2.08	2.25
Uniformity mean	3.44	3.41
Uniformity %STD	9.74%	8.95%
SOR(%STD) water	0.025(18.9%)	0.052(37.4%)
SOR(%STD) air	0.035(19.7%)	0.069(51.8%)

7.5.2 Big torso phantom analysis

7.5.2.1 Method

According to the NEMA NU 2-2001 standard, the big torso phantom should be simulated for the image quality evaluation of WB PET systems. The torso phantom consists of three parts: a body, a lung insert, and six fillable spheres of various sizes that are placed inside the body. Figure 7.15 shows a general view of a real torso phantom used for WB PET systems.

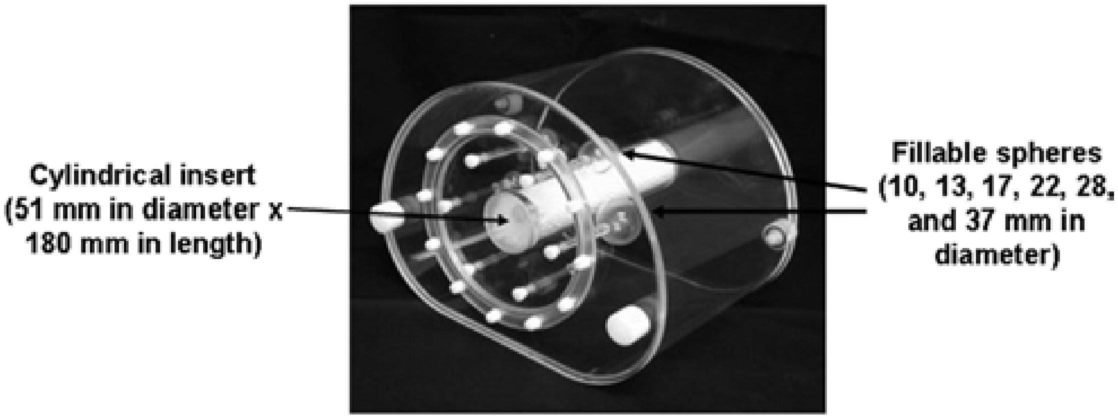

Figure 7.15: NEMA NU 2-2001 torso phantom for the image quality evaluation of WB PET systems. The figure is taken from [185].

According to the NEMA NU 2-2001 protocol, the body should have at least 180 mm in interior length. Its external height is 230 ± 1 mm and the longest radius is 150 ± 1 mm.

The lung insert is necessary to simulate the attenuation of lung. It is a cylinder with outside diameter of 50 ± 2 mm, wall thickness less than 4 mm and length equal to the length of the body. The insert is filled with a low atomic material with of an average density equal to 0.3 ± 0.1 g/cm^3. It should be centered inside the body as shown in Figure 7.15.

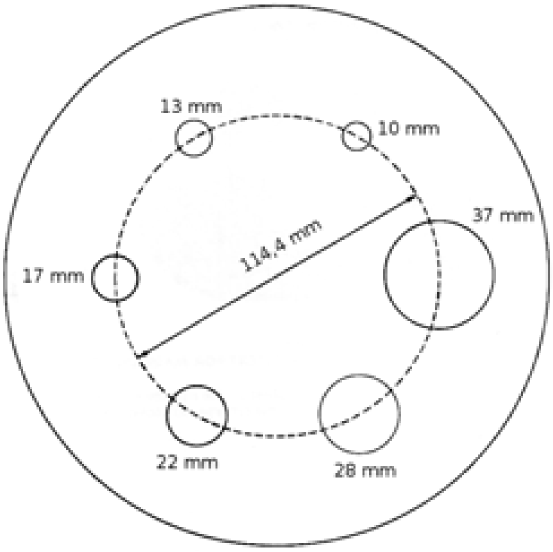

FIGURE 7.16: Transaxial positions of the six fillable spheres in the body of the torso phantom. The figure is taken from [163].

The six fillable spheres have internal diameters 10, 13, 17, 22, 28, and 37 mm and wall thicknesses of ≤ 1 mm. The centers of the all spheres should be placed at the 68 mm distance from the body back wall, so that the centers are axially in the same transverse slice (Figure 7.15). Transaxially, the centers of the spheres should be placed at a radius of 5.72 cm from the center of the body (Figure 7.16). NEMA NU 2-2001 requires to place the center of the 17 mm diameter sphere along the horizontal axis of the body.

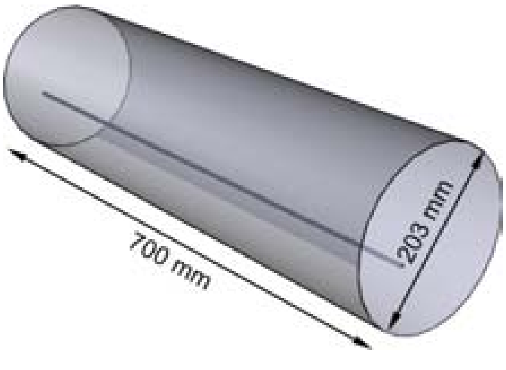

FIGURE 7.17: The test phantom with a radioactive line source inside, used for the NEMA NU 2-2001 torso phantom analysis.

The body of the phantom should be filled with ^{18}F radioactive water with activity concentration of 5.3 kBq/cm^3 ± 5% at the start of imaging. This activity concentration corresponds to a typical injected dose for WB studies (370 MBq per 70,000 cm^3). The phantom should be placed inside the FOV of the scanner along its axial direction, such that the centers of the spheres are at the axial center of the scanner (± 3 mm) and positioned transaxially so that the transaxial center of the phantom is in the transaxial center of the FOV. The lung insert should not contain any activity inside of it. The two spheres with diameters of 37 mm and 28 mm should be filled with nonradioactive water for cold lesion imaging. The other four spheres of 22, 17, 13, and 10 mm in diameters should be filled with ^{18}F radioactive water for hot lesion imaging. The activity concentration in the four smallest spheres should be 8 times (for the first data acquisition) and 4 times (for the second data acquisition) higher than the background activity concentration in the body.

Additionally, to imitate the clinical situation of having activity outside the scanner, a long test phantom with a line source of certain activity should be also placed inside the FOV of the scanner (Figure 7.17). The line source is a polyethylene tube at $\geq$800 mm in length, with an inside diameter of 3.2 ± 0.2 mm and an outside diameter of 4.8 ± 0.2 mm. The central 700 ± 5 mm length should be filled with 116 MBq ^{18}F and put inside the 6.4 mm hole of a test phantom. The test phantom is a solid cylinder composed of polyethylene and has an outside diameter of 203 ± 3 mm and a length of 700 ± 5 mm. A hole of 6.4 ± 0.2 mm is drilled parallel to the central axis of the cylinder at a radial distance of 45 ± 1 mm. The test phantom should be placed at the head end of the body phantom abutting it (Figure 7.18).

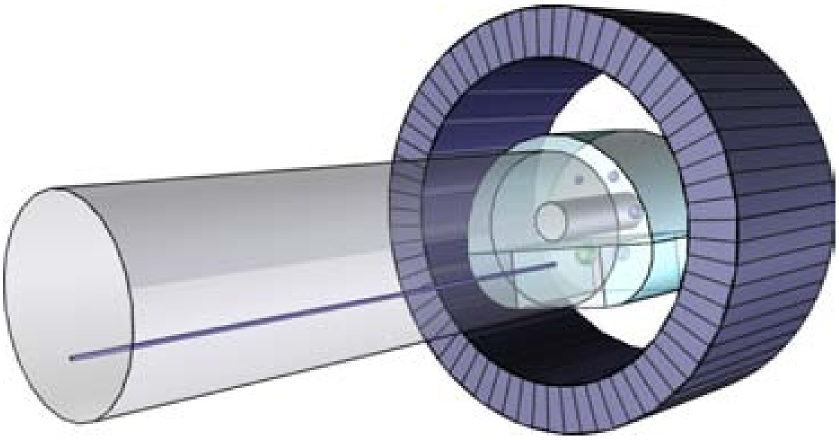

FIGURE 7.18: Position of the test phantom and torso phantom in the scanner s FOV according to the NEMA NU 2-2001.

The NEMA NU 2-2001 standard requires to calculate the data acquisition duration time as follows:

$$T_{T,E} = \frac{60\ min}{dist} \cdot axial\ step \tag{7.13}$$

where $T_{T,E}$ includes both emission and transmission scan durations and any other transition time (for moving the source, uploading data, e.t.c.), the $dist = 100$ cm, and the *axial step* is the distance the torso phantom is moved between positions in a WB study. The emission and transmission duration times should be recorded as well as the total axial imaging distance. The image should be reconstructed will applying all possible corrections.

For the image quality analysis, a slice centered on the hot and cold spheres should be used. NEMA NU 2-2001 requires to create circular ROIs around each sphere. The diameter of each ROI should be equal to the physical inner diameter of the sphere being measured. The ROI analysis tool should take into account partial pixels and allow to move the ROIs in increments of 1 mm or smaller.

ROIs should be also created in the background region of the torso phantom on the same plane that passes through the centers of the spheres. Twelve 37 mm in diameter ROIs should be drawn throughout the background at a distance of 15 mm from the edge of the phantom but no closer than 15 mm to any sphere. After, the following sets of circular ROIs should be created:

- 12 ROIs of 28 mm in diameters,
- 12 ROIs of 22 mm in diameters,
- 12 ROIs of 17 mm in diameters,
- 12 ROIs of 13 mm in diameters,
- 12 ROIs of 10 mm in diameters.

All these ROIs should be drawn concentric to the 37 mm in diameters background ROIs (Figure 7.19). The same procedure should be repeated on the slices as close as possible to ± 1 cm and ± 2 cm on either side of the central slice. Thus, the total of 60 background ROIs of each size (12 background ROIs of each size on each of 5 slices) should be created. The average counts in each ROI should be recorded.

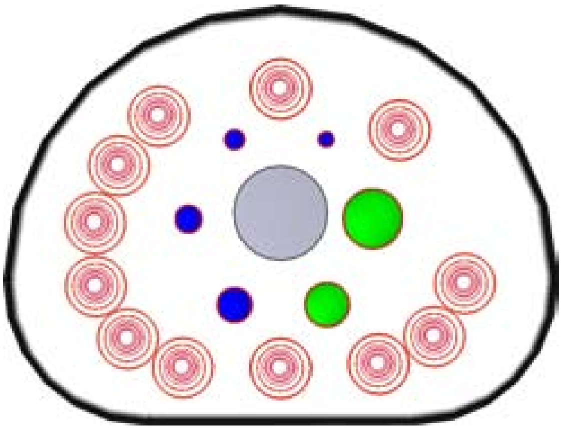

FIGURE 7.19: Positions of 72 background ROIs (red concentric circles) on the plane that passes through the centers of the spheres of the torso phantom. Green color indicates the positions of 2 cold spheres, and dark blue color indicates the positions of 4 hot spheres. Light blue color corresponds to the cold lung insert.

The contrast $Q_{H,j}$ for each hot sphere j is calculated, in percentage, as follows:

$$Q_{H,j} = \frac{C_{H,j}/C_{B,j} - 1}{a_H/a_B - 1} \cdot 100\% \tag{7.14}$$

Where $C_{H,j}$ is the average counts in the ROI for sphere j, $C_{B,j}$ is the average of the background ROI counts for sphere j, a_H is the activity concentration in the hot spheres, and a_B is the activity concentration in the background. The contrast $Q_{C,j}$ for each cold sphere j is calculated, in percentage, as follows:

$$Q_{C,j} = \left(1 - \frac{C_{C,j}}{C_{B,j}}\right) \cdot 100\% \tag{7.15}$$

Where $C_{C,j}$ is the average counts in the ROI for sphere j, $C_{B,j}$ is the average of the background ROI counts for sphere j. The background variability N_j for sphere j can be calculated, in percentage, as follows:

$$N_j = \frac{SD_j}{C_{B,j}} \cdot 100\% \tag{7.16}$$

Where SD_j is the standard deviation of the background ROI counts for sphere j. It is calculated as:

$$SD_j = \sqrt{\frac{\sum_{k=1}^{K}(C_{B,j,k} - C_{B,j})^2}{K-1}}, \; K = 60 \tag{7.17}$$

In order to calculate the accuracy of the attenuation and the scatter corrections, a circular ROIs with a diameter of 30 ± 2 mm should be centered on the lung insert on each image slice. The average pixel value in each ROI ($C_{lung,i}$) for each slice i should be measured. After, 12 circular background ROIs with diameters of 30 ± 2 mm should be created on each slice at the locations specified for the background ROIs mentioned in the previous paragraph. Average pixel values within these background ROIs ($C_{B,i}$) for each slice i should be found. In order to measure the residual error in scatter and attenuation corrections, the relative error (the difference between the expected count and the measured counts, expressed as a percentage) $\Delta C_{lung,i}$ for each slice i should be calculated as follows:

$$\Delta C_{lung,i} = \frac{C_{lung,i}}{C_{B,i}} \cdot 100\% \tag{7.18}$$

Where $C_{lung,i}$ is the average counts in the lung insert ROI, and $C_{B,i}$ is the average of the 60 37-mm background ROIs.

7.5.2.2 Simulation approach, results, and comparison

The phantom geometry was built using GAMOS software package mostly following the prescriptions of the NEMA NU2-2001 standard. As the protocol requires, it consists of a body, a lung insert and six spheres with various sizes that are placed inside the body. However, the shape and the size of the body is changed. The cylindrical shape of the body, instead of the torso-like one that the NEMA protocol requires, was chosen to simplify the simulation of the torso phantom in GAMOS (Figure 7.20). Additionally, the body, the spheres and the lung insert do not have any plastic walls, so the phantom consists only of water and a material of human lungs density. The simulated body s diameter is 240 mm, it has a length of 180 mm and it is made of ^{18}F radioactive water of total ~39 MBq background activity (corresponds to 5.3 kBq/cm^3). The lung insert is made of human lung material with density of 1.05 mg/cm^3. The simulated human lung material consists of 10.3% of hydrogen, 10.5% of carbon, 3.1% of nitrogen, 74.9% of oxygen, 0.2% of phosphorus, 0.2% of sodium, 0.3% of sulphur, 0.3% of chlorine, and 0.2% of potassium. Inside the phantom there are 4 spheres with diameters of 22, 17, 13 and 10 mm filled with ^{18}F radioactive water of hot activity and 2 cold spheres with diameters of 37 and 28 mm filled with nonradioactive water. All the spheres are placed at 70 mm from the front wall of the phantom.

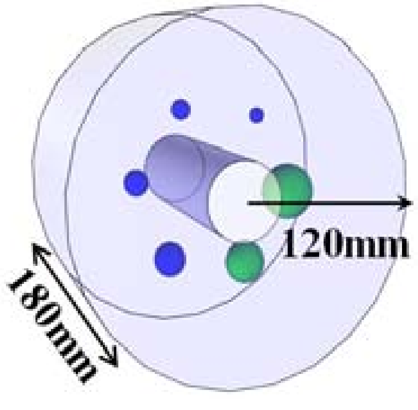

Figure 7.20: The simulated torso phantom. The green spheres are filled with non-radioactive water and the blue ones are filled with radioactive water. Center insert is made of human lung material and does not have any activity.

The simulation is performed with hot spheres to background activity ratios of 8:1 and 4:1 as NEMA NU 2-2001 standard requires. In both cases 10 million coincidence sinograms have been collected to reconstruct the image. The image is reconstructed using the OSEM algorithm. The OSEM algorithm is chosen because the STIR package provides data attenuation correction for it. Since the torso phantom is big, attenuation of photons greatly distorts the image. Thus, despite OSEM shows the worst results obtained in section 7.1 and 7.3, the qualities of the FBP and LM-OSEM images reconstructed without the correction for photon attenuation are much worse.

The sinogram pixel size is set to 0.75 mm. The optimal pixel size for the VIP-PET scanner is 0.25 mm. However, in this test, a relatively small number of coincidences was used to reconstruct the image. Thus, a bigger image pixel size is chosen in order to increase the SNR of each individual pixel (Eq. 3.13). The slice thickness is 2 mm and the matrix size is 401 × 401.

The image quality was evaluated after 40 iterations using only 1 subset. These numbers of the iterations and the subsets have shown the best result. The 3-D median filter is used for the image smoothing.

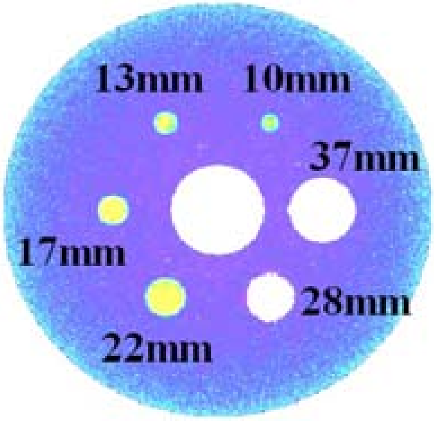

FIGURE 7.21: ^{18}F activity distribution of the simulated torso phantom.

To quantify the image quality, ROIs with diameters equal to the physical inner diameters of the spheres are drawn on the spheres and throughout the background. Six background ROIs are drawn in the central slice, as well as in slices ± 10 mm and ± 20 mm away, for a total 30 background ROIs of each size. All image quality parameters for both concentration ratios are computed following the NEMA NU2-2001 prescription.

Figure 7.21 shows the ^{18}F activity distribution of the simulated NEMA NU2-2001 torso phantom. Figure 7.22 shows a representative image of the torso phantom from the study with 8:1 (a) and 4:1 (b) ratio of the hot spheres to background activity. The line profiles for the 2 smallest hot spheres for both studies are demonstrated in Figure 7.23. The NEMA NU2-2001 image quality parameters are summarized in Table 7.5.

As can be seen, in both cases the smallest hot sphere is clearly visible. The image quality analysis shows that the VIP scanner produces low background variation and high cold and hot contrasts even in the more challenging condition of 4:1 hot spheres to background ratio. The VIP scanner provides very low values of ΔC_{lung} corresponding to almost no residual reconstructed radioactivity concentration in the lung insert.

These results become more significant if one takes into account the small number of coincidences that were used to reconstruct the image and the use of not optimal reconstruction method.

The comparison is done using the real measurements of four Siemens ECAT PET scanners: HR+, EXACT, ACCEL, and EMERGE [186]. ECAT EXACT and ECAT HR+ are based on BGO detectors with dimensions of 6.75 × 6.75 × 20 mm^3 and 4.05 × 4.39 × 30 mm^3 respectively. ECAT ACCEL and ECAT EMERGE, use LSO crystals with dimensions of 6.45 × 6.45 × 25 mm^3 each one. The four scanners have the same transverse FOV of 583 mm. The EXACT, ACCEL, and EMERGE have the same

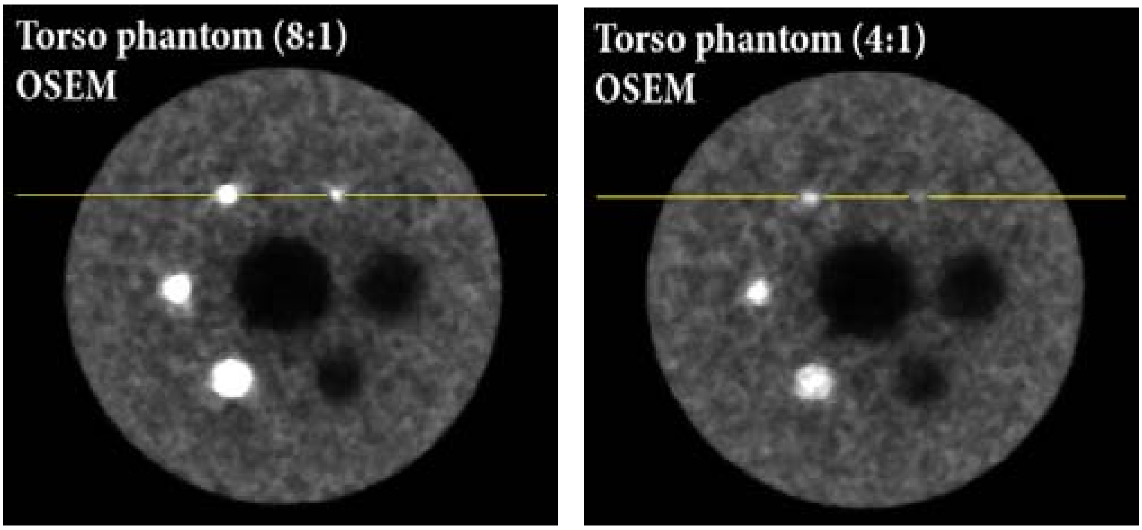

a **b**

FIGURE 7.22: Torso phantom reconstructed images. The hot spheres to background activity ratio is **a**: 8:1, and **b**: 4:1. Both images are reconstructed with 10 million coincidence sinograms.

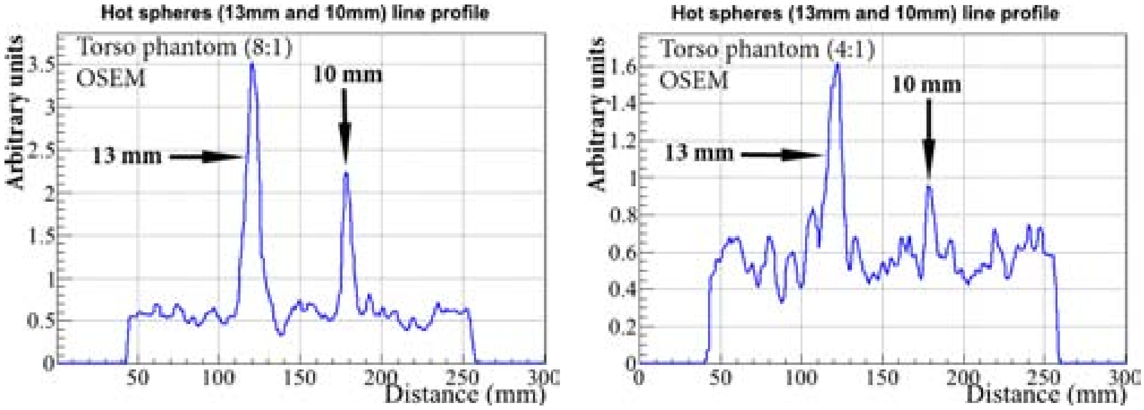

a **b**

FIGURE 7.23: Corresponding activity line profiles along the 13 mm and 10 mm hot spheres. The hot spheres to background activity ratio is **a**: 8:1, and **b**: 4:1.

TABLE 7.5: Image quality parameters of reconstructed torso phantom image obtained with VIP PET

		8:1	**4:1**		**8:1**	**4:1**
37mm	Cold cont.	73.1%	73.9%	Backg.var.	3.0%	2.8%
28mm	Cold cont.	64.2%	60.6%	Backg.var.	4.5%	3.7%
22mm	Hot cont.	66.6%	24.9%	Backg.var.	5.8%	4.3%
17mm	Hot cont.	55.3%	21.5%	Backg.var.	6.9%	4.9%
13mm	Hot cont.	38.8%	13.6%	Backg.var.	8.0%	5.8%
10mm	Hot cont.	20.7%	5.6%	Backg.var.	9.4%	7.4%
Aver.	ΔC_{lung}	6.6%	6.1%			

axial FOV of 162 mm, while one of HR+ is 155 mm. For the NEMA NU 2-2001 image quality test all scanners were operated in 3-D data acquisition mode.

The 70-cm-long line source of the test phantom is filled with 35 MBq ^{18}F for the ACCEL system and with 90 MBq ^{18}F for the other three scanners. The background activity concentration of the torso phantom ranges from 2.8 to 7.5 kBq/cm^3. The cold lung insert is filled with unboiled noodles and has a density of 0.33 g/cm^3. The attenuation correction is applied for the data of each PET scanner. The images are reconstructed with the OSEM algorithm using 8 subsets and 2 iterations followed by a Gaussian filtering.

The main numbers resulting from the image quality test are summarized in Table 7.6, and the reconstructed images for all scanners are presented in Figure 7.24.

TABLE 7.6: Quality parameters of reconstructed torso phantom of four Siemens ECAT PET scanners

	Scanner							
Parameter Transverse FOV	**HR+ 583 mm**		**EXACT 583 mm**		**ACCEL 583 mm**		**EMERGE 583 mm**	
Hot Sphere/Backg.	**8:1**	**4:1**	**8:1**	**4:1**	**8:1**	**4:1**	**8:1**	**4:1**
Backg.var.(37mm),%	5.3	6.2	5.0	5.4	3.8	4.1	5.5	6.2
Backg.var.(10mm),%	10.6	13.4	9.2	9.8	5.1	4.9	13.7	11.6
Hot cont.(22mm),%	43.1	46.2	34.2	64.8	35.9	37.2	49.9	60.3
Hot cont.(10mm),%	12.6	1.4	6.0	13.7	7.2	1.1	4.9	20.8
Cold cont.(37mm),%	56.4	54.1	40.2	44.8	55.5	57.0	46.9	44.8
Aver. ΔC_{lung},%	34.3	34.0	40.7	42.3	47.8	44.3	28.7	29.9

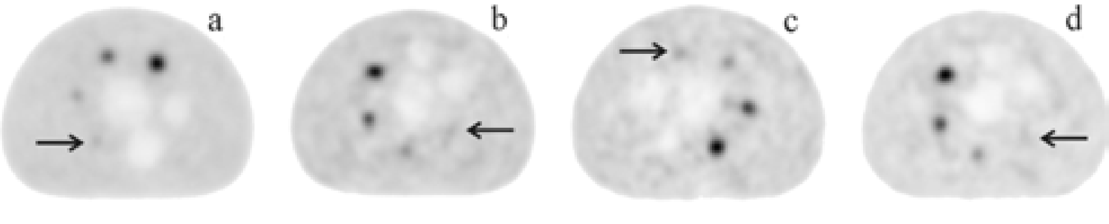

FIGURE 7.24: Transverse images of the torso phantom done with the hot sphere/background ratio of 8:1. The images show the section across the center of the spheres. **a**: ACCEL. **b**: EXACT. **c**: HR+. **d**: EMERGE. The 10 mm sphere is indicated by arrows. The figures are taken from [186].

The VIP scanner is clearly outperforming the results of the commercial devices. Higher contrast and lower background variation is observed in almost all cases, and it is especially significant if to consider the big difference in the number of coincidences used to produce the images. A simple calculation shows that the HR+ and EXACT scanners used about 200 million coincidences, and the ACCEL and EMERGE scanners collected about 100 million coincidences to reconstruct the image, whereas the VIP needs only

10 million coincidences to get the image of better quality. Taking into account the VIP sensitivity of 14.37 cps/kBq for a 700-mm-long line source, and high activity of the torso phantom (39 MBq), one can expect that total 10 million coincidences can be collected during ∼20 s acquisition time.

7.5.3 Modified torso phantom analysis

7.5.3.1 Method

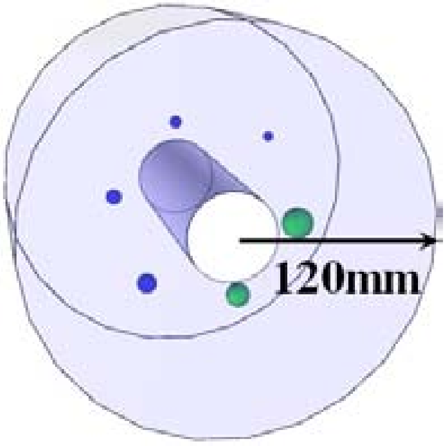

FIGURE 7.25: Simulated modified torso phantom. All sphere diameters are reduced by factor of 2.

The simulation of the torso phantom and the correspondent assessment of the reconstructed image quality is aimed to evaluate the performance of the WB scanners. For this reason, the imaging of the torso phantom is not optimal for a scanner meant for brain imaging such as the VIP. So, a modified torso phantom is simulated to provide more challenging conditions for a more stringent test of the image quality performance. In the modified phantom, diameters of all the spheres are reduced by a factor of 2 while keeping the other dimensions the same as in the torso phantom described in the previous section (Figure 7.25). The modified torso phantom is filled with ^{18}F radioactive water of activity concentration of ∼39 MBq. The test was performed with a hot spheres to background activity ratio of 8:1. The image quality parameters are computed the same way as the NEMA NU 2-2001 standard requires.

7.5.3.2 Simulation approach, results, and comparison

A total of 30 million coincidence sinograms have been collected for the OSEM reconstruction. The sinogram pixel size is set to 0.75 mm, the axial slice thickness is 2 mm and the matrix size is 401 × 401. The attenuation correction was applied. The image quality was evaluated after 80 iterations using only 1 subset. The median filter was used to reduce the noise. Figure 7.26 shows the activity distribution in the modified torso phantom and the diameters of the hot and cold spheres that were used for image analysis. The image was reconstructed with the OSEM algorithm. Figure 7.27(a) shows the reconstructed image that corresponds to the study with 8:1 hot spheres to background activity. The reconstructed activity for all spheres, but 5 mm, is well above the background. Because of the little statistics of this test, the reconstructed activity of the 5 mm diameter sphere is at the level of the background fluctuations.

All NEMA NU2-2001 image quality parameters are presented in Table 7.7. As expected, the results show a deterioration of the contrast with decreasing sphere diameter and the corresponding increasing of the background variability. Despite the low contrast values for the smallest hot sphere, the line profile in Figure 7.27(b) clearly shows enhanced activity in correspondence to its position.

For the detection of small lesions and/or small size metabolism of a brain when there is background activity, the much bigger number of coincidences and the optimization of the reconstructed parameters are necessary. Nevertheless the ability of the VIP scanner to locate such small hot objects in the warm background using a small number of coincidences shows its excellent potential in terms of spatial resolution and image contrast.

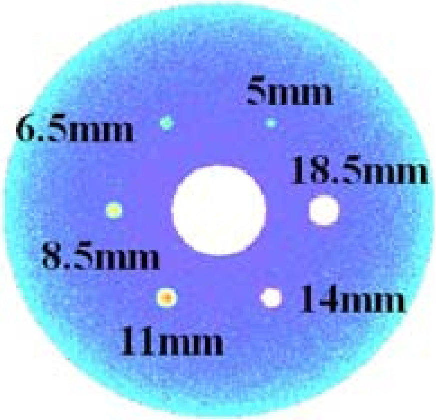

FIGURE 7.26: ^{18}F activity distribution in the modified torso phantom.

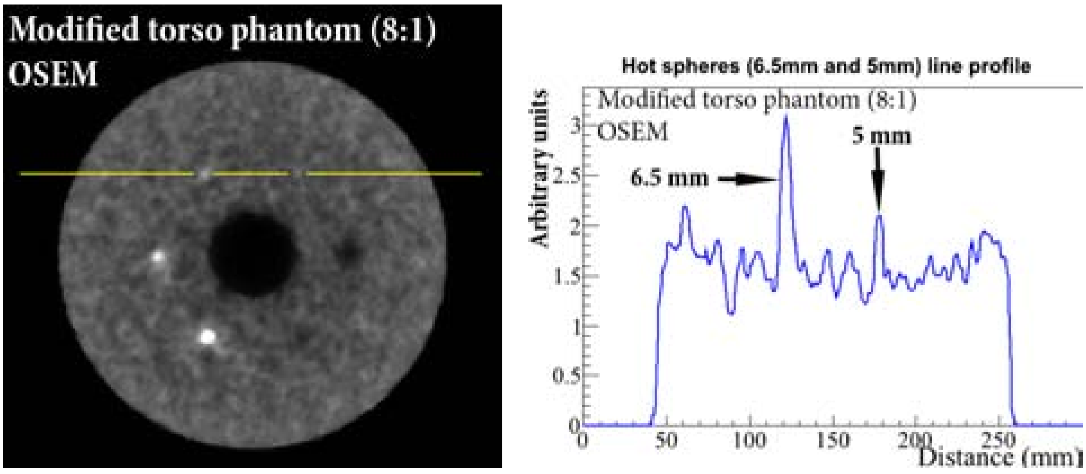

a **b**

FIGURE 7.27: **a**: reconstructed image of the modified torso phantom. **b**: corresponding activity line profiles along the 6.5 mm and 5 mm hot spheres.

Table 7.7: Image quality parameters of reconstructed modified torso phantom obtained with VIP PET

		8:1		**8:1**
18.5mm	Cold cont.	52.4%	Backg.var.	3.9%
14mm	Cold cont.	34.8%	Backg.var.	5.5%
11mm	Hot cont.	27.2%	Backg.var.	6.8%
8.5mm	Hot cont.	16.6%	Backg.var.	8.0%
6.5mm	Hot cont.	8.8%	Backg.var.	9.2%
5mm	Hot cont.	2.6%	Backg.var.	10.0%
Aver.	ΔC_{lung}	2.1%		

7.6 Simulation and image reconstruction of real 3-D human head phantom

7.6.0.3 Method

In order to assess the expected imaging VIP performance in pseudo-clinical conditions, a realistic 3-D human brain phantom is simulated. The brain phantom is created using GEANT4 from a set of 20 DICOM files [187] representing the voxelized digital images of 20 axial slices of a real brain obtained with a CT scan. It contains about 1 million voxels. Each voxel represents different human head material such as gray matter, white matter, water, skull, skin etc. Each material has a density corresponding to typical values for adults. The phantom is filled with ^{18}F radioactive source of 111 MBq total activity that is 30% of a typical injected dose for body studies (370 MBq). The gray matter to white matter specific activity ratio is 3:2, corresponding to a realistic distribution in case of studies with ^{18}F positron source [90]. 100 million total coincidences are collected. The image was reconstructed using 2-D FBP method without applying any data correction. The pixel size is 0.89 mm and the slice thickness is 6.83 mm. These dimensions were chosen to be the same as corresponding dimensions of the DICOM image voxels.

7.6.0.4 Results

An example of one DICOM file is shown in Figure 7.28(a). The Figure 7.28(b) demonstrates a slice of the simulated 3-D phantom that corresponds to this DICOM image. The brighter gray regions correspond to higher ^{18}F metabolism. The resulting image reconstructed using FBP is presented in Figure 7.28(c). The result does not include the attenuation correction. The figure represents the chosen brain slice (the same one as in Figures 7.28(a) and 7.28(b)) after scanning the whole reconstructed phantom. The brain structure and its ^{18}F metabolism are clearly visible from the simulation results.

Though, the obtained result (Figure 7.28c) is very good, this test is under estimating the performance capability of the VIP scanner. The test was not carried out at the optimized dose of 32 MBq (see section 6.8.1), and the attenuation correction was not applied for the reconstructed data.

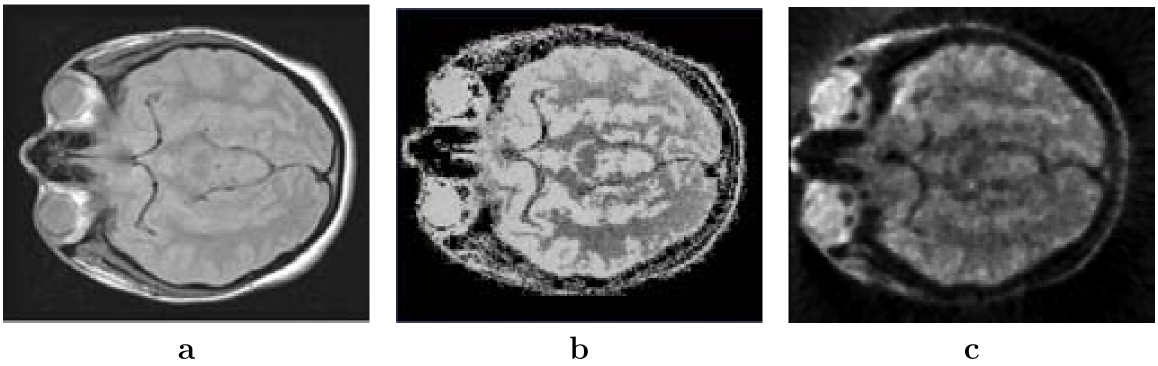

FIGURE 7.28: **a:** example of one DICOM file. **b:** a slice of the simulated 3-D brain phantom corresponding to the DICOM file on the left. **c:** the same slice as one on the left after the whole brain reconstruction.

Chapter 8

Conclusions

The VIP project is under development and the results presented in this thesis are based on simulation using GAMOS software package. The assumptions and the parameters that were used for the VIP PET simulation at the level of physics, geometry, and electronics are from the technical design of the VIP scanner and from the lab tests for the case of the CdTe detectors and VIP-PIX ASIC. In order to assess the quality of the simulation, the Siemens ECAT HRRT PET scanner was simulated and its performance was tested. The results obtained in the section 6.4 show good agreement with the experimental data collected by ECAT HRRT PET. Additionally, to make our results more robust, the VIP PET scanner simulation was repeated assuming some defects in the VIP geometry and electronics. The results of this test shows the big impact on the SF and the total sensitivity (section 6.4). However, the overall performance of the VIP scanner in such a worst case scenario stays considerably good.

The counting and the image quality performance of the simulated VIP scanner was completely characterized using the NEMA NU 4-2008 and NEMA NU 2-2001 protocols. Additionally, the scanner was tested in pseudo-clinical conditions with the simulation of the screening of a real human head.

The crack-free geometry of the VIP scanner with a stopping power of 4 cm CdTe provides a sensitivity of 14.37 cps/kBq (according to NEMA NU 2-2001 standard). A very low scatter fraction is achieved due to the good energy resolution provided by the CdTe detectors. The high number of channels in the VIP scanner (450 channels/cm3) makes the full system less affected by the dead time of the individual detector voxels. This effect, together with the good energy resolution, leads to a very good NEC rate. The calculated NEC peak values are 908 kcps at 1.6 MBq/mL for the NEMA NU 4-2008 mouse phantom, and 122 kcps at 5.3 kBq/mL for the NEMA NU 2-2001 test. The high sensitivity together with the virtually noise-free data acquisition allows to dramatically reduce the scan time and thereby reduce the image blurring due to the motion of the patient. On the other hand, the patient dose can be significantly reduced while keeping the time of the screening the same. It permits to perform a large number of consecutive low-dose scans in order to control and accurately follow the disease treatment or the drug development.

Tests based on both NEMA NU 2-2001 and NEMA NU 4-2008 standards show excellent spatial resolution ($\sim$1 mm) in the FOV center. Nowadays, such a good spatial resolution is achievable only by small pre-clinical state-of-the-art PET scanners. Moreover, simulated images acquired with the VIP are generally characterized by high contrast and low noise, and are obtained with a very small number of coincidences. The system is shown in simulations to be capable to detect down to 1 mm diameter hot rods without background activity down to 5 mm diameter hot spheres in the presence of background activity with only few seconds scan time needed to get good quality images. No deterioration of the image quality is observed in the presence of a dense scattering volume between the imaged source and the VIP scanner. This effect is again due to the excellent energy resolution of CdTe and the resulting very narrow energy acceptance window. This is a unique feature of the VIP scanner, not achievable by standard devices based on scintillating crystals.

The cutting edge potential of the VIP design is finally proven by the results of the simulation of the screening of a real human head. Despite the use of not optimal dose (111 MBq instead of 32 MBq), the data without the attenuation correction, and, finally, challenging condition represented by the high density of the brain material and the small variation of the sugar uptake in different regions of the brain, the brain structure are neatly visible in the reconstructed images.

Though the VIP team is aware of the big engineering challenge of translating the simulation findings into a real working device, the results of this study are very promising and show the high potential of the VIP concept for the future PET generation.

In conclusion, it has been proven that the VIP novel design has the potential to revolutionize the PET technique by providing unprecedented high-resolution/high-sensitivity images. Simulation results presented in this thesis are driving the development and the optimization of a fully operative prototype that will prove the feasibility of the VIP concept.

Bibliography

[1] E. Mikhaylova, G. De Lorenzo, M. Chmeissani, M. Kolstein, M. Canadas, P. Arce, Y. Calderon, D. Uzun, G. Arino, J.G. Macias-Montero, R. Martinez, C. Puigdengoles, and E. Cabruja. Simulation of the expected performance of a seamless scanner for brain PET based on highly pixelated CdTe detectors. *Medical Imaging, IEEE Transactions on*, 33(2):332 339, February 2014. URL `http://ieeexplore.ieee.org/stamp/stamp.jsp?tp=&arnumber=6620952&isnumber=6729093`.

[2] P. A. M. Dirac. The quantum theory of the electron. *Proceedings of The Royal Society*, 117(778):610 624, February 1928. URL `http://rspa.royalsocietypublishing.org/content/117/778/610.full.pdf+html`.

[3] P. A. M. Dirac. Quantised singularities in the electromagnetic field. *Proceedings of The Royal Society*, 133(821):60 72, September 1931. URL `http://rspa.royalsocietypublishing.org/content/133/821/60.full.pdf+html`.

[4] C. D. Anderson. The positive electron. *Physical Review*, 43(6):491 494, March 1933. URL `http://link.aps.org/doi/10.1103/PhysRev.43.491`.

[5] M. Charlton and J. W. Humberston. *Positron Physics.* Cambridge University Press, 2001.

[6] K. S. Krane. *Introductory Nuclear Physics.* Wiley, 1987.

[7] D. Griffiths. *Introduction to Elementary Particles.* Wiley, 2nd edition, 2008.

[8] H. Nishino and et al. (Super-Kamiokande Collaboration). Search for proton decay via $p \quad e^+\pi^0$ and $p \quad \mu^+\pi^0$ in a Large Water Cherenkov Detector. *Physical Review Letters*, 102:141801, April 2009. URL `http://link.aps.org/doi/10.1103/PhysRevLett.102.141801`.

[9] J. Cal-González, J. L. Herraiz, S. Espana, P. M. G. Corzo, J. J. Vaquero, M. Desco, and J. M. Udias. Positron range estimations with PeneloPET. *Physics in Medicine and Biology*, 58(15):5127 5152, 2013. URL `http://stacks.iop.org/0031-9155/58/i=15/a=5127`.

[10] Gopal B. Saha. *Basics of PET imaging. Physics, chemistry, and regulations.* Springer Science, 2005.

[11] URL `http://tech.snmjournals.org/cgi/content-nw/full/29/1/4/F1`.

[12] S. DeBenedetti, C. E. Cowan, W. R. Konneker, and H. Primakoff. On the angular distribution of two-photon annihilation radiation. *Physical Review*, 77(2):205 212, January 1950. URL `http://link.aps.org/doi/10.1103/PhysRev.77.205`.

[13] S. Berko and F. L. Hereford. Experimental studies of positron interactions in solids and liquids. *Reviews of Modern Physics*, 28:299 307, July 1956. URL `http://link.aps.org/doi/10.1103/RevModPhys.28.299`.

[14] A. P. Patro and P. Sen. Parapositronium lifetime. *Journal of Physics A: General Physics*, 4(6):856 858, 1971. URL `http://iopscience.iop.org/0022-3689/4/6/011/`.

[15] C. I. Westbrook, D. W. Gidley, R. S. Conti, and A. Rich. New precision measurement of the orthopositronium decay rate: A discrepancy with theory. *Physical Review Letters*, 58(13):1328 1331, March 1987. URL `http://link.aps.org/doi/10.1103/PhysRevLett.58.1328`.

[16] Y. Kataoka. *Test of bound state QED higher order correction: precision measurement of orthopositronium decay rate.* PhD thesis, University of Tokyo, March 2007. URL `http://tabletop.icepp.s.u-tokyo.ac.jp/oPs-life/main.final.pdf`.

[17] URL `http://www.nist.gov/pml/data/xcom/index.cfm`.

[18] D. L. Bailey, D. W. Townsend, P. E. Valk, and M. N. Maisey, editors. *Positron Emission Tomography. Basic Sciences.* Springer-Verlag, 2005.

[19] O. Klein and Y. Nishina. Uber die streuung von strahlung durch freie elektronen nach der neuen relativistischen quantendynamik von Dirac. *Zeitschrift für Physik*, 52(11 12):853 868, 1929. URL `http://dx.doi.org/10.1007/BF01366453`.

[20] URL `http://en.wikipedia.org/wiki/Ionization_chamber`.

[21] URL `http://en.wikipedia.org/wiki/Proportional_counter`.

[22] K. Kleinknecht. *Detectors for particle radiation.* Cambridge University Press, 1986.

[23] S. R. Cherry, J. A. Sorenson, and M. E. Phelps. *Physics in nuclear medicine.* Saunders, 3rd edition, 2003.

[24] URL `http://en.wikipedia.org/wiki/P-n_junction`.

[25] W. van Roosbroeck and W. Shockley. Photon-radiative recombination of electrons and holes in Germanium. *Physical Review*, 94(6):1558 1560, June 1954. URL `http://link.aps.org/doi/10.1103/PhysRev.94.1558`.

[26] T. Takahashi and S. Watanabe. Recent progress in CdTe and CdZnTe detectors. *Nuclear Science, IEEE Transactions on*, 48(4):950 959, August 2001. URL `http://ieeexplore.ieee.org/stamp/stamp.jsp?tp=&arnumber=958705&isnumber=20712`.

[27] J. J. Pedroso de Lima, editor. *Nuclear Medicine Physics*. Series in Medical Physics and Biomedical Engineering. CRC Press, Taylor and Francis Group, 2011.

[28] K. Hamacher, H. H. Coenen, and G. Stocklin. Efficient stereospecific synthesis of no-carrier-added 2-[^{18}F]-fluoro-2-deoxy-D-glucose using aminopolyether supported nucleophilic substitution. *Journal of Nuclear Medicine*, 27(2):235 238, February 1986. URL `http://jnm.snmjournals.org/content/27/2/235.long`.

[29] O. Warburg. On the origin of cancer cells. *Science*, 123(3191):309 314, February 1956. URL `http://www.sciencemag.org/content/123/3191/309.long`.

[30] M. Canadas Castro. *Aspectos metodológicos para la evaluación de sistemas de tomografía por emisión de positrones empleando técnicas Montecarlo, protocolos estandarizados y diferentes trazadores*. PhD thesis, Universidad Politécnica de Madrid, 2012. URL `http://oa.upm.es/14654/`.

[31] P. P. Bruyant. Analytic and iterative reconstruction algorithms in SPECT. *Journal of Nuclear Medicine*, 43(10):1343 1358, October 2002. URL `http://jnm.snmjournals.org/content/43/10/1343`.

[32] P. E. Kinahan, M. Defrise, and R. Clackdoyle. Analytic image reconstruction methods. In M. N. Wernick and J. N. Aarsvold, editors, *Emission Tomography: The Fundamentals of SPECT and PET*. Elsevier Academic Press, 2004.

[33] R. A. Powsner, M. R. Palmer, and E. R. Powsner. *Essentials of Nuclear Medicine Physics and Instrumentation*. Wiley-Blackwell, Oxford, 3rd edition, 2013.

[34] M. Lyra and A. Ploussi. Filtering in SPECT image reconstruction. *International Journal of Biomedical Imaging*, 2011:1 14, April 2011. URL `http://www.hindawi.com/journals/ijbi/2011/693795/abs/`.

[35] L. A. Shepp and Y. Vardi. Maximum likelihood reconstruction for emission tomography. *Medical Imaging, IEEE Transactions on*, 1(2):113 122, October 1982. URL `http://ieeexplore.ieee.org/xpls/abs_all.jsp?arnumber=4307558&tag=1`.

[36] H. M. Hudson and R. S. Larkin. Accelerated image reconstruction using ordered subsets of projection data. *Medical Imaging, IEEE Transactions on*, 13(4):601 609, December 1994. URL `http://ieeexplore.ieee.org/stamp/stamp.jsp?tp=&arnumber=363108&isnumber=8321`.

[37] S. J. Wilderman, N. H. Clinthorne, J. A. Fessler, C.-H. Hua, and W. L. Rogers. List mode EM reconstruction of Compton scatter camera images in 3-D. In *Nuclear Science Symposium Conference Record, 2000 IEEE*, volume 2, pages 15/292 15/295, 2000. URL `http://ieeexplore.ieee.org/stamp/stamp.jsp?tp=&arnumber=950123&isnumber=20551`.

[38] S. J. Wilderman, J. A. Fessler, N. H. Clinthorne, J. W. LeBlanc, and W. L. Rogers. Improved modeling of system response in list mode EM reconstruction of Compton scatter camera images. *Nuclear Science, IEEE Transactions on*, 48 (1):111 116, February 2001. URL `http://ieeexplore.ieee.org/stamp/stamp.jsp?tp=&arnumber=845842&isnumber=18330`.

[39] A. Sitek. Representation of photon limited data in emission tomography using origin ensembles. *Physics in Medicine and Biology*, 53(12):3201 3216, June 2008. URL `http://iopscience.iop.org/0031-9155/53/12/009/`.

[40] C. S. Levin and E. J. Hoffman. Calculation of positron range and its effect on the fundamental limit of positron emission tomography system spatial resolution. *Physics in Medicine and Biology*, 44(3):781 799, March 1999. URL `http://www.ncbi.nlm.nih.gov/pubmed/10211810`.

[41] J. Seidel, J. J. Vaquero, S. Siegel, W. R. Gandler, and M. V. Green. Depth identification accuracy of a three layer phoswich PET detector module. *Nuclear Science, IEEE Transactions on*, 46(3):485 490, June 1999. URL `http://ieeexplore.ieee.org/xpls/abs_all.jsp?arnumber=775567&tag=1`.

[42] A. Braem, M. Chamizo Llatas, E. Chesi, J. G. Correia, F. Garibaldi, C. Joram, S. Mathot, E. Nappi, M. Ribeiro da Silva, F. Schoenahl, J. Séguinot, P. Weilhammer, and H. Zaidi. Feasibility of a novel design of high resolution parallax-free Compton enhanced PET scanner dedicated to brain research. *Physics in Medicine and Biology*, 49(12):2547 2562, May 2004. URL `http://iopscience.iop.org/0031-9155/49/12/006/`.

[43] W. W. Moses. Fundamental limits of spatial resolution in PET. *Nuclear Instruments and Methods in Physics Research Section A: Accelerators, Spectrometers, Detectors and Associated Equipment*, 648, Supplement 1(0):S236 S240, 2011. URL `http://www.sciencedirect.com/science/article/pii/S0168900210026276`.

[44] W. W. Moses and S. E. Derenzo. Empirical observation of resolution degradation in positron emission tomographs utilizing block detectors. *Journal of Nuclear Medicine*, 34:101P, 1993. URL `http://cfi.lbl.gov/instrumentation/Pubs/JNM-34.pdf`.

[45] S. Weber, B. Gundlich, and M. Khodaverdi. Normalization factors for the ClearPET/spl trade/ Neuro. In *Nuclear Science Symposium Conference Record, 2005 IEEE*, volume 5, pages 2632 2635, October 2005. URL `http://ieeexplore.ieee.org/xpls/abs_all.jsp?arnumber=1596878`.

[46] E.J. Hoffman, T.M. Guerrero, G. Germano, W.M. Digby, and M. Dahlbom. PET system calibrations and corrections for quantitative and spatially accurate images. *Nuclear Science, IEEE Transactions on*, 36(1):1108 1112, February 1989. URL `http://ieeexplore.ieee.org/xpls/abs_all.jsp?arnumber=34613`.

[47] R. D. Badawi and P. K. Marsden. Developments in component-based normalization for 3D PET. *Physics in Medicine and Biology*, 44(2):571 594, February 1999. URL `http://www.ncbi.nlm.nih.gov/pubmed/10070802`.

[48] B. Bendriem and D. W. Townsend, editors. *The Theory and Practice of 3D PET*. Springer-Science, 1998.

[49] H. Zaidi and B. H. Hasegawa. Determination of the attenuation map in emission tomography. *Journal of Nuclear Medicine*, 44(2):291 315, February 2003. URL `http://jnm.snmjournals.org/content/44/2/291.long`.

[50] N. B. Smith and A. Webb. *Introduction to medical imaging : physics, engineering, and clinical applications*. Cambridge University Press, 2001.

[51] S. Siegel and M. Dahlbom. Implementation and evaluation of a calculated attenuation correction for PET. *Nuclear Science, IEEE Transactions on*, 39(4):1117 1121, August 1992. URL `http://ieeexplore.ieee.org/stamp/stamp.jsp?tp=&arnumber=159770&isnumber=4183`.

[52] M. Bergstrom, J. Litton, L. Eriksson, C. Bohm, and G. Blomqvist. Determination of object contour from projections for attenuation correction in cranial positron emission tomography. *Journal of Computer Assisted Tomography*, 6(2):365 372, April 1982. URL `http://www.ncbi.nlm.nih.gov/pubmed/6978896`.

[53] L. R. Carroll, P. Kretz, and G. Orcutt. The orbiting rod source: Improving performance in PET transmission correction scans. In P. D. Esser, editor, *Emission Computed Tomography: Current Trends*. Society of Nuclear Medicine, 1983.

[54] Hermann Ostertag, WolfgangK. Kubler, Josef Doll, and WalterJ. Lorenz. Measured attenuation correction methods. *European Journal of Nuclear Medicine*, 15 (11):722 726, 1989. URL `http://dx.doi.org/10.1007/BF00631764`.

[55] R.H. Huesman, S.E. Derenzo, J.L. Cahoon, A. B. Geyer, W.W. Moses, D. C. Uber, T. Vuletich, and T.F. Budinger. Orbiting transmission source for positron tomography. *Nuclear Science, IEEE Transactions on*, 35(1):735 739, February 1988. URL `http://ieeexplore.ieee.org/stamp/stamp.jsp?tp=&arnumber=12822&isnumber=545`.

[56] M.E. Daube-Witherspoon, R.E. Carson, and M.V. Green. Post-injection transmission attenuation measurements for PET. *Nuclear Science, IEEE Transactions on*, 35(1):757 761, February 1988. URL `http://ieeexplore.ieee.org/stamp/stamp.jsp?tp=&arnumber=12827&isnumber=545`.

[57] R. E. Carson, M. E. Daube-Witherspoon, and M. V. Green. A method for postinjection PET transmission measurements with a rotating source. *Journal of Nuclear Medicine*, 29(9):1558 1567, September 1988. URL `http://jnm.snmjournals.org/content/29/9/1558.long`.

[58] P. K. Hooper, S. R. Meikle, S. Eberl, and M. J. Fulham. Validation of post injection transmission measurements for attenuation correction in neurologic FDG PET studies. *Journal of Nuclear Medicine*, 37(1):128 136, January 1996. URL `http://jnm.snmjournals.org/content/37/1/128.long`.

[59] C. J. Thompson, N. Ranger, A. C. Evans, and A. Gjedde. Validation of simultaneous PET emission and transmission scans. *Journal of Nuclear Medicine*, 32 (1):154 160, January 1991. URL `http://jnm.snmjournals.org/content/32/1/154.long`.

[60] C. J. Thompson, N. T. Ranger, and A. C. Evans. Simultaneous transmission and emission scans in positron emission tomography. *Nuclear Science, IEEE Transactions on*, 36(1):1011 1016, February 1989. URL `http://ieeexplore.ieee.org/stamp/stamp.jsp?tp=&arnumber=34595&isnumber=1426`.

[61] S. R. Meikle, D. L. Bailey, P. K. Hooper, S. Eberl, B. F. Hutton, W. F. Jones, R. R. Fulton, and M. J. Fulham. Simultaneous emission and transmission measurements for attenuation correction in whole-body PET. *Journal of Nuclear Medicine*, 36 (9):1680 1688, September 1995. URL `http://jnm.snmjournals.org/content/36/9/1680.long`.

[62] S. R. Meikle, S. Eberl, P. K. Hooper, and M. J. Fulham. Simultaneous emission and transmission (SET) scanning in neurological PET studies. *Journal of Computer*

Assisted Tomography, 21(3):487 497, May June 1997. URL `http://www.ncbi.nlm.nih.gov/pubmed/9135664`.

[63] M. A. Lodge, R. D. Badawi, and P. K. Marsden. A clinical evaluation of the quantitative accuracy of simultaneous emission/transmission scanning in whole-body positron emission tomography. *European Journal of Nuclear Medicine*, 25 (4):417 423, 1998. URL `http://dx.doi.org/10.1007/s002590050240`.

[64] P. E. Kinahan, D. W. Townsend, T. Beyer, and D. Sashin. Attenuation correction for a combined 3D PET/CT scanner. *Medical Physics*, 25(10):2046 2053, October 1998. URL `http://www.ncbi.nlm.nih.gov/pubmed/9800714`.

[65] C. Bai, L. Shao, A. J. D. Silva, and Z. Zhao. A generalized model for the conversion from CT numbers to linear attenuation coefficients. *Nuclear Science, IEEE Transactions on*, 50(5):1510 1515, October 2003. URL `http://ieeexplore.ieee.org/stamp/stamp.jsp?tp=&arnumber=1239533&isnumber=27795`.

[66] V. Sossi, B. Pointon, P. Cohen, R. R. Johnson, and T.J. Ruth. Effect of shielding the radioactivity outside the field of view on image quality in a dual head coincidence [PET camera]. *Nuclear Science, IEEE Transactions on*, 47(4):1561 1566, August 2000. URL `http://ieeexplore.ieee.org/stamp/stamp.jsp?tp=&arnumber=873016&isnumber=18895`.

[67] E. J. Hoffman and M. E. Phelps. Positron emission tomography: principles and quantitation. In M. E. Phelps, J. Mazziotta, and H. Schelbert, editors, *Positron Emission Tomography and Autoradiography: Principles and Applications for the Brain and Heart*. Raven Press, 1986.

[68] S.R. Cherry and S-C Huang. Effects of scatter on model parameter estimates in 3D PET studies of the human brain. *Nuclear Science, IEEE Transactions on*, 42 (4):1174 1179, August 1995. URL `http://ieeexplore.ieee.org/stamp/stamp.jsp?tp=&arnumber=467730&isnumber=9846`.

[69] G. F. Knoll. *Radiation detection and measurement*. Wiley, 4th edition, 2010.

[70] E. J. Hoffman, S. C. Huang, and M. E. Phelps. Quantitation in positron emission computed tomography: 1. effect of object size. *Journal of Computer Assisted Tomography*, 3(3):299 308, June 1979. URL `http://www.ncbi.nlm.nih.gov/pubmed/438372`.

[71] R. N. Bracewell. *The Fourier Transform and Its Applications*. McGraw-Hill Higher Education, 3th edition, 2000.

[72] G. L. Brownell and W. H. Sweet. Localization of brain tumors with positron emitters. *Nucleonics*, 11:40 45, 1953.

[73] G. L. Brownell. A history of positron imaging. *Presentation prepared in celebration of the 50th year of services by the author to the Massachusetts General Hospital*, 1999.

[74] W. H. Sweet. The uses of nuclear disintegration in the diagnosis and treatment of brain tumor. *New England Journal of Medicine*, 245(23):875 878, 1951. URL `http://www.nejm.org/doi/full/10.1056/NEJM195112062452301`.

[75] F. R. Wrenn, M. L. Good, and P Handler. The use of positron-emitting radioisotopes for the localization of brain tumors. *Science*, 113(2940):525 527, 1951. URL `http://www.sciencemag.org/content/113/2940/525.short`.

[76] G. L. Brownell, C. A. Burnham, S. Wilensky, S. Aronow, H. Kazemi, and D. Strieder. New developments in positron scintigraphy and the application of cyclotron-produced positron emitters. In *Proceeding of the Symposium an Medical Radioisotope Scintigraphy*, pages 163 176, 1968.

[77] G. L. Brownell and C. A. Burnham. MGH positron camera. *NEREM 1972 RECORD*, 2:117, 1972.

[78] C.A. Burnham and G.L. Brownell. A multi-crystal positron camera. *Nuclear Science, IEEE Transactions on*, 19(3):201 205, June 1972. URL `http://ieeexplore.ieee.org/stamp/stamp.jsp?tp=&arnumber=4326726&isnumber=4326690`.

[79] D. A. Chesler. Three-dimensional activity distribution from multiple positron scintigraphs. *Journal of Nuclear Medicine*, 12:347 348, 1971.

[80] D. A. Chesler. Positron tomography and three-dimensional reconstruction technique. In G. S. Freedman, editor, *Tomographic Imaging in Nuclear Medicine*. The Society of Nuclear Medicine, New York, 1973.

[81] D. A. Chesler, B. Jr. Hoop, and G. L. Brownell. Transverse section imaging of myocardium with $^{13}nh_4$. *Journal of Nuclear Medicine*, 14:623, 1973.

[82] J. S. Robertson, R. B. Marr, M. Rosenblum, V. Radeka, and Y. L. Yamamoto. 32-crystal positron transverse section detector. In G. S. Freedman, editor, *Tomographic Imaging in Nuclear Medicine*. The Society of Nuclear Medicine, New York, 1973.

[83] Z. H. Cho, L. Eriksson, and J. K. Chan. A circular ring transverse axial positron camera. In M. M. Ter-Pogossian, editor, *Reconstruction Tomography in Diagnostic Radiology and Nuclear Medicine*. University Park Press, Baltimore, 1975.

[84] S.E. Derenzo, T.F. Budinger, John L. Cahoon, William L. Greenberg, R.H. Huesman, and Tony Vuletich. The Donner 280-crystal high resolution positron tomograph. *Nuclear Science, IEEE Transactions on*, 26(2):2790 2793, April 1979. URL `http://ieeexplore.ieee.org/xpl/abstractAuthors.jsp?arnumber=4330537`.

[85] C. Burnham, J. Bradshaw, D. Kaufman, D. Chesler, and G.L. Brownell. One dimensional scintillation cameras for positron Ect ring detectors. *Nuclear Science, IEEE Transactions on*, 28(1):109 113, February 1981. URL `http://ieeexplore.ieee.org/stamp/stamp.jsp?tp=&arnumber=4331149&isnumber=4331124`.

[86] C. A. Burnham, J. Bradshaw, D. Kaufman, D. A. Chesler, and G. L. Brownell. Positron source position sensing detector and electronics. Number 4,531,058. July 1985.

[87] G. L. Brownell, C. A. Burnham, and D. A. Chesler. High resolution tomograph using analog coding. In T. Greitz, D. H. Ingvar, and L. Widen, editors, *The metabolism of the human brain studies with positron emission tomography.* Raven Press, New York, 1985.

[88] C.A. Burnham, D.E. Kaufman, D.A. Chesler, C.W. Stearns, D. R. Wolfson, and G.L. Brownell. Cylindrical PET detector design. *Nuclear Science, IEEE Transactions on*, 35(1):675 679, February 1988. URL `http://ieeexplore.ieee.org/stamp/stamp.jsp?tp=&arnumber=12810&isnumber=545`.

[89] G. L. Brownell, C. A. Burnham, C. W. Stearns, D. A. Chesler, A.-L. Brownell, and M. R. Palmer. Developments in high-resolution positron emission tomography at MGH. *International Journal of Imaging Systems and Technology*, 1(2):207 217, 1989. URL `http://dx.doi.org/10.1002/ima.1850010210`.

[90] P. E. Valk, D. Delbeke, D. L. Bailey, D. W. Townsend, and M. N. Maisey, editors. *Positron emission tomography. Clinical practice.* Springer-Verlag, Lexington KY, 2011.

[91] C. Catana, D. Procissi, Y. Wu, M. S. Judenhofer, J. Qi, B. J. Pichler, R. E. Jacobs, and S. R. Cherry. Simultaneous in vivo positron emission tomography and magnetic resonance imaging. *Proceedings of the National Academy of Sciences*, 105(10):3705 3710, March 2008. URL `http://www.pnas.org/content/105/10/3705.long`.

[92] Wai-Hoi Wong, J. Uribe, K. Hicks, and Guoji Hu. An analog decoding BGO block detector using circular photomultipliers. *Nuclear Science, IEEE Transactions on*, 42(4):1095 1101, August 1995. URL `http://ieeexplore.ieee.org/stamp/stamp.jsp?tp=&arnumber=467742&isnumber=9846`.

[93] S.R. Cherry, Y. Shao, R.W. Silverman, K. Meadors, S. Siegel, A. Chatziioannou, J.W. Young, W.F. Jones, J. C. Moyers, D. Newport, A. Boutefnouchet, T.H. Farquhar, M. Andreaco, M.J. Paulus, D.M. Binkley, R. Nutt, and M.E. Phelps. MicroPET: a high resolution PET scanner for imaging small animals. *Nuclear Science, IEEE Transactions on*, 44(3):1161 1166, June 1997. URL `http://ieeexplore.ieee.org/stamp/stamp.jsp?tp=&arnumber=596981&isnumber=13077`.

[94] H. O. Anger. Scintillation camera and multiplane tomographic scanner. *Kaku Igaku*, 62:125 148, 1969.

[95] B. Pichler, E. Lorenz, R. Mirzoyan, W. Pimpl, F. Roder, M. Schwaiger, and S.I. Ziegler. Performance test of a LSO-APD PET module in a 9.4 Tesla magnet. In *Nuclear Science Symposium, 1997. IEEE*, volume 2, pages 1237 1239 vol.2, November 1997. URL `http://ieeexplore.ieee.org/stamp/stamp.jsp?tp=&arnumber=670533&isnumber=14740`.

[96] R. Lecomte, J. Cadorette, P. Richard, S. Rodrigue, and D. Rouleau. Design and engineering aspects of a high resolution positron tomograph for small animal imaging. *Nuclear Science, IEEE Transactions on*, 41(4):1446 1452, August 1994. URL `http://ieeexplore.ieee.org/stamp/stamp.jsp?tp=&arnumber=322930&isnumber=7706`.

[97] S. I. Ziegler, B. J. Pichler, G. Boening, M. Rafecas, W. Pimpl, E. Lorenz, N. Schmitz, and M. Schwaiger. A prototype high-resolution animal positron tomograph with avalanche photodiode arrays and LSO crystals. *European Journal of Nuclear Medicine and Molecular Imaging*, 28(2):136 143, February 2001. URL `http://www.ncbi.nlm.nih.gov/pubmed/11303882`.

[98] M. S. Judenhofer, H. F. Wehrl, D. F. Newport, C. Catana, S. B. Siegel, M. Becker, A. Thielscher, M. Kneilling, M. P. Lichy, M. Eichner, K. Klingel, G. Reischl, S. Widmaier, M. Rocken, R. E. Nutt, H. J. Machulla, K. Uludag, S. R. Cherry, C. D. Claussen, and B. J. Pichler. Simultaneous PET-MRI: a new approach for functional and morphological imaging. *Nature Medicine*, 14(4):459 465, April 2008. URL `http://www.ncbi.nlm.nih.gov/pubmed/18376410`.

[99] A. N. Otte, J. Barral, B. Dogolshein, J. Hose, S. Klemin, E. Lorenz, R. Mirzoyan, E. Popova, and M. Teshima. A test of silicon photomultipliers as readout for PET. *Nuclear Instruments and Methods in Physics Research Section A*, (545):705 715, 2005. URL `http://publications.mppmu.mpg.de/?action=search&mpi=MPP-2005-17`.

[100] Samuel Espana, Gustavo Tapias, Luis M. Fraile, Joaquin L. Herraiz, E. Vicente, Jose Udias, M. Desco, and Juan J. Vaquero. Performance evaluation of SiPM detectors for PET imaging in the presence of magnetic fields. In *Nuclear Science Symposium Conference Record, 2008. NSS '08. IEEE*, pages 3591 3595, October 2008. URL `http://ieeexplore.ieee.org/stamp/stamp.jsp?tp=&arnumber=4774097&isnumber=4774073`.

[101] P. E. Valk, D. L. Bailey, D. W. Townsend, and M. N. Maisey. *Positron Emission Tomography: Basic Science and Clinical Practice.* Springer-Verlag, New York, 2004.

[102] A. B. Brill and R. N. Beck. Evolution of clinical emission tomography. In M. N. Wernick and J. N. Aarsvold, editors, *Emission Tomography. The Fundamentals of SPECT and PET*. Elsevier, San Diego, 2004.

[103] Y. Demura, T. Tsuchida, T. Ishizaki, S. Mizuno, Y. Totani, S. Ameshima, I. Miyamori, M. Sasaki, and Y. Yonekura. 18F-FDG accumulation with PET for differentiation between benign and malignant lesions in the thorax. *Journal of Nuclear Medicine*, 44(4):540 548, April 2003. URL `http://jnm.snmjournals.org/content/44/4/540.long`.

[104] Shiga T., Morimoto Y., Kubo N., Katoh N., Katoh C., Takeuchi W., Usui R., Hirata K., Kojima S., Umegaki K., Shirato H., and Tamaki N. A new PET scanner with semiconductor detectors enables better identification of intratumoral inhomogeneity. *Journal of Nuclear Medicine*, 50(1):148 155, January 2009. URL `http://jnm.snmjournals.org/content/50/1/148.long`.

[105] De Lorenzo G., Chmeissani M., Uzun D., Kolstein M., Ozsahin I., Mikhaylova E., Arce P., Canadas M., Arino G., and Calderón Y. Pixelated CdTe detectors to overcome intrinsic limitations of crystal based positron emission mammographs. *Journal of Instrumentation*, 8(C01030), January 2013. URL `http://www.ncbi.nlm.nih.gov/pmc/articles/PMC3672962/`.

[106] Weidong Luo, E. Anashkin, and C.G. Matthews. Performance evaluation of a PEM scanner using the NEMA NU 4-2008 Small Animal PET standards. *Nuclear Science, IEEE Transactions on*, 57(1):94 103, February 2010. URL `http://ieeexplore.ieee.org/xpls/abs_all.jsp?arnumber=5409986&tag=1`.

[107] Raylman R.R., Majewski S., Weisenberger A. G., Popov V., Wojcik R., Kross B., Schreiman J. S., and Bishop H. A. Positron emission mammography-guided breast biopsy. *Journal of Nuclear Medicine*, 42(6):960 966, June 2001. URL `http://jnm.snmjournals.org/content/42/6/960.long`.

[108] P. H. Jarritt, K. J. Carson, A. R. Hounsell, and D. Visvikis. The role of PET/CT scanning in radiotherapy planning. *The British Journal of Radiology*, 79:S27 S35, 2006. URL `http://dx.doi.org/10.1259/bjr/35628509`.

[109] Grégoire V., Haustermans K., Geets X., Roels S., and Lonneux M. PET-based treatment planning in radiotherapy: a new standard? *Journal of Nuclear Medicine*, 48(1):68S 77S, January 2007. URL `http://jnm.snmjournals.org/content/48/1_suppl/68S.long`.

[110] S. M. Bentzen. Radiation therapy: Intensity modulated, image guided, biologically optimized and evidence based. *Radiotherapy and Oncology*, 77(3): 227 230, 2005. URL `http://www.sciencedirect.com/science/article/pii/S0167814005004949`.

[111] Bernier J., Hall E. J., and Giaccia A. Radiation oncology: a century of achievements. *Nature Reviews Cancer*, 4(9):737 747, September 2004. URL `http://www.nature.com/nrc/journal/v4/n9/full/nrc1451.html`.

[112] H. Zaidi, H. Vees, and M. Wissmeyer. Molecular PET/CT imaging-guided radiation therapy treatment planning. *Academic Radiology*, 16(9): 1108 1133, 2009. URL `http://www.sciencedirect.com/science/article/pii/S1076633209001445`.

[113] Ford E. C., Herman J., Yorke E., and Wahl R. L. 18F-FDG PET/CT for image-guided and intensity-modulated radiotherapy. *Journal of Nuclear Medicine*, 50 (10):1655 1665, October 2009. URL `http://jnm.snmjournals.org/content/50/10/1655.long`.

[114] Gupta T. and Beriwal S. PET/CT-guided radiation therapy planning: from present to the future. *Indian Journal of Cancer*, 47(2):126 133, April-June 2010. URL `http://www.ncbi.nlm.nih.gov/pubmed/20448373`.

[115] URL `http://www.abta.org/news/brain-tumor-fact-sheets/`.

[116] Jemal A., Siegel R., Xu J., and Ward E. Cancer statistics, 2010. *CA: A Cancer Journal for Clinicians*, 60(5):277 300, September-October 2010. URL `http://www.ncbi.nlm.nih.gov/pubmed/20610543`.

[117] Alzheimer s Association. 2012 Alzheimer s disease facts and figures. *Alzheimer's & Dementia*, 8(2), 2012.

[118] R. Brookmeyer, S. Gray, and C. Kawas. Projections of Alzheimer s disease in the United States and the public health impact of delaying disease onset. *American Journal of Public Health*, 88(9):1337 1342, September 1998. URL `http://www.ncbi.nlm.nih.gov/pmc/articles/PMC1509089/`.

[119] Minoshima S., Giordani B., Berent S., Frey K. A., Foster N. L., and Kuhl D. E. Metabolic reduction in the posterior cingulate cortex in very early Alzheimer s disease. *Annals of Neurology*, 42(1):85 94, July 1997. URL `http://www.ncbi.nlm.nih.gov/pubmed/9225689`.

[120] Hu M. T., Taylor-Robinson S. D., Chaudhuri K. R., Bell J. D., Labbé C., Cunningham V. J., Koepp M. J., Hammers A., Morris R. G., Turjanski N., and Brooks D. J. Cortical dysfunction in non-demented Parkinson s disease patients: a combined (31)P-MRS and (18)FDG-PET study. *Brain*, 123(Pt 2):340 352, February 2000. URL `http://brain.oxfordjournals.org/content/123/2/340.long`.

[121] Engel J. Jr., Kuhl D. E., and Phelps M. E. Regional brain metabolism during seizures in humans. *Advances in Neurology*, 34:141 148, 1983.

[122] Leiderman D. B., Albert P., Balish M., Bromfield E., and Theodore W. H. The dynamics of metabolic change following seizures as measured by positron emission tomography with fludeoxyglucose F-18. *Archives of Neurology*, 51(9):932 936, 1994. URL `http://dx.doi.org/10.1001/archneur.1994.00540210106019`.

[123] P. A. Erba, M. Sollini, E. Lazzeri, and G. Mariani. FDG-PET in cardiac infections. *Seminars in Nuclear Medicine*, 43(5):377 395, 2013. URL `http://www.sciencedirect.com/science/article/pii/S000129981300038X`.

[124] James O. G., Christensen J. D., Wong T. Z., Borges-Neto S., and Koweek L. M. Utility of FDG PET/CT in inflammatory cardiovascular disease. *RadioGraphics*, 31(5):1271 1286, 2011. URL `http://pubs.rsna.org/doi/abs/10.1148/rg.315105222`.

[125] T. H. Marwick, K. Shan, S. Patel, R. T. Go, and M. S. Lauer. Incremental value of Rubidium-82 positron emission tomography for prognostic assessment of known or suspected coronary artery disease. *The American Journal of Cardiology*, 80(7):865 870, 1997. URL `http://www.sciencedirect.com/science/article/pii/S0002914997005377`.

[126] P. Suetens. *Fundamentals of medical imaging.* Cambridge University Press, New York, 2nd edition, 2009.

[127] M. Conti. Focus on time-of-flight PET: the benefits of improved time resolution. *European Journal of Nuclear Medicine and Molecular Imaging*, 38(6):1147 1157, 2011. URL `http://dx.doi.org/10.1007/s00259-010-1711-y`.

[128] Allemand R., Gresset C., and Vacher J. Potential advantages of a cesium fluoride scintillator for a time-of-flight positron camera. *Journal of Nuclear Medicine*, 21 (2):153 155, February 1980. URL `http://jnm.snmjournals.org/content/21/2/153.long`.

[129] N. A. Mullani, D. C. Ficke, R. Hartz, J. Markham, and G. Wong. System design of fast PET scanners utilizing time-of-flight. *Nuclear Science, IEEE Transactions on*, 28(1):104 108, February 1981. URL `http://ieeexplore.ieee.org/xpls/abs_all.jsp?arnumber=4331148&tag=1`.

[130] W.W. Moses and S.E. Derenzo. Prospects for time-of-flight PET using LSO scintillator. *Nuclear Science, IEEE Transactions on*, 46(3):474 478, June 1999. URL `http://ieeexplore.ieee.org/xpls/abs_all.jsp?arnumber=775565`.

[131] M. Moszynski, M. Kapusta, A. Nassalski, T. Szczesniak, D. Wolski, L. Eriksson, and C.L. Melcher. New prospects for time-of-flight PET with LSO scintillators. *Nuclear Science, IEEE Transactions on*, 53(5):2484 2488, October 2006. URL `http://ieeexplore.ieee.org/stamp/stamp.jsp?tp=&arnumber=1710226&isnumber=36084`.

[132] Conti M., Bendriem B., Casey M., Chen M., Kehren F., Michel C., and Panin V. First experimental results of time-of-flight reconstruction on an LSO PET scanner. *Physics in Medicine and Biology*, 50(19):4507 4526, October 2005. URL `http://www.ncbi.nlm.nih.gov/pubmed/16177486`.

[133] Surti S., Kuhn A., Werner M. E., Perkins A. E., Kolthammer J., and Karp J. S. Performance of Philips Gemini TF PET/CT scanner with special consideration for its time-of-flight imaging capabilities. *Journal of Nuclear Medicine*, 48(3):471 480, March 2007. URL `http://jnm.snmjournals.org/content/48/3/471.long`.

[134] R. Lecomte. Novel detector technology for clinical PET. *European Journal of Nuclear Medicine and Molecular Imaging*, 36(1):69 85, 2009. URL `http://dx.doi.org/10.1007/s00259-008-1054-0`.

[135] C. Degenhardt, G. Prescher, T. Frach, A. Thon, R. de Gruyter, A. Schmitz, and R. Ballizany. The digital silicon photomultiplier a novel sensor for the detection of scintillation light. In *Nuclear Science Symposium Conference Record (NSS/MIC), 2009 IEEE*, pages 2383 2386, October 2009. URL `http://ieeexplore.ieee.org/xpls/abs_all.jsp?arnumber=5402190`.

[136] E. Even-Sapir, Z. Keidar, and R. Bar-Shalom. Hybrid imaging (SPECT/CT and PET/CT) improving the diagnostic accuracy of functional/metabolic and anatomic imaging. *Seminars in Nuclear Medicine*, 39(4):264 275, 2009. URL `http://www.sciencedirect.com/science/article/pii/S0001299809000178`.

[137] D. Delbeke, H. Schoder, W. H. Martin, and R. L. Wahl . Hybrid imaging (SPECT/CT and PET/CT): Improving therapeutic decisions. *Seminars in Nuclear Medicine*, 39(5):308 340, 2009. URL `http://www.sciencedirect.com/science/article/pii/S0001299809000154`.

[138] Beyer T., Townsend D. W., Brun T., Kinahan P. E., Charron M., Roddy R., Jerin J., Young J., Byars L., and Nutt R. A combined PET/CT scanner for clinical oncology. *Journal of Nuclear Medicine*, 41(8):1369 1379, August 2000. URL `http://jnm.snmjournals.org/content/41/8/1369.long`.

[139] D. W. Townsend and T. Beyer. A combined PET/CT scanner: the path to true image fusion. *The British Journal of Radiology*, 75:24 30, November 2002. URL `http://www.ncbi.nlm.nih.gov/pubmed/12519732`.

[140] W. D. Heiss. The potential of PET/MR for brain imaging. *European Journal of Nuclear Medicine and Molecular Imaging*, 36(1):105 112, 2009. URL `http://dx.doi.org/10.1007/s00259-008-0962-3`.

[141] G. Antoch and A. Bockisch. Combined PET/MRI: a new dimension in whole-body oncology imaging? *European Journal of Nuclear Medicine and Molecular Imaging*, 36(1):113 120, 2009. URL `http://dx.doi.org/10.1007/s00259-008-0951-6`.

[142] S. G. Nekolla, A. Martinez-Moeller, and A. Saraste. PET and MRI in cardiac imaging: from validation studies to integrated applications. *European Journal of Nuclear Medicine and Molecular Imaging*, 36(1):121 130, 2009. URL `http://dx.doi.org/10.1007/s00259-008-0980-1`.

[143] B. E. Hammer, N. L. Christensen, and B. G. Heil. Use of a magnetic field to increase the spatial resolution of positron emission tomography. *Medical Physics*, 21 (12):1917 1920, December 1994. URL `http://www.ncbi.nlm.nih.gov/pubmed/7700198`.

[144] M. S. Judenhofer, H. F. Wehrl, D. F. Newport, C. Catana, S. B. Siegel, M. Becker, A. Thielscher, M. Kneilling, M. P. Lichy, M. Eichner, K. Klingel, G. Reischl, S. Widmaier, M. Rocken, R. E. Nutt, H. J. Machulla, K. Uludag, S. R. Cherry, C. D. Claussen, and B. J. Pichler. Simultaneous PET-MRI: a new approach for functional and morphological imaging. *Nature Medicine*, 14(4):459 465, April 2008. URL `http://dx.doi.org/10.1038/nm1700`.

[145] B. J. Pichler, H. F. Wehrl, A. Kolb, and M. S. Judenhofer. Positron emission tomography/Magnetic resonance imaging: The next generation of multimodality imaging? *Seminars in Nuclear Medicine*, 38(3):199 208, 2008. URL `http://www.sciencedirect.com/science/article/pii/S000129980800024X`.

[146] Catana C., Wu Y., Judenhofer M. S., Qi J., Pichler B. J., and Cherry S. R. Simultaneous acquisition of multislice PET and MR images: initial results with a MR-compatible PET scanner. *Journal of Nuclear Medicine*, 47(12):1968 1976, December 2006. URL `http://jnm.snmjournals.org/content/47/12/1968.long`.

[147] D. J. Wagenaar. CdTe and CdZnTe semiconductor detectors for nuclear medicine imaging. In M. N. Wernick and J. N. Aarsvold, editors, *Emission Tomography. The Fundamentals of SPECT and PET*. Elsevier, San Diego, 2004.

[148] J.C. Lund, R. Olsen, J. M. Van Scyoc, and R.B. James. The use of pulse processing techniques to improve the performance of Cd1-xZnxTe gamma-ray spectrometers. *Nuclear Science, IEEE Transactions on*, 43(3):1411 1416, June 1996. URL `http://ieeexplore.ieee.org/stamp/stamp.jsp?tp=&arnumber=507075&isnumber=10977`.

[149] Y. Gu, J. L. Matteson, R. T. Skelton, A. C. Deal, E. A. Stephan, F. Duttweiler, T. M. Gasaway, and C. S. Levin. Study of a high-resolution, 3D positioning cadmium zinc telluride detector for PET. *Physics in Medicine and Biology*, 56(6):1563 1584, March 2011. URL `http://www.ncbi.nlm.nih.gov/pubmed/21335649`.

[150] P. Vaska, D. H. Kim, S. Southekal, J.-F. Pratte, J. Fried, S. Krishnamoorthy, S. Stoll, and A. Bolotnikov. Ultra-high resolution PET: A CZT-based scanner for the mouse brain. *Journal of Nuclear Medicine Meeting Abstracts*, 50(2): 293, 2009. URL `http://jnumedmtg.snmjournals.org/cgi/content/short/50/2_MeetingAbstracts/293`.

[151] P. Vaska, A. Dragone, W. Lee, D. H Kim, J-F Pratte, Y. G Cui, J. Fried, S. Krishnamoorthy, A. Bolotnikov, S. J Park, P. O Connor, F. A. Dilmanian, and R.B. James. A prototype CZT-based PET scanner for high resolution mouse brain imaging. In *Nuclear Science Symposium Conference Record, 2007. NSS '07. IEEE*, volume 5, pages 3816 3819, October 2007. URL `http://ieeexplore.ieee.org/stamp/stamp.jsp?tp=&arnumber=4436952&isnumber=4436808`.

[152] Shiga T., Morimoto Y., Kubo N., Katoh N., Katoh C., Takeuchi W., Usui R., Hirata K., Kojima S., Umegaki K., Shirato H., and Tamaki N. A new PET scanner with semiconductor detectors enables better identification of intratumoral

inhomogeneity. *Journal of Nuclear Medicine*, 50(1):148 155, January 2009. URL `http://jnm.snmjournals.org/content/50/1/148.long`.

[153] Y. Morimoto, Y. Ueno, W. Takeuchi, S. Kojima, K. Matsuzaki, T. Ishitsu, K. Umegaki, Y. Kiyanagi, N. Kubo, C. Katoh, T. Shiga, H. Shirato, and N. Tamaki. Development of a 3D brain PET scanner using CdTe semiconductor detectors and its first clinical application. *Nuclear Science, IEEE Transactions on*, 58(5):2181 2189, October 2011. URL `http://ieeexplore.ieee.org/stamp/stamp.jsp?tp=&arnumber=5771139&isnumber=6041077`.

[154] URL `www.vip-erc.com`.

[155] Y. Calderon, M. Kolstein, D. Uzun, G. De Lorenzo, M. Chmeissani, P. Arce, G. Arino, E. Cabruja, M. Canadas, J.G. Macias-Montero, R. Martinez, E. Mikhaylova, I. Ozsahin, and C. Puigdengoles. Modeling, simulation, and evaluation of a Compton camera based on a pixelated solid-state detector. In *Nuclear Science Symposium and Medical Imaging Conference (NSS/MIC), 2011 IEEE*, pages 2708 2715, October 2011. URL `http://ieeexplore.ieee.org/stamp/stamp.jsp?tp=&arnumber=6152954&isnumber=6152483`.

[156] G. Arino, M. Chmeissani, C. Puigdengoles, G. De Lorenzo, R. Diener, P. Arce, E. Cabruja, Y. Calderon, M. Canadas, M. Kolstein, J. Macias-Montero, R. Martinez, E. Mikhaylova, I. Ozsahin, and D. Uzun. Characterization of CdTe detector for use in PET. In *Nuclear Science Symposium and Medical Imaging Conference (NSS/MIC), 2011 IEEE*, pages 4598 4603, October 2011. URL `http://ieeexplore.ieee.org/stamp/stamp.jsp?tp=&arnumber=6154742&isnumber=6152483`.

[157] J. S. Karp, R. Freifelder, M. J. Geagan, G. Muehllehner, P. E. Kinahan, R. M. Lewitt, and L. Shao. Three-dimensional imaging characteristics of the HEAD PENN-PET scanner. *Journal of Nuclear Medicine*, 38(4):636 643, April 1997. URL `http://jnm.snmjournals.org/content/38/4/636.long`.

[158] J.-G. Macias-Montero, M. Sarraj, M. Chmeissani, C. Puigdengoles, G. De Lorenzo, and R. Martinez. Toward VIP-PIX: A low noise readout ASIC for pixelated CdTe gamma-ray detectors for use in the next generation of PET scanners. *Nuclear Science, IEEE Transactions on*, 60(4):2898 2904, August 2013. URL `http://ieeexplore.ieee.org/stamp/stamp.jsp?tp=&arnumber=6558497&isnumber=6579689`.

[159] G. Blanchot, M. Chmeissani, A. Díaz, F. Díaz, J. Fernández, E. García, J. García, F. Kainberger, M. Lozano, M. Maiorino, R. Martínez, J.P. Montagne, I. Moreno,

G. Pellegrini, C. Puigdengoles, M. Sentís, L. Teres, M. Tortajada, and M. Ullán. Dear-Mama: A photon counting X-ray imaging project for medical applications. *Nuclear Instruments and Methods in Physics Research Section A: Accelerators, Spectrometers, Detectors and Associated Equipment*, 569(1):136 139, 2006. URL `http://www.sciencedirect.com/science/article/pii/S0168900206016147`.

[160] C.E. Ordonez, A. Bolozdynya, and Wei Chang. Doppler broadening of energy spectra in Compton cameras. In *Nuclear Science Symposium, 1997. IEEE*, volume 2, pages 1361 1365, November 1997. URL `http://ieeexplore.ieee.org/stamp/stamp.jsp?tp=&arnumber=670574&isnumber=14740`.

[161] W. L. Rogers, N. H. Clinthorne, and A. Bolozdynya. Compton camera for nuclear medical imaging. In M. N. Wernick and J. N. Aarsvold, editors, *Emission Tomography: The Fundamentals of SPECT and PET*. Elsevier Academic Press, 2004.

[162] P. Arce, J. I. Lagares, L. Harkness, D. Pérez-Astudillo, M. Canadas, P. Rato, M. De Prado, Y. Abreu, G. De Lorenzo, M. Kolstein, and A. Díaz. Gamos: A framework to do Geant4 simulations in different physics fields with an user-friendly interface. *Nuclear Instruments and Methods in Physics Research Section A: Accelerators, Spectrometers, Detectors and Associated Equipment*, 735(0):304 313, 2014. URL `http://www.sciencedirect.com/science/article/pii/S0168900213012709`.

[163] *NEMA standards publication NU 2-2001: Performance measurements of positron emission tomographs*. National Electrical Manufacturers Association, Rosslyn, VA, 2001.

[164] *NEMA standards publication NU 4-2008: Performance measurements for small animal positron emission tomographs*. National Electrical Manufacturers Association, Rosslyn, VA, 2008.

[165] Geant4 a simulation toolkit. *Nuclear Instruments and Methods in Physics Research Section A: Accelerators, Spectrometers, Detectors and Associated Equipment*, 506(3):250 303, 2003. URL `http://www.sciencedirect.com/science/article/pii/S0168900203013688`.

[166] K. Thielemans, S. Mustafovic, and C. Tsoumpas. STIR: Software for tomographic image reconstruction release 2. In *Nuclear Science Symposium Conference Record, 2006. IEEE*, volume 4, pages 2174 2176, October 2006. URL `http://ieeexplore.ieee.org/stamp/stamp.jsp?tp=&arnumber=4179459&isnumber=4179395`.

[167] P.J. Sellin, A. W. Davies, A. Lohstroh, M.E. Ozsan, and J. Parkin. Drift mobility and mobility-lifetime products in CdTe:Cl grown by the travelling heater method. *Nuclear Science, IEEE Transactions on*, 52(6):3074 3078, December 2005. URL `http://ieeexplore.ieee.org/stamp/stamp.jsp?tp=&arnumber=1589323&isnumber=33494`.

[168] G. Arino, M. Chmeissani, G. De Lorenzo, C. Puigdengoles, E. Cabruja, Y. Calderon, M. Kolstein, J. G. Macias-Montero, R. Martinez, E. Mikhaylova, and D. Uzun. Energy and coincidence time resolution measurements of CdTe detectors for PET. *Journal of Instrumentation*, 8, February 2013. http://www.ncbi.nlm.nih.gov/pubmed/23750177.

[169] Gerard Arino. Characterization and simulation of a CdTe detector for use in PET. Master s thesis, Universitat Autónoma de Barcelona, Spain, 2012.

[170] Edmund J. F. Dickinson, H. Ekstrom, and E. Fontes. COMSOL multiphysics®: Finite element software for electrochemical analysis. a mini-review. *Electrochemistry Communications*, 40:71 74, 2014. URL `http://www.sciencedirect.com/science/article/pii/S1388248113004840`.

[171] H. W. de Jong, F. H. van Velden, R. W. Kloet, F. L. Buijs, R. Boellaard, and A. A. Lammertsma. Performance evaluation of the ECAT HRRT: an LSO-LYSO double layer high resolution, high sensitivity scanner. *Physics in Medicine and Biology*, 52(5):1505 1526, March 2007. URL `http://www.ncbi.nlm.nih.gov/pubmed/17301468`.

[172] J. S. Karp, S. Surti, M. E. Daube-Witherspoon, R. Freifelder, C. A. Cardi, L. E. Adam, K. Bilger, and G. Muehllehner. Performance of a brain PET camera based on anger-logic gadolinium oxyorthosilicate detectors. *Journal of Nuclear Medicine*, 44(8):1340 1349, August 2003. URL `http://jnm.snmjournals.org/content/44/8/1340.long`.

[173] W. Wong. A positron camera detector design with cross-coupled scintillators and quadrant sharing photomultipliers. *Nuclear Science, IEEE Transactions on*, 40(4):962 966, August 1993. URL `http://ieeexplore.ieee.org/stamp/stamp.jsp?tp=&arnumber=256693&isnumber=6500`.

[174] Wai-Hoi Wong, J. Uribe, K. Hicks, and M. Zambelli. A 2-dimensional detector decoding study on BGO arrays with quadrant sharing photomultipliers. *Nuclear Science, IEEE Transactions on*, 41(4):1453 1457, August 1994. URL `http://ieeexplore.ieee.org/stamp/stamp.jsp?tp=&arnumber=322918&isnumber=7706`.

[175] M. Canadas, M. Embid, Eduardo Lage, M. Desco, J.J. Vaquero, and J.M. Pérez. NEMA NU 4-2008 performance measurements of two commercial small-animal PET scanners: ClearPET and rPET-1. *Nuclear Science, IEEE Transactions on*, 58(1):58 65, February 2011. URL `http://ieeexplore.ieee.org/stamp/stamp.jsp?tp=&arnumber=5621941&isnumber=5710485`.

[176] Q. Bao, D. Newport, M. Chen, D. B. Stout, and A. F. Chatziioannou. Performance evaluation of the Inveon dedicated PET preclinical tomograph based on the NEMA NU-4 standards. *Journal of Nuclear Medicine*, 50(3):401 408, March 2009. URL `http://jnm.snmjournals.org/content/50/3/401.long`.

[177] R. Prasad, O. Ratib, and H. Zaidi. NEMA NU-04-based performance characteristics of the LabPET-8TM small animal PET scanner. *Physics in Medicine and Biology*, 56(20):6649 6664, October 2011. URL `http://www.ncbi.nlm.nih.gov/pubmed/21941029`.

[178] M. E. Daube-Witherspoon and G. Muehllehner. Treatment of axial data in three-dimensional PET. *Journal of Nuclear Medicine*, 28(11):1717 1724, November 1987. URL `http://www.ncbi.nlm.nih.gov/pubmed/3499493`.

[179] URL `http://www.nucleide.org/DDEP_WG/Nuclides/F-18_tables.pdf`.

[180] C. X. Wang, W. E. Snyder, G. Bilbro, and P. Santago. Performance evaluation of filtered backprojection reconstruction and iterative reconstruction methods for PET images. *Computers in Biology and Medicine*, 28(1):13 25, 1998. URL `http://www.sciencedirect.com/science/article/pii/S0010482597000310`.

[181] T. Villafana. *Advantages, limitations and signigicance of the modulation transfer function in radiologic practice (Current problems in diagnostic radiology)*. Year-Book Medical Publishers, Chicago, IL, 1978.

[182] T. F. Budinger, S. E. Derenzo, G. T. Gullberg, W. L. Greenberg, and R. H. Huesman. Emission computer assisted tomography with single-photon and positron annihilation photon emitters. *Journal of Computer Assisted Tomography*, 1(1): 131 145, January 1977. URL `http://www.ncbi.nlm.nih.gov/pubmed/615887`.

[183] J. R. Stickel and S. R. Cherry. High-resolution PET detector design: modelling components of intrinsic spatial resolution. *Physics in Medicine and Biology*, 50(2): 179 195, January 2005. URL `http://www.ncbi.nlm.nih.gov/pubmed/15742938`.

[184] A. Todd-Pokropek, T. D. Cradduck, and F. Deconinck. A file format for the exchange of nuclear medicine image data: a specification of Interfile version 3.3. URL `http://www.nucmed.si.mahidol.ac.th/nucmed1/pip/interfil1.html`.

[185] URL `http://www.rpdinc.com/pet-phantom-nema-2007-iec-2008-4971.html`.

[186] H. Herzog, L. Tellmann, C. Hocke, U. Pietrzyk, M.E. Casey, and T. Kuwert. NEMA NU 2-2001 guided performance evaluation of four Siemens ECAT PET scanners. *Nuclear Science, IEEE Transactions on*, 51(5):2662 2669, October 2004. URL `http://ieeexplore.ieee.org/stamp/stamp.jsp?tp=&arnumber=1344391&isnumber=29604`.

[187] URL `medical.nema.org/dicom/geninfo/Brochure.pdf`.